

Fluorescence fluctuation spectroscopy techniques to quantify molecular interactions and dynamics in complex biological systems

KUMULATIVE DISSERTATION

zur Erlangung des akademischen Grades

Doctor rerum naturalium (Dr. rer. nat.)

in der Wissenschaftsdisziplin *Biologische Physik*

eingereicht an der

Mathematisch-Naturwissenschaftlichen Fakultät der Universität Potsdam

Institut für Physik und Astronomie

von

Valentin Dunsing, M.Sc.

geboren am 08.09.1989 in Berlin-Köpenick

Gutachter:

1. Prof. Dr. Salvatore Chiantia
2. Prof. Dr. Carsten Beta
3. Prof. Dr. Thorsten Wohland

Tag der mündlichen Prüfung: 15. Juli 2020



Published online on the
Publication Server of the University of Potsdam:
<https://doi.org/10.25932/publishup-47849>
<https://nbn-resolving.org/urn:nbn:de:kobv:517-opus4-478494>

Zusammenfassung

Die Funktion lebender Zellen basiert auf Transport und Interaktion von Biomolekülen. Zur genauen Untersuchung dieser dynamischen Prozesse in lebenden Zellen eignen sich Fluoreszenzfluktuationsspektroskopieverfahren (FFS). Diese nutzen durch Diffusion oder andere Prozesse auftretende Fluktuationen, um Größen auf molekularer Skala durch statistische Analyse des Signals fluoreszenzmarkierter Moleküle zu ermitteln. Insbesondere können die Konzentration der Moleküle und ihre mittlere Verweildauer im Beobachtungsvolumen quantifiziert werden. Außerdem lassen sich molekulare Interaktionen anhand des mittleren Signals pro Molekül, der sogenannten molekularen Helligkeit, und der Kreuzkorrelation der Signale verschieden markierter Moleküle untersuchen.

In der vorliegenden Arbeit wurden verschiedene FFS Methoden etabliert und zur Erforschung biologischer Prozesse genutzt. Um Dynamiken und Bindungsvorgänge an der Zellmembran zu untersuchen, wurde Fluoreszenzkorrelationsspektroskopie (FCS) unter Nutzung eines linearen Scanwegs (sFCS) verwendet. Außerdem wurde die Oligomerisierung von Proteinen mittels Number&Brightness (N&B) Analyse räumlich aufgelöst. Verschiedene Korrekturverfahren wurden validiert und angewandt, um die erhobenen Daten von Störquellen wie Bleichen der Fluorophore oder Hintergrundsignalen zu bereinigen sowie instrumentelle Größen wie Detektionsrauschen zu kalibrieren. Darüber hinaus konnten durch spektral aufgelöste Aufnahme des Fluoreszenzsignals sowie Analyse höherer statistischer Momente mehrere Molekülpopulationen gleichzeitig detektiert werden.

Mittels Zweifarben-sFCS und -N&B wurde anschließend das Amyloidvorläuferprotein APLP1 untersucht, welches an Synapsen, den Kontaktstellen von Neuronen, lokalisiert. Mit dem verwendeten Ansatz konnte zum ersten Mal direkt in lebenden Zellen nachgewiesen werden, dass APLP1 spezifische Bindungen an Zellkontaktstellen eingeht. Des Weiteren konnte gezeigt werden, dass Zinkionen eine Anreicherung und verstärkte Interaktion von APLP1 induzieren. Diese Beobachtungen unterstützen die Hypothese, dass APLP1 die Adhäsion benachbarter Zellen vermittelt und diese Funktion konzentrationsabhängig durch Zinkionen reguliert wird.

Zur Untersuchung von APLP1 wurde es genetisch mit Fluoreszenzproteinen wie dem rot fluoreszierenden Protein mCardinal fusioniert. Bei der Bestimmung des Oligomerisierungszustands von APLP1 ergaben sich unter Verwendung verschiedener Fluorophore unterschiedliche Ergebnisse. Diese deuteten darauf hin, dass ein Teil der mCardinal Proteine nicht fluoreszierte. Um zu einem tieferen Verständnis dieses Phänomens und dessen Einfluss auf Interaktionsmessungen zu gelangen, wurden häufig

verwendete Fluoreszenzproteine systematisch evaluiert. Auf diese Weise konnten zwei Proteine identifiziert werden, grün fluoreszierendes mEGFP und rot fluoreszierendes mCherry2, die den geringsten Anteil an nicht fluoreszierenden Zuständen aufweisen und sich deshalb am besten für Interaktionsmessungen eignen. Mittels eines einfachen Korrekturschemas basierend auf der experimentellen Bestimmung des nicht fluoreszierenden Anteils konnten genaue Messungen des Oligomerisierungszustandes von Proteinen in lebenden Zellen vorgenommen werden, was für biologisch relevante Proteine mit bis zu 12 Untereinheiten erfolgreich gezeigt werden konnte.

Im letzten Teil der Arbeit wurden Diffusionsvorgänge in bakteriellen Biofilmen untersucht. Biofilme werden von Bakterienkolonien gebildet, die auf Oberflächen wachsen und beispielsweise zur Verbreitung multiresistenter Keime in Krankenhäusern beitragen. Bei der Bildung von Biofilmen spielen Polymere, die von Bakterien produziert werden, eine entscheidende Rolle. Diese füllen die Zwischenräume im Biofilm mit einer Art Gel, der sogenannten Biofilmmatrix. Anhand von FCS und Einzelpartikelverfolgung konnte gezeigt werden, dass Diffusion von Partikeln in einem rekonstituierten Gel stark von deren Größe sowie der Konzentration der Polymere abhängt. Das untersuchte System bestand hierbei aus langkettigen Zuckermolekülen, die von Biofilmen aufgereinigt wurden und als Modellsystem für die Biofilmmatrix dienten. Im physiologischen Konzentrationsbereich bildete sich ein Polymernetzwerk aus, durch das sich kleine Teilchen frei bewegen konnten, größere Partikel wie z.B. Bakteriophagen jedoch stark verlangsamt wurden. Dies lässt vermuten, dass die Biofilmmatrix die Funktion eines größenabhängigen Filters aufweist. Zersetzung der Polymere mittels Enzymen, die natürlich in Bakteriophagen vorkommen, führte zu freier Diffusion auch größerer Partikel. Die gewonnenen Ergebnisse deuten darauf hin, dass solche Enzyme für Phagen eine Schlüsselfunktion besitzen, um Biofilme besser durchdringen und somit Bakterien effizienter infizieren zu können. In Kombination mit Bakteriophagen könnten (zielgerichtet optimierte) Enzyme dieser Art eine vielversprechende, spezifischere Alternative zu konventionellen Antibiotika bei der Bekämpfung multiresistenter Keime darstellen.

Abstract

Living cells rely on transport and interaction of biomolecules to perform their diverse functions. A powerful toolbox to study these highly dynamic processes in the native environment is provided by fluorescence fluctuation spectroscopy (FFS) techniques. In more detail, FFS takes advantage of the inherent dynamics present in biological systems, such as diffusion, to infer molecular parameters from fluctuations of the signal emitted by an ensemble of fluorescently tagged molecules. In particular, two parameters are accessible: the concentration of molecules and their transit times through the observation volume. In addition, molecular interactions can be measured by analyzing the average signal emitted per molecule - the molecular brightness - and the cross-correlation of signals detected from differently tagged species.

In the present work, several FFS techniques were implemented and applied in different biological contexts. In particular, scanning fluorescence correlation spectroscopy (sFCS) was performed to measure protein dynamics and interactions at the plasma membrane (PM) of cells, and number and brightness (N&B) analysis to spatially map molecular aggregation. To account for technical limitations and sample related artifacts, e.g. detector noise, photobleaching, or background signal, several correction schemes were explored. In addition, sFCS was combined with spectral detection and higher moment analysis of the photon count distribution to resolve multiple species at the PM.

Using scanning fluorescence cross-correlation spectroscopy and cross-correlation N&B, the interactions of amyloid precursor-like protein 1 (APLP1), a synaptic membrane protein, were investigated. It is shown for the first time directly in living cells, that APLP1 undergoes specific interactions at cell-cell contacts. It is further demonstrated that zinc ions induce formation of large APLP1 clusters that enrich at contact sites and bind to clusters on the opposing cell. Altogether, these results provide direct evidence that APLP1 is a zinc ion dependent neuronal adhesion protein.

In the context of APLP1, discrepancies of oligomeric state estimates were observed, which were attributed to non-fluorescent states of the chosen red fluorescent protein (FP) tag mCardinal (mCard). Therefore, multiple FPs and their performance in FFS based measurements of protein interactions were systematically evaluated. The study revealed superior properties of monomeric enhanced green fluorescent protein (mEGFP) and mCherry2. Furthermore, a simple correction scheme allowed unbiased *in situ* measurements of protein oligomerization by quantifying non-fluorescent state fractions of FP tags. The procedure was experimentally confirmed for biologically relevant protein complexes consisting of up to 12 monomers.

In the last part of this work, fluorescence correlation spectroscopy (FCS) and single particle tracking (SPT) were used to characterize diffusive transport dynamics in a bacterial biofilm model. Biofilms are surface adherent bacterial communities, whose structural organization is provided by extracellular polymeric substances (EPS) that form a viscous polymer hydrogel. The presented study revealed a probe size and polymer concentration dependent (anomalous) diffusion hindrance in a reconstituted EPS matrix system caused by polymer chain entanglement at physiological concentrations. This result indicates a meshwork-like organization of the biofilm matrix that allows free diffusion of small particles, but strongly hinders diffusion of larger particles such as bacteriophages. Finally, it is shown that depolymerization of the matrix by phage derived enzymes rapidly facilitated free diffusion. In the context of phage infections, such enzymes may provide a key to evade trapping in the biofilm matrix and promote efficient infection of bacteria. In combination with phage application, matrix depolymerizing enzymes may open up novel antimicrobial strategies against multiresistant bacterial strains, as a promising, more specific alternative to conventional antibiotics.

Contents

Zusammenfassung	I
Abstract	III
1 Introduction	1
1.1 Fluorescence fluctuation spectroscopy	1
1.2 Particle transport in biological systems	6
1.2.1 Directed transport and diffusion	6
1.2.2 Measuring particle transport with single particle tracking and fluorescence correlation spectroscopy	8
1.3 Aims and content of the thesis	10
1.3.1 Implementation of fluorescence fluctuation spectroscopy to quantify protein-protein interactions mediating cell-cell adhe- sion, applied to amyloid precursor-like protein 1	11
1.3.2 Systematic evaluation of fluorescent proteins for molecular brightness and cross-correlation analysis	12
1.3.3 Characterization of diffusion dynamics in bacterial biofilms . .	14
1.3.4 Publications	16
2 Results	19
2.1 [P1] Direct evidence of amyloid precursor-like protein 1 <i>trans</i> inter- actions in cell-cell adhesion platforms investigated via fluorescence fluctuation spectroscopy	19
2.2 [P2] A fluorescence fluctuation spectroscopy assay of protein-protein interactions at cell-cell contacts	35
2.3 [P3] Optimal fluorescent protein tags for quantifying protein oligomer- ization in living cells	53
2.4 [P4] Purely polysaccharide-based biofilm matrix provides size-selective diffusion barriers for nanoparticles and bacteriophages	75

3	Discussion and Outlook	97
3.1	Fluorescence fluctuation spectroscopy is suitable to detect protein interactions at cell-cell contacts	97
3.2	The choice of fluorescent protein tags affects molecular brightness analysis in living cells	102
3.3	Bacterial biofilm matrix hinders diffusion probe size dependently . . .	108
4	Appendix	111
4.1	Introduction to FCS/sFCS and theoretical background	111
4.1.1	Derivation of the FCS correlation function	111
4.1.2	Particle number, molecular brightness and effective detection volume	113
4.1.3	Photophysical transition dynamics	115
4.1.4	FCS correlation function for anomalous diffusion	116
4.1.5	Two-focus FCS	117
4.1.6	Dual-color FCCS	118
4.1.7	sFCS perpendicular to the membrane	121
4.2	N&B analysis	123
4.2.1	Theoretical background	123
4.2.2	Cross-correlation N&B	124
4.2.3	Detector noise characterization	126
4.3	Simulation of sFCS and N&B for 2D diffusion	127
4.4	FFS analysis software	129
4.5	sFCS simulations	129
4.6	N&B simulations	131
4.7	Experimental test of the sFCS implementation	134
4.7.1	sFCS on GUVs	134
4.7.2	sFCS on the plasma membrane of living cells	136
4.8	Supplementary data related to APLP1	141
4.9	Artifacts in FFS measurements	142
4.9.1	Photobleaching	142
4.9.2	Background	145
4.9.3	Instabilities	146
4.9.4	Statistical Limitations	149
4.10	FCA and TIFCA	152
4.10.1	Distinguishing oligomeric species via protein concentration . .	159
4.11	Spectral sFCCS	160

List of Figures	XI
Bibliography	XIII
Danksagung (Acknowledgements)	XXV
Eigenständigkeitserklärung (Declaration)	XXVII

1 Introduction

Biological processes rely on transport and interactions of biomolecules in living cells and tissues. Classical biochemical or biophysical methods investigate biomolecules after isolation from their native environment. The advent of high resolution light microscopy and spectroscopy techniques has revolutionized life sciences, enabling the direct observation of molecular processes in living systems. In particular, these techniques not only visualize cellular components, but also provide tools to extract quantitative information such as the concentration and stoichiometry of protein complexes involved in biochemical reactions underlying major cellular functions. In addition, molecular transport types and rates are accessible, contributing to a mechanistic understanding of dynamic cellular processes. Such quantitative parameters form the basis for physical models of biological systems, enabling to quantitatively predict cellular behavior or identify key factors that could be targeted for the treatment of certain pathologies.

1.1 Fluorescence fluctuation spectroscopy

In the last decades, FFS techniques have emerged that provide the above-mentioned quantitative analyses. These spectroscopy techniques are based on statistical analyses of the fluctuating signal that is emitted by fluorescent molecules. The most prominent variant is FCS, which was experimentally realized for the first time in a seminal and fascinating work by Magde et al. (1972) to measure diffusion and binding of ethidium bromide to DNA. A technical comparison of nowadays standard confocal FCS setups to the experimental system used at that time further highlights the groundbreaking work. While sub-fL focal volumes and ns time resolution are achieved today with high numerical aperture (NA) objectives and fast photon counting detectors, the setup of Magde et al. had a more than 10,000-fold larger focal volume and poor time resolution of around 10 ms. Moreover, instead of using nowadays available dichroic beam splitters, excitation and detection light were separated using a solution filter

that absorbed the excitation wavelength.

Only few years later, the same setup was used to measure lipid diffusion in planar lipid bilayers (Fahey et al., 1977) and receptor diffusion in the PM of rat myoblast cells (Elson et al., 1976), marking the first application of FCS in living cells. Major advancements in microscopy technologies, e.g. the emergence of stable laser sources, high NA objectives, and fast sensitive single-photon counting detectors promoted the transition from a cuvette to a microscopy based technique using the confocal scheme, which was implemented in the 1970s and 1980s.

Besides technical challenges in early years, the principle of FCS, illustrated in fig. 1.1, is fairly simple. In the standard point fluorescence correlation spectroscopy (pFCS) mode, the fluorescence signal $F(t)$ of a low concentration ($< 1 \mu\text{M}$) of fluorescent or fluorescently tagged molecules moving through the focal volume is measured over time. This signal is obtained by focusing laser light through a high NA objective and detecting the fluorescence with high temporal resolution, e.g. using an avalanche photo diode (APD). Then, the auto-correlation function (ACF) $G(\tau)$,

$$G(\tau) = \frac{\langle \delta F(t) \delta F(t + \tau) \rangle_t}{\langle F(t) \rangle_t^2}, \quad (1.1)$$

of the signal fluctuations, $\delta F(t) = F(t) - \langle F(t) \rangle_t$, is analyzed. The fluctuations arise from the motion of particles through the focal spot. Finally, suitable mathematical fit models $G_{\text{fit}}(\tau)$ that take the particular transport dynamics into account are applied to extract quantitative parameters. In particular, the number of particles N that are on average present in the focal volume and the average transit time τ_d are determined. In the case of diffusion, τ_d is an approximate measure of how much time it takes particles on average to diffuse through the focal volume. The particle number N is obtained from the amplitude of the ACF, $N = 1/G_{\text{fit}}(0)$ (see fig. 1.1). This relation is a consequence of the Poisson statistics governing the fluctuations of the number of particles present in the focal volume.

To determine absolute parameters, calibration of the focal volume dimensions is required. Assuming a Gaussian profile, characterized by the lateral elongation ω_0 and axial elongation $z_0 = S\omega_0$, where S is the structure parameter (typically between 4 and 8), the effective detection volume is given by $V_{\text{eff}} = \pi^{3/2} S \omega_0^3$ (typically around 0.5-1 fL). Using this expression, the average particle concentration and translational diffusion coefficient can be calculated:

$$c = \frac{V_{\text{eff}}}{N}, \quad (1.2)$$

$$D = \frac{\omega_0^2}{4\tau_d}. \quad (1.3)$$

In addition to translational diffusion, faster processes such as photophysical transitions of dye molecules or even rotational diffusion dynamics can be analyzed. Another important parameter is the molecular brightness, $\epsilon = \langle F(t) \rangle_t / N$, i.e the average number of photons detected per diffusing molecule and unit of time. This quantity provides a measure of molecular aggregation.

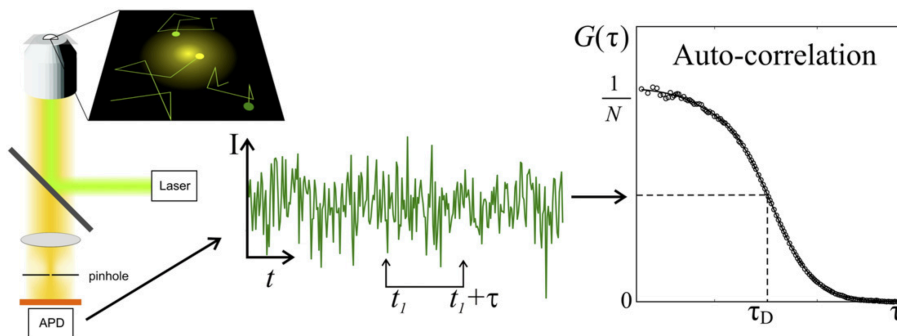


Figure 1.1: Scheme of FCS (from Chiantia et al. (2009)). The ACF $G(\tau)$ of the detected fluorescence signal is calculated according to eq. 1.1. A mathematical model $G_{\text{fit}}(\tau)$ (solid line in the graph on the right-hand side), derived for the dynamic process driving the fluctuations, e.g. diffusion, is fitted to the ACF to extract quantitative parameters such as the average particle number N or the transit time τ_d .

An important achievement for biomolecular applications was the development of fluorescence cross-correlation spectroscopy (FCCS) by Schwille et al. (1997), who extended FCS to two spectral channels, allowing to study hetero-interactions of two differently tagged molecule species. The FCCS analysis is based on the spectral cross-correlation $G_{gr}(\tau)$ of signals $F_g(t)$, $F_r(t)$ detected in two channels, as a measure of the coincidence of signal fluctuations,

$$G_{gr}(\tau) = \frac{\langle \delta F_g(t) \delta F_r(t + \tau) \rangle_t}{\langle F_g(t) \rangle_t \langle F_r(t) \rangle_t}. \quad (1.4)$$

In this context, the application of FPs as genetically encoded protein tags provided a key technology (Chalfie et al., 1994). In combination with FCCS, it was finally possible to quantify biomolecular interactions directly inside a living cell (fig. 1.2). The success of FCS/FCCS in cellular applications also results from the fact that these techniques requires low, sub-micromolar concentrations (corresponding to few 10s to 100s of particles or less), thus coinciding with endogenous concentrations of many cellular molecules.

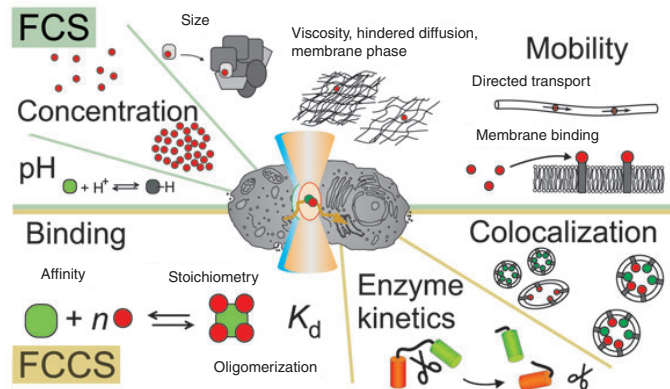


Figure 1.2: Applications of FCS and FCCS (from Bacia et al. (2006)). FCS and FCCS have evolved to widely used *in situ* techniques, which have been applied to quantify, for example, the concentration of biomolecules inside living cells, phase partitioning of biomembranes, binding of ligands to membrane receptors, the stoichiometry of biochemical reactions, and the kinetics of enzymatic processes.

While well suited for measurements in homogeneous solutions, pFCS has, however, still several limitations for broad applications in cellular systems. Most importantly, it lacks spatial information since the measurement is only performed in a small volume at a specific location inside the cell. For comparison, the volume of a HeLa cell is around 2,500 fL (BioNumbers, BNID 103725), thus ca. 5,000 times bigger than a typical focal volume in pFCS. Moreover, pFCS in systems showing slow dynamics, for example biomembranes, suffers from significant photobleaching. Due to the continuous illumination, fluorophores may bleach before the tagged molecules exhibits number fluctuations caused by diffusion.

To overcome these issues, several FCS modalities have been developed (see fig. 1.3), such as sFCS (Petrásek and Schwille, 2008, Ries et al., 2009a, Ries and Schwille, 2006), two-focus FCS (2fFCS) (Dertinger et al., 2007), and imaging FCS (Krieger et al., 2015), the latter requiring fast, sensitive cameras as well as parallelized illumination of multiple pixels, achieved through spinning disc (Sisan et al., 2006), total internal reflection (TIRF) (Kannan et al., 2007), or light sheet illumination (Wohland et al., 2010). Some of these techniques, e.g. sFCS and 2fFCS, exploit spatial correlations, i.e. cross-correlation of signals detected in distinct pixels or detection volumes, allowing to extract absolute parameters without an external focal volume calibration.

The first sFCS implementation was already presented by Petersen (1986) using the concept of fast beam scanning. In the mid 1980s, this technology replaced the previous, much slower scanning scheme of first confocal microscopes that moved the sample to scan an image. For measurements on cellular membranes, sFCS perpendicular to the PM proved beneficial. This modality provides the possibility to correct for

lateral movement of cells and thus enables the extended acquisition times that are required to investigate particularly slow diffusion dynamics (Ries and Schwille, 2006). The intrinsic stability paved the way for sFCS measurements of receptor-ligand interactions in living embryos of multicellular organisms (Ries et al., 2009c).

In addition to FCS, many more fluorescence fluctuation methods have been developed in the last 20 years, such as raster image correlation spectroscopy (RICS) (Digman et al., 2005), pair-correlation function (pCF) analysis (Digman and Gratton, 2009), N&B (Digman et al., 2008), photon counting histogram (PCH) (Chen et al., 1999), fluorescence cumulant analysis (FCA) or time-integrated fluorescence cumulant analysis (TIFCA) (Müller, 2004, Wu and Müller, 2005), spatial intensity distribution analysis (spiDA) (Godin et al., 2011), and image mean square displacement (iMSD) (Rienzo et al., 2013). All these variants are mostly performed on confocal microscopy systems. Together with two-color extensions based on cross-correlation analysis of two distinct spectral channels they expand the FFS toolbox.

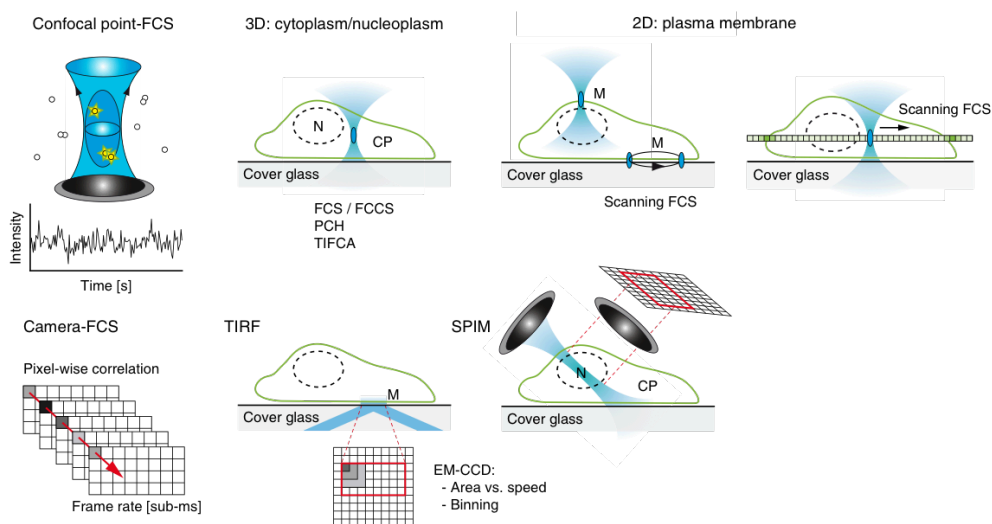


Figure 1.3: Schematic of pFCS/sFCS and imaging FCS modalities (adapted from Weidemann et al. (2014)). Standard pFCS can be used to measure in solution, the cell cytoplasm, and at the apical or basal PM. Point acquisition is also performed for techniques that analyze higher moments of the photon count distribution, such as the PCH or TIFCA. Alternatively, sFCS based on circular or linear beam scanning can be applied to measure on the PM. Imaging FCS uses fast camera acquisition (e.g. on an EM-CCD) combined with TIRF or light sheet illumination (e.g. for basal membrane or intracellular measurements), providing concentration or diffusion maps via pixelwise correlation analysis.

It is important to emphasize that the general concept underlying all FFS techniques, i.e. detection of fluctuations of a signal that is on average constant, induced by a microscopic, stochastic process, is based on an intrinsic equilibrium assumption.

This assumption is often violated in biological systems, showing long-term non-equilibrium dynamics such as a decay of the average fluorophore concentration due to photobleaching or vesicles entering the focus via active transport in living cells. Multiple schemes have been developed to correct for such artifacts and are explained in the appendix (chapter 4).

1.2 Particle transport in biological systems

1.2.1 Directed transport and diffusion

In biological systems, two main modes of transport occur. First, passive transport, i.e. diffusion, induced by random collisions of molecules with solvent or other molecules, driven by thermal energy. Second, active transport, accomplished by energy consuming cellular machines, e.g. molecular motors pulling cargo vesicles along microtubules inside cells. These two modes of transport follow different physical laws determining their time evolution. An experimentally accessible quantity that can be used to distinguish both types of motion is the ensemble mean square displacement (MSD), i.e. the second moment of the probability distribution function $P(\vec{r}, t)$ of a particles position,

$$\text{MSD}(t) = \langle \vec{r}^2(t) \rangle = \int \vec{r}^2 P(\vec{r}, t) d^3\vec{r}. \quad (1.5)$$

Alternatively, the time-averaged mean square displacement (taMSD) of a single particle moving along a trajectory $\vec{r}(t)$ is evaluated in many studies. For a trajectory of length T , it can be defined as

$$\text{taMSD}(\tau) = \frac{1}{T - \tau} \int_0^{T-\tau} |\vec{r}(t + \tau) - \vec{r}(t)|^2 dt. \quad (1.6)$$

Often, an average of the taMSD over an ensemble of N trajectories is taken,

$$\langle \text{taMSD}(\tau) \rangle = \frac{1}{N} \sum_{i=1}^N \text{taMSD}_i(\tau). \quad (1.7)$$

For Brownian motion and sufficiently long measurement times, ensemble MSD and taMSD are equal, $\langle \vec{r}^2(\tau) \rangle = \lim_{T \rightarrow \infty} \text{taMSD}(\tau)$, i.e. the process is ergodic.

The time dependent scaling of the MSD for different types of motion is shown in fig. 1.4.

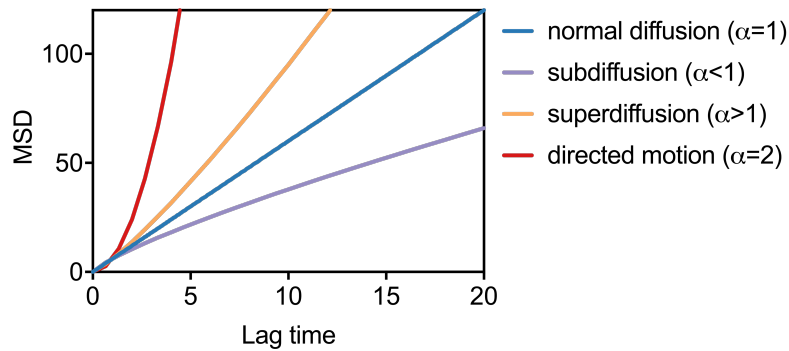


Figure 1.4: Time dependence of the MSD for different types of transport in biological systems. Plotted are calculated MSDs with $D = 1$ (normal diffusion, eq. 1.8), $\Gamma = 1$, $\alpha = 0.75$ (subdiffusion, eq. 1.11), $\Gamma = 1$, $\alpha = 1.25$ (superdiffusion, eq. 1.11), $v^2 = 6$ (directed motion, eq. 1.9), for transport in 3D, in arbitrary units.

For normal Brownian motion with diffusion coefficient D in a d -dimensional space, the MSD grows linearly with lag time τ ,

$$\text{MSD}(\tau) = 2dD\tau, \quad (1.8)$$

whereas for purely directed motion with speed v , it scales with the square of the lag time,

$$\text{MSD}(\tau) = v^2\tau^2. \quad (1.9)$$

Thus, particularly for long-range transport, directed motion is much more efficient than diffusion. A popular example illustrating the significance of active motion is the transport of neurotransmitter carrying vesicles that are pulled along axons to the synapse of nerve cells. If transported by mere diffusion, it would take vesicles a few years to reach the synapse at a distance of 10 mm from the Golgi apparatus, where cargo vesicles are packed and released.

In simple fluids, particles exhibit normal Brownian diffusion, characterized by the diffusion coefficient D that depends on the temperature T and viscosity η_s of the solvent, as well as on the size of particles (hydrodynamic radius R_h for spherical particles), as stated by the Stokes-Einstein relation,

$$D = \frac{k_B T}{6\pi\eta_s R_h}, \quad (1.10)$$

where k_B is the Boltzman's constant.

In more complex systems, e.g. crowded biological fluids, anomalous diffusion has frequently been observed, showing a power-law scaling of the MSD with time,

$$\text{MSD}(\tau) = 2d\Gamma\tau^\alpha. \quad (1.11)$$

Here Γ is the generalized diffusion coefficient, having units $\text{m}^2/\text{s}^\alpha$, and α the anomaly exponent. Normal diffusion and directed motion are special cases of this relation with $\alpha = 1$ and $\alpha = 2$, respectively.

Subdiffusion, i.e. MSD scaling with $\alpha < 1$, has been observed in multiple systems. For example, macromolecules and nanoparticles diffusing in the cytoplasm of cells show subdiffusion (Etoc et al., 2018, Weiss et al., 2004). Superdiffusion ($1 < \alpha < 2$), on the other hand, has been attributed to a combination of directed and diffusive motion and was observed, for instance, for the motion of microorganisms (Cherstvy et al., 2018) and intracellular vesicle transport (Reverey et al., 2015). There are a multitude of theoretical models that explain anomalous diffusion behaviors, such as obstructed diffusion in highly crowded media, continuous time random walks (CTRWs), fractional Brownian motion (FBM), or Lévy flights (Höfling and Franosch, 2013, Metzler et al., 2016, 2014, Weiss, 2014). Generally, the challenge in biophysical research is to relate these models to the molecular nature of biological systems, and to understand the interactions and dynamics that biomolecules undergo in such systems.

1.2.2 Measuring particle transport with single particle tracking and fluorescence correlation spectroscopy

A widely used technique to quantitatively investigate transport on the single particle level is SPT. The history of SPT experiments goes back to Jean Perrin, who experimentally confirmed the kinetic theory of Brownian motion by Einstein (1905) in seminal work. By following the Brownian motion of grains in liquids and tracking their positions over time (fig. 1.5), he was able to determine the Boltzmann's constant with remarkable accuracy, using eqs. 1.8, 1.10, and the measured MSDs. In his nobel lecture in 1926, he stated: *"In several series of measurements I varied, with the aid of several collaborators, the size of the grains (in the ratio of 1 to 70,000) as well as the nature of the liquid (water, solutions of sugar or urea, glycerol) and its viscosity (in the ratio of 1 to 125). They gave values between 55×10^{22} and 72×10^{22} , with differences which could be explained by experimental errors. The agreement is such that it is impossible to doubt the correctness of the kinetic theory of the translational Brownian movement."* (Perrin, 1926)

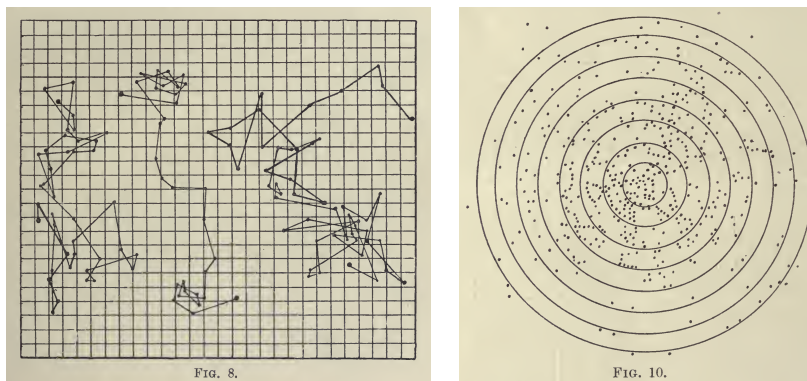


Figure 1.5: SPT experiments performed by Jean Perrin (Perrin, 1916). Perrin recorded trajectories of mastic grains of $0.53\ \mu\text{m}$ diameter in intervals of 30 s (left-hand side), using a camera lucida, an instrument to record objects observed at the microscope. Detected positions of 500 particles of $0.37\ \mu\text{m}$ size (right-hand side) were plotted by aligning their initial positions to a common origin and the number of detections in equally spaced rings counted to test the theoretical prediction for the MSD (eq. 1.8).

In a conventional fluorescence based SPT experiment, single fluorescent particles are imaged with high frame rate on a fluorescence microscope. Then, particle trajectories are reconstructed from the image stack by, first, localizing the central positions of particles and, second, linking particle positions in subsequent frames. From the trajectories, statistical parameters, such as the MSD, step lengths, or angles between steps can be calculated in order to determine the type of motion underlying particle dynamics, as illustrated in fig. 1.4. In biological applications, SPT measurements often suffer from limited trajectory lengths, e.g. due to photobleaching, leading to poor statistics for single trajectory parameters. Furthermore, particle concentrations are required to be sufficiently low to localize single particles. The latter limitation may be circumvented by using photoactivatable fluorophores, allowing to control the concentration of fluorescent particles via the activation light intensity (Manley et al., 2008). Nevertheless, the signal emitted by such fluorophores is limited and they often suffer from poor photostability.

An alternative is provided by ensemble based FFS techniques such as FCS. They are particularly suited for samples in which the concentration of molecules is higher than in the single molecule regime. As illustrated in fig. 1.6, the shape of the ACF in FCS shows characteristic differences between normal, directed, and anomalous transport that can be exploited when fitting different transport models.

In addition, several FCS variants and FFS modalities have been developed to quantify transport on multiple length scales, similar to MSD analysis in SPT. These methods are based on FCS with variable focus size, e.g. spot-variation FCS

(svFCS) (Wawrezynieck et al., 2005), stimulated emission depletion FCS (STED-FCS) (Eggeling et al., 2009), and imaging FCS with pixel binning (Sankaran et al., 2013) to obtain FCS diffusion laws, or exploit spatial correlations, e.g. pCF analysis (Baum et al., 2014), iMSD (Di Rienzo et al., 2014, Rienzo et al., 2013).

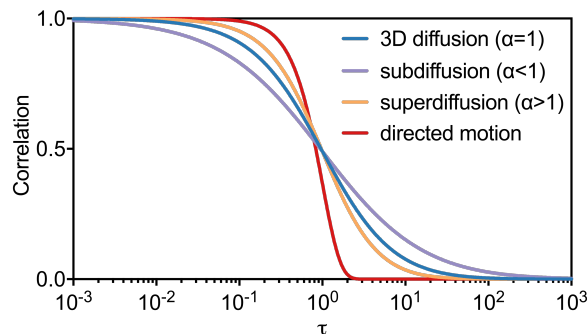


Figure 1.6: Shape of ACF in FCS for different types of transport in biological systems. ACF curves were calculated for diffusive transport in 3D (eq. 4.27), with $\tau_d = 1$, $\alpha = 1$ (normal diffusion), $\tau_d = 1$, $\alpha = 0.8$ (subdiffusion), $\tau_d = 1$, $\alpha = 1.2$ (superdiffusion), and directed motion (eq. 4.32 in 1D, $d = 0$, $D = 0$, $\omega_0/v = 1$), all with $N = 1$, in arbitrary units.

1.3 Aims and content of the thesis

The central aims of this work were, first, to implement and optimize FFS techniques for *in situ* measurements of molecular interactions and dynamics, and, second, to apply these techniques to solve challenging biological questions: How do interactions of amyloid precursor-like proteins contribute to their function at neuronal synapses? Does the bacterial biofilm matrix provide diffusion barriers for nanoparticles, antibiotics, or novel antimicrobial agents such as bacterial pathogens?

To answer these questions, several FFS methods such as sFCS, pFCS and N&B were performed in both, one-color and cross-correlation mode. Additionally, SPT was used. The FFS techniques are introduced in more detail in the appendix, including description of data analysis workflows and results of simulations as well as experiments validating their successful implementation. Additionally, several technical limitations, sample related artifacts, and correction schemes are explored. In this context, it was intended to investigate to which extent FP properties affect the quantification of protein interactions in live cell measurements. Finally, spectral sFCCS is presented, a technique that combines scanning fluorescence cross-correlation spectroscopy (sFCCS) and spectral unmixing to enable multi-color sFCCS in living cells.

1.3.1 Implementation of fluorescence fluctuation spectroscopy to quantify protein-protein interactions mediating cell-cell adhesion, applied to amyloid precursor-like protein 1

Cell-cell contacts are important interfaces in multicellular systems. A variety of cell-cell interactions, e.g. adhesion or recognition, take place at such sites. On the molecular level, these interactions are typically mediated by proteins that are expressed at the cell surface and form complexes with proteins on neighboring cells (*trans* interactions). An important type of cell-cell contacts are neuronal synapses, where neurons transmit signals to neighboring neurons. The formation, maintenance, and remodeling of neuronal synapses plays a key role in physiological processes such as brain development and memory formation.

In the work presented in chapter 2.1, the neuronal type I transmembrane protein APLP1 was investigated. APLP1 belongs to the family of amyloid precursor proteins (APPs), which are involved in the pathogenesis of Alzheimer's disease. In previous work, it was shown that APLP1 has the strongest surface localization among all APP family members (Kaden et al., 2009). Furthermore, it was found that APLP1 oligomerizes at the PM, triggered by μM concentrations of metal ions (Mayer et al., 2014). Using N&B analysis in living cells, it could be shown in collaboration with the Multhaup group (McGill University) that zinc ions specifically trigger APLP1 *cis* interactions (i.e. APLP1 oligomerization in one cell) and induce the formation of large protein clusters (Mayer et al., 2016). Strikingly, these clusters were found to enrich at cell-cell contact sites (fig. 1.7). It was therefore hypothesized that APLP1 clusters may function as neuronal adhesion complexes, as indicated by previous functional and bulk experiments (Schilling et al., 2017, Soba et al., 2005). Nevertheless, experimental evidence that could directly reveal the existence of such complexes was missing due to a lack of assays capable of specifically probing *trans* interactions in living cells. This provided the motivation for the work presented in chapters 2.1, 2.2 of this thesis. Scanning FCS based on beam scanning perpendicular to the membrane is well suited to quantify protein interactions and dynamics at cell-cell contacts of living cells. For this purpose, pFCS acquisition, that is commonly applied at the basal membrane of cells, has severe limitations. It suffers from lateral cell movement, i.e. cell-cell junctions would quickly move out of a static focus. In contrast, the intrinsic stability of sFCS, facilitated by a simple alignment correction for lateral movement, makes it an ideal tool to investigate proteins involved in cell-cell adhesion, presumably showing slow diffusion dynamics.

The aim of this work was to implement a specific assay to detect and monitor *cis*

and *trans* interactions of proteins at cell-cell contact sites. To specifically probe and resolve such interactions, two-color approaches, e.g. sFCCS or cross-correlation number and brightness (ccN&B), should be pursued. Once established, it was aimed to quantify the size and dynamics of APLP1 complexes using the implemented methodology and to elucidate whether APLP1 forms *trans* complexes at such sites. Finally, the role of zinc in modifying the molecular organization of APLP1 should be explored.

As a cellular model system that is more tractable than neurons and well suited for sFCS (see fig. 4.15 in appendix), Human embryonic kidney (HEK) 293T cells should be used. These cells are absent of endogenous, i.e. untagged, APLP1 expression.

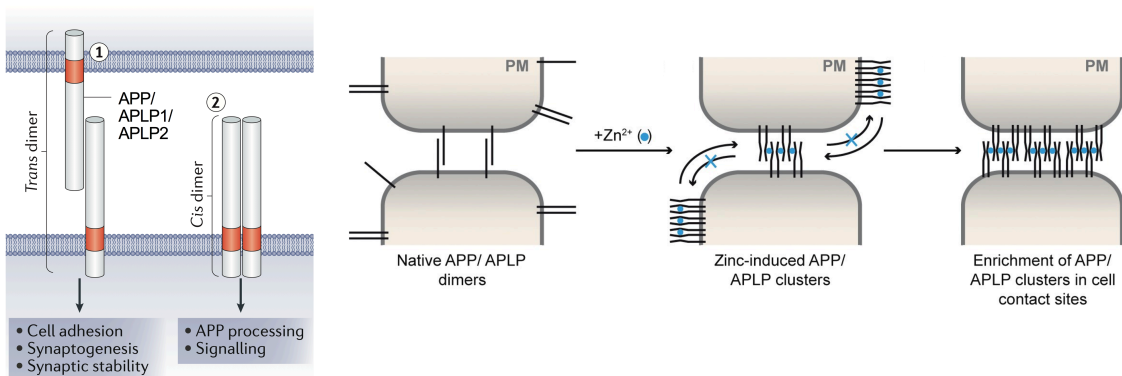


Figure 1.7: Proposed functions and interactions of APP family members at neuronal synapses. Adapted from Müller et al. (2017) and Mayer et al. (2016). The APP family members APP, APLP1, and APLP2 may undergo *cis* and *trans* interactions (e.g. dimer formation of proteins in the same or in opposing membranes) at neuronal synapses in a homo- or heterotypic manner (left-hand side). These protein complexes are hypothesized to carry out important physiological functions, such as cell-cell adhesion, generation or stabilization of synaptic contacts (Müller et al., 2017). Zinc ions mediate reorganization of APP family members (right-hand side), e.g. protein clustering and enrichment at cell-cell contact sites (Mayer et al., 2016).

1.3.2 Systematic evaluation of fluorescent proteins for molecular brightness and cross-correlation analysis

The quality of FFS measurements in cells and the accuracy of quantified parameters strongly depend on the properties of the FPs used to tag proteins of interest. In the context of APLP1, monomeric enhanced yellow fluorescent protein (mEYFP) and mCard were used for cross-correlation measurements. In combination with the previously characterized APLP1-mEYFP, the red FP mCard was chosen due to its emission in the far red spectrum, allowing to minimize cross-talk from mEYFP

emission into the second (mCard) detection channel. In the final study, cross-talk was, however, circumvented by implementing an alternating-laser excitation (ALEX) scheme. Nevertheless, measurements on APLP1 revealed suboptimal properties of mCard, observed in both, cross-correlation measurements and molecular brightness analysis. As shown in chapter 2.1 (fig. S1) and in the appendix (chapter 4, fig. 4.12), strongly different ACF amplitudes were observed in sFCCS measurements on mEYFP-mCard hetero-dimers, for which the same number of molecules is expected in both channels. Similarly, the molecular brightness distributions in both spectral channels of ccN&B measurements on APLP1 strongly differed (4.16 in appendix), although similar distributions should be observed due to the symmetry of the system. Therefore, it was hypothesized that many protein complexes contain non-fluorescent mCard subunits. This phenomenon was previously discussed in a publication by Foo et al. (2012), who presented a thorough investigation of factors affecting the cross-correlation in FCCS measurements. Unfortunately, although of remarkable importance for quantitative measurements, comprehensive investigations on potential dark states of FPs were lacking in the FFS field.

Driven by these observations, it was intended to characterize the performance of FPs commonly used in cross-correlation or brightness studies, with a particular focus on red FPs, which often show suboptimal properties and complex photophysics (Foo et al., 2012, Hendrix et al., 2008, Wu et al., 2009). Therefore, several novel red FPs that have been developed in the last years should be additionally tested. To this aim, brightness measurements on FP homo-dimers should be performed and factors affecting their brightness relative to FP monomers systematically investigated, as illustrated in fig. 1.8.

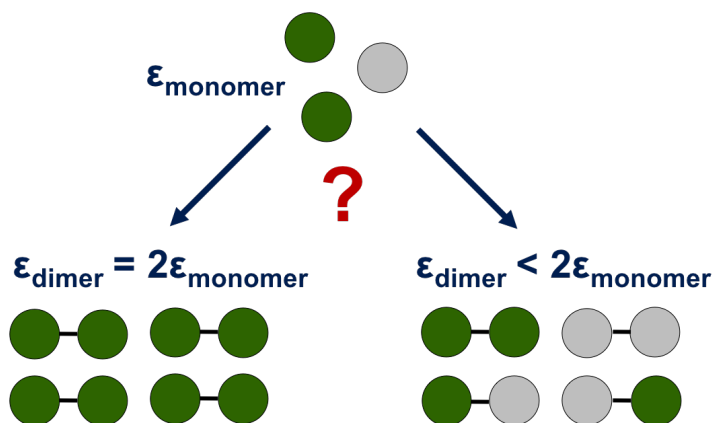


Figure 1.8: Effect of non-fluorescent states on molecular brightness analysis. An ensemble of FP homo-dimers shows an average relative brightness of 2, or a brightness between 1 and 2, depending on the absence or presence of non-fluorescent FP units (gray), respectively.

1.3.3 Characterization of diffusion dynamics in bacterial biofilms

In the work presented so far, FFS techniques were mainly used as a tool to quantify interactions of biomolecules in their cellular context. In addition, FFS allows to accurately quantify transport dynamics of biomolecules via temporal analysis of detected signal fluctuations. In biofilms, surface adherent bacterial communities of typically 10s to 100s of microns thickness (fig. 1.9A), diffusion is the main mode of transport. Molecules such as nutrients or ions diffuse within biofilms and in exchange with the surrounding medium. This also applies to drugs that are used to clear or inhibit further growth of biofilms, e.g. antibiotics and pathogens such as bacteriophages that specifically target bacteria for replication.

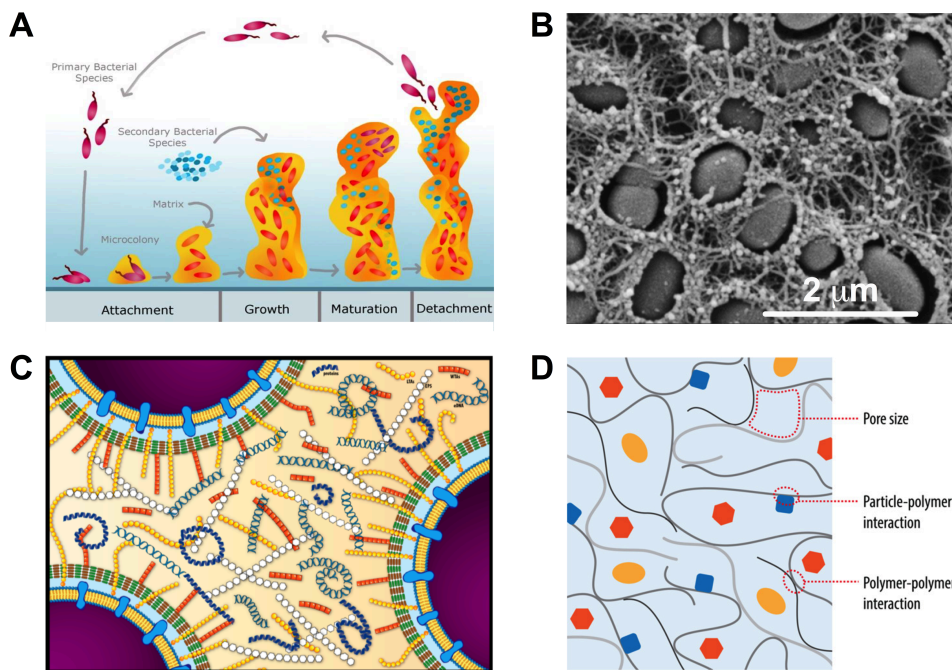


Figure 1.9: Bacterial biofilm development and the biofilm EPS matrix. **A:** Development of a biofilm. Single planktonic bacteria attach to a surface and start to produce EPS. Microcolonies grow over time and form a complex 3D structure, potentially incorporating secondary bacterial species. Eventually, biofilms disperse, i.e. single bacteria detach from the biofilm and reenter the planktonic state (from Jacques et al. (2010)). **B:** An electron microscopy (EM) image of *E.coli* cells embedded in a tightly packed EPS matrix (here curli protein fibers) (from Serra et al. (2013)). **C:** The EPS of bacterial biofilms consists of a variety of macromolecules, e.g. polysaccharides (white), fibrillar proteins (dark blue), and extracellular DNA (light blue), filling the extracellular space (from Colagiorgi et al. (2016)). **D:** Particle transport in a biofilm matrix may depend on the matrix pore size (e.g. determined by polymer-polymer interactions) and particle-polymer interactions (from Billings et al. (2015)).

In contrast to liquid cultures where bacteria are easily accessible, bacteria inside biofilms are embedded in a complex multi-component matrix of macromolecules (fig. 1.9B,C). This matrix consists of EPS, e.g. polysaccharides, fibrillar proteins, and extracellular DNA, forming a hydrated polymer network (fig. 1.9D). The EPS contribute up to 90% of a biofilms dry weight, providing structural organization and mechanical rigidity to bacterial colonies.

The aim of the presented work was to investigate particle transport in a reconstituted polysaccharide EPS matrix system, as a model for the EPS of intact biofilms, using quantitative diffusion measurements. This approach was motivated by the fact that previous studies investigating diffusion dynamics directly in biofilms did not allow to link the observed properties to the macromolecular organization and amount of EPS. Therefore, biofilms of the plant pathogen *P.stewartii* were chosen as a model system, containing one predominant EPS component, the MDa anionic polysaccharide stewartan. It was intended to first characterize pure stewartan hydrogels and then perform continuative investigations of intact *P.stewartii* biofilms at a later stage.

To this aim, complementary FCS and SPT measurements should be performed on particles with variable size in stewartan matrices reconstituted under multiple conditions (e.g. pH) and at different concentrations. In order to infer their structural organization (e.g. the matrix mesh size), microscopic diffusion measurements should be complemented with macroscopic viscosity measurements. This approach follows several recent studies that showed a critical dependence of the rheological properties of polymer solutions on polymer concentration via polymer chain associations and entanglement (Ganesan et al., 2016).

Furthermore, it was intended to mimic bacteriophage transport by selecting nanoparticles in a particular size range similar to the typical size of bacteriophage particles. This was motivated by theoretical work which suggested that the mobility of phage particles may be a key parameter that determines the dynamic equilibrium of bacteria and phages in the course of infections (Simmons et al., 2018). Moreover, recent experimental work indicated that EPS matrix, e.g. fibrillar curli proteins (see fig. 1.9B), confines the mobility of phages in biofilms (Vidakovic et al., 2018). Ultimately, it was aimed to elucidate to which extent the stewartan matrix provides diffusion barriers for the transport of small molecules, nanoparticles and bacteriophages.

1.3.4 Publications

The following manuscripts constitute the main part of this cumulative dissertation:

[P1] **Dunsing, V.**, Mayer, M., Liebsch, F., Multhaup, G., Chiantia, S.

Direct evidence of amyloid precursor-like protein 1 *trans* interactions in cell-cell adhesion platforms investigated via fluorescence fluctuation spectroscopy

Molecular Biology of the Cell, (2017) 28:25, 3609-3620

Author contributions: Valentin Dunsing and Salvatore Chiantia conceived the study, with input from Magnus Mayer, Filip Liebsch and Gerhard Multhaup. Valentin Dunsing performed all experiments, wrote analysis software, performed data analysis and visualization. Valentin Dunsing and Salvatore Chiantia co-wrote the manuscript.

Approved:

Prof. Dr. Salvatore Chiantia

[P2] **Dunsing, V.**, Chiantia, S.

A Fluorescence Fluctuation Spectroscopy Assay of Protein-Protein Interactions at Cell-Cell Contacts

J. Vis. Exp., (2018) (142), e58582

Author contributions: Valentin Dunsing and Salvatore Chiantia conceived the work. Valentin Dunsing performed experiments, data analysis and visualization. Valentin Dunsing wrote the manuscript with editing by Salvatore Chiantia.

Approved:

Prof. Dr. Salvatore Chiantia

[P3] **Dunsing, V.[#]**, Luckner, M.[#], Zühlke, B., Petazzi, R. A., Herrmann, A., and Chiantia, S.

Optimal fluorescent protein tags for quantifying protein oligomerization in living cells

Scientific Reports, (2018) 8(1):10634

[#] authors contributed equally

Author contributions: Valentin Dunsing, Madlen Luckner and Salvatore Chiantia conceived the work. Valentin Dunsing, Madlen Luckner, Boris Zühlke and Roberto A. Petazzi performed experiments. Madlen Luckner performed the

cloning work, with help from Valentin Dunsing and Roberto A. Petazzi. Valentin Dunsing wrote the analysis software. Valentin Dunsing, Madlen Luckner and Boris Zühlke analyzed data. Valentin Dunsing and Madlen Luckner visualized data. Valentin Dunsing, Madlen Luckner, Andreas Herrmann and Salvatore Chiantia wrote the manuscript.

Approved: _____

Prof. Dr. Salvatore Chiantia

[P4] **Dunsing, V.**, Irmscher, T., Barbirz, S., Chiantia, S.

Purely polysaccharide-based biofilm matrix provides size-selective diffusion barriers for nanoparticles and bacteriophages

Biomacromolecules, (2019), 20, 3842-3854

Author contributions: Valentin Dunsing, Tobias Irmscher, Stefanie Barbirz and Salvatore Chiantia conceived the work. Valentin Dunsing performed FCS/SPT experiments. Tobias Irmscher performed purification and labeling of biological material. Valentin Dunsing wrote analysis software, analyzed and visualized all data. Valentin Dunsing, Stefanie Barbirz and Salvatore Chiantia wrote the manuscript with input from Tobias Irmscher.

Approved: _____

Prof. Dr. Salvatore Chiantia

In addition, the author contributed to the following publications:

[P5] Mayer, M., Schauenburg, L., Thompson-Steckel, G., **Dunsing, V.**, Kaden, D., Voigt, P., Schaefer, M., Chiantia, S., Kennedy, T. , Multhaup, G.

Amyloid precursor-like protein 1 (APLP1) exhibits stronger zinc-dependent neuronal adhesion than amyloid precursor protein and APLP2

J. Neuroch., (2016) 137, 266-276

[P6] Bobone, S., Hilsch, M., Storm, J., **Dunsing, V.**, Herrmann, A., Chiantia, S.
Phosphatidylserine Lateral Organization Influences the Interaction of Influenza Virus Matrix Protein 1 with Lipid Membranes

J Virol, (2017) 91, e00267-17

2 Results

2.1 [P1] Direct evidence of amyloid precursor-like protein 1 *trans* interactions in cell-cell adhesion platforms investigated via fluorescence fluctuation spectroscopy

This is a downloaded version of the article that was published in *Molecular Biology of the Cell*, volume 28, number 25 on pages 3609-3620 in 2017, available online at: <https://www.molbiolcell.org/doi/10.1091/mbc.e17-07-0459> (doi: 10.1091/mbc.E17-07-0459).

Direct evidence of amyloid precursor–like protein 1 *trans* interactions in cell–cell adhesion platforms investigated via fluorescence fluctuation spectroscopy

Valentin Dunsing^a, Magnus Mayer^{b,†}, Filip Liebsch^c, Gerhard Multhaupt^c, and Salvatore Chiantia^{a,*}

^aInstitute of Biochemistry and Biology, University of Potsdam, 14476 Potsdam, Germany; ^bInstitute of Chemistry and Biochemistry, Free University of Berlin, 14195 Berlin, Germany; ^cDepartment of Pharmacology and Therapeutics/Integrated Program in Neuroscience, McGill University, Montreal, QC H3G 1Y63, Canada

ABSTRACT The amyloid precursor–like protein 1 (APLP1) is a type I transmembrane protein that plays a role in synaptic adhesion and synaptogenesis. Past investigations indicated that APLP1 is involved in the formation of protein–protein complexes that bridge the junctions between neighboring cells. Nevertheless, APLP1–APLP1 *trans* interactions have never been directly observed in higher eukaryotic cells. Here, we investigated APLP1 interactions and dynamics directly in living human embryonic kidney cells using fluorescence fluctuation spectroscopy techniques, namely cross-correlation scanning fluorescence correlation spectroscopy and number and brightness analysis. Our results show that APLP1 forms homotypic *trans* complexes at cell–cell contacts. In the presence of zinc ions, the protein forms macroscopic clusters, exhibiting an even higher degree of *trans* binding and strongly reduced dynamics. Further evidence from giant plasma membrane vesicles suggests that the presence of an intact cortical cytoskeleton is required for zinc-induced *cis* multimerization. Subsequently, large adhesion platforms bridging interacting cells are formed through APLP1–APLP1 *trans* interactions. Taken together, our results provide direct evidence that APLP1 functions as a neuronal zinc-dependent adhesion protein and allow a more detailed understanding of the molecular mechanisms driving the formation of APLP1 adhesion platforms.

Monitoring Editor

Mark H. Ginsberg
University of California,
San Diego

Received: Jul 17, 2017

Revised: Sep 13, 2017

Accepted: Oct 4, 2017

This article was published online ahead of print in MBoC in Press (<http://www.molbiolcell.org/cgi/doi/10.1091/mbc.E17-07-0459>) on October 11, 2017.

[†]Present address: Miltenyi Biotec GmbH, Robert-Koch-Straße 1, 17166 Teterow, Germany.

*Address correspondence to: Salvatore Chiantia (chiantia@gmail.com).

Abbreviations used: ACF, auto-correlation function; APLP1 and -2, amyloid precursor–like proteins 1 and 2; APP, amyloid precursor protein; Card, mCardinal; CCF, cross-correlation function; ccN&B, cross-correlation number and brightness; FCS, fluorescence correlation spectroscopy; GPI, glycosylphosphatidylinositol; GPMV, giant plasma membrane vesicle; HEK, human embryonic kidney; HEPES, 4-(2-hydroxyethyl)-1-piperazineethanesulfonic acid; myr, myristoylated; N&B, number and brightness; NEM, N-ethylmaleimide; palm, palmitoylated; PM, plasma membrane; sFCS, scanning fluorescence correlation spectroscopy; YFP, yellow fluorescent protein.

© 2017 Dunsing et al. This article is distributed by The American Society for Cell Biology under license from the author(s). Two months after publication it is available to the public under an Attribution–Noncommercial–Share Alike 3.0 Unported Creative Commons License (<http://creativecommons.org/licenses/by-nc-sa/3.0>).

"ASCB®" "The American Society for Cell Biology®" and "Molecular Biology of the Cell®" are registered trademarks of The American Society for Cell Biology.

INTRODUCTION

The amyloid precursor protein family members APP (amyloid precursor protein), APLP1 (amyloid precursor–like protein 1), and APLP2 (amyloid precursor–like protein 2) are type I transmembrane proteins with a crucial role in synaptogenesis and brain development (Coulson et al., 2000; Muller et al., 2017). Cleavage of APP via various secretases (e.g., the α -, β -, and γ -secretases [Vassar et al., 1999; Selkoe, 2001; Eggert et al., 2004; Li and Südhof, 2004]) leads to the release of soluble protein fragments, including the A β -peptides found in amyloid plaques in the brains of Alzheimer's disease patients (Blennow et al., 2006). APP family proteins have been shown to be involved also in neuron differentiation, neurite outgrowth, and synaptic plasticity (Heber et al., 2000; Wang et al., 2009; Weyer et al., 2011; Tyan et al., 2012; Shariati and De Strooper, 2013). All three proteins are pre- and postsynaptically expressed and up-regulated during postnatal development (Schilling et al., 2017).

Among the three proteins, APLP1 is predominantly expressed in the CNS and has the highest surface expression (Kaden *et al.*, 2009). Recent results from coculture assays suggested that APLP1 expression has synaptogenic activity on primary cortical neurons (Schilling *et al.*, 2017). Further, we recently reported that metal ions, especially zinc, affect APLP1 oligomerization (Mayer *et al.*, 2014) and trigger the assembly of *cis* dimers into large protein clusters at the plasma membrane (PM) and their enrichment at cell–cell contact sites (Mayer *et al.*, 2016). Using a cell-substrate adhesion assay, we showed that zinc enhances adhesion of cortical neurons to immobilized APLP1 ectodomains. This evidence, together with results from cell-aggregation experiments and biochemical studies, supports the hypothesis that APLP1 can form homo- or heterotypic *trans* multimers mediating cell–cell interaction (Soba *et al.*, 2005; Kaden *et al.*, 2009). However, direct evidence for APLP1 *trans* interactions in living cells and the role of zinc in modifying these molecular interactions have not been investigated yet.

Here, we address this issue by applying fluorescence fluctuation techniques, namely scanning fluorescence correlation spectroscopy (sFCS) and cross-correlation number and brightness (ccN&B) analysis, to quantify APLP1 dynamics and protein–protein interactions directly in living cells. Both techniques are based on a statistical analysis of fluorescence fluctuations caused by the diffusive motion of fluorescent molecules through the focal volume of a confocal microscope and can provide quantitative information about protein–protein interaction (Digman *et al.*, 2008; Ries *et al.*, 2009; Hilsch *et al.*, 2014; Bobone *et al.*, 2017). Whereas sFCS is particularly suitable for measuring diffusive dynamics in the PM (Ries and Schwille, 2006), N&B analysis can map molecular aggregation in space (Digman *et al.*, 2008; Hilsch *et al.*, 2014; Bobone *et al.*, 2017). Using these techniques with two spectrally distinct fluorescent labels allows us to probe interactions among different species via cross-correlation analysis of the signals measured in two spectral channels (Schwille *et al.*, 1997; Bacia *et al.*, 2006; Digman *et al.*, 2009; Macháň and Wohland, 2014). We show that APLP1 undergoes *trans* homo-multimerization and a consequent reduction in mobility at cell–cell contacts. Also, we demonstrate that zinc induces the formation of large, APLP1-rich adhesion platforms characterized by strong protein–protein *trans* interactions. Finally, we provide evidence that the cellular cytoskeleton is crucial for APLP1 *cis* and *trans* clustering and, as a consequence, for APLP1-mediated cell–cell adhesion. Our data shed light on the molecular basis of APLP1–APLP1 interaction and provide direct evidence that this protein functions as a zinc-dependent cell–cell adhesion receptor.

RESULTS

APLP1 partially interacts in *trans* at cell–cell contact sites

Previous studies hypothesized that APLP1 is involved in *trans* interactions between neighboring cells (Soba *et al.*, 2005; Kaden *et al.*, 2009; Mayer *et al.*, 2016). However, whether such interactions involve APLP1 on one side directly or indirectly interacting with APLP1 on the adjacent cell (rather than, e.g., APLP1 interacting exclusively with other proteins) remains unclear. To investigate the existence of APLP1–APLP1 *trans* interactions, we specifically monitored the presence of homotypic *trans* complexes. We transiently expressed APLP1–yellow fluorescent protein (APLP1–YFP) or APLP1–mCardinal (APLP1–Card) in human embryonic kidney (HEK) cells. In both cases, the fluorescent labels were fused to the intracellular side of the protein to avoid interference with the extracellular binding domains (Baumkötter *et al.*, 2012). The two cell populations were mixed 4 h after transfection. On these mixed samples, we performed two-color

sFCS measurements at contacts between APLP1–YFP– and APLP1–Card–expressing cells, where the proteins are colocalized and have a mostly homogeneous distribution (see, e.g., the continuous arrow in Figure 1A). To avoid cross-talk interferences, we excited and detected the two spectral channels sequentially. It is worth noting that the large distance between the fluorophores (~50–100 nm) would not allow fluorescence energy transfer measurements.

From sFCS measurements, we calculated the auto-correlation function (ACF; green [YFP] and red [Card] data points in Figure 1B) and cross-correlation function (CCF; blue data points in Figure 1B) of the fluorescence fluctuations and fitted a two-dimensional diffusion model to the data (green, red, and blue curves). From the amplitude ratios of the three curves, we obtained the relative cross-correlation, which is a measure of the correlation of fluorescence fluctuations in the green (APLP1–YFP) and red (APLP1–Card) channels. Relative cross-correlation varies between 0 (i.e., no red–green complexes) and 1 (i.e., highest number of red–green complexes). The decay times of the ACFs provide information about diffusion dynamics of APLP1s in the membrane (discussed in the next paragraph). It is worth noting that in order to maximize the fluorescence fluctuation signal, cells with the lowest detectable protein expression were selected.

sFCS analysis revealed a positive cross-correlation between fluorescence fluctuations in the two spectral channels, that is, evidence of codiffusion of YFP- and Card-labeled APLP1 (Figure 1, B and C). The average relative cross-correlation of 0.45 ± 0.21 (mean \pm SD, $n = 17$ cells from three independent measurements; Figure 1C) is ~50% of the maximum relative cross-correlation detected for complete binding (0.96 ± 0.18 , mean \pm SD, $n = 14$ cells from three independent measurements; Supplemental Figure S1), as verified with a myristoylated-palmitoylated-mCardinal–YFP (myr-palm-Card–YFP) tandem construct as a positive cross-correlation control. As a negative control, we examined junctions between one cell expressing myr-palm–YFP and one expressing myr-palm–Card. In this case, we found a much lower relative cross-correlation (0.08 ± 0.10 , mean \pm SD, $n = 17$ cells from three independent measurements; Figure 1C and Supplemental Figure S2).

To estimate the stoichiometry of APLP1 complexes, we calculated the molecular brightness from sFCS data at cell–cell contacts. After a normalization using the molecular brightness of a monomeric standard (see *Materials and Methods*), the normalized brightness provides a direct measurement of protein multimerization state (e.g., a normalized brightness value of 1 indicates the presence of monomers, a value of 2 indicates the presence of dimers, and so on). For APLP1–YFP, we obtained a normalized brightness distribution centered around 3.0 ± 2.9 (Figure 2D, median \pm SD, $n = 17$ from three independent measurements). Note that sFCS brightness analysis cannot resolve mixtures of multimers with different sizes but, rather, provides an average multimerization value. In conclusion, these data indicate that small APLP1 oligomers (on average, trimers) on one cell membrane interact in *trans* with other small APLP1 oligomers in the facing membrane. It is worth noting that our technical approach cannot exclude the presence of other PM components in the observed *trans* complexes. Therefore, it might be also possible that APLP1 *trans* interactions are mediated by other, yet unidentified, proteins. Furthermore, the measured average cross-correlation value suggests that there is a significant fraction of APLP1 on each side of the junction that is not involved in *trans* interactions. In a simplified scenario in which only one APLP1 multimeric species is present and all APLP1 is fluorescent, ~45% of the protein would be part of *trans* complexes.

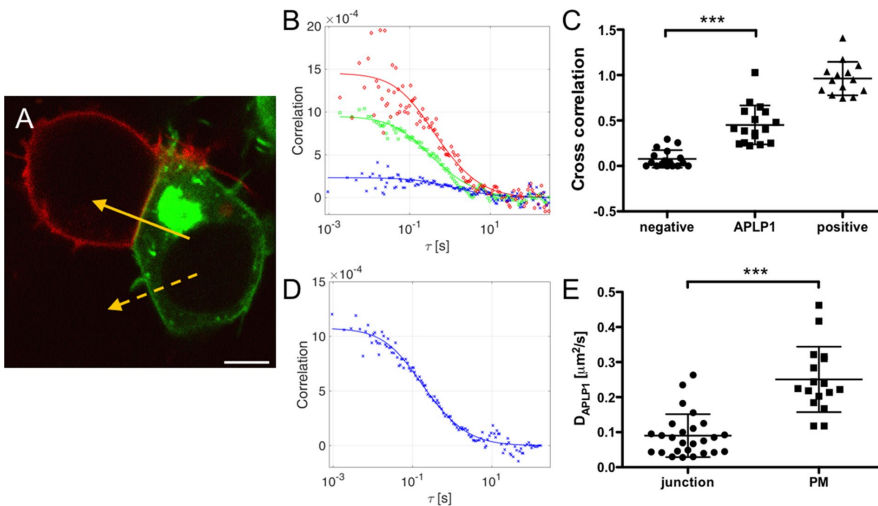


FIGURE 1: APLP1-YFP and APLP1-Card interact in *trans* at cell–cell contact sites. (A) HEK cells expressing APLP1-YFP (green) or APLP1-Card (red). Yellow arrows represent sFCS line scans (solid arrow, two-color scan at cell–cell contact; dashed arrow, one-color scan outside junction). Scale bar is 5 μm . (B) Representative correlation functions and fit curves for two-color sFCS analysis of APLP1 at cell–cell contacts. Red, ACF in red channel (APLP1-Card); green, ACF in green channel (APLP1-YFP); blue, CCF calculated for both spectral channels. Fit curves (solid lines) were obtained from fitting a two-dimensional diffusion model to the data. (C) Relative cross-correlation from two-color sFCS measurements of APLP1-YFP and APLP1-Card mixed cells ($n = 17$ cells, three independent samples). Cross-correlation values for myr-palm-Card-YFP tandem-expressing cells, measured under the same conditions, are shown as positive control for cross-correlation (“positive,” $n = 14$ cells, three independent samples; see also Supplemental Figure S1). Cross-correlation values for mixed cells expressing myr-palm-YFP and myr-palm-Card, measured under the same conditions, are shown as negative control for cross-correlation (“negative,” $n = 17$ cells, three independent samples; see also Supplemental Figure S1). (D) Representative ACF for APLP1-YFP from one-color sFCS measurement outside junction and fit (solid line) of a two-dimensional diffusion model. (E) Diffusion coefficients of APLP1 at cell–cell contacts ($n = 26$ cells, four independent samples) and outside junctions ($n = 17$ cells, three independent samples) calculated from ACF-derived diffusion times of APLP1-YFP. Error bars represent mean \pm SD. Asterisks indicate statistically significant differences with $***p < 0.0001$ determined with Welch’s two-sided *t* test.

Diffusion of APLP1 within cell–cell contact sites moderately decreases in the absence of zinc

If APLP1 is involved in specific interactions bridging two facing cells, reduced protein dynamics might be expected at cell–cell contacts (Trimble and Grinstein, 2015). To quantify the diffusion coefficient of APLP1 in living cells, we performed sFCS measurements within and outside junctions in HEK cells expressing APLP1-YFP and/or APLP1-Card (see, e.g., the two arrows in Figure 1A). We did not observe significant differences between the dynamics of APLP1-YFP and APLP1-Card and, therefore, restricted our analysis to APLP1-YFP. From the decay times of the ACFs (Figure 1, B and D), we calculated the diffusion coefficients in both PM regions, as described in *Materials and Methods*. Briefly, diffusion times were obtained by fitting a two-dimensional diffusion model to the ACF shown, for example, in Figure 1, B and D. Typical observed diffusion times for APLP1-YFP were ~ 50 ms outside junctions and ~ 100 ms within junctions. Through calibration of the size of the observation volume, we were able to obtain diffusion coefficients (D). As shown in Figure 1E, we found a significant reduction of APLP1 diffusion in cell–cell contacts ($D_{\text{APLP1}} = 0.09 \pm 0.06 \mu\text{m}^2/\text{s}$, mean \pm SD, $n = 26$ cells from three independent samples) compared with noncontact areas ($D_{\text{APLP1}} = 0.25 \pm 0.09 \mu\text{m}^2/\text{s}$, mean \pm SD, $n = 17$ cells from three independent samples).

To verify that the reduction in mobility is not induced by, for example, differences in membrane organization (e.g., lipid or

protein composition, underlying cytoskeleton) between cell–cell contacts and other regions of the PM, we monitored the diffusion of myr-palm-YFP (associated to the PM inner leaflet [Engel *et al.*, 2010]) and GPI-YFP (glycosylphosphatidylinositol-anchored YFP, associated to the PM outer leaflet [Scolari *et al.*, 2009]). We found no difference in diffusion coefficients of either construct between the two regions of the PM ($D \sim 1 \mu\text{m}^2/\text{s}$; see Supplemental Figure S3). Thus, the reduction in APLP1 diffusivity in cell–cell contacts seems to be due to specific interactions involving the protein.

Zinc induces formation of APLP1 clusters at cell–cell contacts with reduced diffusivity and enhanced *trans* interactions

Recently, we found that physiological concentrations of zinc in the micromolar range trigger the formation of APLP1 multimers and their enrichment at cell–cell contact sites (Mayer *et al.*, 2014, 2016). We hypothesized that these multimers may involve APLP1 *trans* interactions and act as cell–cell adhesion complexes. To clarify the effect of zinc on APLP1 *trans* interactions, we performed two-color sFCS experiments after a 20-min incubation of the samples with 50 μM ZnCl_2 . After zinc addition, we observed a strong colocalization of APLP1-YFP and APLP1-Card at cell–cell contact sites and the formation of large protein clusters within ~ 2 min (see, e.g., Figures 2A and 3B and Supplemental Figure S4).

We performed sFCS measurements across these clusters for ~ 10 min on several cell–cell junctions and obtained the corresponding correlation functions (Figure 2B), that is, two ACFs for APLP1-YFP (green) and APLP1-Card (red) and a CCF (blue) between the two channels. As anticipated, correlation functions showed large decay times of ~ 10 s and low signal-to-noise ratios at large correlation times. The data noise, caused by the extremely slow diffusion and limited acquisition times, prevented a quantitative analysis of protein dynamics. Thus, diffusion coefficients could only be estimated to be on the order of $10^{-3} \mu\text{m}^2/\text{s}$ (i.e., ~ 100 -fold reduction compared with diffusion in the absence of zinc). On the other hand, we were able to calculate the cross-correlation values from the fluorescence fluctuations in both channels at short correlation times (i.e., the leftmost points of the CCF in Figure 2B, blue data points and line). The measured average relative cross-correlation of 0.8 ± 0.3 (mean \pm SD, $n = 17$ cells) is $\sim 35\%$ higher than the one measured before zinc treatment (Figure 2C) and close to the maximum cross-correlation measured on myr-palm-Card-YFP tandem-expressing cells (0.96 ± 0.18 , mean \pm SD, $n = 14$ cells from three independent measurements; Supplemental Figure S1). This indicates that most of APLP1 is involved in *trans* interactions. In a simplified example in which only one APLP1 multimeric species is present and all APLP1 is fluorescent, $\sim 80\%$ of the protein would be part of *trans* complexes. Note that, because of the presence of photobleaching, the measured relative cross-correlation might be slightly lower than

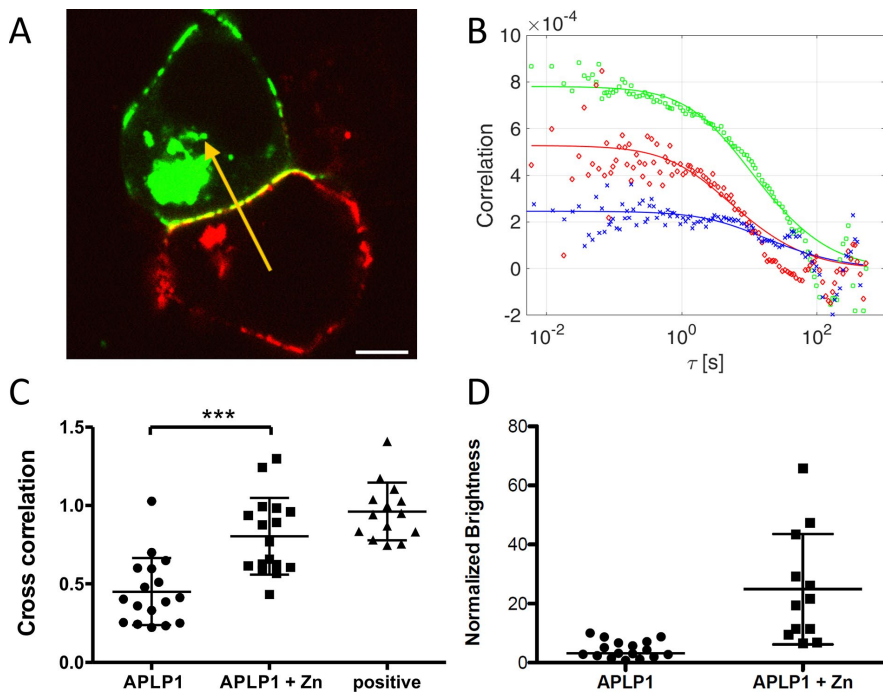


FIGURE 2: Zinc induces formation of slow APLP1-YFP/APLP1-Card clusters at cell-cell contacts showing enhanced *trans* interactions. (A) HEK cells expressing APLP1-YFP (green) or APLP1-Card (red) 20 min after incubation with 50 μM ZnCl_2 . The yellow arrow represents a typical two-color sFCS line scan across a protein cluster in the cell-cell junction. Scale bar is 5 μm . (B) Representative correlation functions and fit curves for two-color sFCS measurements according to a two-dimensional diffusion model (see the text for details). Red, ACF in red channel (APLP1-Card); green, ACF in green channel (APLP1-YFP); blue, CCF calculated between the two spectral channels. (C) Cross-correlation values from all measurements (three independent experiments) for zinc-treated APLP1 cells (17 cells), nontreated cells (17 cells), and cells expressing myr-palm-Card-YFP tandem (14 cells; see also Figure 1) as positive control for cross-correlation. Asterisks indicate statistically significant differences with $***p < 0.001$ determined with Welch's two-sided t test. (D) Brightness of APLP1-YFP with and without zinc, calculated from sFCS measurements in cell-cell contacts (normalized to myr-palm-YFP brightness). Error bars represent mean \pm SD.

the real one and, therefore, the reported values are to be considered low estimates.

We also calculated the brightness of APLP1 clusters from sFCS data and found a strong increase in brightness upon zinc addition compared with values measured without zinc (Figure 2D). The measured values are in the range of ~ 10 – 50 monomers per *cis* multimer, that is, up to ~ 100 APLP1 monomers in a whole protein cluster across the cell junction.

The large APLP1 clusters observed at cell-cell contacts have a typical size of $\sim 10^2$ – 10^3 nm. Thus, sFCS (i.e., scanning in a line pattern with diffraction-limited thickness) captures only a portion of the clusters. To monitor APLP1 *trans* interactions along the whole contact region, we performed ccN&B because this method can map molecular aggregation in space (Digman *et al.*, 2008, 2009; Hilsch *et al.*, 2014; Bobone *et al.*, 2017). This analysis provides single-channel brightness and cross-correlation brightness values (B_{cc}), pixel by pixel. The normalized single-channel brightness value is a direct indication of the multimeric state of a fluorescent protein complex. The normalization procedure is performed exactly as already described for sFCS. B_{cc} values are a measurement of the interaction between spectrally distinguished molecules. B_{cc} values distributed around 0 indicate the absence of fluorescence fluctuation cross-correlation, that is, the lack of

interaction between YFP- and Card-labeled molecules. Positive B_{cc} average values indicate the presence of an interaction (i.e., coordinated diffusion) between YFP- and Card-labeled molecules.

We analyzed several junctions of mixed cells expressing APLP1-YFP and APLP1-Card in the absence of zinc (see, e.g., Figure 3A) or in the presence of 50 μM ZnCl_2 (see, e.g., Figure 3B). After selecting the pixels corresponding to these junctions as regions of interest, we calculated the single-channel normalized brightness and B_{cc} values pixel-wise and pooled the results from all measured junctions in histograms for the brightness of APLP1-YFP (Figure 3, G and H, normalized as described in *Materials and Methods*) and B_{cc} (Figure 3, D–F).

In both experimental conditions (i.e., no zinc or 50 μM ZnCl_2), we measured a positive average value for the B_{cc} of the pixels corresponding to cell-cell contacts compared with a negative control (Figure 3, D–F). Without zinc, we determined an average B_{cc} of 0.068 ± 0.004 (mean \pm SEM, $n = 18$ cells from three independent measurements). After zinc addition, we observed an increase of B_{cc} to 0.266 ± 0.006 (mean \pm SEM, $n = 19$ cells from three independent measurements). The negative control sample consisted of mixed cells expressing either myr-palm-YFP or myr-palm-Card and was observed under the same acquisition conditions as those used for observation of the other samples. The B_{cc} distribution obtained in this case had a mean value of 0.022 ± 0.002 (mean \pm SEM, $n = 26$ cells from three independent measurements).

The normalized brightness histograms of APLP1-YFP at cell-cell contacts show a shift from brightness values corresponding to small oligomers in the absence of zinc (Figure 3G, distribution peak ~ 2) to large multimers in the presence of zinc (Figure 3H, range of ~ 10 – 60), in good agreement with sFCS brightness data. Thus, we conclude that zinc enhances the formation of APLP1 clusters at cell-cell contacts. These clusters appear to be stabilized by protein *trans* interactions.

Zinc does not induce APLP1 multimerization in giant plasma membrane vesicles (GPMVs)

The appearance of large APLP1 clusters upon zinc addition raises the question of whether further cellular components are involved in APLP1 interactions and cluster formation. Considering the putative role of APLP1 *trans* clusters as adhesion complexes, the cortical actin cytoskeleton underlying the membranes is of particular interest. To unravel its role in APLP1 clustering, we investigated APLP1 interactions in cytoskeleton-free, yet native, membrane systems (Schneider *et al.*, 2017). We produced GPMVs from APLP1-YFP-expressing cells and measured the diffusion coefficient and molecular brightness of APLP1-YFP with sFCS in the absence and presence of zinc ions. Interestingly, upon zinc addition, the lateral organization of APLP1 in the vesicular membrane remains homogeneous (Figure 4, A and B).

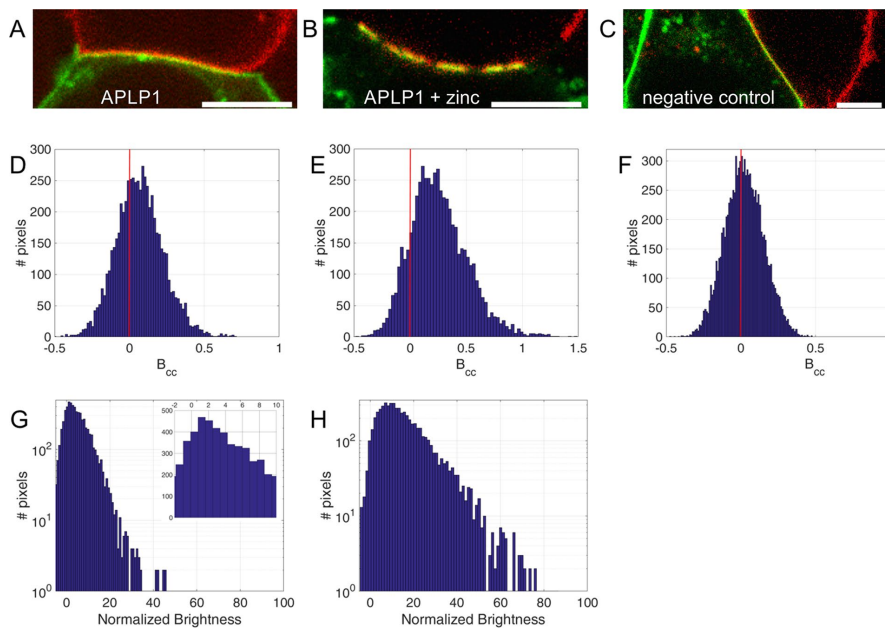


FIGURE 3: Two-color ccN&B analysis reveals *trans* interactions among APL1 molecules in zinc-induced macroscopic clusters. (A) Fluorescence image frame extracted from a ccN&B image stack of a typical contact area between APL1-YFP- and APL1-Card-expressing cells. (B) Fluorescence image frame of APL1-YFP/APL1-Card contact area acquired 20 min after zinc incubation. (C) Image frame from ccN&B image stack measured on myr-palm-YFP/myr-palm-Card cell-cell contact (negative control). (D-F) Cross-correlation brightness (B_{cc}) histograms of all examined pixels and cells in the context of ccN&B analysis of cell-cell contacts in APL1 samples without zinc (D; $n = 18$ cells from three independent measurements), with zinc (E; $n = 19$ cells from three independent measurements) and in myr-palm-YFP/myr-palm-Card control sample (F; $n = 26$ cells from three independent measurements). Vertical red lines correspond to $B_{cc} = 0$. (G, H) Normalized brightness histograms of APL1-YFP in the absence of zinc (G) and after 20 min $ZnCl_2$ incubation (H), measured at APL1-YFP/APL1-Card junctions. Normalized brightness histograms were obtained from the analysis of the same cells and regions of interest used for the calculation of B_{cc} . Inset in G shows a magnification in the normalized brightness range of -2 to 10 .

In both conditions, we measured the same average diffusion coefficient for the protein in the membrane, that is, $2.1 \pm 1.3 \mu m^2/s$ (median \pm SD, $n = 33$ GPMVs from three independent measurements) with zinc and $2.1 \pm 1.1 \mu m^2/s$ (median \pm SD, $n = 33$ GPMVs from three independent measurements) without zinc (Figure 4C). A more detailed analysis reveals also that APL1 diffusion is comparable to the monomeric reference myr-palm-YFP in GPMVs, whereas it is much slower in cells (outside junctions): $D_{myr-palm-YFP}/D_{APL1-YFP}$ is 5 ± 1 in cells (Figure 1E and Supplemental Figure S3), whereas the corresponding value measured in GPMVs is 1.5 ± 0.7 (Figure 4C).

To determine the oligomerization state of APL1 in the GPMVs, we measured the brightness of myr-palm-YFP in GPMVs on the same day and normalized the measured APL1-YFP brightness to that value. As shown in Figure 4D, the average normalized brightness of APL1 is 1.9 ± 1.4 (median \pm SD, $n = 33$ GPMVs from three independent measurements) in the absence of zinc and 2.0 ± 2.3 (median \pm SD, $n = 33$ from three independent measurements) in the presence of $50 \mu M$ zinc ions. These data indicate that the protein forms, on average, *cis* dimers in GPMVs independent of the presence of zinc.

APL1 does not interact in *trans* at contacts of cells and GPMVs

The experiments on GPMVs described in the preceding paragraph focused on the role of the cytoskeleton in influencing APL1

cis interactions and macromolecular clustering. To extend these experiments to *trans* interactions and adhesion, we performed measurements on GPMV-cell contacts, both in the presence and absence of zinc. GPMVs produced from APL1-YFP-expressing cells were mixed with APL1-Card-expressing cells (see *Materials and Methods* for details), and vesicles in contact with fluorescent cells were analyzed. (Note that an analogous experiment carried out by mixing GPMVs containing APL1-YFP and GPMVs containing APL1-Card could not be performed because stable contacts between GPMVs were observed only very rarely.) In the absence of zinc, we observed a homogeneous distribution of APL1 in the contact area, both in GPMVs and in cells (Figure 5A). Upon zinc addition, we observed rapid clustering of APL1 only at the PM of intact cells but no change in the homogeneous distribution of APL1 in GPMVs. We observed neither an enrichment of APL1-YFP nor the formation of APL1-YFP/APL1-Card clusters at the GPMV-cell contacts (see Figure 5B). To quantitatively probe APL1 *trans* interactions at GPMV-cell contacts, we performed two-color sFCS measurements across these contacts in both the presence and absence of zinc. Figure 5 shows the ACFs and CCFs obtained from the analysis of fluorescence fluctuations before (Figure 5C) and after (Figure 5D) the addition of $50 \mu M$ $ZnCl_2$. The amplitudes of the obtained curves were used to calculate relative cross-correlations, as described in the preceding paragraphs. In both cases, we detected no

significant cross-correlation of the GPMV and cell signal, that is, no correlated dynamics of APL1-YFP and APL1-Card at GPMV-cell contact sites. As shown in Figure 5E, the relative cross-correlation values obtained in the absence (0.07 ± 0.05 , mean \pm SD, $n = 6$ cells from three independent measurements) and presence (0.05 ± 0.09 , mean \pm SD, $n = 12$ cells from three independent measurements) of zinc were in the range of the values obtained for the negative control in cell-cell measurements (0.08 ± 0.10 , mean \pm SD, $n = 17$ cells from three independent measurements; Supplemental Figure S2 and Figure 1C). Thus, we conclude that APL1 *trans* interactions are not detectable at contacts between GPMVs and cells, independently from the presence of zinc. The analysis of ACFs shown in Figure 5, C and D, also yields normalized brightness and diffusion times (and diffusion coefficients) for APL1 at the contacts between cells and GPMVs in the absence and presence of zinc. Tables 1 and 2 show a summary of the obtained results and include those reported in the preceding paragraphs as well. In the absence of zinc, we observed a reduction of APL1 (in GPMVs) dynamics at cell-GPMV junctions, similar to what we observed in cell-cell junctions. Interestingly, dynamics of APL1 in cells were not affected in this case. In the presence of zinc, we observed only a 30% reduction in APL1 diffusivity in GPMVs (Figure 5F). The observed decrease in protein dynamics is very small compared with that observed in cell membranes under the same conditions. Similarly, we observed

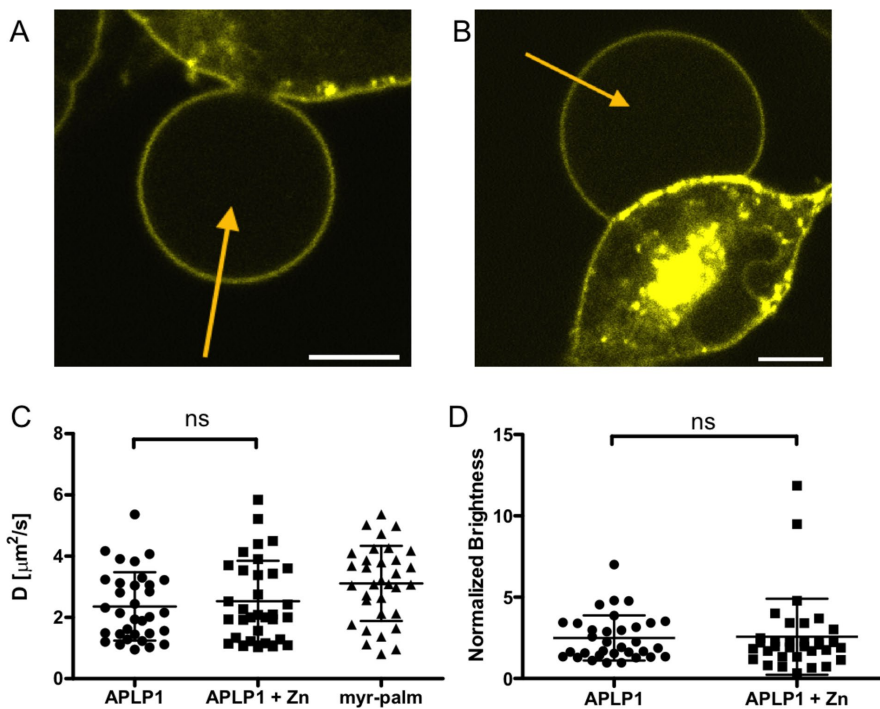


FIGURE 4: APLP1-YFP oligomerization and diffusion in GPMVs are not affected by zinc. (A) A GPMV forming from an APLP1-YFP-expressing HEK cell. Yellow arrow represents an sFCS line scan across the GPMV. (B) A GPMV forming from an APLP1-YFP-expressing HEK cell incubated with 50 μM ZnCl_2 for 20 min after 45 min of incubation with NEM (see *Materials and Methods*). (C) Diffusion coefficients measured for APLP1-YFP (before and after incubation with zinc) and myr-palm-YFP in GPMVs. (D) Normalized brightness values measured for APLP1-YFP in GPMVs before and after incubation with zinc. Values are normalized to the average brightness measured for myr-palm-YFP in GPMVs under the same conditions. Data are pooled from 33 GPMVs measured in three independent experiments. Error bars represent mean \pm SD. “ns” indicates no statistically significant differences were determined with Welch’s two-sided *t* test.

only a modest increase in APLP1 (in GPMVs) multimerization in cell-GPMV junctions compared with the increase observed for cell-cell junctions under the same conditions (see also Figures 2D, 3, G and H, and 5G).

Finally, in order to further investigate the possibility that the actin meshwork is involved in APLP1 multimerization, we stained filamentous actin in cells expressing APLP1-Card using Lifeact-green fluorescent protein (Lifeact-GFP; Riedl *et al.*, 2010). Our results (Supplemental Figure S5) indicate that the presence of zinc induces accumulation of filamentous actin at cell-cell junctions, in proximity of APLP1 *trans* clusters.

DISCUSSION

APP and its paralogues APLP1 and APLP2 have an important role in nervous system development and associated pathologies (Vassar *et al.*, 1999; Coulson *et al.*, 2000; Selkoe, 2001; Eggert *et al.*, 2004; Li and Südhof, 2004; Blennow *et al.*, 2006). Various studies proposed that APLP1 acts as a homotypic neuronal adhesion receptor (Soba *et al.*, 2005; Kaden *et al.*, 2009; Mayer *et al.*, 2016; Schilling *et al.*, 2017) although, until now, little evidence of protein-protein *trans* interactions (i.e., among proteins from two different cells at a junction) has been provided in living cells (Soba *et al.*, 2005; Kaden *et al.*, 2009).

In this study, we addressed the mechanisms of multimerization and the diffusion dynamics of APLP1 with experimental assays that allowed us to specifically probe *cis* and *trans* interactions of APLP1

directly in living HEK cells. This specific cellular model was chosen based on earlier studies (Mayer *et al.*, 2014, 2016) demonstrating that zinc-mediated multimerization at the PM occurs similarly in HEK and neuronal cells. Furthermore, HEK cells do not express endogenous APLP1 (Lorent *et al.*, 1995; Su *et al.*, 2004). As a consequence, APLP1 multimers contain only fluorescent APLP1 molecules, and their stoichiometry can be correctly characterized by fluorescence fluctuation analysis.

Cross-correlation sFCS and N&B analysis indicate the presence of *trans* binding of small APLP1 *cis* oligomers (i.e., APLP1-YFP/APLP1-Card complexes), as evidenced by the data in Figures 1C and 3D. It is worth noting that the techniques used in this work detect the formation of (*cis* or *trans*) complexes by quantifying the codiffusion of its components. It cannot be excluded, in general, that such complexes also include proteins other than APLP1. Nevertheless, brightness measurements clearly indicate that the observed *cis* oligomers contain, on average, approximately three APLP1 monomers (see Figures 2D and 3G). Notably, APLP1 *trans* binding appears to be incomplete, that is, a considerable fraction of APLP1 proteins forms exclusively *cis* oligomers and does not interact with other APLP1 molecules in the neighboring cell. The existence of intermolecular interactions involving APLP1 occurring specifically at cell-cell junctions is also corroborated by our diffusion measurements. We found a significantly reduced mobility of APLP1 at cell-cell contacts compared with other areas of the PM (Figure 1E), in good agreement with previously published fluorescence recovery after photobleaching data (Kaden *et al.*, 2009).

Recent studies indicated a crucial role of metal ions, predominantly zinc and copper, in driving the oligomerization of APP family proteins (Baumkötter *et al.*, 2014; Mayer *et al.*, 2014; Wild *et al.*, 2017). Zinc ions binding to the extracellular domain of the protein induce multimerization of APLP1 and enrichment of these multimers at cell-cell contact sites (Mayer *et al.*, 2014, 2016). Nevertheless, the role of zinc in specifically promoting APLP1 *trans* interactions in a junction between living cells had not been directly proven yet. For this reason, we performed experiments on mixed-cell populations expressing two differently labeled APLP1 constructs in the presence of zinc. We observed a rapid formation of large protein platforms at cell-cell contact sites containing APLP1 from both neighboring cells (see Figures 2A and 3B and Supplemental Figure S4). Two-color sFCS measurements indicated remarkably slow dynamics for these APLP1 clusters (i.e., 10^{-3} $\mu\text{m}^2/\text{s}$, which is 100-fold lower than APLP1 without zinc), probably because of their size. Furthermore, we detected a cross-correlation significantly higher than that measured in the absence of zinc (Figure 2C). Using a complementary approach (i.e., ccN&B), we found once more a cross-correlation significantly higher than that measured in the absence of zinc (Figure 3, D and E) or for a negative control sample featuring no *trans* interactions (Figure 3F). Thus we conclude that zinc enhances, at least indirectly, the formation of APLP1 *trans* complexes along cell-cell contacts. On the basis

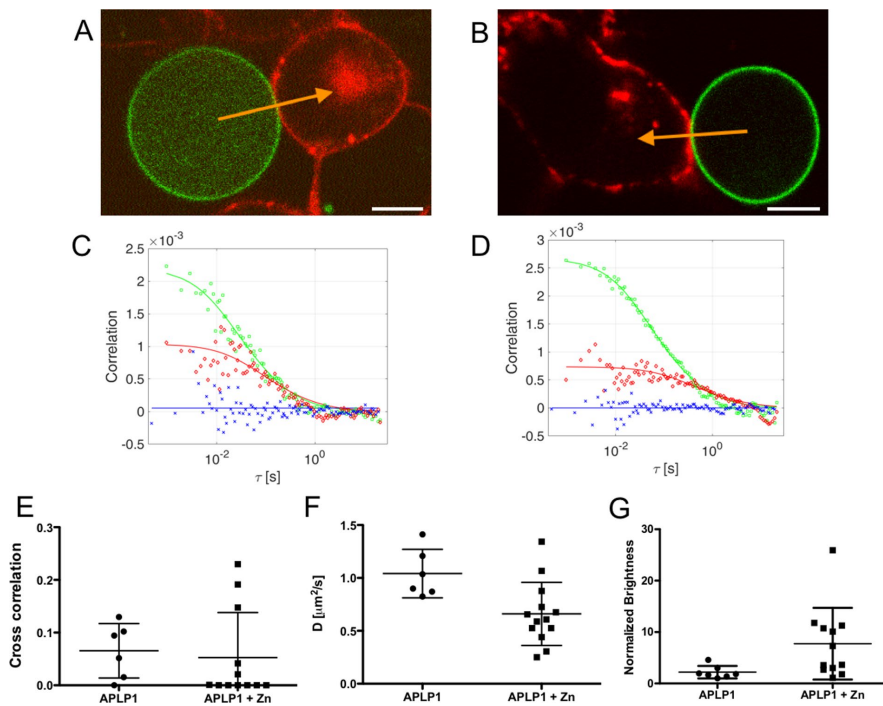


FIGURE 5: APLP1 does not interact in *trans* at GPMV-cell contacts independently from zinc. (A, B) A GPMV containing APLP1-YFP in contact with an APLP1-Card-expressing HEK cell before (A) and after (B) 20-min zinc incubation. Yellow arrows represent a two-color sFCS line scan across the contact area. Scale bar is 5 μm . (C, D) Representative correlation functions and fit curves for two-color sFCS measurements without (C) and with (D) zinc. Red, ACF in red channel (APLP1-Card in cell); green, ACF in green channel (APLP1-YFP in GPMV); blue, CCF calculated between the two spectral channels. Correlation curves (solid lines) were obtained by fitting a two-dimensional diffusion model to the data. (E–G) Cross-correlation values (E), diffusion coefficients in GPMVs (F; normalized to APLP1 average value), and normalized brightness of APLP1-YFP in GPMVs (G) from all GPMV-cell contact measurements (six cells without and 12 cells with zinc in three independent experiments, shown as mean \pm SD).

of a brightness analysis (Figures 2D and 3H) deriving from both sFCS and cross-correlation analysis, we found that these complexes can consist of up to ≈ 50 –100 APLP1 monomers interacting in *trans* through the junction.

Several studies on various cell–cell interactions show that adhesion and signaling of transmembrane receptors are closely linked to the cytoskeletal organization underneath the membrane (Nelson, 2008; Mui *et al.*, 2016). The cytoskeleton also strongly affects lateral distribution and dynamics of membrane constituents (lipids, proteins), for example, by restricting the free diffusion of transmem-

brane proteins spatially (Kusumi *et al.*, 1993; Kusumi and Sako, 1996; Iino *et al.*, 2001; Fujiwara *et al.*, 2002; Saha *et al.*, 2015). Given the size and putative role of APLP1 clusters as adhesion platforms, it might be possible that the cellular cytoskeleton is involved in APLP1–APLP1 interactions. Therefore, we investigated APLP1 diffusion and oligomerization in cell-derived GPMVs, a cytoskeleton-free, native membrane model system (Sezgin *et al.*, 2012; Schneider *et al.*, 2017). To our surprise, we did not find any zinc-induced alteration of APLP1 localization, diffusion, or brightness. Both before and after zinc treatment, APLP1-YFP was homogeneously distributed in GPMVs. Of interest, APLP1 normalized brightness measured via sFCS was ≈ -2 , indicating the presence of APLP1 *cis* dimers on average in both the presence and absence of zinc. This value is in line with previous measurements of APLP1 *cis* oligomerization in cells using N&B (Mayer *et al.*, 2016) and biochemical studies (Mayer *et al.*, 2014) and indicates that zinc does not have a significant effect on APLP1–APLP1 interaction in this specific model. Furthermore, we observed that APLP1 diffusion in the PM is significantly slower than a model inner leaflet-associated protein (myr-palm-YFP). On the other hand, APLP1 and myr-palm-YFP dynamics are very similar in GPMVs, suggesting that APLP1 interacts with the cytoskeleton in intact cells (Figure 4C). These observations support the possibility that APLP1 dynamics and lateral interactions are influenced by the stable actin mesh via, for example, a corralling mechanism (see, e.g., the “picket fence” model [Kusumi *et al.*, 2012]). This putative specific interaction between cytoskeleton and APLP1 (e.g., via the YENPTY motif; see Guénette *et al.* [2017] and Sosa *et al.* [2017]) appears to be required for zinc-induced *cis* oligomerization to occur.

The results we presented so far are in full agreement with the model we have previously proposed, according to which, in general, zinc ions mediate APLP1–APLP1 interactions. Nevertheless, it is not yet clear whether zinc mediates both *cis* and *trans* interaction via the same molecular mechanism. To investigate this issue,

	Cell PM	Cell–cell	GPMV	Cell-GPMV (GPMV side)	Cell-GPMV (cell side)
APLP1	0.25 ± 0.09	0.09 ± 0.06	2.1 ± 1.1	1.04 ± 0.23	0.30 ± 0.11
APLP1 + Zn	$(\sim 10^{-2} - 10^{-3})$	$\sim 10^{-3}$	2.1 ± 1.3	0.7 ± 0.3	N/A
myr-palm-YFP	1.3 ± 0.4	1.3 ± 0.3	3.2 ± 1.3	N/A	N/A
GPI-YFP	1.1 ± 0.3	1.1 ± 0.3	N/A	N/A	N/A

Diffusion coefficients (D [$\mu\text{m}^2/\text{s}$]) were measured by analyzing the decay of sFCS ACFs outside cell–cell junctions, within cell–cell junctions, in free-standing GPMVs, and in junctions between cells and GPMVs. In the latter case, values are provided for APLP1-YFP in GPMVs (GPMV side) or APLP1-Card in cells (cell side). Measurements were performed also in the presence of 50 μM ZnCl_2 (see the text) and for model membrane-associated proteins myr-palm-YFP and GPI-YFP. Values are shown as mean \pm SD.

TABLE 1: Summary of diffusion coefficients measured via sFCS.

	Cell PM	Cell-cell	GPMV	Cell-GPMV (GPMV side)
APLP1	N/A	3.0 ± 2.9	1.9 ± 1.4	1.8 ± 1.2
APLP1 + Zn	N/A	21 ± 20	2.0 ± 2.3	6 ± 7

Normalized APLP1-YFP brightness was measured by analyzing sFCS ACFs outside cell-cell junctions, within cell-cell junctions, in free-standing GPMVs, and in junctions between cells and GPMVs. In the latter case, values are provided only for APLP1-YFP in GPMVs (GPMV side). Measurements were also performed in the presence of 50 μ M ZnCl₂ (see the text). Values are shown as median \pm SD.

TABLE 2: Summary of normalized brightness values measured via sFCS.

we produced mixed samples of GPMVs and cells and probed APLP1 *trans* interactions at GPMV-cell contact sites using two-color sFCS. This experiment aimed at verifying whether zinc can, in general, also promote *trans* interactions between small *cis* oligomers and large *cis* multimers (or, alternatively, whether large *cis* multimers are required on both cells). In contrast to the case of cell-cell contacts, we detected no significant cross-correlation between the fluorescence signals from APLP1 in GPMVs and in cell membranes, also in the presence of zinc (Figure 5E). Also, no spatial colocalization of large protein domains was observed. In more detail, we observed zinc-induced APLP1 clustering in cells, as expected from the previous results, whereas APLP1 in the neighboring GPMV remained homogeneously distributed, featuring only a minor reduction in diffusivity and a modest increase in brightness compared with those observed in intact cell membranes (see Tables 1 and 2). It must be noted, however, that GPMVs differ from PMs not only in the absence of cytoskeleton, but also in terms of lipid composition and transmembrane asymmetry (Sezgin *et al.*, 2012). On one hand, these factors might also affect protein dynamics and protein-protein interaction. On the other hand, previous studies (Gu nette *et al.*, 2017; Sosa *et al.*, 2017) and the direct observation of filamentous actin enrichment at the sites of zinc-induced APLP1 clustering (Supplemental Figure S5) support the possibility that the cytoskeleton plays an important role in APLP1-APLP1 interactions.

Taken together, our results indicate that zinc promotes the formation of large APLP1 *cis* multimers in the presence of an intact cytoskeleton. Nevertheless, the absence of *trans* interactions between large *cis* multimers and small *cis* oligomers in the presence of zinc suggests that the metal does not directly mediate such *trans* interactions. We propose, therefore, that zinc promotes first the formation of large *cis* multimers (see Figure 6). Subsequently, interactions between facing *cis* multimers are established and likely stabilized by the large free energy gain derived from multiple and concurrent APLP1-APLP1 *trans* interactions. In agreement with this model, *trans* interactions involving small *cis* multimers can occur but appear weaker and/or transient in the absence (Figures 1C and 3D) or presence (Figure 5) of zinc. This model is also supported by recent observations indicating that zinc binding is mediated by the E2 domain of APLP1 (Mayer *et al.*, 2014), whereas *trans* interactions occur via the E1 domain (Stahl *et al.*, 2014).

On the basis of previous measurements (Mayer *et al.*, 2014, 2016), we argue that the results we obtained for HEK cells might be transferable and highly relevant also in the context of cell-cell interaction in the nervous system *in vivo*. In more detail, it was shown that APLP1 forms clusters along the soma and dendritic PM of rat hippocampal neurons in the presence of zinc (Mayer *et al.*, 2014). In addition, we previously observed zinc-enhanced cell adhesion of

cortical neurons on a substrate printed with immobilized APLP1 ectodomain (Mayer *et al.*, 2016). Finally, a very recent study shows that APLP1 is pre- and postsynaptically expressed in brain tissue and up-regulated during postnatal development coinciding with synaptogenesis (Schilling *et al.*, 2017). According to the model presented in this work, the formation of large *cis* complexes (caused by the presence of zinc ions and supported by the actin cortex) is required for the establishment of stable APLP1-APLP1 *trans* interactions and, therefore, might enable APLP1 to function as a synaptic adhesion molecule *in vivo*.

MATERIALS AND METHODS

Cell culture

HEK cells from the 293T line (ACC 305; DMSZ, Braunschweig, Germany) were cultured in DMEM with the addition of fetal bovine serum (10%) and L-glutamine (1%) and passaged every 3 d and no more than 10 times. Mycoplasma contamination tests and morphology tests were performed every 3 mo and 2 wk, respectively. All solutions, buffers, and media used for cell culture were purchased from PAN-Biotech (Aidenbach, Germany). For one-color experiments and measurements involving the myr-palm-Card-YFP tandem, 6×10^5 cells were seeded in 35-mm dishes (CellVis, Mountain View, CA) with optical glass bottoms 24 h before transfection. For cell-mixing experiments, cells were seeded in a six-well plate (Eppendorf, Wesseling-Berzdorf, Germany) with 8×10^5 cells per well.

Plasmids and cloning

The APLP1-YFP (Mayer *et al.*, 2014) and mCardinal-N1 (Chu *et al.*, 2014) plasmids were used to clone the APLP1-Card plasmid. The mCardinal-N1/C1 constructs were gifts from Michael Davidson (Florida State University; Addgene plasmids no. 54590 and 54799). APLP1 insert was amplified using custom-designed primers and a standard PCR protocol, digested by *Xho*I and *Age*I Fast Digest Enzymes (Thermo Fisher Scientific, Darmstadt, Germany), and ligated to the digested mCardinal-N1 vector with T4 DNA Ligase (Thermo Fisher Scientific, Darmstadt, Germany). Myr-palm-YFP (myristoylated and palmitoylated peptide fused to YFP) was a gift from Andreas Herrmann (Humboldt Universitaet zu Berlin). It encodes the amino acid sequence MGCIKSKRKDNLNDDPEPPVAT derived from the N-terminus of the Lyn kinase (Engel *et al.*, 2010). A monomeric YFP was first obtained from pEYFP-N1 (Addgene plasmid no. 2689) including the A206K mutation in order to reduce any tendency to build homodimers (von Stetten *et al.*, 2012). The myristoylation/palmitoylation sequence was then subcloned into the multicloning site of mEYFP-N1 (Engel *et al.*, 2010). GPI-YFP, also containing the A206K mutation, was a gift from Roland Schwarzer (Gladstone Institute, San Francisco; Schwarzer *et al.*, 2014).

The myr-palm-Card plasmid was cloned using a modified mCardinal-C1 vector. First, a *Scal* restriction site was inserted into the mCardinal-C1 vector by using the QuickChange protocol. Second, the myr-palm peptide was amplified from the myr-palm-YFP plasmid using custom-designed primers. After digestion with *Nhe*I and *Scal*, the peptide was ligated to the digested mCardinal-C1 vector.

To clone the myr-palm-Card-YFP plasmid, YFP was amplified from myr-palm-YFP using custom-made primers. YFP insert and myr-palm-Card vector were digested with *Hind*III and *Kpn*I, and the products were ligated using the T4 DNA Ligase. CD86 was amplified from CD86-enhanced green fluorescent protein (a kind gift from Richard J. Ward, University of Glasgow; Zakrys *et al.*, 2014) using custom-made primers, digested with *Kpn*I and *Age*I restriction enzymes, and ligated with the digested mEYFP-N1

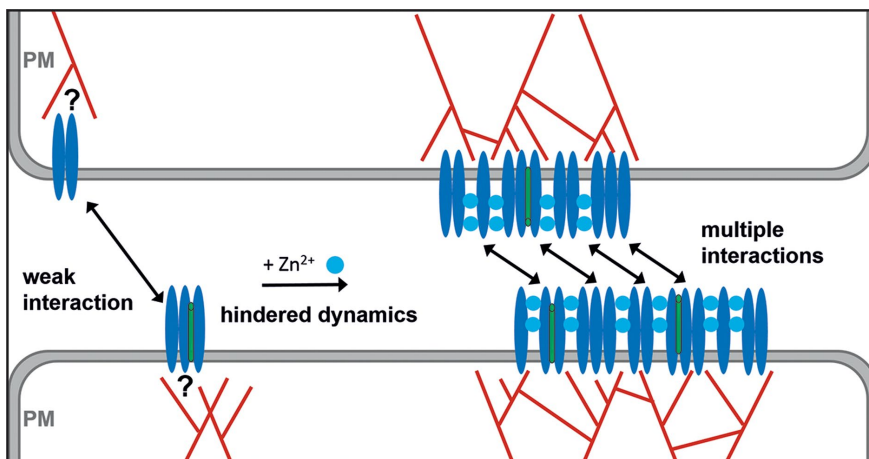


FIGURE 6: Model for APLP1–APLP1 interaction in the presence of zinc and formation of APLP1 cell–cell adhesion platforms. In the absence of zinc, only small *cis* oligomers are present. *Trans* interactions among protein complexes across cell–cell junctions are weak. Our data regarding protein diffusion suggest the existence of possible interactions between APLP1 and cortical actin network (red). The exact nature of such interaction has yet to be identified. In the presence of physiological zinc concentration (and an intact cortical actin cytoskeleton), APLP1 *cis* oligomers coalesce into large *cis* multimers (~10–50 molecules, figure not drawn to scale). Such protein clusters interact strongly across the cell junction, possibly because of the establishment of multiple APLP1–APLP1 *trans* interactions. It might be possible that unknown proteins (green) are also included in APLP1 multimers.

vector using the T4 DNA Ligase, thus obtaining CD86-YFP. Sequences of all vectors were verified by DNA sequencing (LGC Berlin, Germany). Lifeact-GFP was a kind gift from the Eggeling Lab (Oxford University; Schneider *et al.*, 2017).

Preparation for microscopy experiments

For one-color measurements, cells were transfected 16–20 h before the experiment using between 250 ng (myr-palm-Card/-YFP) and 1 μ g (APLP1-Card/-YFP) plasmid per dish. Plasmids were incubated for 20 min with 2.5–4 μ l Turbofect (Thermo Fisher Scientific, Darmstadt, Germany) per dish and 50 μ l serum-free medium according to the manufacturer instructions and then added dropwise to the cells. For cell-mixing experiments, cells were washed 4 h after transfection with phosphate-buffered saline (+/+), and detached by gentle shaking using 50 μ l trypsin EDTA. Then, cells were resuspended in 2 ml medium by pipetting up and down, mixed, and seeded on new dishes.

For measurements of APLP1 multimerization, culture medium was replaced by 4-(2-hydroxyethyl)-1-piperazineethanesulfonic acid (HEPES) buffer (10 mM HEPES, pH 7.1, containing 135 mM NaCl, 6 mM KCl, and 5.5 mM glucose) after two washing steps with the same buffer. When zinc was required, the buffer was supplemented with 50 μ M ZnCl₂. Microscopy was performed after 20 min of incubation in zinc-containing buffer at room temperature.

GPMV preparation

GPMVs were produced following the *N*-ethylmaleimide (NEM) protocol (Sezgin *et al.*, 2012). Briefly, cells were washed twice and incubated for 45 min in NEM buffer (2 mM NEM, 10 mM HEPES, 150 mM NaCl, 2 mM CaCl₂, pH 7.4) at 37°C. Afterward, the NEM buffer was replaced by the HEPES buffer used for all imaging experiments. For sFCS measurements, blebs that were still attached to cells were selected to avoid out-of-focus movement or drift.

For GPMV-cell contact measurements, blebbing of APLP1-YFP-expressing cells was induced for 45 min in NEM buffer. After incubation, most of the GPMVs were still attached to adherent cells. Cells were washed once in HEPES buffer and detached in 150 μ l HEPES buffer by pipetting and gentle shaking. The resulting 150- μ l suspension was added to the center of a dish containing APLP1-Card-expressing cells previously washed with HEPES buffer. To increase the number of GPMVs and thus the probability of finding GPMVs and cells in contact, GPMVs from two dishes were pooled and added to one cell dish. After 10 min of initial settling, HEPES buffer was added to a final volume of 2 ml per dish. Imaging was started 30 min after mixing to allow GPMVs to settle down. When zinc was required, 50 μ M ZnCl₂ was added after settling and incubated for 20 min before imaging.

Confocal microscopy imaging

Confocal imaging, sFCS, and ccN&B measurements were performed on a Zeiss LSM780 system (Carl Zeiss, Oberkochen, Germany) using a 40 \times , 1.2 numerical aperture water-immersion objective. Samples were excited with a 488-nm argon laser (YFP fluorophore) or a 561-nm diode laser (Card fluorophore). For one-color measurements, fluorescence was detected between 499 and 695 nm, after passing through a 488-nm dichroic mirror, using GaAsP detectors. For two-color measurements, fluorophores were excited and detected sequentially for different regions of the spectrum. Excitation and detection light were separated using a 488/561-nm dichroic mirror. YFP fluorescence was detected between 499 and 695 nm, and mCardinal fluorescence was detected between 570 and 695 nm.

sFCS

For one-color sFCS measurements, a line scan of 128 \times 1 pixels (pixel size 160 nm) was performed perpendicular to the membrane with a 472.73- μ s (for GPMV measurements) or 945.45- μ s scan time (for cell measurements). Typically, 250,000–300,000 lines were acquired (total scan time ~2–4 min) in photon counting mode. Laser powers were adjusted to keep depletion due to photobleaching below 50%. Typical values were ~0.7 μ W for cell measurements and ~1.8 μ W for GPMV measurements. For two-color measurements, a scan time of 1890 μ s was used for both channels, that is, sequential scans with 945.45 μ s per channel. In the absence of zinc (faster APLP1 dynamics), ~0.7- μ W (488-nm) and ~3- μ W (561-nm) laser powers were used. In the presence of zinc (and thus much slower APLP1 dynamics), a 5-ms break in between each complete scan was introduced, and 100,000 scans were acquired with laser powers of ~0.35 μ W (488 nm) and ~1.5 μ W (561 nm). To maximize the fluorescence fluctuation signal, cells with the lowest detectable protein expression were selected. Scanning data were exported as TIFF files, imported, and analyzed in MATLAB (MathWorks, Natick, MA) using custom-written code. sFCS analysis follows the procedure described in Ries and Schwille (2006). Briefly, all lines were aligned as kymographs and divided into blocks of 1000 lines. In each block, lines were summed up column-wise, and the x position with maximum fluorescence was determined. This position defines

the position of the membrane in each block and is used to align all lines to a common origin. Then, all aligned line scans were averaged over time and fitted with a Gaussian function. The pixels corresponding to the membrane were defined as the pixels that are within $\pm 2.5 \sigma$ of the peak. In each line, these pixels were integrated, providing the membrane fluorescence time series $F(t)$. When needed, a background correction was applied by subtracting the average pixel fluorescence value in the cytosol multiplied by 2.5 σ (in pixel units) from the membrane fluorescence, in blocks of 1000 lines (Dörlich *et al.*, 2015). To correct for depletion due to photobleaching, the fluorescence time series was fitted with a two-component exponential function, and the previously introduced correction formula was applied (Ries *et al.*, 2009). For two-color measurements, the alignment and correction procedure was independently performed for each channel. Finally, ACFs (G_{auto}) and, in the case of two-color experiments (g = green channel, r = red channel), CCFs (G_{cross}) were calculated as follows:

$$G_{\text{auto}}(\tau) = \frac{\langle \delta F_i(t) \delta F_i(t + \tau) \rangle}{\langle \delta F_i(t) \rangle^2}$$

$$G_{\text{cross}}(\tau) = \frac{\langle \delta F_g(t) \delta F_r(t + \tau) \rangle}{\langle F_g(t) \rangle \langle F_r(t) \rangle}$$

where $\delta F_i = F_i(t) - \langle F_i(t) \rangle$ and $i = g, r$.

A model for two-dimensional diffusion in the membrane and a Gaussian focal volume geometry was fitted to the ACFs (Ries and Schwille, 2006):

$$G(\tau) = \frac{1}{N} \left(1 + \frac{\tau}{\tau_d} \right)^{-1/2} \left(1 + \frac{\tau}{\tau_d S^2} \right)^{-1/2}$$

To calibrate the focal volume, point fluorescence correlation spectroscopy (FCS) measurements with Alexa 488 and rhodamine B dissolved in water at 50 nM were performed. In the fitting routine, the structure parameter S was fixed to the value determined in the calibration measurement (typically around 5). For one-color measurements, the particle number N and diffusion time τ_d were obtained from the fit. Diffusion coefficients (D) were calculated using the calibrated waist of the focal volume, $D = \omega_0^2 / 4\tau_d$. The molecular brightness was calculated by dividing the mean count rate by the particle number determined from the fit, $B = \langle F(t) \rangle / N$. For two-color measurements, all correlation functions were used to fit the diffusion model described above. Relative cross-correlation values were calculated from the amplitudes of the ACFs and CCFs:

$$\max \left\{ \frac{G_{\text{cross}}(0)}{G_{\text{auto}}^g(0)}, \frac{G_{\text{cross}}(0)}{G_{\text{auto}}^r(0)} \right\}$$

where $G_{\text{cross}}(0)$ is the amplitude of the CCF and $G_{\text{auto}}^i(0)$ is the amplitude of the ACF in the i th channel ($i = r, g$). Diffusion coefficients and brightness values were calculated from the obtained fit parameters of the ACFs. Average diffusion coefficients and brightness values in the text are provided as mean or median (in the case of strongly skewed data distributions) \pm SD from all measured cells or GPMVs.

ccN&B analysis

ccN&B experiments were performed as described in Digman *et al.* (2009) with a modified acquisition mode. Briefly, 100 images of 512 \times 512 pixels were acquired per measurement using a 74-nm pixel size

and 6.3- μ s pixel dwell time sequentially for the two detection channels (switching channel every line). Laser powers were maintained low enough to keep bleaching below 10% of the initial fluorescence signal (typically $\sim 0.7 \mu\text{W}$ for 488 nm and $\sim 3 \mu\text{W}$ for 561 nm). For measurements in the presence of zinc, a 5-s break was introduced between each frame (in order to account for the slow dynamics of APLP1 clusters). CZI image output files were imported into MATLAB using the Bioformats package (Linkert *et al.*, 2010) and analyzed using a self-written script. Before further analysis, pixels corresponding to cell-cell contacts were selected manually as regions of interest. Frames were aligned to the first frame by maximizing the spatial correlation between subselections in consecutive frames, averaged over both channels, as a function of arbitrary translations (Trullo *et al.*, 2013). Brightness values (in both spectral channels and cross-correlation brightness) were calculated as described in Digman *et al.* (2008, 2009), and a boxcar algorithm was applied to filter extraneous long-lived fluctuations (Hellriegel *et al.*, 2011; Mayer *et al.*, 2016). Pixels with count rates > 2 MHz were excluded from the analysis to avoid pile-up effects. To further calibrate the detector response, we measured the brightness on a reflective metal surface in each channel. The thus-obtained brightness-versus-intensity plot (which should be constant and equal to 0 for all intensity values) was used to correct the actual experimental data (Digman *et al.*, 2008). Brightness and cross-correlation data are presented as histograms displaying values of all pixels corresponding to cell-cell contacts. Final values are provided as average or median (in the case of strongly skewed data distributions) cross-correlation brightness \pm SEM.

Brightness calibration and fluorophore maturation

The molecular brightness, that is, the photon count rate per molecule, is used as a measure of the multimerization state by calibration with the brightness of a monomeric reference. This analysis is often based on the assumption that all fluorophores within a multimer are fluorescent. However, fluorescent proteins can undergo dark state transitions or be in a nonmature, nonfluorescent state (Chen *et al.*, 2010). This issue has been reported in particular for red fluorescent proteins (Hendrix *et al.*, 2008) and can be noticed in different amplitudes of the fluorescence ACF of tandem dimers (Foo *et al.*, 2012). We have observed that the ACF amplitude for the Card channel is typically much higher than that of YFP in two-color sFCS measurements of a myr-palm-Card-YFP tandem control (Supplemental Figure S1). We attribute this effect to a lower maturation probability of Card compared with YFP. Therefore, to maximize the dynamic range of the brightness analysis, we restricted our analysis to YFP.

To estimate the maturation probability of YFP, we designed a myr-palm-YFP-YFP tandem and measured its brightness using sFCS and N&B. We found a normalized brightness of ~ 1.6 for the dimer, which corresponds to a maturation probability p_m of $\approx 60\%$. We used this value to normalize all brightness data of APLP1-YFP (sFCS and N&B) using the transformation

$$\text{normalized brightness} = 1 + \frac{B_{n,\text{app}} - B_1}{p_m}$$

where $B_{n,\text{app}}$ is the measured apparent molecular brightness and B_1 is the molecular brightness of a monomer (e.g., myr-palm-YFP). The transformation formula was derived assuming a binomial probability distribution for the fluorescence of the n fluorescence units in an n -mer. The normalized brightness indicates then the true oligomeric size of the complexes. This calibration procedure was applied to both sFCS and N&B measurements.

Code availability

MATLAB custom-written code is available upon request from the corresponding author.

ACKNOWLEDGMENTS

This work was supported by grants from the Deutsche Forschungsgemeinschaft (MU901 and CH 1238/3 to G.M. and S.C., respectively) and Canadian Institute of Health Research Grant no. MOP-133411 (to G.M.). G.M. holds a Canada Research Chair in Molecular Pharmacology.

REFERENCES

- Bacia K, Kim SA, Schwille P (2006). Fluorescence cross-correlation spectroscopy in living cells. *Nat Methods* 3, 83–89.
- Baumkötter F, Schmidt N, Vargas C, Schilling S, Weber R, Wagner K, Fiedler S, Klug W, Radzimanowski J, Nickolaus S, et al. (2014). Amyloid precursor protein dimerization and synaptogenic function depend on copper binding to the growth factor-like domain. *J Neurosci* 34, 11159–11172.
- Baumkötter F, Wagner K, Eggert S, Wild K, Kins S (2012). Structural aspects and physiological consequences of APP/APLP trans-dimerization. *Exp Brain Res* 217, 389–395.
- Blennow K, de Leon MJ, Zetterberg H (2006). Alzheimer's disease. *Lancet Neurol* 368, 387–403.
- Bobone S, Hilsch M, Storm J, Dunsing V, Herrmann A, Chiantia S (2017). Phosphatidylserine lateral organization influences the interaction of influenza virus matrix protein 1 with lipid membranes. *J Virol* 91, e00267-17.
- Chen Y, Johnson J, Macdonald P, Wu B, Mueller JD (2010). Observing protein interactions and their stoichiometry in living cells by brightness analysis of fluorescence fluctuation experiments. *Methods Enzymol* 472, 345–363.
- Chu J, Haynes RD, Corbel SPY, Li P, González-González E, Burg JS, Ataie NJ, Lam AJ, Cranfill PJ, Baird MA, et al. (2014). Non-invasive intravital imaging of cellular differentiation with a bright red-excitable fluorescent protein. *Nat Methods* 11, 572–578.
- Coulson EJ, Paliga K, Beyreuther K, Masters CL (2000). What the evolution of the amyloid protein precursor supergene family tells us about its function. *Neurochem Int* 36, 175–184.
- Digman MA, Dalal R, Horwitz AF, Gratton E (2008). Mapping the number of molecules and brightness in the laser scanning microscope. *Biophys J* 94, 2320–2332.
- Digman MA, Wiseman PW, Choi C, Horwitz AR, Gratton E (2009). Stoichiometry of molecular complexes at adhesions in living cells. *Proc Natl Acad Sci USA* 106, 2170–2175.
- Dörlich RM, Chen Q, Niklas Hedde P, Schuster V, Hippler M, Wesslowski J, Davidson G, Nienhaus GU (2015). Dual-color dual-focus line-scanning FCS for quantitative analysis of receptor-ligand interactions in living specimens. *Sci Rep* 5, 10149.
- Eggert S, Paliga K, Soba P, Evin G, Masters CL, Weidemann A, Beyreuther K (2004). The proteolytic processing of the amyloid precursor protein gene family members APLP-1 and APLP-2 involves α -, β -, γ -, and -like cleavages. *J Biol Chem* 279, 18146–18156.
- Engel S, Scolari S, Thaa B, Krebs N, Korte T, Herrmann A, Veit M (2010). FLIM-FRET and FRAP reveal association of influenza virus haemagglutinin with membrane rafts. *Biochem J* 425, 567–573.
- Foo YH, Naredi-Rainer N, Lamb DC, Ahmed S, Wohland T (2012). Factors affecting the quantification of biomolecular interactions by fluorescence cross-correlation spectroscopy. *Biophys J* 102, 1174–1183.
- Fujiwara T, Ritchie K, Murakoshi H, Jacobson K, Kusumi A (2002). Phospholipids undergo hop diffusion in compartmentalized cell membrane. *J Cell Biol* 157, 1071–1082.
- Guénette S, Strecker P, Kins S (2017). APP protein family signaling at the synapse: insights from intracellular APP-binding proteins. *Front Mol Neurosci* 10, 87.
- Heber S, Herms J, Gajic V, Hainfellner J, Aguzzi A, Rüllicke T, von Kretschmar H, von Koch C, Sisodia S, Tremml P, et al. (2000). Mice with combined gene knock-outs reveal essential and partially redundant functions of amyloid precursor protein family members. *J Neurosci* 20, 7951–7963.
- Hellriegel C, Caiola VR, Corti V, Sidenius N, Zamai M (2011). Number and brightness image analysis reveals ATF-induced dimerization kinetics of uPAR in the cell membrane. *FASEB J* 25, 2883–2897.
- Hendrix J, Flors C, Dedecker P, Hofkens J, Engelborghs Y (2008). Dark states in monomeric red fluorescent proteins studied by fluorescence correlation and single molecule spectroscopy. *Biophys J* 94, 4103–4113.
- Hilsch M, Goldenbogen BR, Sieben C, Höfer CT, Rabe P Jr, Klipp E, Herrmann A, Chiantia S (2014). Influenza A matrix pM1 multimerizes upon binding to lipid membranes. *Biophys J* 107, 912–923.
- Iino R, Koyama I, Kusumi A (2001). Single molecule imaging of green fluorescent proteins in living cells: E-cadherin forms oligomers on the free cell surface. *Biophys J* 80, 2667–2677.
- Kaden D, Voigt P, Munter L-M, Bobowski KD, Schaefer M, Multhaup G (2009). Subcellular localization and dimerization of APLP1 are strikingly different from APP and APLP2. *J Cell Sci* 122, 368–377.
- Kusumi A, Fujiwara TK, Chadda R, Xie M, Tsunoyama TA, Kalay Z, Kasai RS, Suzuki KG (2012). Dynamic organizing principles of the plasma membrane that regulate signal transduction: commemorating the fortieth anniversary of Singer and Nicolson's fluid-mosaic model. *Annu Rev Cell Dev Biol* 28, 215–250.
- Kusumi A, Sako Y (1996). Cell surface organization by the membrane skeleton. *Curr Opin Cell Biol* 8, 566–574.
- Kusumi A, Sako Y, Yamamoto M (1993). Confined lateral diffusion of membrane receptors as studied by single particle tracking (nanovid microscopy). Effects of calcium-induced differentiation in cultured epithelial cells. *Biophys J* 65, 2021–2040.
- Li Q, Südhof TC (2004). Cleavage of amyloid-beta precursor protein and amyloid-beta precursor-like protein by BACE 1. *J Biol Chem* 279, 10542–10550.
- Linkert M, Rueden CT, Allan C, Burel J-M, Moore W, Patterson A, Loranger B, Moore J, Neves C, MacDonald D, et al. (2010). Metadata matters: access to image data in the real world. *J Cell Biol* 189, 777–782.
- Lorent K, Overbergh L, Moechars D, De Strooper B, Van Leuven F, Van den Berghe H (1995). Expression in mouse embryos and in adult mouse brain of three members of the amyloid precursor protein family, of the alpha-2-macroglobulin receptor/low density lipoprotein receptor-related protein and of its ligands apolipoprotein E, lipoprotein lipase, alpha-2-macroglobulin and the 40,000 molecular weight receptor-associated protein. *Neuroscience* 65, 1009–1025.
- Machán R, Wohland T (2014). Recent applications of fluorescence correlation spectroscopy in live systems. *FEBS Lett* 588, 3571–3584.
- Mayer MC, Kaden D, Schauenburg L, Hancock MA, Voigt P, Roeser D, Barucker C, Than ME, Schaefer M, Multhaup G (2014). Novel zinc-binding site in the E2 domain regulates amyloid precursor-like protein 1 (APLP1) oligomerization. *J Biol Chem* 289, 19019–19030.
- Mayer MC, Schauenburg L, Thompson-Steckel G, Dunsing V, Kaden D, Voigt P, Schaefer M, Chiantia S, Kennedy TE, Multhaup G (2016). Amyloid precursor-like protein 1 (APLP1) exhibits stronger zinc-dependent neuronal adhesion than amyloid precursor protein and APLP2. *J Neurochem* 137, 266–276.
- Mui KL, Chen CS, Assoian RK (2016). The mechanical regulation of integrin-cadherin crosstalk organizes cells, signaling and forces. *J Cell Sci* 129, 1093–1100.
- Muller UC, Deller T, Korte M (2017). Not just amyloid: physiological functions of the amyloid precursor protein family. *Nat Rev Neurosci* 18, 281–298.
- Nelson WJ (2008). Regulation of cell-cell adhesion by the cadherin-catenin complex. *Biochem Soc Trans* 36, 149–155.
- Riedl J, Flynn KC, Raducanu A, Gartner F, Beck G, Bosl M, Bradke F, Massberg S, Aszodi A, Sixt M, Wedlich-Soldner R (2010). Lifeact mice for studying F-actin dynamics. *Nat Methods* 7, 168–169.
- Ries J, Chiantia S, Schwille P (2009). Accurate determination of membrane dynamics with line-scan FCS. *Biophys J* 96, 1999–2008.
- Ries J, Schwille P (2006). Studying slow membrane dynamics with continuous wave scanning fluorescence correlation spectroscopy. *Biophys J* 91, 1915–1924.
- Saha S, Lee IH, Polley A, Groves JT, Rao M, Mayor S (2015). Diffusion of GPI-anchored proteins is influenced by the activity of dynamic cortical actin. *Mol Biol Cell* 26, 4033–4045.
- Schilling S, Mehr A, Ludewig S, Stephan J, Zimmermann M, August A, Strecker P, Korte M, Koo EH, Muller UC, et al. (2017). APLP1 is a synaptic cell adhesion molecule, supporting maintenance of dendritic spines and basal synaptic transmission. *J Neurosci* 37, 5345–5365.
- Schneider F, Waithe D, Clausen MP, Galiani S, Koller T, Ozhan G, Eggeling C, Sezgin E (2017). Diffusion of lipids and GPI-anchored proteins in

- actin-free plasma membrane vesicles measured by STED-FCS. *Mol Biol Cell* 28, 1507–1518.
- Schwarzer R, Levental I, Gramatica A, Scolari S, Buschmann V, Veit M, Herrmann A (2014). The cholesterol-binding motif of the HIV-1 glycoprotein gp41 regulates lateral sorting and oligomerization. *Cell Microbiol* 16, 1565–1581.
- Schwille P, Meyer-Almes FJ, Rigler R (1997). Dual-color fluorescence cross-correlation spectroscopy for multicomponent diffusional analysis in solution. *Biophys J* 72, 1878–1886.
- Scolari S, Engel S, Krebs N, Plazzo AP, De Almeida RFM, Prieto M, Veit M, Herrmann A (2009). Lateral distribution of the transmembrane domain of influenza virus hemagglutinin revealed by time-resolved fluorescence imaging. *J Biol Chem* 284, 15708–15716.
- Selkoe DJ (2001). Alzheimer's disease: genes, proteins, and therapy. *Physiol Rev* 81, 741–766.
- Sezgin E, Kaiser H-J, Baumgart T, Schwille P, Simons K, Levental I (2012). Elucidating membrane structure and protein behavior using giant plasma membrane vesicles. *Nat Protoc* 7, 1042–1051.
- Shariati SAM, De Strooper B (2013). Redundancy and divergence in the amyloid precursor protein family. *FEBS Lett* 587, 2036–2045.
- Soba P, Eggert S, Wagner K, Zentgraf H, Siehl K, Kreger S, Löwer A, Langer A, Merdes G, Paro R, et al. (2005). Homo- and heterodimerization of APP family members promotes intercellular adhesion. *EMBO J* 24, 3624–3634.
- Sosa LJ, Caceres A, Dupraz S, Oksdath M, Quiroga S, Lorenzo A (2017). The physiological role of the amyloid precursor protein as an adhesion molecule in the developing nervous system. *J Neurochem* 143, 11–29.
- Stahl R, Schilling S, Soba P, Rupp C, Hartmann T, Wagner K, Merdes G, Eggert S, Kins S (2014). Shedding of APP limits its synaptogenic activity and cell adhesion properties. *Front Cell Neurosci* 8, 410.
- Su AI, Wiltshire T, Batalov S, Lapp H, Ching KA, Block D, Zhang J, Soden R, Hayakawa M, Kreiman G, et al. (2004). A gene atlas of the mouse and human protein-encoding transcriptomes. *Proc Natl Acad Sci USA* 101, 6062–6067.
- Trimble WS, Grinstein S (2015). Barriers to the free diffusion of proteins and lipids in the plasma membrane. *J Cell Biol* 208, 259–271.
- Trullo A, Corti V, Arza E, Caiolfa VR, Zamai M (2013). Application limits and data correction in number of molecules and brightness analysis. *Microsc Res Tech* 76, 1135–1146.
- Tyan S-H, Shih AY-J, Walsh JJ, Maruyama H, Sarsoza F, Ku L, Eggert S, Hof PR, Koo EH, Dickstein DL (2012). Amyloid precursor protein (APP) regulates synaptic structure and function. *Mol Cell Neurosci* 51, 43–52.
- Vassar R, Bennett BD, Babu-Khan S, Kahn S, Mendiaz EA, Denis P, Teplow DB, Ross S, Amarante P, Loeloff R, et al. (1999). Beta-secretase cleavage of Alzheimer's amyloid precursor protein by the transmembrane aspartic protease BACE. *Science* 286, 735–741.
- von Stetten D, Noirdlerc-Savoye M, Goedhart J, Gadella TWJ, Royant A, Royant A (2012). Structure of a fluorescent protein from *Aequorea victoria* bearing the obligate-monomer mutation A206K. *Acta Crystallogr F Struct Biol Commun* 68, 878–882.
- Wang Z, Wang B, Yang L, Guo Q, Aithmitti N, Songyang Z, Zheng H (2009). Presynaptic and postsynaptic interaction of the amyloid precursor protein promotes peripheral and central synaptogenesis. *J Neurosci* 29, 10788–10801.
- Weyer SW, Klevanski M, Delekate A, Voikar V, Aydin D, Hick M, Filippov M, Drost N, Schaller KL, Saar M, et al. (2011). APP and APLP2 are essential at PNS and CNS synapses for transmission, spatial learning and LTP. *EMBO J* 30, 2266–2280.
- Wild K, August A, Pietrzik CU, Kins S (2017). Structure and synaptic function of metal binding to the amyloid precursor protein and its proteolytic fragments. *Front Mol Neurosci* 10, 21.
- Zakrys L, Ward RJ, Pediani JD, Godin AG, Graham GJ, Milligan G (2014). Roundabout 1 exists predominantly as a basal dimeric complex and this is unaffected by binding of the ligand Slit2. *Biochem J* 461, 61–73.

Supplemental Material, Dunsing et al.

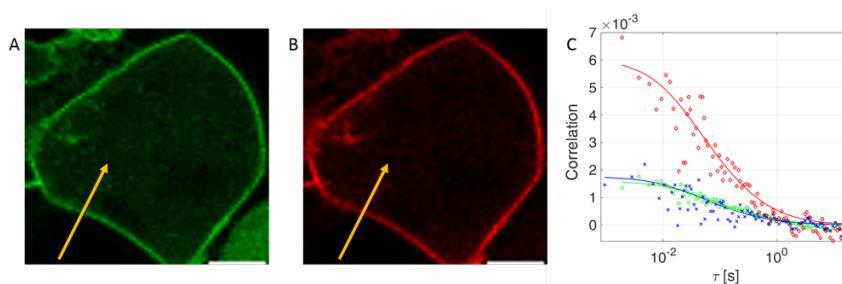


Figure S1: sFCS cross-correlation positive control. A, B: Representative image of a HEK cell expressing a myr-palm-YFP-Card tandem. YFP is detected in the green channel (A) and Card in the red channel (B). The yellow arrow represents a typical two-color sFCS line scan. Scale bar is 5 μm . C: Representative ACFs and CCF from two-color sFCS analysis of the cell represented in panels A and B. Red: ACF for the red channel (Card), green: ACF for the green channel (YFP), blue: CCF calculated between the two spectral channels. Solid lines represent the fit of a two-dimensional diffusion model to the data. 14 cells from three independent measurements were analyzed. All measurements were performed at room temperature.

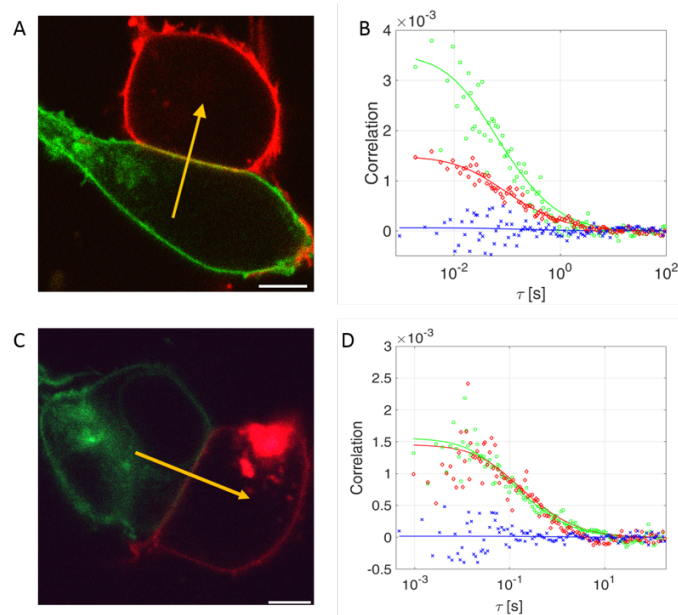


Figure S2: sFCS cross-correlation negative controls for *trans* binding. A: Representative image of HEK cells expressing myr-palm-YFP (green) or myr-palm-Card (red). The yellow arrow represents a typical two-color sFCS line scan. Scale bar is 5 μm . B: Representative ACFs and CCF from two-color sFCS analysis of cells represented in panel A. Red: ACF for the red channel (myr-palm-Card), green: ACF for the green channel (myr-palm-YFP), blue: CCF calculated between the two spectral channels. Solid lines represent the fit of a two-dimensional diffusion model to the data. 17 cells from three independent measurements were analyzed.

As an additional control, we monitored junctions between cells expressing APLP1-Card or CD86-YFP. CD86 is a transmembrane protein that is supposed to have a diffusion coefficient similar to that of APLP1. Also, no *trans* interaction is expected between CD86 and APLP1. C: Representative image of HEK cells expressing CD86-YFP (green) or APLP1-Card (red). The yellow arrow represents a typical two-color sFCS line scan. In this experiment, the fastest available scan speed (945.45 μ s for both lines) was used. Scale bar is 5 μ m. D: Representative ACFs and CCF from two-color sFCS analysis of cells represented in panel C. Red: ACF for the red channel (APLP1-Card), green: ACF for the green channel (CD86-YFP), blue: CCF calculated between the two spectral channels. Solid lines represent the fit of a two-dimensional diffusion model to the data. 12 cells from two independent measurements were analyzed. The average relative cross-correlation was 0.04 ± 0.06 and the diffusion coefficient of CD86-YFP was 0.29 ± 0.15 $\mu\text{m}^2/\text{s}$ (mean \pm s.d.). The diffusion coefficient of CD86-YFP is indeed comparable to that measured for APLP1-YFP (0.25 ± 0.09 $\mu\text{m}^2/\text{s}$, see Main Text). All measurements were performed at room temperature.

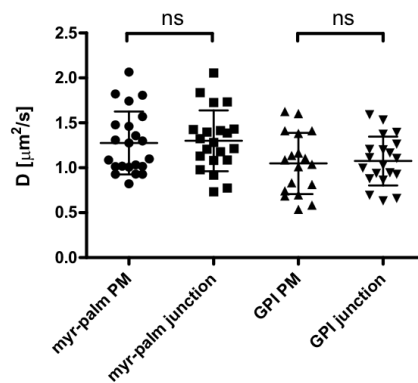


Figure S3: Diffusion coefficients of simple model membrane proteins, within or outside cell-cell junctions. Diffusion coefficients of myr-palm-YFP and GPI-YFP measured with one-color sFCS on 18-22 cells each, in two independent experiments. “ns” indicates that no statistically significant difference could be determined with a Welch’s two-sided t-test. All measurements were performed at room temperature.

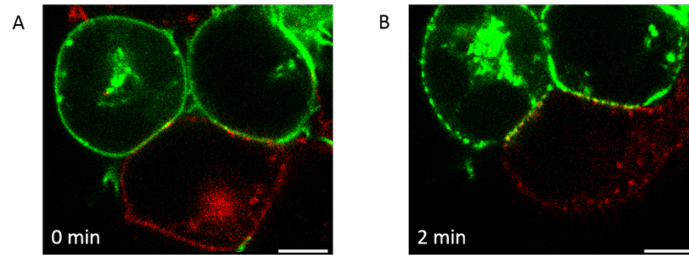


Figure S4: Zinc induces the rapid formation of APLP1 clusters. HEK cells were transfected with APLP1-Card (red) or APLP1-YFP (green). A: Representative image of HEK cells expressing the two fluorescent APLP1 constructs in the absence of zinc. The buffer was then supplemented with 50 μM ZnCl_2 and time-series images were acquired. B: Representative image of the same HEK cells in panel A, 2 min after the addition of zinc. These results indicate that zinc induces the formation of both *cis* and *trans* APLP1 clusters already within ~ 2 min. Scale bar is 5 μm . All measurements were performed at room temperature. The experiment was replicated at least twice using independent samples.

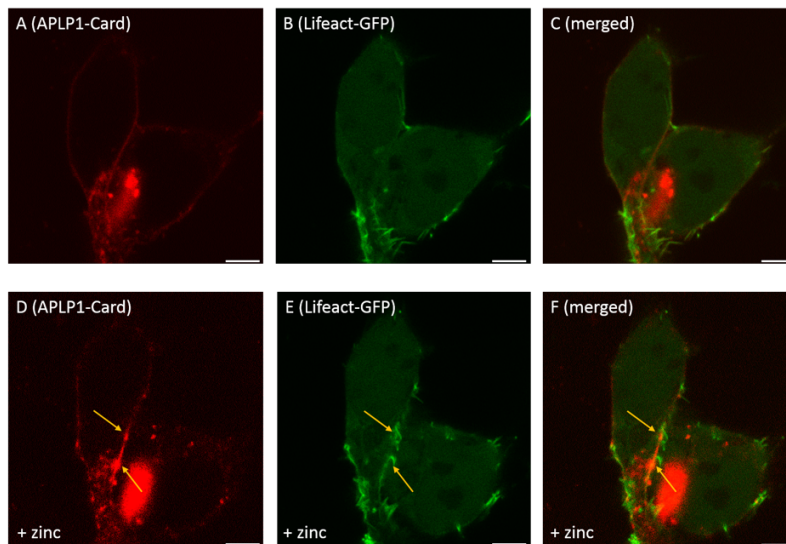


Figure S5: Filamentous actin accumulates in correspondence of zinc-induced APLP1 clusters at cell-cell junctions. A, B: Representative images of HEK cells expressing APLP1-Card (A) and Lifeact-GFP (B) forming a junction in the absence of zinc. APLP1-Card is distributed homogeneously in the PM. The actin-labelling probe is visible throughout the cytoplasm and enriched in certain regions of the PM, but not at the cell-cell junction. C: Merged channels from panels A and B. The buffer was next supplemented with 50 μM ZnCl_2 and, after 20 min, the same cells were imaged (D-F). The yellow arrows indicate APLP1-Card clusters forming at the cell-cell junction. Enrichment of filamentous actin can be observed in close proximity of APLP1 clusters, thus suggesting an involvement of actin in APLP1-APLP1 interaction. Scale bar is 5 μm . All measurements were performed at room temperature. The experiment was replicated at least twice using independent samples.

2.2 [P2] A fluorescence fluctuation spectroscopy assay of protein-protein interactions at cell-cell contacts

Video Article

A Fluorescence Fluctuation Spectroscopy Assay of Protein-Protein Interactions at Cell-Cell Contacts

Valentin Dunsing¹, Salvatore Chiantia¹

¹Institute for Biochemistry and Biology, Cell Membrane Biophysics Group, University of Potsdam

Correspondence to: Salvatore Chiantia at chiantia@uni-potsdam.de

URL: <https://www.jove.com/video/58582>

DOI: [doi:10.3791/58582](https://doi.org/10.3791/58582)

Keywords: Biochemistry, Issue 142, Protein-protein interactions, cell-cell interactions, cell-cell adhesion, fluorescence fluctuation spectroscopy, fluorescence correlation spectroscopy, number and brightness, N&B

Date Published: 12/1/2018

Citation: Dunsing, V., Chiantia, S. A Fluorescence Fluctuation Spectroscopy Assay of Protein-Protein Interactions at Cell-Cell Contacts. *J. Vis. Exp.* (142), e58582, doi:10.3791/58582 (2018).

Abstract

A variety of biological processes involves cell-cell interactions, typically mediated by proteins that interact at the interface between neighboring cells. Of interest, only few assays are capable of specifically probing such interactions directly in living cells. Here, we present an assay to measure the binding of proteins expressed at the surfaces of neighboring cells, at cell-cell contacts. This assay consists of two steps: mixing of cells expressing the proteins of interest fused to different fluorescent proteins, followed by fluorescence fluctuation spectroscopy measurements at cell-cell contacts using a confocal laser scanning microscope. We demonstrate the feasibility of this assay in a biologically relevant context by measuring the interactions of the amyloid precursor-like protein 1 (APLP1) across cell-cell junctions. We provide detailed protocols on the data acquisition using fluorescence-based techniques (scanning fluorescence cross-correlation spectroscopy, cross-correlation number and brightness analysis) and the required instrument calibrations. Further, we discuss critical steps in the data analysis and how to identify and correct external, spurious signal variations, such as those due to photobleaching or cell movement.

In general, the presented assay is applicable to any homo- or heterotypic protein-protein interaction at cell-cell contacts, between cells of the same or different types and can be implemented on a commercial confocal laser scanning microscope. An important requirement is the stability of the system, which needs to be sufficient to probe diffusive dynamics of the proteins of interest over several minutes.

Video Link

The video component of this article can be found at <https://www.jove.com/video/58582/>

Introduction

Many biological processes occur at the sites of cell-cell interactions, e.g., cell-cell adhesion^{1,2,3}, cell-cell fusion⁴ and cellular recognition⁵. Such events are particularly important during the development of multicellular organisms and for cell-cell communication, e.g., during immune responses. These processes are typically mediated by proteins that are localized at the surface, i.e., at the plasma membrane (PM) of neighboring cells and undergo specific interactions at the cell-cell contact that are precisely regulated in space and time. In many cases, these interactions are direct homo- or heterotypic protein-protein *trans* interactions, but may also involve ions or ligands acting as extracellular linkers¹. Although of fundamental importance, there is a lack of assays probing these specific protein-protein interactions directly in the native environment of living cells. Many methods either require cell disruption (e.g., biochemical assays such as co-immunoprecipitation⁶), fixation (e.g., some of the super-resolution optical microscopy techniques and electron microscopy of cell-cell contacts⁷), or are non-specific, e.g., aggregation/adhesion assays^{8,9}. To overcome this issue, fluorescence techniques have been implemented based on fluorescence resonance energy transfer (FRET)¹⁰ or fluorescence complementation¹¹. However, to achieve sufficiently small distances between fluorophores, these methods require fluorescent labels on the extracellular side of the proteins¹⁰, potentially interfering with *trans* interactions.

Here, we present an alternative fluorescence-based assay for protein-protein interactions at cell-cell contacts. This approach combines fluorescence cross-correlation approaches (scanning fluorescence cross-correlation spectroscopy (sFCCS), cross-correlation number and brightness (ccN&B)) and mixing of cells expressing a fusion construct of the protein of interest, e.g., an adhesion receptor. The investigated receptors in the two interacting cells are labeled with two spectrally separated fluorescent proteins (FPs), from the intracellular side (see **Figure 1A**).

The employed methods are based on the statistical analysis of fluorescence fluctuations induced by the diffusive motion of fluorescent fusion proteins through the focal volume of a confocal laser scanning microscope. More in detail, the assay probes the co-diffusion of the proteins of interest in both neighboring PMs at cell-cell contacts. If the proteins undergo *trans* interactions, these *trans* complexes will carry fluorescent proteins emitting in both spectral channels, causing correlated fluorescence fluctuations of both emitters. On the other hand, if no binding occurs, the number fluctuations of proteins in facing PMs will be independent, causing no correlated fluctuations. The acquisition can be performed in two ways: 1) sFCCS is based on a line-shaped scan across the cell-cell contact and effectively probes the interactions in a spot located in the contact region. Through a temporal analysis of fluorescence fluctuations, sFCCS provides also dynamics information, i.e., the diffusion

coefficients of protein complexes; 2) ccN&B is based on a pixel-wise analysis of a sequence of images acquired at the cell-cell contact regions. It has capability to probe and map interactions along the whole contact region (in one focal plane), but does not provide information on dynamics. Both methods can be combined with an analysis of the molecular brightness, *i.e.*, the average fluorescence signal emitted in the time unit by single diffusing protein complexes and, thus, provide estimates of the stoichiometry of protein complexes at cell-cell contacts.

In this article, we provide detailed protocols for sample preparation, instrument calibration, data acquisition and analysis to perform the presented assay on a commercial confocal laser scanning microscope. The experiments can be performed on any instrument equipped with photon counting or analog detectors and an objective with high numerical aperture. We further discuss critical steps of the protocol and provide correction schemes for several processes causing artefactual signal fluctuations, *e.g.*, detector noise, photobleaching or cell movement. Originally developed to probe interactions between adherent cells, the assay may be modified for suspension cells, or adapted to model membrane systems, *e.g.*, giant unilamellar vesicles (GUVs) or giant plasma membrane vesicles (GPMVs), allowing the quantification of interactions in different lipid environments or in the absence of an organized cytoskeleton^{12,13}.

Scanning fluorescence cross-correlation spectroscopy is a modified version of fluorescence cross-correlation spectroscopy¹⁴ and was specifically designed to probe slow diffusive dynamics in lipid membranes¹⁵. It is based on a line scan acquisition perpendicular to the PM containing the fluorescent proteins of interest. To probe interactions of two differently labeled protein species, the acquisition is performed in two spectral channels using two laser lines and two detection windows for spectrally separated fluorophores. Due to the slow diffusion dynamics of proteins in the PM ($D \leq 1 \mu\text{m}^2/\text{s}$), a cross-talk-free measurement can be performed by alternating the excitation scheme from line to line¹⁵. The analysis starts with: 1) an alignment algorithm correcting for lateral cell movement based on block-wise averaging of ~1000 lines, 2) determination of the position with maximum fluorescence signal, *i.e.*, the PM position, in each block and 3) shifting of all blocks to a common origin^{12,15}, separately in each channel. Then, an automatic selection of pixels corresponding to the PM is performed by selecting the central region from a Gaussian fit of the sum of all aligned lines (*i.e.*, center $\pm 2.5\sigma$). Integration of the signal in each line yields the membrane fluorescence time series $F(t)$ in each channel (g = green channel, r = red channel). Note that the pixel size has to be small enough, *e.g.*, <200 nm, to reconstruct the shape of the point spread function and find its center, corresponding to the position of the PM. In the presence of substantial photobleaching, the fluorescence time series in each channel may be modeled with a double-exponential function and then corrected with the following formula:¹⁶

$$F(t)^c = \frac{F(t)}{\sqrt{f(t)/f(0)}} + f(0)(1 - \sqrt{f(t)/f(0)}). \quad (1)$$

It is important to note that this formula effectively corrects both the amplitudes and diffusion times obtained from correlation analysis of $F(t)^c$, compared to parameter estimates that would be obtained from the uncorrected $F(t)$. Then, the auto- and cross-correlation functions (ACFs/CCFs) of the fluorescence signals are calculated:

$$G_{\text{auto}}(\tau) = \frac{\langle \delta F_i(t) \delta F_i(t+\tau) \rangle}{\langle F_i(t) \rangle^2}, \quad (2)$$

$$G_{\text{cross}}(\tau) = \frac{\langle \delta F_g(t) \delta F_r(t+\tau) \rangle}{\langle F_g(t) \rangle \langle F_r(t) \rangle}, \quad (3)$$

where $\delta F_i = F_i(t) - \langle F_i(t) \rangle$ and $i = g, r$.

A two-dimensional diffusion model is then fitted to all correlation functions (CFs):

$$G(\tau) = \frac{1}{N} \left(1 + \frac{\tau}{\tau_d}\right)^{-1/2} \left(1 + \frac{\tau}{\tau_d S^2}\right)^{-1/2}. \quad (4)$$

Here, N denotes the number of fluorescent proteins in the observation volume and τ_d the diffusion time for each channel. This model takes into account that in the described experimental setting, diffusion of proteins in the PM occurs in the x-z plane, in contrast to the commonly used configuration of fluorescence correlation spectroscopy (FCS) experiments on membranes probing diffusion in the x-y plane of the confocal volume¹⁷. The waist w_0 and the structure factor S , describing the elongation w_z of the focal volume in z , $S = w_z/w_0$, are obtained from a point FCS calibration measurement performed with spectrally similar dyes and same optical settings using already available values for the diffusion coefficient D_{dye} :

$$w_0 = \sqrt{4\tau_{d,\text{dye}} D_{\text{dye}}}, \quad (5)$$

where $\tau_{d,\text{dye}}$ is the measured average diffusion time of the dye molecules, obtained from fitting a model for three-dimensional diffusion to the data, taking into account transitions of a fraction T of all N molecules to a triplet state with a time constant τ_T :

$$G(\tau) = \frac{1}{N} \left(1 + \frac{\tau}{1-T} e^{-\frac{\tau}{\tau_T}}\right) \left(1 + \frac{\tau}{\tau_{d,\text{dye}}}\right)^{-1} \left(1 + \frac{\tau}{\tau_{d,\text{dye}} S^2}\right)^{-1/2}. \quad (6)$$

Finally, diffusion coefficients (D), molecular brightness values (ϵ) and the relative cross-correlation of sFCCS data (*rel.cc.*) are calculated as follows:

$$D = \omega_0^2 / 4\tau_d, \quad (7)$$

$$\epsilon = \frac{\langle F(t) \rangle}{N}, \quad (8)$$

$$rel. cc. = \max \left\{ \frac{G_{cross}(0)}{\sigma_{auto}^2(0)}, \frac{G_{cross}(0)}{\sigma_{auto}^2(0)} \right\}, \quad (9)$$

where $G_{cross}(0)$ is the amplitude of the cross-correlation function and $G_{auto}^i(0)$ is the amplitude of the autocorrelation function in the i -th channel.

This definition of the relative cross-correlation, *i.e.* using *max* instead of *mean* in Equation 9, takes into account that the maximum number of complexes of two protein species present at different concentrations is limited by the species present in a lower number.

Cross-correlation number and brightness is based on a moment analysis of the fluorescence intensity for each pixel of an image stack acquired over time at a fixed position in the sample, typically consisting of ~100-200 frames, with two spectral channels (g = green channel, r = red channel). From the temporal mean $\langle I \rangle_i$ and variance σ_i^2 , the molecular brightness ϵ_i and number n_i are calculated in each pixel and spectral channel ($i = g, r$)¹⁸:

$$\epsilon_i = \frac{\sigma_i^2}{\langle I \rangle_i} - 1, \quad (10)$$

$$n_i = \frac{\langle I \rangle_i^2}{\sigma_i^2 - \langle I \rangle_i}, \quad (11)$$

It is important to note that the given equations apply to the ideal case of a true photon-counting detector. For analog detection systems, the following equations apply^{19,20}:

$$\epsilon_i = \frac{\sigma_i^2 - \sigma_0^2}{S(\langle I \rangle_i - offset)} - 1, \quad (12)$$

$$n_i = \frac{(\langle I \rangle_i - offset)^2}{\sigma_i^2 - \sigma_0^2 - S(\langle I \rangle_i - offset)}. \quad (13)$$

Here, S is the conversion factor between detected photons and the recorded digital counts, σ_0^2 is the readout noise and *offset* refers to the detector intensity offset. Generally, these quantities should be calibrated, for any detector type, based on measuring the detector variance as a function of intensity for steady illumination¹⁹, *e.g.*, a reflective metal surface or dried dye solution. The *offset* can be determined by measuring the count rate for a sample without excitation light. By performing a linear regression of the detector-associated variance σ_a^2 versus intensity (I) plot, S and σ_0^2 can be determined¹⁹:

$$\sigma_a^2 = S(I) - S \cdot offset + \sigma_0^2. \quad (14)$$

Finally, the cross-correlation brightness is calculated in each pixel and is defined in general as²¹

$$B_{cc} = \frac{\sigma_{cc}^2}{\sqrt{\langle I_g \rangle \langle I_r \rangle}}, \quad (15)$$

where σ_{cc}^2 is the cross-variance $\sigma_{cc}^2 = \langle (I_g - \langle I_g \rangle)(I_r - \langle I_r \rangle) \rangle$.

In order to filter long-lived fluctuations, all ccN&B calculations are performed following a boxcar filtering, independently for each pixel²². Briefly, n_i , ϵ_i ($i = g, r$) and B_{cc} are calculated in sliding segments of *e.g.*, 8-15 frames. The values thus obtained can be then averaged to obtain the final pixel number and brightness values.

Stoichiometry analysis

In order to estimate the stoichiometry of protein complexes at cell-cell contacts, the molecular brightness can be separately analyzed in each spectral channel for the sFCCS or ccN&B data. In sFCCS, one brightness value is obtained per measurement in each channel. In ccN&B, a brightness histogram of all pixels corresponding to the cell-cell contact is obtained and the average (or median) value can be used as representative brightness for the measurement. By performing the same analysis on a monomeric reference, all brightness values can be normalized to directly obtain the average oligomeric state of the detected protein complexes. At this point, it is important to correct for the presence of non-fluorescent FPs that may result in an underestimation of the oligomeric state. This is typically performed by measuring the brightness of a homo-dimeric reference protein^{23,24} using one-color sFCS or number and brightness (N&B).

Protocol

1. Sample Preparation: Cell-Cell Mixing Assay

NOTE: The following protocol describes the mixing procedure for adherent cells. It may be modified for cells cultured in suspension.

1. Seed an appropriate number of cells on a 6-well plate, *e.g.*, 800,000 HEK 293T cells (counted with a Neubauer counting chamber), a day before transfection. The number can be modified depending on the time between seeding and transfection and adjusted for other cell types. To perform a basic experiment (*i.e.*, proteins of interest and negative control), prepare at least 4 wells. Culture cells at 37 °C, 5% CO₂ in Dulbecco's Modified Eagle Medium (DMEM) medium, supplemented with fetal bovine serum (10%) and L-glutamine (1%).
2. Transfect cells according to the manufacturer's instructions (see the **Table of Materials**).

1. To perform a basic experiment, transfect, in separate wells, plasmids for the protein of interest fused to a 'green' (e.g., monomeric enhanced green fluorescent protein (mEGFP), or yellow fluorescent protein (mEYFP)) or 'red' (e.g., mCherry, or mCardinal) fluorescent protein.
 NOTE: In this protocol, we focus on APLP1-mEYFP and APLP1-mCardinal¹², and the corresponding negative control, e.g., myristoylated-palmitoylated-mEYFP (myr-palm-mEYFP) and -mCardinal (myr-palm-mCardinal)¹². Generally, 200 ng - 1 µg of plasmid DNA are sufficient. High transfection efficiency increases the chance to find 'red' and 'green' cells in contact. Modify the amount of plasmid and transfection reagent to optimize transfection efficiency. **Critical:** Cell confluency should be around 70% when transfecting the cells. If cells are over-confluent, the transfection efficiency will decrease. If cells are not confluent enough, transfection and mixing may induce stress and prevent many cells from proper attachment after mixing.

3. Perform cell mixing ~4 ± 2 h after transfection.
 1. Remove growth medium and wash each well gently with 1 mL PBS supplemented with Mg²⁺ and Ca²⁺. Then, remove the PBS. **(Critical)** Drop PBS on well edge to prevent detachment of cells during washing.
 2. Add ~50 µL trypsin ethylenediaminetetraacetic acid (EDTA) solution drop-wise to each well to facilitate detachment of cells. Incubate at 37 °C for 2 min. Afterwards, slowly shake the 6-well plate laterally to detach the cells.
 NOTE: Extended incubation times may be required for some cell types.
 3. Add 950 µL of growth medium to each well and resuspend cells by pipetting a few times up and down, thereby detaching all cells from the well bottom. **(Critical)** Ensure that cells are resuspended properly and detached from each other by visually checking for the absence of large cell aggregates after resuspension. Otherwise many 'red'-'red' or 'green'-'green' contacts will be obtained after mixing.
 4. Transfer the cell solution of one well (protein of interest or negative control) to the corresponding well, i.e., 'red' (e.g., APLP1-mCardinal transfected) to 'green' (e.g., APLP1-mEYFP transfected) cells. Mix by gently pipetting a few times up and down. Then, seed the mixed cells on 35-mm glass bottom dishes (1 mL of mixed cell solution per dish, plus 1 mL of growth medium) and culture seeded cells for another day at 37 °C, 5% CO₂.

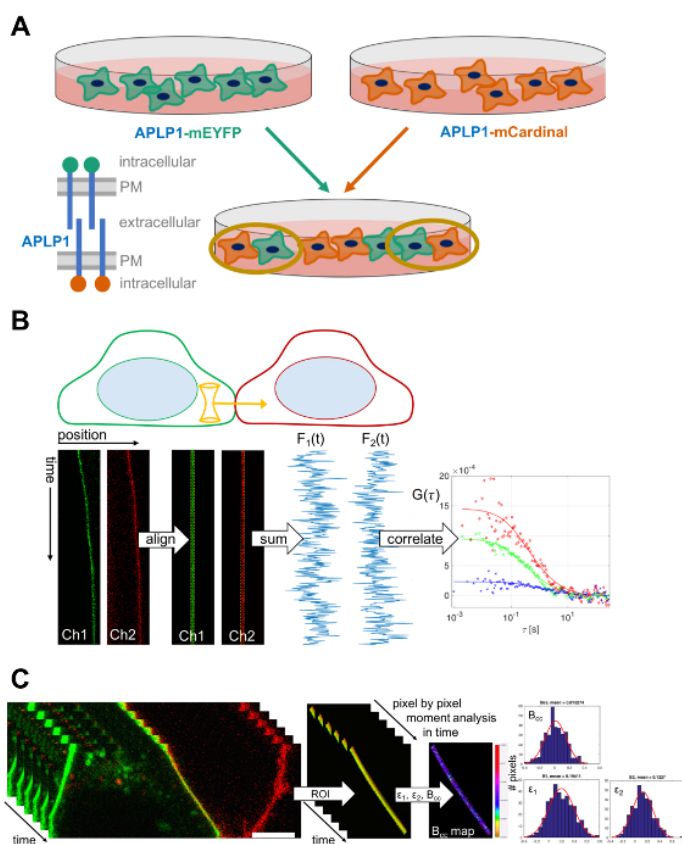


Figure 1. Experimental workflow and schematic representation of scanning fluorescence cross-correlation spectroscopy and cross-correlation number and brightness analysis at cell-cell contacts. (A) Scheme of sample preparation: Two cell populations transfected with the protein of interest (e.g., APLP1) fused to two spectrally distinct fluorescent proteins (e.g., mEYFP and mCardinal) are mixed after transfection. Contacts of differently transfected cells are selected in the microscopy experiments. To avoid interference with extracellular binding domains, the fluorescent protein should be fused to the intracellular terminus of the protein of interest. (B) Scanning FCCS (sFCCS) measurements are performed perpendicular to the cell-cell contact in two spectral channels (channel 1, green and channel 2, red). Scan lines (represented as kymographs) are aligned and membrane pixels summed. Then, ACFs and CCFs are calculated from the intensity traces $F_i(t)$. ACFs are represented in red and green. CCF is represented in blue. (C) Cross-correlation N&B (ccN&B) acquisition results in a three-dimensional (x-y-time) image stack. A ROI is selected around the cell-cell contact. Then channel and cross-correlation brightness (ϵ_1 , ϵ_2 , and B_{cc}) values are calculated in each cell-cell contact pixel. The results are then visualized as histograms, pooling all selected pixels. [Please click here to view a larger version of this figure.](#)

2. Sample Preparation: Positive Control for Cross-Correlation Experiments and Homo-Dimer Construct for Brightness Analysis

1. Seed 600,000 HEK 293T cells, counted with a cell counting chamber, on 35-mm glass bottom dishes one day before transfection. Culture the cells at 37 °C, 5% CO₂ in complete DMEM medium (see step 1.1) for another day.
2. Transfect cells with ~250 ng of plasmid DNA according to manufacturer instructions. For the positive cross-correlation control, use a plasmid encoding a membrane-anchored fluorescent protein hetero-dimer, e.g., myr-palm-mCherry-mEGFP or myr-palm-mCardinal-mEYFP¹² corresponding to the FPs of the protein of interest. For brightness calibration, use plasmids encoding both a membrane-anchored FP monomer and homo-dimer corresponding to the FPs fused to the protein of interest, e.g., myr-palm-mEYFP and myr-palm-mEYFP-mEYFP to calibrate the brightness analysis of APLP1-mEYFP¹².
3. Culture cells at 37 °C, 5% CO₂ in complete DMEM medium (see step 1.1) for another day.

3. Confocal Laser Scanning Microscopy: Setup and Focal Volume Calibration

NOTE: The following protocol is written for experiments performed with mEGFP/mEYFP and mCherry/mCardinal on the laser scanning confocal microscope used in this study. The optical setup, the software settings (laser lines, dichroic mirrors, filters) and choice of calibration dyes may be modified for other FPs and microscope setups.

1. Turn on the microscope and lasers at least an hour before the experiment to ensure laser stability and equilibration of temperature.
2. Prepare 100-200 μ L of appropriate water-soluble fluorescent dye solutions (see the **Table of Materials** for examples) in water or PBS to calibrate the focal volume, with concentrations in the 10-50 nM range.

3. Place the dye solutions on a clean 35-mm glass bottom dish #1.5, *i.e.*, having a thickness of 0.16-0.19 mm.
NOTE: Ideally, use dishes with high performance cover glass having a low thickness tolerance, *e.g.*, 0.170 ± 0.005 mm, allowing an optimal collar ring correction (step 3.6). It is important to use the same type of dish as used later for the following experiments.
4. Place the dish containing the dye solution directly on the objective (preferably, water immersion, with NA 1.2) to ensure focusing into the solution. Alternatively, place the dish on the sample holder and focus into the sample (*e.g.*, 10-20 μ m above the bottom of the dish).
NOTE: We do not recommend using oil objectives due to the poor signal obtained when focusing deep into aqueous samples.
5. Set up the excitation and emission path, *e.g.*, choose the 488 nm laser, a 488/561 nm dichroic mirror, detection window 499-552 nm and a pinhole size of 1 Airy unit (AU). Make sure that the pinhole size is the same as the one that will be used in cross-correlation measurements.
6. Adjust pinhole position (**pinhole adjustment**) and the objective collar ring to maximize count rate. To this aim, turn collar ring until maximum count rate is detected.
NOTE: The collar ring correction accounts for the specific thickness of the cover glass used. Maximizing the count rate, *i.e.*, collecting as many photons per molecule as possible, is crucial to maximize the signal-to-noise ratio (SNR) of the measurements.
7. Perform a series of point FCS measurements (*e.g.*, 6 measurements at different locations, each consisting of 15 repetitions of 10 s, *i.e.*, 2.5 min total time, sampled with 1 μ s dwell time or less) at the same laser power as used in cross-correlation measurements (typically ~1%, *i.e.*, ~1-2 μ W).
8. Fit a three-dimensional diffusion model including a triplet contribution (Equation 6) to the data.
NOTE: Typically, the obtained diffusion times are around 30 μ s and the structure factor is around 4-8.
9. Calculate the waist w_0 from the measured average diffusion time and published values for the diffusion coefficient of the used dye at room temperature²⁵ according to Equation 5. Typical values are 200-250 nm.
10. Repeat the calibration routine (steps 3.4-3.9) with a different fluorescent dye for a second detection channel if needed (*e.g.*, 561 nm excitation and detection between 570 nm and 695 nm). Keep the pinhole position and size as it was set for the first detection channel.
11. Calculate the molecular brightness (Equation 8) from the calibration measurements, and store the obtained values.
NOTE: Typical values for the used setup are ~8-10 kHz/molecule (MOL) for 1.8 μ W 488 nm excitation power. Lower than usual values might indicate dirt on the objective, misalignment of the setup or a reduced laser output. Check and store laser output powers at the objective regularly using a power meter. For comparison of different setups, molecular brightness normalized by the excitation laser power is the most meaningful parameter to assess microscope performance.

4. Scanning Fluorescence Cross-Correlation Spectroscopy: Acquisition

NOTE: The following protocol is written for experiments performed with mEGFP/mEYFP ('green') and mCherry/mCardinal ('red') on the laser scanning confocal microscope used in this study. The optical setup and the software settings (laser lines, dichroic mirrors, filters) may be different for other FPs or microscope setups.

1. Set up the optical path, *e.g.*, 488 nm and 561 nm excitation and a 488/561 nm dichroic mirror, pinhole on 1 AU for 488 nm excitation. To avoid spectral cross-talk, select two separate tracks to excite and detect mEGFP/mEYFP (488 nm excitation, green channel) and mCherry/mCardinal (561 nm excitation, red channel) sequentially and select **switch tracks every line**. For the detection, use appropriate filters for both channels, *e.g.*, 499-552 nm in the green channel and 570-695 nm in the red channel.
2. If alternated excitation is not possible, use appropriate filter settings for the red channel to minimize spectral cross-talk (*i.e.* detect mCherry/mCardinal fluorescence not below 600 nm). This may reduce the amount of photons detected in the red channel and thus reduce the SNR.
3. Place the dish containing the mixed cells on the sample holder. Wait at least 10 min to ensure temperature equilibration and to reduce focus drift.
4. Focus on the cells using transmission light in the **Locate** menu.
5. Search for a pair of a 'red' and a 'green' cell in contact with each other. For the positive cross-correlation or homo-dimer brightness control (see section 2), search for an isolated cell emitting fluorescence in both channels or the respective homo-dimer signal at the PM.
NOTE: (**Critical**) Minimize sample exposure while searching for cells to avoid pre-bleaching, which may reduce the cross-correlation²⁶. Therefore, scan at the fastest scan speed and low laser powers. To avoid detector saturation while imaging strongly expressing cells, search in **integration mode**. However, to minimize exposure, scanning at lower laser powers is possible in **photon counting mode**.
6. Select a scan path perpendicular to cell-cell contact (or to PM of a single cell for the positive cross-correlation or homo-dimer brightness control) using the **Crop** button as depicted in **Figures 1B** and **2A**.
NOTE: Some older microscopes do not allow arbitrary scan directions. In this case, cell-cell contacts with an orientation perpendicular to the scan direction have to be located.
7. **Zoom** to achieve a pixel size of 50-200 nm and select **Line in Scan Mode**. Set **Frame Size** to 128 \times 1 pixels.
NOTE: Typical pixel size is 160 nm, corresponding to a scan length of around 20 μ m.
8. Set **Scan speed** to the maximum allowed value, *e.g.*, 472.73 μ s per line.
NOTE: For an alternate excitation scheme, this corresponds to 954.45 μ s scan time, *i.e.* ~1000 scans/s on the setup used. The scan speed may be adjusted depending on the diffusion coefficient of the protein of interest. For membrane-anchored proteins, typical diffusion times are around 10-20 ms. The scan time should be at least ten times smaller than the diffusion times. Lower scan speeds may induce stronger photobleaching and require lower illumination powers. Alternatively, one can impose a pause, *e.g.*, 5 ms, in between each scan for very slowly diffusing complexes using **Interval** in the **Time Series** submenu.
9. Choose the appropriate laser powers, *e.g.*, ~1-2 μ W for 488 nm and ~5-10 μ W for 561 nm excitation.
NOTE: Higher laser powers improve SNR, but increase photobleaching. Therefore, laser powers should be chosen such that photobleaching is less than 50% of the initial count rate.
10. Set **Cycles** to 100,000-500,000.
NOTE: The number of scans, *i.e.*, duration of the measurement, may vary: Longer measurement times will improve SNR and may be more appropriate for slowly diffusing molecules, however, motion of the cells and photobleaching limit the maximal measurement time. Data presented here were routinely acquired for ~3-6 min, *i.e.*, 200,000-400,000 line scans.
11. Set detectors to **Photon counting** mode. Press **Start Experiment** to start the acquisition. Repeat steps 4.5-4.11 to measure another cell.
NOTE: It is recommended to measure 10-15 cells per sample at different expression levels. (**Critical**) Avoid detector saturation at high expression levels. The maximum count rate should not exceed ~1 MHz.

- If brightness analysis is carried out to determine oligomeric states, perform homo-dimer brightness calibration measurements according to modified steps 4.1-4.11: Measure each fluorescent protein homo-dimer separately (in isolated cells, prepared using protocol section 2) and perform measurements only in one spectral channel.

5. Scanning Fluorescence Cross-Correlation Spectroscopy: Data Analysis

NOTE: The following protocol follows an implementation of the analysis procedure described in detail in previous articles^{12,15}. The software code is available upon request to the authors.

- Export the raw data (e.g., CZI) files to an RGB TIFF image in raw data format. This file will contain a kymograph with the green and red channel data, in the channel termed G and R of the image, respectively.
- Import the TIFF file with the appropriate analysis software and proceed to perform the analysis.
NOTE: The following steps (steps 5.3-5.7) are applied separately to each channel:
- Align the lines by performing a segment-wise or moving time average with blocks of 500-1000 lines. Determine the membrane position, *i.e.*, the pixel position with the maximum count rate, in each block. Shift all blocks to the same lateral position. This procedure corrects for lateral displacement of the cell-cell contact, *e.g.*, due to cell movement.
- Sum up all aligned lines along the time axis and fit the average intensity profile using a Gaussian function. In the presence of significant intracellular background, use a Gaussian plus a sigmoid function. Define the pixels corresponding to the membrane as all pixels within $\pm 2.5\sigma$ of the membrane position and sum up the intensity of these pixels in each line, obtaining a single fluorescence signal value for each time point (*i.e.*, for each line scan).
- If needed (e.g., background >10% of the membrane signal), apply a background correction by subtracting the average pixel intensity in the cytoplasm multiplied by 2.5 σ (in pixel units) from the membrane fluorescence, in blocks of 1000 lines. Avoid bright intracellular vesicles when selecting background pixels.
- If photobleaching is observed, apply a bleaching correction. Therefore, fit the membrane fluorescence time series with a double-exponential function and apply the appropriate correction formula, Equation 1¹⁶.
NOTE: Alternatively, Fourier spectrum based correction schemes may be applied²⁷. (**Critical**) If photobleaching is present but not corrected for, the CFs may be severely distorted and parameter estimates may be strongly biased (e.g., see **Figure 5E**).
- Calculate the ACFs and CCFs according to Equations 2 and 3 using, *e.g.*, a multiple-tau algorithm²⁸. To improve the reliability of the analysis and avoid artefacts, perform the calculations for 10-20 equal segments of the total measurement. Inspect the fluorescence time series and CFs in each segment and remove clearly distorted segments (see examples in **Figure 4A- 4D**). Average all non-distorted segments.
NOTE: This procedure can be automated to avoid a subjective bias to the data²⁹. For very unstable measurements having many short segments may be helpful. However, the length of a segment should still be at least three orders of magnitude above the diffusion time to avoid statistical undersampling errors^{29,30,17}.
- Fit a two-dimensional diffusion model, Equation 4, to the obtained CFs. Therefore, fix the structure factor to the value obtained in calibration measurement (Protocol section 3). The accuracy of the fit can be improved by performing a weighted fit using the statistical weights of each data point obtained from the multiple tau algorithm.
- Calculate the diffusion coefficient using the calibrated waist according to Equation 7.
- Calculate the molecular brightness by dividing the average fluorescence intensity in each channel by the corresponding number of particles, Equation 8. Normalize the determined brightness value in each channel by the average brightness of the corresponding monomeric reference to obtain the oligomeric state, taking into account non-fluorescent FPs²³. To this aim, determine average homo-dimer brightness values from one-color analysis to calculate the fraction of non-fluorescent FPs²³.
- Calculate the relative cross-correlation according to Equation 9.

6. Cross-Correlation Number and Brightness: Detector Calibration

NOTE: The following protocol provides a general guideline regarding how to calibrate the detection system. This procedure is mandatory for analog detection systems, but is not strictly needed when true photon counting detectors are used.

- Dry appropriate water-soluble dye solutions (see **Table of Materials** for examples) on a 35-mm glass bottom dish. Set the optical path accordingly, *i.e.*, 488 or 561 nm excitation and detection at 499-552 nm or 570-695 nm, respectively.
NOTE: Alternatively, a reflective metal surface can be used instead of dried dye solutions by placing the metal piece directly on top of the objective.
- Perform one-color N&B measurements in regions with different dye concentrations or at different laser powers. Therefore, use **Zoom** to achieve a pixel size of 300 nm, **Scan speed** to set appropriate pixel dwell time, *e.g.*, 25 μ s and set **Cycles** to 100-200 frames.
- Set detectors to **photon counting** (or **analog mode** if measurements are performed with analog detection) and press **Start Experiment** to start the acquisition. Perform measurement at zero excitation power to determine the intensity offset.
- Plot pixel variance as a function of pixel intensity for all measured pixels and perform a linear fit of these data. Determine S as the slope of the linear fit. Calculate the readout noise from the y-intercept, using S and the determined intensity offset according to Equation 14.

7. Cross-Correlation Number and Brightness: Acquisition

- Follow steps 4.1-4.4 of the sFCCS acquisition protocol.
- Use **Crop** to select a frame of 512 \times 128 pixels around a cell-cell contact (or isolated PM for homo-dimer brightness control) and **Zoom** to achieve a pixel size of 50-100 nm.
- Use **Scan speed** to set appropriate pixel dwell time, *e.g.*, 6.3 μ s.
NOTE: In N&B, the pixel dwell time should be much smaller than the diffusion time of the protein of interest. If an alternate excitation scheme is chosen, *e.g.*, switching tracks every line, the time between the two tracks should be smaller than the diffusion time of the protein of interest. Otherwise the detectable cross-correlation is reduced.

4. Set **Cycles** to 100-200 frames.
NOTE: A higher frame number will improve the SNR, however, cell movement may limit the total measurement time. The scan time per frame should be much higher than the diffusion time of the protein of interest. Otherwise the apparent brightness is reduced, *i.e.*, particles appear to be immobile. For very slowly diffusing complexes, impose a pause, *e.g.*, 2 s, in between frames using *Interval* in the *Time Series* submenu.
5. Set laser powers to appropriate values (typical values are ~1-2 μW for 488 nm and ~5-10 μW for 561 nm excitation).
NOTE: Higher laser power leads to higher brightness and improved SNR, but also enhanced photobleaching. Laser powers should be high enough to achieve a detected brightness of at least ~1 kHz/MOL but kept low enough to avoid more than 10-20% photobleaching. For mEGFP/mEYFP or mCherry/mCardinal, less than 10% photobleaching are usually obtained.
6. Set detectors to **photon counting** (or **analog mode** if measurements are performed with analog detection). Press **Start Experiment** to start the acquisition.
7. Evaluate the photon count rate. If count rates in cell-cell contact pixels exceed 1 MHz, reduce the laser power or select cells with lower expression levels. Repeat the steps 7.2-7.7. to measure the next pair of cells. It is recommended to measure 10-15 cells per experiment at different expression levels.
8. If brightness analysis is performed to quantify oligomerization, perform homo-dimer brightness calibration measurements according to modified steps 7.1-7.7: Measure each fluorescent protein homo-dimer separately (in isolated cells, prepared using protocol section 2) and perform measurements only in one spectral channel.

8. Cross-correlation Number and Brightness: Data Analysis

NOTE: The following protocol follows a previously described analysis procedure^{12,31}. The software code is available from the authors upon request.

1. Import the raw data (*e.g.*, CZI files can be imported using the Bioformats³² package). Average all frames and select a region of interest (ROI) around the cell-cell contact.
2. Perform an image alignment algorithm³³, *e.g.*, by maximizing the spatial correlation between ROIs in subsequent frames for arbitrary lateral translations, averaged over both channels. This procedure will correct for lateral movement of the cells.
3. Apply a boxcar filter²² to reduce extraneous long-lived fluctuations, originating from, *e.g.*, residual cell movement or background bleaching. Alternatively, a detrending method may be applied to correct for photobleaching³⁴.
NOTE: If no segment-wise analysis or detrending is applied, the apparent brightness may be largely overestimated.
 1. Define sliding segments of, *e.g.*, 8 to 15 frames (*e.g.*, frames 1 to 8, 2 to 9 and so forth) and calculate the channel and cross-correlation brightness values according to Equations 10, 11 and 15 pixel-wise in each segment. If detectors are not true photon counting detectors, take the calibrated detector parameters into account when calculating the brightness, *i.e.*, use Equations 12 and 13 instead.
NOTE: Calculating the brightness values in segments of 8 to 15 frames leads to a 10-20% underestimation of the absolute brightness and a 10-20% overestimation of particle numbers. Nevertheless, brightness ratios (*e.g.*, dimer to monomer brightness) are not affected, as long as the segment length is kept constant throughout the analysis (data not shown). The statistical error for a given segment length can be determined via simulations and thus corrected for.
 2. Average the obtained brightness values pixel-wise over all segments. In this step, one may remove the highest and lowest 5% of segment brightness values from the average or exclude segments which show a clear distortion in the intensity, due to, *e.g.*, an intracellular vesicle or aggregate transiently present in these pixels.
4. Plot the pixel brightness values as a function of the pixel intensity and select the population of pixels that corresponds to the cell-cell contact. Background pixels will have very low intensity values. At this point, re-evaluate the maximum count rate. Exclude pixels with count rates above 1 MHz to prevent pile-up effects.
5. Create channel and cross-correlation brightness histograms of selected cell-cell contact pixels and obtain the ROI-averaged brightness values. Normalize the average channel brightness value by the average brightness of the corresponding monomeric reference to obtain the oligomeric state, taking into account non-fluorescent FPs²³. Therefore, determine average homo-dimer brightness values from one-color analysis to calculate the fraction of non-fluorescent FPs²³.
6. For illustration, plot channel and cross-correlation brightness maps.

Representative Results

A first test for the protein-protein interaction assay, *i.e.*, mixing of cells expressing spectrally distinct fluorescent proteins followed by sFCCS/ccN&B measurements (**Figure 1**), should be performed on proteins that are not expected to interact at the cell-cell contact (*i.e.*, a negative control). Therefore, HEK 293T cells expressing myristoylated-palmitoylated-mEYFP (myr-palm-mEYFP) or -mCardinal were mixed and sFCCS was performed across the cell-cell contact (**Figure 2A**). In an ideal case, the fluorescence signal in each channel is supposed to fluctuate around a stable mean, as a consequence of the diffusive motion of the proteins in the PM and the statistical variations of the number of proteins in the focal volume. For proteins that do not interact, the fluctuations in both channels are independent from each other and, thus, the spectral cross-correlation is expected to fluctuate around zero. Indeed, a relative cross-correlation close to zero was observed in typical measurements (**Figure 2C**). The ACFs show characteristic decay times of ~10-20 ms (corresponding to, on average, $D_{\text{myr-palm}} = 1.3 \pm 0.3 \mu\text{m}^2/\text{s}$ (mean \pm SD, $n = 20$ cells)), as expected for the diffusion of myr-palm-mEYFP and -mCardinal in the PM, *e.g.*, $D_{\text{myr-palm}} = 0.88 \pm 0.11 \mu\text{m}^2/\text{s}$ (mean \pm SEM) based on fluorescence recovery after photobleaching (FRAP) experiments³⁵. Notably, these rather slow dynamics allow the use of an alternating excitation scheme, *i.e.*, switching between only green and only red excitation and detection every line, causing a ~0.5 ms delay between signals in both channels but suppressing spectral cross-talk. On average, a very low average cross-correlation of 0.08 ± 0.10 (mean \pm SD, $n = 17$ cells) was obtained for the negative control (**Figure 3E**), as expected.

Next, a positive cross-correlation control was used to calibrate the maximum possible cross-correlation in the optical setup. Therefore, the membrane-anchored hetero-dimer myr-palm-mCardinal-mEYFP was expressed in HEK 293T cells and sFCCS measurements were performed on single cells (**Figure 2B**). The obtained CCFs had positive amplitudes and showed similar decay times as the ACFs, again ~10-20 ms (**Figure 2D**). On average, a relative cross-correlation of 0.96 ± 0.18 (mean \pm SD, $n = 14$ cells) was measured for the positive control (**Figure 3E**).

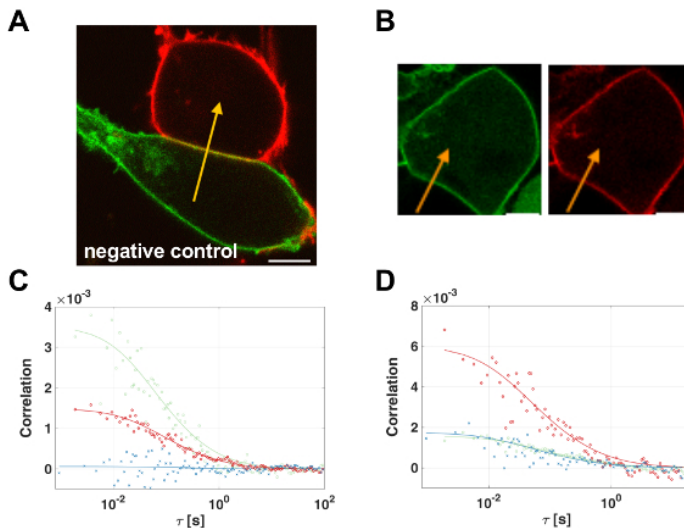


Figure 2. Scanning fluorescence cross-correlation spectroscopy control measurements. (A) Representative images of mixed HEK 293T cells expressing myr-palm-mEYFP/mCardinal as negative control for *trans* interactions. The yellow arrow indicates the sFCCS scan path. Scale bars are 5 μ m. (B) Representative images of HEK 293T cells expressing myr-palm-mCardinal-mEYFP hetero-dimer (left: green channel, right: red channel) as positive cross-correlation control. The yellow arrow indicates the sFCCS scan path. Scale bars are 5 μ m. (C) Representative CFs (green: ACF in green channel (mEYFP), red: ACF in red channel (mCardinal), blue: CCF) obtained in sFCCS measurements for negative control. Solid lines show fits of a two-dimensional diffusion model to the CFs. (D) Representative CFs (green: ACF in green channel (mEYFP), red: ACF in red channel (mCardinal), blue: CCF) obtained in sFCCS measurement of the positive control. Solid lines show fits of a two-dimensional diffusion model to the CFs. [Please click here to view a larger version of this figure.](#)

The suitability of this assay was then investigated in a biologically relevant context by probing the *trans* interactions of the amyloid precursor-like protein 1 (APLP1), a type I transmembrane protein that has been proposed to act as a neuronal adhesion receptor. To this aim, APLP1 fused to mEYFP or mCardinal was expressed in HEK 293T cells. To exclude interference with extracellular binding domains, the FPs were fused to the C-terminus of APLP1, *i.e.*, at the intracellular domain (see **Figure 1A**). Then, sFCCS measurements were performed on cell-cell contacts between APLP1-mEYFP and APLP1-mCardinal expressing cells (**Figure 3A**), resulting in ACFs and CCFs (**Figure 3C**) that provide information about APLP1 diffusion and interactions. A positive relative cross-correlation of 0.45 ± 0.21 (mean \pm SD, $n = 17$ cells) was observed, *i.e.*, a value significantly larger than that of the negative control (**Figure 3E**). Interestingly, the average relative cross-correlation was lower than that of the positive control (**Figure 3E**), indicating only partial *trans* binding.

Finally, the assay was used to show that zinc ions facilitate enhanced APLP1 *trans* binding^{12,31}. The sFCCS CFs obtained from measurements across APLP1 clusters at cell-cell contacts (characterized by a strong co-localization of APLP1-mEYFP and APLP1-mCardinal and forming rapidly in the presence of zinc ions, **Figure 3B**) showed strongly reduced dynamics, as evident from large decay times and the oscillations at large lag times (**Figure 3D**). Nevertheless, analysis of the amplitudes at short lag times revealed a significant increase of the relative cross-correlation to 0.8 ± 0.3 (mean \pm SD, $n = 17$ cells), *i.e.*, ~80% of the calibrated maximum (**Figure 3E**). It is to be expected that such slow dynamics induce severe distortions of the correlation curves (see **Figure 3D**) due the limited number of diffusive events that can be detected during the finite measurement time, inducing so-called particle noise³⁰. For an accurate quantification, the maximum lag time should be at least 3 orders of magnitude above the diffusion time (see previous reviews^{30,17} for further details).

The molecular brightness from the sFCCS APLP1 data was further analyzed, using the myr-palm negative control as a monomeric reference in each channel and correcting for the amount of non-fluorescent proteins²³. Upon zinc ion addition, the molecular brightness significantly increased from small oligomers (~dimers) to larger multimers consisting of ~10-50 monomers on each cell (**Figure 3F**). Thus, on average, up to ~100 APLP1 monomers are present in a whole protein cluster across the cell-cell junction.

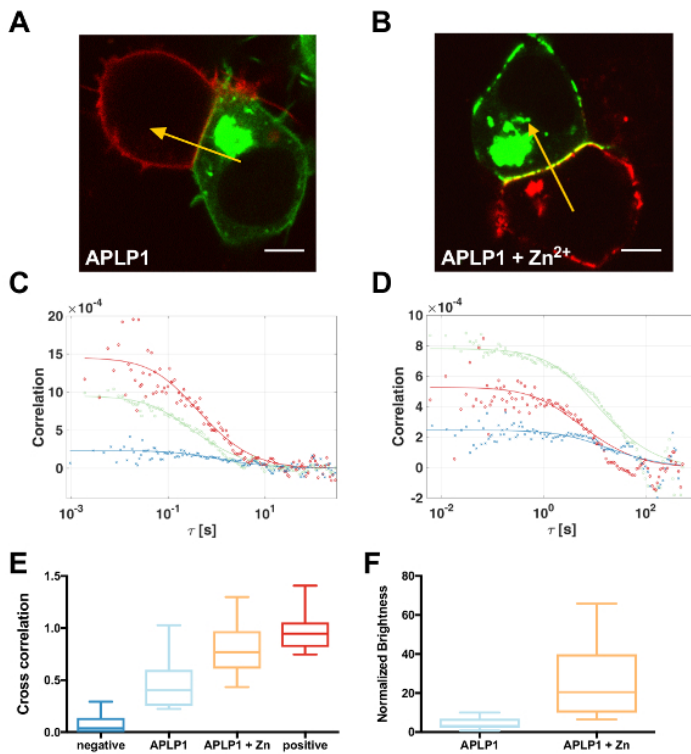


Figure 3. Scanning fluorescence cross-correlation spectroscopy measurements of APLP1 interactions at cell-cell contacts. (A, B) Representative images of HEK 293T cells expressing APLP1-mEYFP (green)/ APLP1-mCardinal (red) before (A) and 30 min after zinc ion treatment (B, different cells). The yellow arrows indicate the sFCCS scan paths. Scale bars are 5 μm . (C, D) Representative CFs (green: ACFs in green channel (mEYFP), red: ACFs in red channel (mCardinal), blue: CCFs) obtained in sFCCS measurements for (C) APLP1 before zinc ion treatment and (D) after zinc ion treatment. Solid lines show fits of a two-dimensional diffusion model to the CFs. (E) Box plots of relative cross-correlation obtained from sFCCS analysis of negative control ("negative"), APLP1 in absence and presence of zinc ions, and positive cross-correlation control ("positive"). Plots show median values and whiskers ranging from minimum to maximum values. (F) Box plots of normalized molecular brightness in green channel (mEYFP) obtained from sFCCS analysis of APLP1 at cell-cell contacts in the absence and presence of zinc ions. Brightness values were corrected for non-fluorescent mEYFP based on sFCS measurements of myr-palm-mEYFP-mEYFP homodimers expressed in HEK 293T cells, measured under the same conditions²³. Plots show median values and whiskers ranging from minimum to maximum values. [Please click here to view a larger version of this figure.](#)

All the measurements shown so far were corrected for additional, spurious fluctuations occurring in the cells that, if not taken into account, would make the sFCCS analysis challenging. For the negative control, for example, these may cause a false-positive cross-correlation, if no correction schemes are applied. Two major processes that can severely distort the CFs are: 1) instabilities in the recorded fluorescence signal due to intracellular vesicles that transiently enter the focal volume or slow membrane dynamics, *e.g.*, drift in z-direction, and 2) photobleaching. To identify transient instabilities, it is recommended to divide the full measurements in 10-20 equally sized segments and to visually inspect the intensity time series and CFs in each segment. This procedure is illustrated in **Figure 4**, which gives an example of clearly distorted segments obtained in the analysis of a negative control measurement. Transient instabilities (**Figure 4A**, intensity traces of segments 1 and 2) may result in a CCF having negative values (**Figure 4B**, segment 1) or a high false-positive cross-correlation (**Figure 4B**, segment 2). Typically, such instabilities are visible in the intensity series as slow signal variations (**Figure 4A**). The corresponding CFs typically deviate strongly from the CFs of the majority of segments, displaying, *e.g.*, higher amplitude and much slower decay times on the \sim second scale (see **Figure 4B-4D**). It is recommended to remove such segments from the analysis and to calculate the final CFs by averaging all non-distorted segments, *i.e.*, segments characterized by CFs not deviating from the majority of CFs. Typically, this is done in a graphical interface by 1) iteratively examining the segments, 2) removing clearly distorted segments from the average and 3) inspecting the CFs of remaining segments with respect to the updated average CFs of segments that were not removed. By applying this procedure, partially distorted long measurements (**Figure 5A**), showing slowly decaying (corrupted) CFs (**Figure 5B**) were successfully corrected and meaningful correlation curves were recovered (**Figure 5C**). Generally, this correction procedure can be automatized²⁹, avoiding a visual inspection by the user, which may be prone to subjective bias. In comparison to intensity based filtering methods³⁶, in which small bins of the measurement are evaluated based on their intensity compared to the average intensity of the full measurement and removed if exceeding a threshold parameter, the described procedure does not rely on external parameters and is sensitive also to minor instabilities.

In order to compensate for photobleaching, the described mathematical correction, **Equation 1**, was applied. Typically, photobleaching can be identified by an exponential decay of the fluorescence signals (**Figure 5D**), dominating the CFs, which then show a false-positive cross-correlation and decay times on the \sim min scale (see the typical curve shape in **Figure 5E**). The correction procedure recovered the non-distorted CFs (**Figure 5F**). As already mentioned, similar intensity variations within single measurements may be also caused by PM movement, e.g., z-drift, or large slowly moving structures. However, if similar exponential decays appear in all measurements, photobleaching will be the most likely source. Generally, correction schemes can be combined, e.g., intensity filtering, CF based filtering and further methods such as Fourier transform based filtering of slow signal variations in frequency space²⁷.

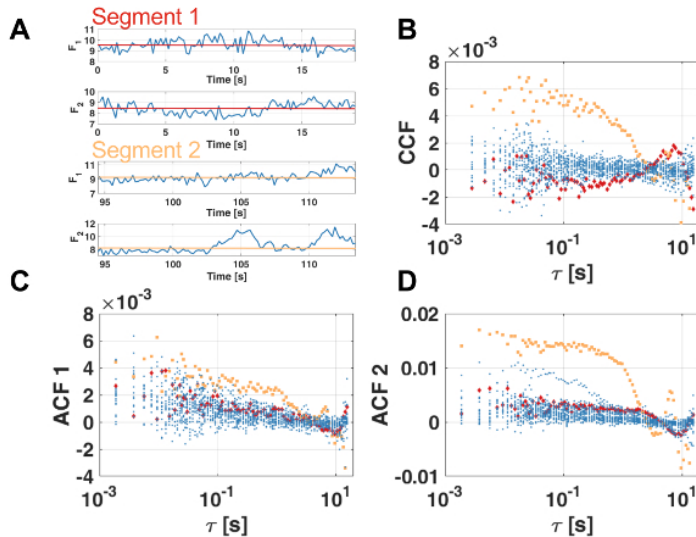


Figure 4. Segment-wise analysis of scanning fluorescence cross-correlation spectroscopy measurements of negative cross-correlation control. (A) Fluorescence intensity in green (F_1) and red channel (F_2) of two different time segments (each measurement was analyzed in 20 segments of ~ 20 s each), obtained from sFCCS measurement of negative control. (B) CCFs of each of the 20 segments. The CCFs for segments 1 and 2 are highlighted in red and orange, respectively. (C, D) ACFs of each segment in green (C) and red (D) channel. The ACFs for segments 1 and 2 are highlighted in red and orange, respectively. [Please click here to view a larger version of this figure.](#)

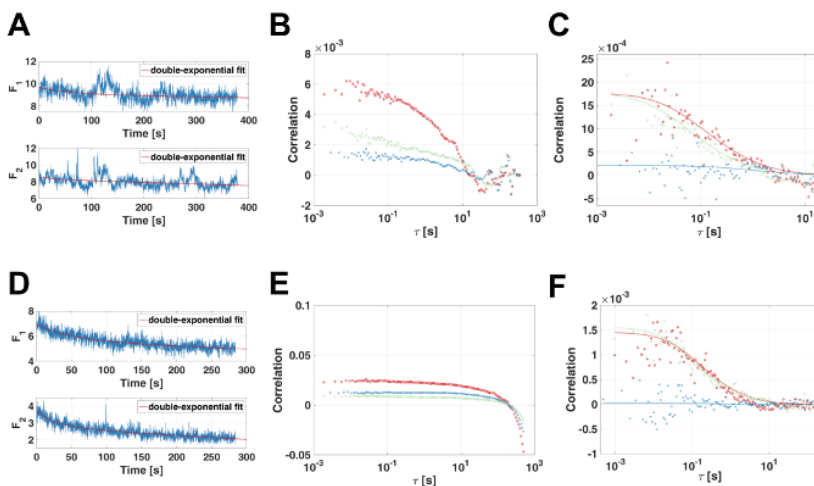


Figure 5. Perturbations in scanning fluorescence cross-correlation spectroscopy measurements at cell-cell contacts, exemplified for negative cross-correlation control. (A) Full fluorescence time series for an exemplar measurement in green (F_1) and red channel (F_2). The solid red lines represent a double-exponential fit of the time series in each channel. (B, C) CFs (green: ACFs in green channel, red: ACFs in red channel, blue: CCFs) of the fluorescence time series shown in A, calculated by (B) correlating the whole measurement or (C) correlating 20 segments separately and averaging the least distorted CFs of $\sim 80\%$ (green channel) and $\sim 50\%$ (red channel) of the segments. Solid lines represent fit of a two-dimensional diffusion model to the data. (D) Full fluorescence time series and double-exponential fit (solid red lines) of measurement characterized by substantial bleaching in green (F_1) and red channel (F_2). (E, F) CFs (green: ACFs in green channel, red: ACFs in red channel, blue: CCFs) of the fluorescence time series shown in D, calculated by (E) correlating the whole measurement or (F) applying the bleaching correction, Equation 1, correlating 20 segments separately and averaging the least distorted CFs of $\sim 90\%$ (both channels) of the segments. Solid lines represent fit of a two-dimensional diffusion model to the data. [Please click here to view a larger version of this figure.](#)

As a complementary approach to sFCCS, ccN&B (**Figure 1C**) can be used to detect protein-protein interactions after cell mixing. In contrast to sFCCS, ccN&B provides no information on protein dynamics, but allows measuring *trans* interactions along the whole cell-cell contact in one focal plane. Measurements on APLP1 samples were performed before and after treatment with 50 μM ZnCl_2 , as well as on the negative myr-palm control. These measurements are sensitive to cell movements, especially for zinc ion treated samples, requiring prolonged acquisition times to account for the slow dynamics of APLP1 clusters. Therefore, an image alignment algorithm was implemented to correct for lateral movement of the cells³³. Also, a boxcar filter²² (8 frames box size, ~ 5 s) was applied to remove low frequency fluctuations of the measured signals. This procedure is very similar to other filters used in N&B analysis involving local averaging³⁷ or detrending^{18,34}, but keeps the original data unaltered, *i.e.*, pixels are treated independently and no averaging or subtraction of signals is performed. This procedure effectively suppresses long-lived fluctuations on time scales longer than the box size²². Following such data analysis, the cross-correlation brightness values for all samples were compared by pooling all cell-cell contact pixels in a cross-correlation brightness histogram. For APLP1 in the absence of zinc ions (**Figure 6A and 6D**), a positive average B_{cc} of 0.068 ± 0.004 (mean \pm SEM, $n = 18$ cells) was observed. After zinc ion addition (**Figure 6B and 6E**), the B_{cc} value increased to 0.266 ± 0.006 (mean \pm SEM, $n = 19$ cells). For the negative control (**Figure 6C and 6F**), a lower average cross-correlation brightness was detected ($B_{cc} = 0.022 \pm 0.002$, mean \pm SEM, $n = 26$ cells). To estimate the stoichiometry of APLP1 complexes at cell-cell contacts, the brightness of APLP1-mEYFP was normalized using the average value obtained for myr-palm-mEYFP (*i.e.*, the negative control) and corrected for the amount of non-fluorescent proteins²³. In agreement with sFCCS data, the brightness distribution was centered around a value corresponding to dimers (**Figure 6G**), in the absence of zinc ions, suggesting an average 2:2 stoichiometry. After zinc ion treatment, the normalized brightness strongly shifted to larger values, ranging from ~ 10 to ~ 60 (**Figure 6H**), *i.e.*, stoichiometries of at least 10:10 or larger, again in good agreement with sFCCS data.

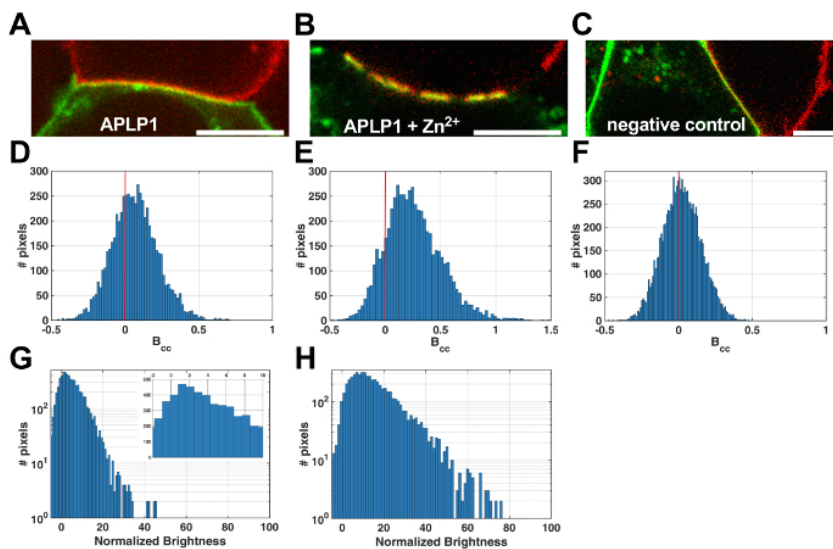


Figure 6. Cross-correlation Number and Brightness measurements of APLP1 interactions at cell-cell contacts. (A-C) Representative ccN&B image frames of cell-cell contacts between APLP1-mEYFP and APLP1-mCardinal expressing HEK 293T cells without (A) and with zinc ions (B) or myr-palm-mEYFP and myr-palm-mCardinal expressing cells as negative cross-correlation control (C). Scale bars are 5 μm . (D-F) Cross-correlation brightness (B_{cc}) histograms of all examined pixels and cells obtained from ccN&B analysis of cell-cell contacts in APLP1 samples (D), zinc-treated APLP1 samples (E) and samples containing myr-palm-mEYFP and myr-palm-mCardinal (F). (G, H) Normalized brightness histograms of APLP1 samples (G: without zinc ions, H: with zinc ions) for the green channel (mEYFP) obtained from brightness analysis of the same cells and ROIs used for the calculation of B_{cc} . Inset in G shows a magnification in the normalized brightness range of -2 to 10. Brightness values were corrected for non-fluorescent mEYFP based on N&B measurements of myr-palm-mEYFP-mEYFP homo-dimers expressed in HEK 293T cells, measured under the same conditions²³. [Please click here to view a larger version of this figure.](#)

In order to perform the ccN&B analysis, a careful calibration of the detectors should be performed. For the experimental setup used in this study, the need for such a calibration became apparent when the molecular brightness was analyzed in fixed samples (*i.e.*, in the absence of number fluctuations). In this case, the molecular brightness is expected to be zero according to Equation 10, since the variance should only originate from detector noise. However, when a ROI that contains only (immobile) background pixels was analyzed (**Figure 7A and 7B**), a positive brightness of ~ 0.1 cts./ $(\text{MOL} \times \text{dwell time})$ was determined. A similar value was obtained performing N&B measurements of HEK 293T cells expressing glycosylphosphatidylinositol-mCherry (GPI-mCherry, **Figure 7C**) with varying laser powers and extrapolating the measured molecular brightness to zero laser power. To correct for this effect, we performed a systematic calibration of the detector, as previously reported (see Equation 12)^{19,20}. We therefore measured the variance as a function of detector count rate on a sample consisting of a dried fluorescent dye solution and determined the parameters S , σ_0^2 and the dark count rate offset. The latter was obtained from measuring the intensity at zero laser power and was, in our case, negligible. From a linear fit of the variance versus intensity plot, we determined, according to Equation 14, a slope of $S = 1.1$, and a negligible readout noise. The determined values ($S = 1.1$, $\sigma_0^2 = 0$, *offset* = 0) were then used to correctly calculate molecular brightness and number according to Equations 12 and 13¹⁹. Alternatively, a more empirical correction scheme can be applied based on the fact that a superpoissonian detector noise, *i.e.*, $\sim 10\%$ larger noise than Poissonian shot noise, would also explain the observation of a positive molecular brightness in pixels without number fluctuations. Using this assumption, the determined brightness of ~ 0.1 cts./ $(\text{MOL} \times \text{dwell time})$ in such pixels can be considered as a constant brightness offset and should thus be subtracted from all brightness values calculated with Equation 10. Most importantly, both described approaches lead to the same results when calculating brightness ratios, as long as σ_0^2 and *offset* are negligible. It is worth mentioning that among different microscopes of the same type (same vendor, same model, GaAsP detectors in photon counting mode) different S values were observed, highlighting the necessity for a careful detector calibration on each individual setup.

A further important parameter affecting the detector performance in brightness measurements is the detector dead time. As it has been previously shown, the detector dead time can substantially reduce the detected molecular brightness, even at medium count rates (above 10^2 - 10^3 kHz)³⁸. To avoid this artefact, measurements should either be performed at lower count rates, or the dead time should be calibrated based on performing N&B or FCS in a dilution series of, *e.g.*, EGFP in buffer solution. Then, measured count rates can be corrected using a calibrated dead time³⁸. For the setup used in this study, such a calibration using N&B on diluted dye solutions revealed stable molecular brightness values up to count rates of ~ 0.5 MHz and a corresponding dead time of ~ 6 ns (**Figure 7E**). The decrease at higher count rates can be thus corrected by using a previously published correction formula³⁸, resulting in a constant brightness value of ~ 8 kHz/MOL.

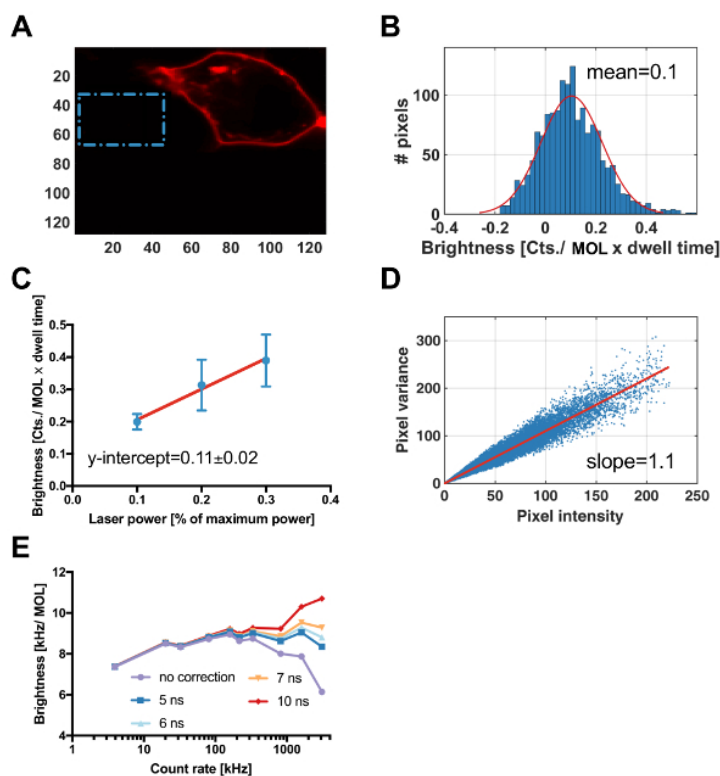


Figure 7. Detector calibration for Number and Brightness analysis. (A) Representative image from N&B measurements of HEK 293T cells expressing GPI-mCherry. A ROI (blue dashed rectangle) was selected in the background. (B) Pixel brightness histogram of all pixels corresponding to the ROI shown in A. The average pixel brightness, obtained from fitting the pixel brightness histogram with a Gaussian function, is ~ 0.1 cts./ (MOL x dwell time). Data were acquired at 25 μ s pixel dwell time. (C) Molecular brightness obtained from N&B analysis of GPI-mCherry expressed in HEK 293T cells, measured at three different laser powers (6 cells each, 561 nm excitation, 25 μ s pixel dwell time). Data are displayed as mean \pm SD. A linear regression (red line) provides an offset value of 0.11 ± 0.02 cts./ (MOL x dwell time). (D) Plot of pixel variance as a function of pixel intensity from N&B measurements of a dried solution of a fluorescent dye (excited at 561 nm), pooled from all pixels of multiple measurements in different regions of the sample. The solid red line shows a linear fit of the data, resulting in a slope of 1.1, providing the S factor of the detector calibration. (E) Molecular brightness as a function of detector count rate, obtained from N&B measurements of diluted fluorophore solutions (excited at 488 nm). A previously published correction scheme³⁸ was applied using different possible values for the detector dead time. [Please click here to view a larger version of this figure.](#)

Discussion

The experimental procedure described here allows the investigation of protein-protein *trans* interactions at cell-cell contacts, employing fluorescence fluctuation spectroscopy techniques, namely sFCCS and ccN&B. These methods involve a statistical analysis of fluorescence fluctuations emitted by two spectrally separated FPs fused to the protein(s) of interest at a contact of two neighboring cells, each expressing one or the other fusion protein. The presence of *trans* complexes is quantified by probing the degree of co-diffusion of proteins in neighboring PMs. In addition to detailed protocols on sample preparation, data acquisition and analysis, this article provides experimental evidence of the successful application of the assay on the neuronal adhesion protein APLP1. We show that APLP1 undergoes specific, homotypic *trans* interactions at cell-cell contacts. Further, zinc ions promote the formation of APLP1 clusters at cell-cell contacts that provide a multivalent platform for *trans* interactions and, thus, induce enhanced *trans* binding.

In contrast to previous assays to detect such interactions based on disruptive biochemical methods⁶, the presented approach can be performed directly on living cells, with no need for fixation or isolation of protein complexes. Moreover, it provides molecular specificity and information by detection of fluorescent proteins genetically fused to the protein of interest, in contrast to previous qualitative assays^{8,9}. Differently from other fluorescence based approaches such as FRET¹⁰ and fluorescence complementation¹¹, there is no requirement for the fluorescent labels to be localized on the extracellular side (potentially interfering with protein-protein interactions). Nevertheless, it has to be noted that C-terminal FPs might still alter the binding to intracellular components, e.g., adaptor proteins that mediate interactions with the cytoskeleton. Notably, the assay is applicable to both homo- and heterotypic interactions.

A few requirements for a successful application of the presented assay are worth mentioning. The performed fluorescence fluctuation methods are based on temporal measurements that require bright and photostable monomeric FPs, which is a major constraint for many red FPs²³. Even though the presented scanning scheme is particularly well suited for the investigation of the slow dynamics of transmembrane proteins, which are typically involved in cell-cell interactions, residual photobleaching may still occur. Therefore, we present a detailed description of correction schemes, i.e., a bleaching correction for sFCCS and boxcar filter for ccN&B, which minimize such perturbations. Further, we discuss numerical alignment algorithms that effectively correct for other systematic perturbations, such as lateral movement of cells, and provide guidelines to

remove transient instabilities. A major source of such instabilities is vesicular transport, *i.e.*, intracellular vesicles carrying the protein of interest that transiently enter the focal volume. Although varying from case to case, this phenomenon can in general severely disturb data acquisition and analysis. However, the application of correction algorithms improves the stability of the acquisition, allowing extended measurement times that are needed to probe the especially slow diffusive dynamics. In this regard, it has to be underlined that the presence of diffusive dynamics is an essential condition for the method to work. The example of zinc ion mediated APLP1 clustering shows a drastic example of large, very slow protein complexes ($D \approx 0.001 \mu\text{m}^2/\text{s}$) that push the technique to its limits and prevent an accurate quantification of the underlying dynamics, due to large noise induced by the limited acquisition time^{30,17}.

In this context, recent advances on combining sFCS and super-resolution approaches, *e.g.*, scanning stimulated emission depletion FCS (STED-FCS), may be beneficial by providing a smaller focal volume and thus smaller effective diffusion times^{39,40}. This could also help to resolve protein clusters in case of an inhomogeneous localization of the protein of interest at the cell-cell contacts, as observed for APLP1 in the presence of zinc. Unfortunately, a cross-correlation implementation of scanning STED-FCS, *i.e.*, STED-FCCS, that could be directly applied here, has not been successfully demonstrated yet due to the difficulty of finding compatible dyes for two-color STED-FCS. In the case of sufficiently fast dynamics ($D \geq \sim 0.05 \mu\text{m}^2/\text{s}$), sFCCS analysis allows to quantify the diffusion of proteins at cell-cell contacts or in other regions of the PM¹².

Further, a brightness analysis can be performed for all data (sFCCS and ccN&B), providing an estimate of the stoichiometry of *trans* protein complexes. It should be mentioned that the accuracy of the stoichiometry quantification increases with the amount of proteins that bind in *trans* (*i.e.*, if there are only few *cis* complexes which could also affect the brightness determination). Brightness analysis does not allow resolving mixtures of different oligomeric states, *e.g.*, *cis* monomers and *trans* tetramers. More in general, it should be noted that N&B cannot resolve mixtures of different oligomeric species homogeneously distributed in a sample. If multiple species are present within a pixel, one single value of brightness will be measured (*i.e.*, a weighted average of the brightness of each oligomeric species). The statistical distribution of the observed brightness values (*e.g.*, in different pixels) is not directly connected to the relative amounts of oligomeric species. To resolve such mixtures, other methods should be used (*e.g.*, spatial intensity distribution analysis (SpIDA)⁴¹, photon counting histogram (PCH)⁴²). Similarly, the quantification of the spectral cross-correlation in sFCCS provides an accurate quantification of the fraction of bound and unbound proteins only for simple, known stoichiometries, *e.g.*, 1:1. For a more complex stoichiometry, further assumptions have to be made⁴³. Overall, brightness analysis remains a powerful experimental tool, if the detector system and the fraction of non-fluorescent FPs are calibrated²³ as described in the protocols.

Although the application presented here is focused on protein-protein interactions in adherent cells, the assay can be applied to a wider range of samples, *e.g.*, suspension cells. For such systems, correction for lateral cell movement may be particularly crucial. In addition, it can be easily applied to model membrane systems such as GUVs or GPMVs, allowing the quantification of molecular interactions under well controlled conditions, *e.g.*, different lipid compositions or membranes lacking an organized cytoskeleton. When performing sFCCS on such vesicles, vertical motion may cause additional signal fluctuations, but can be minimized when focusing on large vesicles. In this context, multiple combinations are promising, *e.g.*, GUV-/ GPMV-cell mixing¹². As shown in a recent publication, the formation of immune synapses can be successfully modeled by such systems⁴⁴. Thus, the presented assay will certainly be useful for the investigation of a large variety of cell-cell interactions.

Disclosures

The authors have nothing to disclose.

Acknowledgements

This work was partially supported by the Deutsche Forschungsgemeinschaft (DFG) grant 254850309. The authors thank Madlen Luckner for critical reading of the manuscript.

References

1. Alberts, B., Johnson, A., Lewis, J., Raff, M., Roberts, K., Walter, P. *Molecular biology of the cell*. Garland Science. (2002).
2. Tepass, U., Truong, K., Godt, D., Ikura, M., Peifer, M. Cadherins in embryonic and neural morphogenesis. *Nature Reviews Molecular Cell Biology*. **1** (2), 91-100 (2000).
3. Harris, T. J. C., Tepass, U. Adherens junctions: from molecules to morphogenesis. *Nature Reviews Molecular Cell Biology*. **11** (7), 502-514 (2010).
4. Hernández, J. M., Podbilewicz, B. The hallmarks of cell-cell fusion. *Development (Cambridge, England)*. **144** (24), 4481-4495 (2017).
5. Huppa, J. B., Davis, M. M. T-cell-antigen recognition and the immunological synapse. *Nature Reviews Immunology*. **3** (12), 973-983 (2003).
6. Kaden, D., Voigt, P., Munter, L., Bobowski, K. D., Schaefer, M., Multhaup, G. Subcellular localization and dimerization of APLP1 are strikingly different from APP and APLP2. *Journal of cell science*. **122** (Pt 3), 368-377 (2009).
7. Yap, A. S., Michael, M., Parton, R. G. Seeing and believing: recent advances in imaging cell-cell interactions. *F1000Research*. **4** (F1000 Faculty Rev), 273 (2015).
8. Kashef, J., Franz, C. M. Quantitative methods for analyzing cell-cell adhesion in development. *Developmental Biology*. **401** (1), 165-174 (2015).
9. Soba, P. *et al.* Homo- and heterodimerization of APP family members promotes intercellular adhesion. *The EMBO Journal*. **24** (20), 3624-3634 (2005).
10. Kim, S. A., Tai, C. -Y., Mok, L. -P., Mosser, E. A., Schuman, E. M. Calcium-dependent dynamics of cadherin interactions at cell-cell junctions. *Proceedings of the National Academy of Sciences of the United States of America*. **108** (24), 9857-62 (2011).
11. Feinberg, E. H. *et al.* GFP Reconstitution Across Synaptic Partners (GRASP) Defines Cell Contacts and Synapses in Living Nervous Systems. *Neuron*. **57** (3), 353-363 (2008).
12. Dunsing, V., Mayer, M., Liebsch, F., Multhaup, G., Chiantia, S. Direct evidence of amyloid precursor-like protein 1 trans interactions in cell-cell adhesion platforms investigated via fluorescence fluctuation spectroscopy. *Molecular biology of the cell*. **28** (25), 3609-3620 (2017).

13. Schneider, F. *et al.* Diffusion of lipids and GPI-anchored proteins in actin-free plasma membrane vesicles measured by STED-FCS. *Molecular Biology of the Cell*. **28** (11), 1507-1518 (2017).
14. Bacia, K., Kim, S. A., Schwille, P. Fluorescence cross-correlation spectroscopy in living cells. *Nature methods*. **3** (2), 83-89 (2006).
15. Ries, J., Schwille, P. Studying Slow Membrane Dynamics with Continuous Wave Scanning Fluorescence Correlation Spectroscopy. *Biophysical Journal*. **91** (5), 1915-1924 (2006).
16. Ries, J., Chiantia, S., Schwille, P. Accurate Determination of Membrane Dynamics with Line-Scan FCS. *Biophysical Journal*. **96** (5), 1999-2008 (2009).
17. Chiantia, S., Ries, J., Schwille, P. Fluorescence correlation spectroscopy in membrane structure elucidation. *Biochimica et Biophysica Acta (BBA) - Biomembranes*. **1788** (1), 225-233 (2009).
18. Digman, M. A., Dalal, R., Horwitz, A. F., Gratton, E. Mapping the number of molecules and brightness in the laser scanning microscope. *Biophysical journal*. **94** (6), 2320-2332 (2008).
19. Dalal, R. B., Digman, M. A., Horwitz, A. F., Vetri, V., Gratton, E. Determination of particle number and brightness using a laser scanning confocal microscope operating in the analog mode. *Microscopy research and technique*. **71** (1), 69-81 (2008).
20. Unruh, J. R., Gratton, E. Analysis of Molecular Concentration and Brightness from Fluorescence Fluctuation Data with an Electron Multiplied CCD Camera. *Biophysical Journal*. **95** (11), 5385-5398 (2008).
21. Digman, M. A., Wiseman, P. W., Choi, C., Horwitz, A.R., Gratton, E. Stoichiometry of molecular complexes at adhesions in living cells. *Proceedings of the National Academy of Sciences of the United States of America*. **106** (7), 2170-2175 (2009).
22. Hellriegel, C., Caiolfa, V. R., Corti, V., Sidenius, N., Zamai, M. Number and brightness image analysis reveals ATF-induced dimerization kinetics of uPAR in the cell membrane. *The FASEB journal : official publication of the Federation of American Societies for Experimental Biology*. **25** (9), 2883-2897 (2011).
23. Dunsing, V., Luckner, M., Zühlke, B., Petazzi, R. A., Herrmann, A., Chiantia, S. Optimal fluorescent protein tags for quantifying protein oligomerization in living cells. *Scientific Reports*. **8** (1), 10634 (2018).
24. Chen, Y., Johnson, J., Macdonald, P., Wu, B., Mueller, J. D. Observing Protein Interactions and Their Stoichiometry in Living Cells by Brightness Analysis of Fluorescence Fluctuation Experiments. *Methods in enzymology*. **472**, 345-363 (2010).
25. Kapusta, P. *Absolute Diffusion Coefficients: Compilation of Reference Data for FCS Calibration*. at <https://www.picoquant.com/images/uploads/page/files/7353/appnote_diffusioncoefficients.pdf> (2010).
26. Foo, Y. H., Naredi-Rainer, N., Lamb, D. C., Ahmed, S., Wohland, T. Factors affecting the quantification of biomolecular interactions by fluorescence cross-correlation spectroscopy. *Biophysical journal*. **102** (5), 1174-83 (2012).
27. Baum, M., Erdel, F., Wachsmuth, M., Rippe, K. Retrieving the intracellular topology from multi-scale protein mobility mapping in living cells. *Nature Communications*. **5**, 4494 (2014).
28. Wohland, T., Rigler, R., Vogel, H. The standard deviation in fluorescence correlation spectroscopy. *Biophysical journal*. **80** (6), 2987-99 (2001).
29. Ries, J. *et al.* Automated suppression of sample-related artifacts in Fluorescence Correlation Spectroscopy. *Optics Express*. **18** (11), 11073 (2010).
30. Ries, J., Schwille, P. New concepts for fluorescence correlation spectroscopy on membranes. *Physical Chemistry Chemical Physics*. **10** (24), 3487 (2008).
31. Mayer, M. C. *et al.* Amyloid precursor-like protein 1 (APLP1) exhibits stronger zinc-dependent neuronal adhesion than amyloid precursor protein and APLP2. *Journal of Neurochemistry*. **137** (2), 266-276 (2016).
32. Linkert, M. *et al.* Metadata matters: access to image data in the real world. *The Journal of Cell Biology*. **189** (5), 777-782 (2010).
33. Trullo, A., Corti, V., Arza, E., Caiolfa, V. R., Zamai, M. Application limits and data correction in number of molecules and brightness analysis. *Microscopy Research and Technique*. **76** (11), 1135-1146 (2013).
34. Nolan, R. *et al.* nandb-number and brightness in R with a novel automatic detrending algorithm. *Bioinformatics (Oxford, England)*. **33** (21), 3508-3510 (2017).
35. Hammond, G. R. V., Sim, Y., Lagnado, L., Irvine, R. F. Reversible binding and rapid diffusion of proteins in complex with inositol lipids serves to coordinate free movement with spatial information. *The Journal of cell biology*. **184** (2), 297-308 (2009).
36. Hendrix, J., Dekens, T., Schrimpf, W., Lamb, D. C. Arbitrary-Region Raster Image Correlation Spectroscopy. *Biophysical journal*. **111** (8), 1785-1796 (2016).
37. Hendrix, J. *et al.* Live-cell observation of cytosolic HIV-1 assembly onset reveals RNA-interacting Gag oligomers. *The Journal of cell biology*. **210** (4), 629-46 (2015).
38. Hendrix, J., Schrimpf, W., Höller, M., Lamb, D. C. Pulsed Interleaved Excitation Fluctuation Imaging. *Biophysical Journal*. **105** (4), 848-861 (2013).
39. Honigsmann, A. *et al.* Scanning STED-FCS reveals spatiotemporal heterogeneity of lipid interaction in the plasma membrane of living cells. *Nature Communications*. **5** (1), 5412 (2014).
40. Chojnacki, J. *et al.* Envelope glycoprotein mobility on HIV-1 particles depends on the virus maturation state. *Nature Communications*. **8** (1), 545 (2017).
41. Godin, A. G. *et al.* Revealing protein oligomerization and densities in situ using spatial intensity distribution analysis. *Proceedings of the National Academy of Sciences of the United States of America*. **108** (17), 7010-5 (2011).
42. Müller, J. D., Chen, Y., Gratton, E. Resolving Heterogeneity on the Single Molecular Level with the Photon-Counting Histogram. *Biophysical Journal*. **78** (1), 474-486 (2000).
43. Kim, S. A., Heinze, K. G., Bacia, K., Waxham, M. N., Schwille, P. Two-Photon Cross-Correlation Analysis of Intracellular Reactions with Variable Stoichiometry. *Biophysical Journal*. **88** (6), 4319-4336 (2005).
44. Jenkins, E. *et al.* Reconstitution of immune cell interactions in free-standing membranes. *Journal of cell science*. **132** (4) (2018).

Materials List for:

A Fluorescence Fluctuation Spectroscopy Assay of Protein-Protein Interactions at Cell-Cell Contacts

Valentin Dunsing¹, Salvatore Chiantia¹

¹Institute for Biochemistry and Biology, Cell Membrane Biophysics Group, University of Potsdam

Correspondence to: Salvatore Chiantia at chiantia@uni-potsdam.de

URL: <https://www.jove.com/video/58582>

DOI: [doi:10.3791/58582](https://doi.org/10.3791/58582)

Materials

Name	Company	Catalog Number	Comments
DMEM growth medium	PAN-Biotech	P04-01548	
DPBS w/o: Ca ²⁺ and Mg ²⁺	PAN-Biotech	P04-36500	
DPBS w: Ca ²⁺ and Mg ²⁺	PAN-Biotech	P04-35500	
Trypsin EDTA	PAN-Biotech	P10-023100	
TurboFect Transfection Reagent	Thermo Fisher Scientific	R0531	
HEK 293T cells	DSMZ	ACC 635	
Alexa Fluor 488 NHS Ester	Thermo Fisher Scientific	A20000	
Rhodamine B	Sigma-Aldrich	83689-1G	
Plasmid DNA	Addgene	NA	See reference 12 (Dunsing et al., MBoC 2017), for a detailed description of all plasmids
6-well plate	Starlab	CC7672-7506	
35-mm glass bottom dishes	CellVis	D35-14-1.5-N	
Zeiss LSM780 confocal	Carl Zeiss	NA	
MATLAB software package	MathWorks	2015b	
Neubauer cell counting chamber	Marienfeld	640110	


2.3 [P3] Optimal fluorescent protein tags for quantifying protein oligomerization in living cells

This is a downloaded version of the article that was published in Scientific Reports, volume 8, 10634 in 2018, available online at: <https://www.nature.com/articles/s41598-018-28858-0> (doi: 10.1038/s41598-018-28858-0).

SCIENTIFIC REPORTS

OPEN

Optimal fluorescent protein tags for quantifying protein oligomerization in living cells

Valentin Dusing¹, Madlen Luckner², Boris Zühlke¹, Roberto A. Petazzi¹, Andreas Herrmann¹ ² & Salvatore Chiantia¹

Received: 14 May 2018

Accepted: 2 July 2018

Published online: 13 July 2018

Fluorescence fluctuation spectroscopy has become a popular toolbox for non-disruptive analysis of molecular interactions in living cells. The quantification of protein oligomerization in the native cellular environment is highly relevant for a detailed understanding of complex biological processes. An important parameter in this context is the molecular brightness, which serves as a direct measure of oligomerization and can be easily extracted from temporal or spatial fluorescence fluctuations. However, fluorescent proteins (FPs) typically used in such studies suffer from complex photophysical transitions and limited maturation, inducing non-fluorescent states. Here, we show how these processes strongly affect molecular brightness measurements. We perform a systematic characterization of non-fluorescent states for commonly used FPs and provide a simple guideline for accurate, unbiased oligomerization measurements in living cells. Further, we focus on novel red FPs and demonstrate that mCherry2, an mCherry variant, possesses superior properties with regards to precise quantification of oligomerization.

A large variety of biological processes relies on transport and interactions of biomolecules in living cells. For a detailed understanding of these events, minimally invasive techniques are needed, allowing the direct quantification of inter-molecular interactions in the native cellular environment. In recent years, fluorescence fluctuation spectroscopy (FFS) approaches have been often used to fulfil this task^{1–6}. FFS is based on the statistical analysis of signal fluctuations emitted by fluorescently labelled molecules. While the temporal evolution of such fluctuations provides information about dynamics, the magnitude of the fluctuations contains information about molecule concentration and interactions (i.e. oligomeric state). In order to probe the oligomerization of a protein directly in living cells, the molecular brightness (i.e. the fluorescence signal originating from a single protein complex) can be determined. To this aim, the protein of interest is genetically fused to a fluorescent protein (FP)^{4,5,7}. Comparison to a monomeric reference allows the quantification of the number of FP units within a protein complex, i.e. its oligomeric state. For example, a tetrameric protein complex is composed of four protein units, each genetically fused to one FP, and thus the complex carries four FP units in total. The molecular brightness is an average single-molecule quantity, obtained by analysing fluorescence fluctuations of an ensemble of molecules. In a simple scenario, it allows to distinguish whether a sample that emits a certain total fluorescence signal is composed of many dim, or few bright molecules. This analysis can be performed with different experimental methods, e.g. Fluorescence Correlation Spectroscopy (FCS)^{1,8}, Photon Counting Histogram (PCH)^{4,9}, Number&Brightness analysis (N&B)^{2,7} or subunit counting^{10,11}. Differently from other fluorescence based approaches to probe protein oligomerization, such as Fluorescence Resonance Energy Transfer (FRET)¹² or Bimolecular Fluorescence Complementation (BiFC)¹³, FFS provides the size of the complex.

Measuring the oligomeric state from the number of fluorescent labels, it is often assumed that all FPs emit a fluorescence signal. However, various *in vitro* studies of FPs revealed complex photophysical properties such as: long-lived dark states of green FPs^{14–17}, transitions between different brightness states (e.g. YFP¹⁸, mCherry¹⁹) and flickering²⁰. Additionally, limited maturation and folding efficiencies were reported for FPs expressed in cells²¹ or as fusions with other proteins²². All together, these observations challenge the suitability of FPs for quantitative brightness analysis⁵. In this context, partially contradicting results are reported: studies performing subunit

¹Institute of Biochemistry and Biology, University of Potsdam, Karl-Liebknecht-Str. 24-25, 14476, Potsdam, Germany. ²Institute for Biology, IRI Life Sciences, Humboldt-Universität zu Berlin, Invalidenstraße 42, 10115, Berlin, Germany. Valentin Dusing and Madlen Luckner contributed equally to this work. Correspondence and requests for materials should be addressed to S.C. (email: chiantia@uni-potsdam.de)

counting typically indicate apparent fluorescence probability (p_f) values of 50–80%^{10,11,23,24} for GFPs. Very few investigations utilizing FFS approaches report similar values^{25,26}, while very often it is simply assumed that all FPs are fluorescent. For commonly used red FPs (mainly RFP and mCherry), published results tend to agree, consistently reporting low p_f values (ca. 20–40%)^{27,28}, with only few exceptions¹⁹.

Notably, many investigations would profit from systematic controls testing the presence of non-fluorescent labels, but so far only few studies take explicitly into account the role of the p_f in the exact quantification of protein-protein interaction^{5,11,25,29}. Importantly, oligomerization data are prone to severe misinterpretations if non-fluorescent labels are not taken into consideration, i.e. the molecular brightness of a protein complex may be strongly underestimated. For example, a tetrameric protein complex appears to be a dimer if only one third of all FPs are fluorescent.

To our knowledge, this is the first report systematically comparing non-fluorescent states and associated p_f for various FPs in one-photon excitation. We found significant amounts of non-fluorescent FPs in different cell types and compartments, and we determined the p_f for each FP. With appropriate corrections, we were able to correctly determine the oligomeric state of the homo-trimeric Influenza A virus Hemagglutinin (HA) glycoprotein, for the first time directly in living cells, as a proof of principle.

To investigate multiple interacting molecular species simultaneously, multicolour FFS analysis is often performed. Compared to alternative methods to detect such interactions, e.g. N-way FRET³⁰, BiFC-FRET³¹ or Three-fragment fluorescence complementation (TFCC)³², it is not constrained to \sim nm distances between the fluorophores and provides an estimate of the true stoichiometry of a protein complex. In multicolour FFS, protein hetero-interactions can be quantified via fluorescence cross-correlation approaches^{1,33}, even in living multicellular organisms^{6,34}. Such methods require well-performing FPs with spectral properties distinguished from the typically used mEGFP. Therefore, current FP development focuses on red and far-red FPs³⁵. Nevertheless, the p_f for these proteins, although playing a fundamental role in brightness and cross-correlation analysis, has not been systematically investigated yet. We therefore screened different red FPs for the presence of non-fluorescent states, and found that mCherry2, a not fully characterized mCherry variant, possesses superior properties compared to all other tested red FPs, i.e. mCherry, mCardinal, mRuby3, mScarlet and mScarlet-I. Additionally, by performing Fluorescence Cross-Correlation Spectroscopy (FCCS) measurements of FP hetero-dimers, we show that mCherry2 improves the quantification of the spectral cross-correlation compared to mCherry and propose to use mEGFP and mCherry2 as a novel standard FP pair for hetero-interaction studies.

Results

The brightness of homo-dimers of conventional FPs is lower than double the brightness of monomers.

In an ideal case, i.e. if all fluorophores within an oligomer were fluorescent, a homo-dimer would emit twice as many photons as a monomer. We expressed several FPs in the cytoplasm of HEK 293T cells and performed FFS measurements. We found that the brightness values of homo-dimers (normalized to the brightness of the corresponding monomer) for three widely used FPs, namely mEGFP ($\epsilon_{\text{dimer}} = 1.69 \pm 0.05$), mEYFP ($\epsilon_{\text{dimer}} = 1.63 \pm 0.05$) and mCherry ($\epsilon_{\text{dimer}} = 1.41 \pm 0.04$), are generally lower than two, indicating the presence of non-fluorescent proteins. The effect is particularly pronounced for mCherry (Fig. 1a) and does not depend on the specific FFS method used or cellular localization, as shown by comparing the results from N&B, point FCS (pFCS) -in cytoplasm and nucleus- and scanning FCS (sFCS) -for FPs associated to the plasma membrane (PM)- (Fig. 1a,b). Interestingly, we observed a 10% lower brightness for FP monomers within the nucleus compared to the cytoplasmic fraction (Supplementary Figure S1). Furthermore, we measured homo-dimer brightness values of mEGFP and mCherry in different cell lines (HEK 293T, A549, CHO, HeLa) and obtained comparable values in all cell types for the same FP (Supplementary Figure S1).

The maturation time of FPs might influence the fraction of non-fluorescent proteins and this, in turn, may be dependent on the temperature at which experiments are performed²¹. For this reason, we compared the homo-dimer brightness of mEGFP at 23 °C and 37 °C, but observed negligible differences (Supplementary Figure S1).

Taken together, our results demonstrate that the effect of non-fluorescent states on brightness quantification for mEGFP, mEYFP and mCherry is mainly a fluorophore-inherent property and is not strongly influenced by the tested experimental conditions.

The oligomeric state of mEGFP homo-oligomers is correctly determined by using a simple correction scheme for non-fluorescent states.

Based on the observed non-fluorescent protein fractions for mEGFP, mEYFP and mCherry, we investigated whether it is possible to nevertheless correctly determine the oligomeric state of higher-order oligomers. To this aim, we expressed mEGFP homo-oligomers of different sizes: 1xmEGFP, 2xmEGFP, 3xmEGFP and 4xmEGFP (i.e. monomers to tetramers). We then performed pFCS measurements in the cytoplasm of living A549 cells (Fig. 2a).

We observed brightness values consistently lower than those expected. For example, the obtained tetramer brightness ($\epsilon_{\text{tetramer}} = 3.01 \pm 0.08$) is very close to the theoretical trimer brightness value (Fig. 2b, white boxes). Hence, we performed a brightness correction based on a simple two-state model^{11,36}, taking into account the probability that each FP subunit emits a fluorescence signal. The p_f values were determined from the brightness of 2xmEGFP ($\epsilon_{\text{dimer}} = 1.65 \pm 0.06$, $p_f = 0.65$). Thus, we were able to correctly determine the oligomeric state of all mEGFP-homo-oligomers investigated in this study (Fig. 2b, grey boxes). Consistent with the brightness data, pFCS analysis revealed an increase of the diffusion times with increasing homo-oligomer size (Supplementary Figure S2 and related SI).

Furthermore, to extend our investigation to larger protein complexes, we performed N&B measurements on U2OS cells expressing the 12-meric *E. coli* glutamine synthetase (GlnA)³⁷ (Fig. 2c). We measured an average normalized brightness of $\epsilon_{\text{GlnA}} = 8.8 \pm 0.3$. However, after correction for non-fluorescent mEGFP subunits

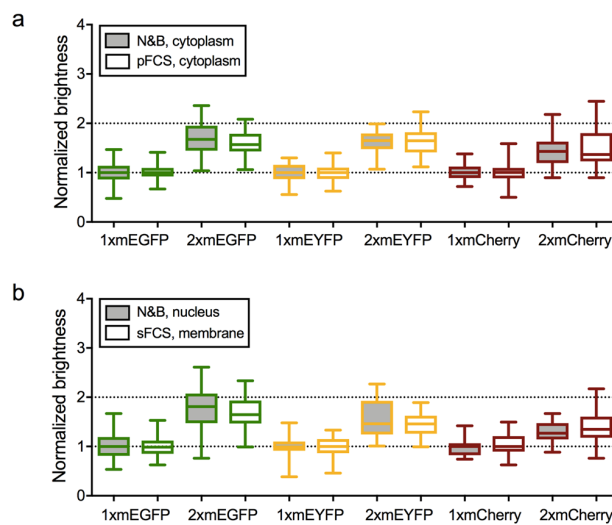


Figure 1. Brightness comparison of different FPs in living HEK 293T cells. **(a)** Box plots of normalized molecular brightness of mEGFP, mEYFP and mCherry monomers and homo-dimers in HEK 293T cells, measured via N&B (grey boxes) or pFCS (white boxes). Monomer and dimer constructs are labeled as “1x” and “2x”, respectively. Data were pooled from at least three independent experiments (N&B/pFCS: 1xmEGFP: $n = 47/39$ cells, 2xmEGFP: $n = 48/38$ cells, 1xmEYFP: $n = 33/37$ cells, 2xmEYFP: $n = 32/39$ cells, 1xmCherry: $n = 50/35$ cells, 2xmCherry: $n = 53/34$ cells). **(b)** Box plots of normalized molecular brightness of mEGFP, mEYFP and mCherry monomers and homo-dimers in the nucleus (grey boxes) and PM (white boxes) of HEK 293T cells, measured with N&B (nucleus) and sFCS (PM). For PM measurements, myristoylated-palmitoylated (mp) 1xmEGFP, mp 2xmEGFP, mp 1xmEYFP, mp 2xmEYFP, glycosylphosphatidylinositol-anchored (GPI) 1xmCherry and GPI 2xmCherry constructs were expressed. See Methods section for a description of the investigated FP constructs. Data were pooled from at least three independent experiments (nucleus: 1xmEGFP: $n = 47$ cells, 2xmEGFP: $n = 48$ cells, 1xmEYFP: $n = 30$ cells, 2xmEYFP: $n = 32$ cells, 1xmCherry: $n = 32$ cells, 2xmCherry: $n = 37$ cells; PM: mp 1xmEGFP: $n = 55$ cells, mp 2xmEGFP: $n = 55$ cells, mp 1xmEYFP: $n = 28$ cells, mp 2xmEYFP: $n = 28$ cells, GPI 1xmCherry: $n = 38$ cells, GPI 2xmCherry: $n = 38$ cells).

($\epsilon_{\text{dimer}} = 1.72 \pm 0.05$, $p_f = 0.72$), we obtained an oligomeric state of $\epsilon_{\text{GlnA}} = 11.9 \pm 0.4$, confirming the expected 12-mer structure of the GlnA complex (Fig. 2d).

Overall, these results highlight the importance of performing control experiments with suitable homo-oligomers for brightness-based oligomerization studies and demonstrate that the simple correction for non-fluorescent states presented here produces reliable results.

Influenza A virus hemagglutinin forms homo-trimers in the plasma membrane. We next verified whether the above-mentioned simple two-state brightness correction provides reliable quantitative results in a biologically relevant context. To this aim, we analysed an mEGFP-fused version of the Influenza A virus hemagglutinin (HA-wt-mEGFP), a biochemically well-characterized trimeric transmembrane protein^{38,39}. We expressed the fluorescent fusion protein in living HEK 293T cells and performed sFCS measurements (Fig. 3a and Supplementary Figure S3) across the PM. After correction for the non-fluorescent FPs contribution, we obtained an average normalized brightness of $\epsilon_{\text{HA-wt-mEGFP}} = 3.17 \pm 0.12$ (Fig. 3b), in line with the expected trimeric structure of HA-wt-mEGFP. We further investigated a hemagglutinin transmembrane domain (HA-TMD-mEGFP) mutant, in which the HA ectodomain is replaced by mEGFP on the extracellular side. This construct was shown to localize as HA-wt-mEGFP in the PM, but in a dimeric form⁴⁰. The observed brightness of HA-TMD-mEGFP was significantly lower than that of HA-wt-mEGFP (Fig. 3b). After correcting for non-fluorescent FPs, we found an average normalized brightness of $\epsilon_{\text{HA-TMD-mEGFP}} = 1.82 \pm 0.07$, suggesting the presence of a large dimer fraction.

In summary, these results clearly demonstrate that a simple two-state model for FFS-derived brightness data correction allows precise quantification of the oligomeric state of proteins in living cells.

The mCherry variant “mCherry2” has a superior performance in FFS measurements, compared to other monomeric red fluorescent proteins. In order to extend brightness measurements to the investigation of hetero-interactions, FPs with spectral properties different from those of mEGFP are needed. Typically, red FPs are well suited for this task since spectral overlap with mEGFP is low, reducing the possibility of FRET or cross-talk. However, for the commonly used mCherry, we and others²⁸ observed a high fraction of non-fluorescent states, i.e. only ca. 40% of the proteins were fluorescent. In order to identify red FPs with higher p_f , we screened the more recently developed FPs mCherry2^{41,42}, mCardinal⁴³, mRuby3⁴⁴, mScarlet⁴⁵ and mScarlet-I⁴⁵. We performed bleaching and N&B measurements of monomers and homo-dimers, expressed in HEK 293T cells. Notably, we observed strong photobleaching for mRuby3, mScarlet and mScarlet-I (Fig. 4a, Table 1) compared to the other three tested FPs. Therefore, N&B measurements on these proteins were conducted

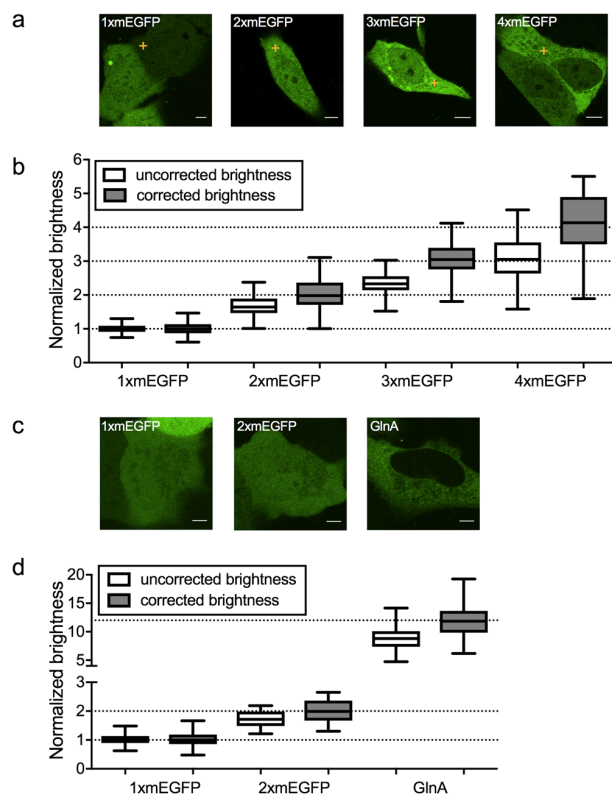


Figure 2. Brightness analysis of mEGFP homo-oligomers. (a) Representative intensity images of A549 cells expressing 1xmEGFP, 2xmEGFP, 3xmEGFP and 4xmEGFP, from left to right. Yellow crosses indicate the positions of the pFCS scan point. Scale bars are 5 μm . (b) Box plots of normalized molecular brightness obtained from pFCS analysis, pooled from at least three independent experiments (1xmEGFP: $n = 52$ cells, 2xmEGFP: $n = 42$ cells, 3xmEGFP: $n = 43$ cells, 4xmEGFP: $n = 59$ cells) before correction (white boxes) and after correction (grey boxes). First, a normalization of the uncorrected brightness data was performed using the median brightness value of 1xmEGFP. Second, a correction was performed as described in the Methods section, using a p_f of 0.65, as obtained from measurements of 2xmEGFP. (c) Representative intensity images of U2OS cells expressing 1xmEGFP, 2xmEGFP and GlnA-mEGFP (GlnA). Scale bars are 5 μm . (d) Box plots of normalized molecular brightness obtained from N&B analysis, pooled from three independent experiments (1xmEGFP: $n = 34$ cells, 2xmEGFP: $n = 35$ cells, GlnA: $n = 41$ cells) before correction (white boxes) and after correction (grey boxes). After normalization using the brightness value of 1xmEGFP, a correction was performed using a p_f of 0.72, as obtained from measurements of 2xmEGFP in U2OS cells.

at lower excitation powers. This reduces their effective brightness, e.g. only 1 kHz for mRuby3, compared to the theoretically three-fold higher brightness when interpolated to the same laser powers used for mCherry, mCherry2 and mCardinal (Fig. 4b). All other FPs exhibit minor difference in the effective brightness ranging from 1.5 kHz (mCherry2) to 2.2 kHz (mCardinal, mScarlet) in our experimental conditions. However, when comparing the normalized homo-dimer brightness, we found strong differences between mCherry2 and the other FPs. We estimated a p_f of 0.71 for mCherry2, which is ~ 1.8 -fold higher than that of mCherry ($p_f = 0.41$) and mScarlet ($p_f = 0.40$), while mCardinal and mRuby3 show very low p_f values of only 0.24 and 0.22, respectively. Notably, mScarlet-1 also features a high p_f ($p_f = 0.63$), but still suffers from considerable photobleaching, even at lower excitation powers (Fig. 4c, Table 1).

The superior performance of mCherry2 was confirmed in other cell types, as we consistently observed a reproducible difference from mCherry (Supplementary Figure S4). Moreover, we compared the homo-dimer brightness of mCherry2 at 23 $^{\circ}\text{C}$ and 37 $^{\circ}\text{C}$ and, similarly to mEGFP, observed only negligible variations (Supplementary Figure S4).

We therefore conclude that mCherry2 possesses cell type- and temperature-independent, superior properties in the context of FFS measurements, compared to all the other tested red FPs.

Quantification of hetero-interactions via fluorescence cross-correlation spectroscopy is improved by using mCherry2. Cross-correlation techniques (e.g. FCCS¹, ccN&B², RICCS³) are powerful methods for the investigation of protein hetero-interactions. These approaches are based on the analysis of simultaneous fluorescence fluctuations emitted by co-diffusing, spectrally distinct labeled molecules. In protein-protein interaction studies, fusion proteins with mEGFP and mCherry or RFP are typically used for this purpose^{1,2,6,46}.

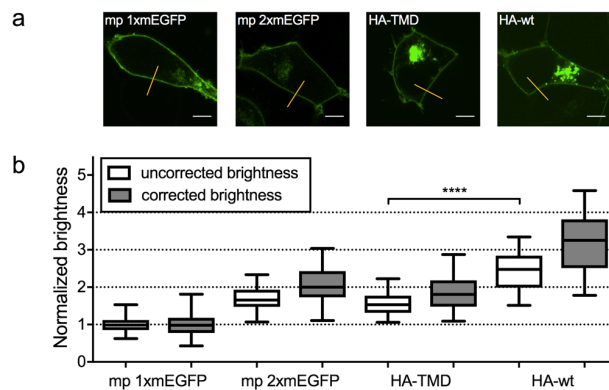


Figure 3. Oligomerization of Influenza A virus hemagglutinin measured with sFCS. **(a)** Representative intensity images of HEK 293T cells expressing mp 1xmEGFP, mp 2xmEGFP, HA-TMD-mEGFP (HA-TMD) and HA-wt-mEGFP (HA-wt), from left to right. Yellow lines indicate sFCS scan lines. Scale bars are 5 μ m. **(b)** Box plots of normalized molecular brightness obtained from sFCS analysis, pooled from at least three independent experiments (mp 1xmEGFP: $n = 55$ cells, mp 2xmEGFP: $n = 54$ cells, HA-TMD: $n = 37$ cells, HA-wt: $n = 36$ cells) before correction (white boxes) and after correction (grey boxes) with $p_t = 0.65$ obtained from mp 2xmEGFP measurements. ****Indicates significance with $p < 0.0001$, obtained by using a two-tailed t-test with Welch's correction.

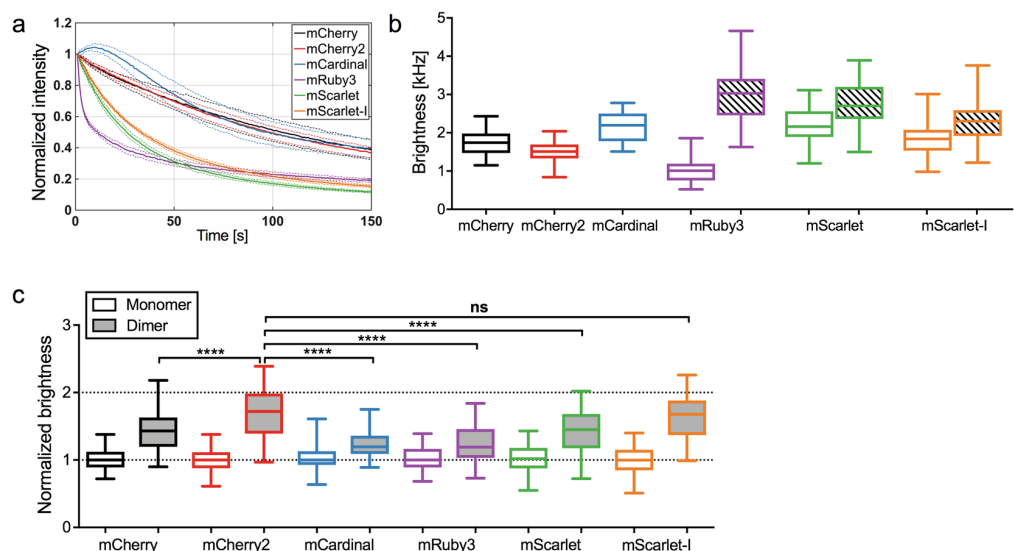


Figure 4. Comparison of different monomeric red FPs in bleaching and N&B measurements. **(a)** Bleaching curves of different red FPs (mCherry, mCherry2, mCardinal, mRuby3, mScarlet and mScarlet-I), expressed in HEK 293T cells, obtained in three independent N&B measurements of 18 cells each, with 19.6 μ W laser power (four-fold compared to standard N&B settings). Solid lines show average curves, dashed lines mean \pm SD. **(b)** Box plots of molecular brightness of different red FP monomers expressed in HEK 293T cells, measured with N&B at 4.9 μ W (mCherry, mCherry2, mCardinal), 3.9 μ W (mScarlet, mScarlet-I) or 1.6 μ W (mRuby3) laser power in three independent experiments (mCherry: $n = 51$ cells, mCherry2: $n = 49$ cells, mCardinal: $n = 32$ cells, mRuby3: $n = 33$ cells, mScarlet: $n = 36$ cells, mScarlet-I: $n = 34$ cells) (white boxes). The shaded boxes for mRuby3, mScarlet and mScarlet-I show brightness values interpolated to 4.9 μ W laser power, assuming a linear increase of the brightness with the excitation power. **(c)** Box plots of normalized molecular brightness of red FP monomers (white boxes) and homo-dimers (grey boxes). Data represent results of three independent experiments (1xmCherry: $n = 50$ cells, 2xmCherry: $n = 53$ cells, 1xmCherry2: $n = 49$ cells, 2xmCherry2: $n = 54$ cells, 1xmCardinal: $n = 42$ cells, 2xmCardinal: $n = 42$ cells, 1xmRuby3: $n = 33$ cells, 2xmRuby3: $n = 31$ cells, 1xmScarlet: $n = 36$ cells, 2xmScarlet: $n = 41$ cells, 1xmScarlet-I: $n = 34$ cells, 2xmScarlet-I: $n = 39$ cells). ****Indicates significance compared to mCherry2 with $p < 0.0001$, ns indicates no significance, obtained by using a one-way ANOVA multiple comparisons test.

FP	$t_{1/2}^*$ [s]	$t_{1/2,1\text{kHz}}^{**}$ [s]	$\epsilon_{\text{N\&B}}$ [kHz]	Bleaching _{N&B} [%]	ϵ^{***} [kHz]	p_f
mCherry	104 ± 23	708 ± 156	1.7	6.2	1.7	0.41
mCherry2	99 ± 13	596 ± 80	1.5	4.3	1.5	0.71
mCardinal	97 ± 25	852 ± 220	2.2	-3.5	2.2	0.24
mRuby3	12 ± 1 ⁻	148 ± 12	1.1	37.5	3.1	0.21
mScarlet	26 ± 2 ⁻	280 ± 20	2.2	31.7	2.7	0.40
mScarlet-I	34 ± 1 ⁻	328 ± 12	1.9	29.0	2.4	0.63

Table 1. Characteristics of all investigated monomeric red FPs. *Bleaching half-time ($t_{1/2}$) measured at four times higher laser power (19.6 μW) than used in N&B measurements. **Bleaching half-time ($t_{1/2,1\text{kHz}}$) obtained by normalizing the measured half time ($t_{1/2}$) for each FP to an initial brightness of 1 kHz/molecule in the bleaching experiment, using the determined molecular brightness ϵ of each FP at 4.9 μW . ***Average molecular brightness in N&B, interpolated to the same laser power (4.9 μW) for all red FPs. ⁻Experimental conditions differ from those used in the original studies (e.g. spinning disk microscopy vs. confocal microscopy, measurements in cells vs. measurements of purified proteins).

However, due to the presence of non-fluorescent states, only a fraction of protein hetero-complexes simultaneously emits fluorescence in both channels (i.e. many complexes will contain fluorescent green proteins and non-fluorescent red proteins). This factor has to be taken into account when calculating e.g. dissociation constants from cross-correlation data²⁸. Given the superior p_f of mCherry2 compared to other red FPs, we hypothesized that mCherry2 would improve the quantification of cross-correlation data, since more complete fluorescent protein complexes should be present. To test this hypothesis, we performed point FCCS (pFCCS) experiments with mCherry-mEGFP and mCherry2-mEGFP hetero-dimers in the cytoplasm of living A549 cells. As presumed, we observed a higher auto-correlation function (ACF) amplitude G in the red than in the green channel ($G_g/G_r = 0.65 \pm 0.03$, Fig. 5a,c) for mCherry-mEGFP, indicating that the apparent concentration of mCherry is ca. 1.5-fold lower than that of mEGFP (i.e. in a significant fraction of hetero-dimers, only mEGFP is fluorescent). This is in agreement with the expected relative amount of hetero-dimers containing fluorescent mEGFP and/or mCherry, based on the above-mentioned p_f values. Furthermore, we expect only ~27% of hetero-dimers to carry both fluorescent mEGFP and mCherry (SI related to Supplementary Figure S5).

For mCherry2-mEGFP in contrast, the amplitudes of the ACFs in the red and green channel were comparable ($G_g/G_r = 0.97 \pm 0.05$, Fig. 5b,c), indicating, as expected, similar apparent concentrations of mCherry2 and mEGFP (SI related to Supplementary Figure S5). Also, the relative amount of hetero-dimers carrying fluorescent mEGFP and mCherry2 is estimated to be ~42%, i.e. 1.5-fold more fully-fluorescent complexes than for mCherry-mEGFP. On the other hand, the expected cross-correlation values for mCherry- and mCherry2-mEGFP should be similar, which is confirmed by our data (Supplementary Figure S5). Nevertheless, the 1.5-fold higher relative fraction of fully-fluorescent hetero-dimers with mCherry2 should improve the quality of cross-correlation data. We therefore compared the signal-to-noise ratio (SNR) of the measured cross-correlation functions (CCFs) for mCherry- and mCherry2-mEGFP, and observed a ~40% higher SNR of mCherry2-mEGFP CCFs ($\text{SNR}_{\text{mCh-mEGFP}} = 1.39 \pm 0.10$, $\text{SNR}_{\text{mCh2-mEGFP}} = 1.93 \pm 0.10$; Fig. 5d).

These results demonstrate that using mCherry2 instead of mCherry in cross-correlation experiments leads to a more accurate quantification of the spectral cross-correlation, i.e. of the degree of binding in hetero-interactions or the mobility of hetero-complexes.

Discussion

In the last decade, FFS-based techniques have become widely used approaches to measure protein dynamics, interactions and oligomerization directly in living cells and organisms^{2,6,34,47-50}. One of the most important quantities in these studies is the molecular brightness, i.e. the photon count rate per molecule, which is used as a measure of oligomerization of fluorescently labelled proteins⁴.

In this work, we present a comprehensive analysis of FPs and their suitability for brightness-based oligomerization and cross-correlation-based interaction studies. Differently from previous reports^{4,5}, we consistently obtained lower than expected values for the normalized brightness of homo-dimers for the most common FPs (i.e. mEGFP, mEYFP and mCherry, Fig. 1a,b). We therefore performed a systematic comparison of frequently used FPs, including also several novel monomeric red FPs (i.e. mCherry2, mRuby3, mCardinal, mScarlet and mScarlet-I), under various conditions. To rule out systematic errors related to the experimental setup or FFS technique used, we performed a combination of pFCS, sFCS and N&B approaches on independent microscopy setups, obtaining reproducible results. Moreover, we excluded potential artefacts deriving from the specific expression system, by comparing different cellular compartments (cytoplasm, nucleus, PM), cell types (HEK 293T, A549, CHO, HeLa) and temperatures (23 °C, 37 °C), as shown in Fig. 1 and Supplementary Figure S1. By performing Fluorescence Lifetime Imaging Microscopy (FLIM) measurements of mEGFP (Supplementary Figure S2), we ruled out the presence of multiple brightness states that might decrease homo-dimer brightness values¹⁹, or energy transfer to non-fluorescent states of mEGFP homo-dimers, in agreement with previous studies¹⁵. Generally, we cannot rule out the possibility of homo-FRET between the same fluorescent states of homo-dimer subunits. However, as previously discussed, homo-FRET will not affect the brightness of FP homo-dimers¹⁹. We thus conclude that the observed brightness decrease of FP homo-dimers indicates the presence of a non-fluorescent protein fraction, independent of the experimental conditions. This conclusion is supported by previous reports discussing FP specific photophysical transitions (e.g. blinking, flickering, long-lived dark states)¹⁴⁻²⁰, maturation times²¹

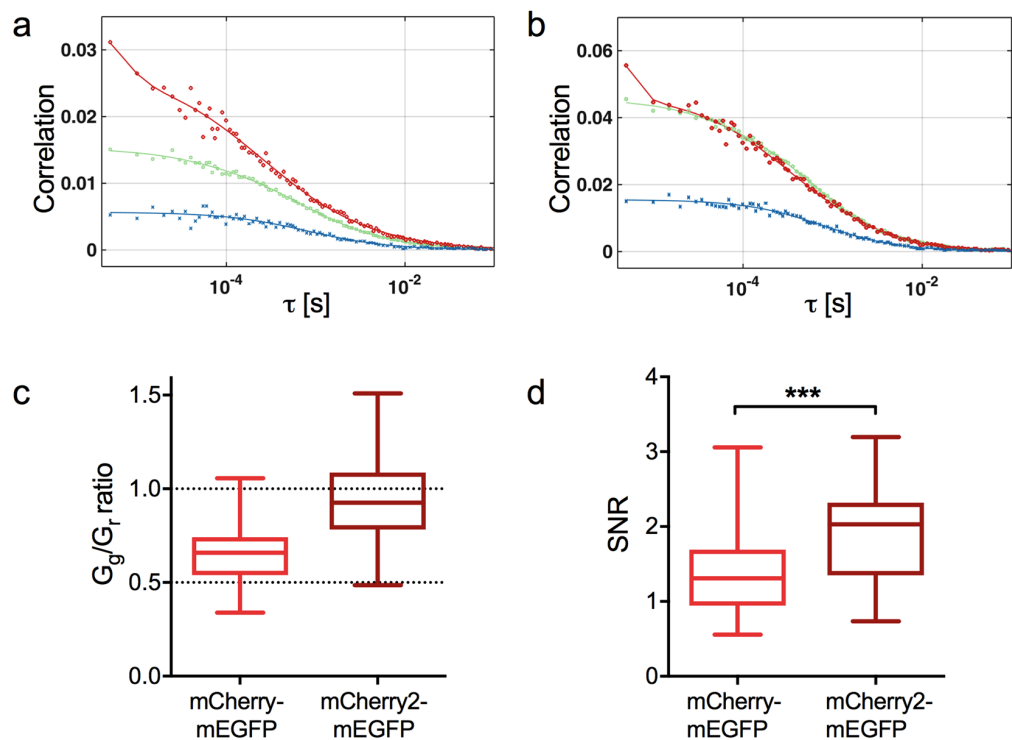


Figure 5. Cross-correlation measurements of mCherry-/mCherry2-mEGFP hetero-dimers. (a) and (b). Representative correlation functions and fit curves for pFCCS measurements of mCherry-mEGFP (a) and mCherry2-mEGFP (b) hetero-dimers expressed in A549 cells. Green, ACF in green channel (mEGFP); red, ACF in red channel (mCherry (a), mCherry2 (b)); blue, CCF calculated for both spectral channels. Fit curves (solid lines) were obtained from fitting a three-dimensional anomalous diffusion model to the data. (c) Box plots of amplitude ratios of the green to red ACFs for mCherry-mEGFP ($n = 35$ cells) and mCherry2-mEGFP ($n = 32$ cells) pooled from three independent experiments performed in A549 cells. (d) Box plots of SNR of the CCFs for mCherry-mEGFP and mCherry2-mEGFP hetero-dimers, calculated from pFCCS measurements in A549 cells, described in (c). ***Indicates significance with $p = 0.0003$, obtained by using a two-tailed t-test with Welch's correction.

and folding efficiencies²². For mEGFP, dark state fractions of 20–40% were reported *in vitro*, depending on pH and excitation power¹⁵. These values agree well with the 25–35% of non-fluorescent mEGFPs that we observed directly in living cells.

We next investigated how the presence of non-fluorescent states exactly affects brightness data of protein complexes of known oligomeric state. This information can then be used to correctly determine the oligomerization state of an unknown protein in general. To this aim, we measured the brightness of mEGFP homo-oligomers as well as two Influenza A virus HA protein variants of different oligomeric states: HA-wt and an HA-TMD mutant. Biochemical studies have shown that the latter proteins assemble as trimers and dimers, respectively^{38–40}. We observed a systematic underestimation of the brightness for all samples compared to the expected values (Figs 2, 3) and showed that a simple two-state model, determining the p_f for each FP from the homo-dimer brightness, successfully yields correct estimates of the oligomeric state. Since the assumption of a constant p_f obtained for 2xmEGFP reproduces the correct oligomeric state of higher oligomers, we conclude that folding efficiency and maturation are constant for each single FP subunit within a certain oligomer. In other words, it is sufficient to know the brightness of a FP monomer and homo-dimer, in order to quantify the oligomeric state of larger complexes. It is worth emphasizing that this procedure works well not only for mEGFP homo-oligomers, but also for large self-assembling protein complexes such as the 12-meric *E. Coli* GlnA³⁷, and transmembrane proteins such as the Influenza A virus HA. An equivalent correction approach was used before in single molecule subunit counting studies, albeit mostly restricted to (m)EGFP^{10,11,24}. Our results clearly show that a precise correction of the non-fluorescent FP fraction and knowledge of the p_f for all involved FPs are absolutely necessary for a correct quantification of protein oligomerization in FFS techniques. Ignoring non-fluorescent FPs leads to a strong misinterpretation of the data, e.g. a tetramer being classified as a trimer (Fig. 2). These systematic errors are particularly pronounced for FPs with a low p_f , as found e.g. for mCherry (~40%), a FP often used in the past to determine the stoichiometry of protein complexes^{2,51}. Moreover, FPs possessing low p_f severely suffer from low dynamic ranges, since the brightness increase per FP subunit is only marginal (Figs 1, 4), e.g. a mCherry tetramer would be only 2.2 times brighter than a monomer, and could be mistakenly identified as dimer. Nevertheless, contradictory results are reported in this context by studies employing FFS techniques. While very few studies confirm the presence of non-fluorescent mEGFP fractions²⁵, others report dimer brightness values of 2 (i.e. the absence of a

non-fluorescent FP fraction)^{4,5}. However, the latter studies were all performed with two-photon excitation, which may influence the transition to non-fluorescent states¹⁹. In this context, our data provide the first complete and systematic comparison of p_f for several FPs, in one-photon excitation setups.

In order to measure multiple species simultaneously, red or near-infrared FPs are required due to their spectral separation from mEGFP. Additionally, they are a preferential choice for tissue and animal imaging, due to reduced light absorption and autofluorescence in the red and far-red spectral region^{35,52}. Given the suboptimal p_f we determined for mCherry, we screened several recently developed monomeric red FPs^{41,43–45}. The p_f is in fact an essential parameter that, until now, has not received appropriate attention in reports of new FPs.

The suitability of FPs for FFS studies depends on three important fluorophore characteristics: (1) a high photostability is required to enable temporal measurements under continuous illumination, (2) a high molecular brightness is needed to obtain a SNR sufficient to detect single-molecule fluctuations, (3) a high p_f is essential for a maximal dynamic range that allows reliable oligomerization measurements. Thus, red FPs which fulfil only one or two of these requirements are not recommended for FFS measurements. Among all red FPs investigated in this study, we found only one fulfilling all three important criteria: mCherry2, a rarely used mCherry variant^{41,42} that has not been entirely characterized yet. However, for the remaining red FPs tested here, we found either low photostability albeit high monomer brightness (mRuby3, mScarlet, mScarlet-I; Fig. 4a,b), and/or low to medium p_f of 20–45% (mCardinal, mCherry, mRuby3, mScarlet; Fig. 4c), very similar to previously published values for mRFP^{27,28} and mCherry²⁸. In contrast, mCherry2 possesses a high p_f of ~70%. Very recent studies of FP maturation times report a faster maturation of mCherry2 and mScarlet-I compared to mCherry/mScarlet²¹. Together with our findings, this indicates that faster FP maturation could be the reason for the observed higher p_f .

Finally, we demonstrate that quantification of hetero-interactions via cross-correlation approaches, so far typically performed with mCherry^{1,2,46}, can be substantially improved by using mCherry2 instead. In agreement with the reported similar p_f of mEGFP and mCherry2 (Figs 1, 4), we observed that the amount of hetero-dimers containing both fluorescent mEGFP and mCherry2 increased significantly compared to those containing mCherry. For this reason, the CCF signal-to-noise ratio for mCherry2-mEGFP complexes increased by 40% compared to that measured for mCherry-mEGFP hetero-dimers (Fig. 5d). This could be particularly relevant for investigations of weak interactions, in which only a small number of hetero-complexes is present, compared to the vast amount of non-interacting molecules. Additionally, cross-correlation techniques have been recently applied in living multicellular organisms^{6,34}, which require low illumination to avoid phototoxicity and thus generally suffer from low SNRs. Therefore, we recommend using mCherry2 as the novel standard red FP in brightness and cross-correlation measurements.

In conclusion, this study provides a useful, comprehensive resource for applying FFS techniques to quantify protein oligomerization and interactions. We provide a clear, simple methodology to test and correct for the presence of non-fluorescent states, and argue that such controls should become a prerequisite in brightness-based FFS studies to avoid systematic errors in the quantification of protein oligomerization. Finally, our results suggest that the apparent fluorescence probability is an important fluorophore characteristic that should be considered and reported when developing new FPs and we provide a simple assay to determine this quantity.

Methods

Cell culture. Human embryonic kidney (HEK) cells from the 293T line (purchased from ATCC[®], CRL-3216[™]), human epithelial lung cells A549 (ATCC[®], CCL-185[™]), chinese hamster ovary (CHO) cells from the K1 line (ATCC[®], CCL-61[™]), human epithelial cervix cells HeLa (ATCC[®], CCL-2[™]) and human bone osteosarcoma epithelial cells U2OS (a kind gift from Ana García Sáez, University of Tübingen) were cultured in Dulbecco's modified Eagle medium (DMEM) with the addition of fetal bovine serum (10%) and L-Glutamine (4 mM). Cells were passaged every 3–5 days, no more than 15 times. All solutions, buffers and media used for cell culture were purchased from PAN-Biotech (Aidenbach, Germany).

Fluorescent protein constructs. A detailed description of the cloning procedure of all constructs is available in the Supplementary Information.

All plasmids generated in this work will be made available on Addgene.

Preparation for Microscopy Experiments. For microscopy experiments, 6×10^5 (HEK) or 4×10^5 (A549, CHO, HeLa, U2OS) cells were seeded in 35 mm dishes (CellVis, Mountain View, CA or MatTek Corp., Ashland, MA) with optical glass bottom, 24 h before transfection. HEK 293T cells were preferred for sFCS measurements since they are sufficiently thick and therefore ideal for sFCS based data acquisition perpendicular to the PM. A549 cells are rather flat and characterized by a large cytoplasmic volume that is more suitable for pFCS measurements in the cytoplasm. Cells were transfected 16–24 h prior to the experiment using between 200 ng and 1 μ g plasmid per dish with Turbofect (HEK, HeLa, CHO) or Lipofectamin3000 (A549, U2OS) according to the manufacturer's instructions (Thermo Fisher Scientific). Briefly, plasmids were incubated for 20 min with 3 μ l Turbofect diluted in 50 μ l serum-free medium, or 15 min with 4 μ l P3000 per 1 μ g plasmid and 2 μ l Lipofectamin3000 diluted in 100 μ l serum-free medium, and then added dropwise to the cells.

Confocal Microscopy System. Confocal imaging and pF(C)CS measurements were performed on an Olympus FluoView FV-1000 system (Olympus, Tokyo, Japan) using a 60x, 1.2NA water immersion objective. sFCS and N&B measurements were performed on a Zeiss LSM780 system (Carl Zeiss, Oberkochen, Germany) using a 40x, 1.2NA water immersion objective. Samples were excited with a 488 nm Argon laser (mEGFP, mEYFP) and a 561 nm (Zeiss instrument) or 559 nm (Olympus) diode laser (mCherry, mCherry2, mCardinal, mRuby3, mScarlet, mScarlet-I). For measurements with 488 nm excitation, fluorescence was detected between 500 and 600 nm, after passing through a 488 nm dichroic mirror, using SPAD (PicoQuant, Berlin, Germany,

mounted on Olympus instrument) or GaAsP (Zeiss instrument) detectors. For 561 nm or 559 nm excitation, fluorescence emission passed through a 488/561 nm (Zeiss) or 405/488/559/635 nm (Olympus) dichroic mirror and was detected between 570 and 695 nm (Zeiss) or using a 635 nm long-pass filter (Olympus). For pFCCS measurements, fluorophores were excited using 488 nm and 559 nm laser lines. Excitation and detection light were separated using a 405/488/559/635 nm dichroic mirror. Fluorescence was separated on two SPAD detectors using a 570 nm dichroic mirror and detected after passing through a 520/35 nm bandpass filter (mEGFP channel) or a 635 nm long-pass filter (mCherry or mCherry2 channel) to minimize cross-talk.

Fluorescence (Cross-) Correlation Spectroscopy. Point F(C)CS measurements were routinely performed for 90 s and recorded using the SymPhoTime64 software (PicoQuant GmbH, Berlin, Germany). Laser powers were adjusted to keep photobleaching below 20%. Typical values were $\sim 3.3 \mu\text{W}$ (488 nm) and $\sim 6 \mu\text{W}$ (559 nm). The size of the confocal pinhole was set to 90 μm . PicoQuant ptu-files containing recorded photon arrival times were converted to intensity time series and subsequently analysed using a custom-written MATLAB Code (The MathWorks, Natick, MA, USA). First, the intensity time series was binned in 5 μs intervals. To correct for signal decrease due to photobleaching, the fluorescence time series was fitted with a two-component exponential function, and a correction was applied⁵³. Then, ACFs and, in case of two-colour experiments (g = green channel, r = red channel), CCFs were calculated as follows, using a multiple tau algorithm:

$$G_i(\tau) = \frac{\langle \delta F_i(t) \delta F_i(t + \tau) \rangle}{\langle F_i(t)^2 \rangle},$$

$$G_{\text{cross}}(\tau) = \frac{\langle \delta F_g(t) \delta F_r(t + \tau) \rangle}{\langle F_g(t) \rangle \langle F_r(t) \rangle},$$

where $\delta F_i = F_i(t) - \langle F_i(t) \rangle$ and $i = g, r$.

To avoid artefacts caused by long-term instabilities or single bright events, CFs were calculated segment-wise (10 segments) and then averaged. Segments showing clear distortions were manually removed from the analysis.

A model for anomalous three-dimensional diffusion and a Gaussian confocal volume geometry was fitted to the ACFs⁵⁴:

$$G(\tau) = \frac{1}{N} \left(1 + \frac{T}{1-T} e^{-\frac{\tau}{\tau_b}} \right) \left(1 + \left(\frac{\tau}{\tau_d} \right)^\alpha \right)^{-1} \left(1 + \frac{1}{S^2} \left(\frac{\tau}{\tau_d} \right)^\alpha \right)^{-1/2},$$

where the exponential term accounts for photophysical transitions of a fraction T of fluorescent proteins. The parameter τ_b was constrained to values lower than 50 μs for mEGFP¹⁴ or mEYFP¹⁸ and 200 μs for mCherry/mCherry2²⁰. The anomaly parameter α was introduced to account for anomalous subdiffusion of proteins in the cytoplasm⁵⁴ and constrained to values between 0.5 and 1. The particle number N and diffusion time τ_d were obtained from the fit. To calibrate the focal volume, pFCS measurements with Alexa Fluor[®] 488 or Rhodamine B dissolved in water at 50 nM were performed at the same laser power. The structure parameter S was fixed to the value determined in the calibration measurement (typically around 4 to 8). The molecular brightness was calculated by dividing the mean count rate by the particle number determined from the fit.

For two-colour measurements, all ACFs were used to fit the diffusion model described above. Relative cross-correlation values were calculated from the amplitudes of ACFs and CCFs:

$$\max \left\{ \frac{G_{\text{cross}}(0)}{G_g(0)}, \frac{G_{\text{cross}}(0)}{G_r(0)} \right\},$$

where $G_{\text{cross}}(0)$ is the amplitude of the CCF and $G_i(0)$ is the amplitude of the ACF in the i -th channel. The SNR of the CCFs was calculated by summing the cross-correlation values divided by their variance over all points of the CCF. The variance of each point of the CCF was calculated by the multiple tau algorithm⁵⁵.

Scanning Fluorescence Correlation Spectroscopy. For sFCS measurements, a line scan of 128×1 pixels (pixel size 160 nm) was performed perpendicular to the membrane with 472.73 μs scan time. Typically, 250,000–500,000 lines were acquired (total scan time 2 to 4 min) in photon counting mode. Laser powers were adjusted to keep photobleaching below 20%. Typical values were $\sim 1.8 \mu\text{W}$ (488 nm) and $\sim 6 \mu\text{W}$ (561 nm). Scanning data were exported as TIFF files, imported and analysed in MATLAB (The MathWorks, Natick, MA) using custom-written code. sFCS analysis follows the procedure described previously^{50,56}. Briefly, all lines were aligned as kymographs and divided in blocks of 1000 lines. In each block, lines were summed up column-wise and the x position with maximum fluorescence was determined. This position defines the membrane position in each block and is used to align all lines to a common origin. Then, all aligned line scans were averaged over time and fitted with a Gaussian function. The pixels corresponding to the membrane were defined as pixels which are within $\pm 2.5\sigma$ of the peak. In each line, these pixels were integrated, providing the membrane fluorescence time series $F(t)$. When needed, a background correction was applied by subtracting the average pixel fluorescence value on the inner side of the membrane multiplied by 2.5σ (in pixel units) from the membrane fluorescence, in blocks of 1000 lines⁴⁶. In order to correct for depletion due to photobleaching, the fluorescence time series was fitted with a two-component exponential function and a correction was applied⁵³. Finally, the ACF was calculated as described above.

A model for two-dimensional diffusion in the membrane and a Gaussian focal volume geometry⁵⁶ was fitted to the ACF:

$$G(\tau) = \frac{1}{N} \left(1 + \frac{\tau}{\tau_d} \right)^{-1/2} \left(1 + \frac{\tau}{\tau_d S^2} \right)^{-1/2}$$

The focal volume calibration was performed as described for pF(C)CS. Diffusion coefficients (D) were calculated using the calibrated waist of the focal volume, $D = \omega_0^2/4\tau_d$. The molecular brightness was calculated by dividing the mean count rate by the particle number determined from the fit: $B = \frac{\langle F(t) \rangle}{N}$.

Number and Brightness Analysis. N&B experiments were performed as previously described⁵⁷, with a modified acquisition mode. Briefly, 200 images of 128×64 – 128 pixels were acquired per measurement, using a 300 nm pixel size and 25 μ s pixel dwell time. Laser powers were maintained low enough to keep bleaching below 10% of the initial fluorescence signal (typically $\sim 0.7 \mu$ W for 488 nm and $\sim 4.9 \mu$ W for 561 nm) except for mRuby3 and mScarlet/ mScarlet-I. CZI image output files were imported in MATLAB using the Bioformats package⁵⁸ and analysed using a custom-written script. Before further analysis, pixels corresponding to cell cytoplasm or nucleus were selected manually as region of interest. Brightness values were calculated as described⁷, applying a boxcar algorithm to filter extraneous long-lived fluctuations^{59,60}. Pixels with count rates above 2 MHz were excluded from the analysis to avoid pile-up effects. To further calibrate the detector response, we measured the brightness on a reflective metal surface and dried dye solutions for all laser lines. The thus obtained brightness-versus-intensity plots (which should be constant and equal to 0 for all intensity values⁷) were used to correct the actual experimental data.

Fluorescence Lifetime Imaging Microscopy. FLIM measurements were performed on an Olympus FluoView FV-1000 system (Olympus, Tokyo, Japan) equipped with a time-resolved LSM upgrade (PicoQuant GmbH, Berlin, Germany) using a 60X, 1.2NA water immersion objective. Images of 512×512 pixels per frame were acquired after excitation with a pulsed-laser diode at 488 nm. Fluorescence was detected using a SPAD detector and a 520/35 nm bandpass filter. In each measurement, a minimum of 10^5 photons were recorded by accumulation of 60 frames over a time period of 90 s. Regions of interest in the cytoplasm of cells were analysed using SymPhoTime64 software (PicoQuant GmbH, Berlin, Germany) taking into account the instrument response function determined by measuring a saturated Erythrosine B solution according to manufacturer's instructions. Resulting decay curves were fitted using a mono-exponential function.

Brightness calibration and fluorophore maturation. The molecular brightness, i.e. the photon count rate per molecule, serves as a measure for the oligomeric state of protein complexes. This quantity is affected by the presence of non-fluorescent FP fractions, which can result from several processes: (1) Photophysical processes such as long-lived dark states, blinking or flickering between an *on* and *off* state, (2) FP maturation, i.e. FPs that have not matured yet, (3) Incorrectly folded FPs. To quantify the amount of non-fluorescent FPs, we consider all these processes together in a single parameter, the apparent fluorescence probability (p_f), i.e. the probability of a FP to emit a fluorescence signal. The fluorescence emitted by an oligomer can then be modelled with a binomial distribution, assuming that each fluorophore monomer emits photons with brightness ε and with a probability p_f . The probability of detecting a brightness value $i\varepsilon$ for an n -mer is thus $p_i = \binom{n}{i} p_f^i (1 - p_f)^{n-i}$. Hence, the ensemble-averaged brightness detected from a number of N n -mers is:

$$\begin{aligned} \varepsilon_n &= \frac{\sum_{i=1}^n (i\varepsilon)^2 N_i}{\sum_{i=1}^n i\varepsilon N_i} \\ &= \frac{\sum_{i=1}^n (i\varepsilon)^2 N \binom{n}{i} p_f^i (1 - p_f)^{n-i}}{\sum_{i=1}^n i\varepsilon N \binom{n}{i} p_f^i (1 - p_f)^{n-i}} \\ &= \varepsilon \frac{np_f (1 - p_f) + n^2 p_f^2}{np_f} \\ &= \varepsilon + \varepsilon(n - 1)p_f \end{aligned}$$

In the analysis, we normalized all brightness values to the median brightness of the corresponding monomer sample measured under the same conditions: $\varepsilon_{n, norm} = \frac{\varepsilon_n}{\varepsilon} = 1 + (n - 1)p_f$. We used the median of the normalized homo-dimer brightness to determine the probability p_f for each construct, $p_f = \varepsilon_{2, norm} - 1$. We can now invert the equation for the n -mer brightness to calculate the true oligomeric state, i.e. the brightness if all subunits were constantly fluorescent, from the measured brightness ε_n : $n = 1 + \frac{\varepsilon_{n, norm} - 1}{p_f}$.

We applied this transformation to every brightness data point and obtained the “corrected” brightness. Notably, this transformation holds true also for fluorophores which have two brightness states rather than an *on* and *off* state¹⁹.

Statistical analysis. All data are displayed as box plots indicating the median values and whiskers ranging from minimum to maximum values. Quantities in the main text are given as mean \pm SEM. Sample sizes and

p-values are given in figure captions. Statistical significance was tested using GraphPad Prism 7.0 (GraphPad Software). The one-way ANOVA analysis for comparison of red FPs (Fig. 4b) gave $F(11, 492) = 46.58$ and was followed by the Bonferroni's multiple comparisons test. Brightness differences between HA-wt and HA-TMD (Fig. 3b) as well as SNR of hetero-dimer complexes in FCCS analysis (Fig. 5d) were analysed using a two-tailed t-test with Welch's correction giving Welch-corrected $t = 9.41$, $df = 60.57$ and Welch-corrected $t = 3.84$, $df = 67$, respectively.

Code availability. MATLAB custom-written code is available upon request from the corresponding author.

Data availability. The datasets analysed during the current study are available from the corresponding author on reasonable request.

References

- Bacia, K., Kim, S. A. & Schwille, P. Fluorescence cross-correlation spectroscopy in living cells. *Nat. Methods* **3**, 83–89 (2006).
- Digman, M. A., Wiseman, P. W., Choi, C., Horwitz, A. R. & Gratton, E. Stoichiometry of molecular complexes at adhesions in living cells. *Proc. Natl. Acad. Sci. USA* **106**, 2170–2175 (2009).
- Digman, M. A., Wiseman, P. W., Horwitz, A. R. & Gratton, E. Detecting protein complexes in living cells from laser scanning confocal image sequences by the cross correlation raster image spectroscopy method. *Biophys. J.* **96**, 707–16 (2009).
- Chen, Y., Wei, L.-N. & Müller, J. D. Probing protein oligomerization in living cells with fluorescence fluctuation spectroscopy. *Proc. Natl. Acad. Sci. USA* **100**, 15492–7 (2003).
- Chen, Y., Johnson, J., Macdonald, P., Wu, B. & Mueller, J. D. Observing Protein Interactions and Their Stoichiometry in Living Cells by Brightness Analysis of Fluorescence Fluctuation Experiments. in: *Methods in enzymology* **472**, 345–363 (2010).
- Ries, J., Yu, S. R., Burkhardt, M., Brand, M. & Schwille, P. Modular scanning FCS quantifies receptor-ligand interactions in living multicellular organisms. *Nat. Methods* **6**, (2009).
- Digman, M. A., Dalal, R., Horwitz, A. F. & Gratton, E. Mapping the number of molecules and brightness in the laser scanning microscope. *Biophys. J.* **94**, 2320–2332 (2008).
- Elson, E. L. & Magde, D. Fluorescence correlation spectroscopy. I. Conceptual basis and theory. *Biopolymers* **13**, 1–27 (1974).
- Chen, Y., Müller, J. D., So, P. T. & Gratton, E. The photon counting histogram in fluorescence fluctuation spectroscopy. *Biophys. J.* **77**, 553–67 (1999).
- Arant, R. J. & Ulbrich, M. H. Deciphering the Subunit Composition of Multimeric Proteins by Counting Photobleaching Steps. *ChemPhysChem* **15**, 600–605 (2014).
- Ulbrich, M. H. & Isacoff, E. Y. Subunit counting in membrane-bound proteins. *Nat. Methods* **4**, 319–321 (2007).
- Kenworthy, A. K. Imaging Protein-Protein Interactions Using Fluorescence Resonance Energy Transfer Microscopy. *Methods* **24**, 289–296 (2001).
- Kerppola, T. K. Bimolecular fluorescence complementation (BiFC) analysis as a probe of protein interactions in living cells. *Annu. Rev. Biophys.* **37**, 465–87 (2008).
- Haupts, U., Maiti, S., Schwille, P. & Webb, W. W. Dynamics of fluorescence fluctuations in green fluorescent protein observed by fluorescence correlation spectroscopy. *Proc. Natl. Acad. Sci. USA* **95**, 13573–8 (1998).
- Vámosi, G. *et al.* EGFP oligomers as natural fluorescence and hydrodynamic standards. *Sci. Rep.* **6**, 33022 (2016).
- Schenk, A., Ivanchenko, S., Röcker, C., Wiedenmann, J. & Nienhaus, G. U. Photodynamics of red fluorescent proteins studied by fluorescence correlation spectroscopy. *Biophys. J.* **86**, 384–94 (2004).
- Widengren, J., Mets, Ü. & Rigler, R. Photodynamic properties of green fluorescent proteins investigated by fluorescence correlation spectroscopy. *Chem. Phys.* **250**, 171–186 (1999).
- Schwille, P., Kummer, S., Heikal, A. A., Moerner, W. E. & Webb, W. W. Fluorescence correlation spectroscopy reveals fast optical excitation-driven intramolecular dynamics of yellow fluorescent proteins. *Proc. Natl. Acad. Sci. USA* **97**, 151–6 (2000).
- Wu, B., Chen, Y. & Müller, J. D. Fluorescence Fluctuation Spectroscopy of mCherry in Living Cells. *Biophys. J.* **96**, 2391–2404 (2009).
- Hendrix, J., Flors, C., Dedecker, P., Hofkens, J. & Engelborghs, Y. Dark states in monomeric red fluorescent proteins studied by fluorescence correlation and single molecule spectroscopy. *Biophys. J.* **94**, 4103–13 (2008).
- Balleza, E., Kim, J. M. & Cluzel, P. Systematic characterization of maturation time of fluorescent proteins in living cells. *Nat. Methods* **15**, 47–51 (2017).
- Pédélecq, J.-D., Cabantous, S., Tran, T., Terwilliger, T. C. & Waldo, G. S. Engineering and characterization of a superfolder green fluorescent protein. *Nat. Biotechnol.* **24**, 79–88 (2006).
- McGuire, H., Aurousseau, M. R. P., Bowie, D. & Bluncks, R. Automating single subunit counting of membrane proteins in mammalian cells. *J. Biol. Chem.* **287**, 35912–35921 (2012).
- Liebsch, F. *et al.* Full-length cellular β -secretase has a trimeric subunit stoichiometry, and its sulfur-rich transmembrane interaction site modulates cytosolic copper compartmentalization. *J. Biol. Chem.* **292**, 13258–13270 (2017).
- Godin, A. G. *et al.* Spatial Intensity Distribution Analysis Reveals Abnormal Oligomerization of Proteins in Single Cells. *Biophys. J.* **109**, 710–721 (2015).
- Slaughter, B. D., Huff, J. M., Wiegraabe, W., Schwartz, J. W. & Li, R. SAM Domain-Based Protein Oligomerization Observed by Live-Cell Fluorescence Fluctuation Spectroscopy. *PLoS One* **3**, e1931 (2008).
- Hillesheim, L. N., Chen, Y. & Müller, J. D. Dual-Color Photon Counting Histogram Analysis of mRFP1 and EGFP in Living Cells. *Biophys. J.* **91**, 4273–4284 (2006).
- Foo, Y. H., Naredi-Rainer, N., Lamb, D. C., Ahmed, S. & Wohland, T. Factors affecting the quantification of biomolecular interactions by fluorescence cross-correlation spectroscopy. *Biophys. J.* **102**, 1174–83 (2012).
- Fricke, F., Beaudouin, J., Eils, R. & Heilemann, M. One, two or three? Probing the stoichiometry of membrane proteins by single-molecule localization microscopy. *Sci. Rep.* **5**, 14072 (2015).
- Hoppe, A. D., Scott, B. L., Welliver, T. P., Straight, S. W. & Swanson, J. A. N-Way FRET Microscopy of Multiple Protein-Protein Interactions in Live Cells. *PLoS One* **8**, e64760 (2013).
- Shyu, Y. J., Suarez, C. D. & Hu, C.-D. Visualization of ternary complexes in living cells by using a BiFC-based FRET assay. *Nat. Protoc.* **3**, 1693–1702 (2008).
- Chen, M. *et al.* Three-Fragment Fluorescence Complementation Coupled with Photoactivated Localization Microscopy for Nanoscale Imaging of Ternary Complexes. *ACS Nano* **10**, 8482–8490 (2016).
- Schwille, P., Meyer-Almes, F. J. & Rigler, R. Dual-color fluorescence cross-correlation spectroscopy for multicomponent diffusional analysis in solution. *Biophys. J.* **72**, 1878–1886 (1997).
- Zhao, Z. W. *et al.* Quantifying transcription factor–DNA binding in single cells *in vivo* with photoactivatable fluorescence correlation spectroscopy. *Nat. Protoc.* **12**, 1458–1471 (2017).
- Cranfill, P. J. *et al.* Quantitative assessment of fluorescent proteins. *Nat. Methods* **13**, 557–562 (2016).
- Hur, K.-H. *et al.* Quantitative measurement of brightness from living cells in the presence of photodepletion. *PLoS One* **9**, e97440 (2014).

37. Finan, K., Raulf, A. & Heilemann, M. A Set of Homo-Oligomeric Standards Allows Accurate Protein Counting. *Angew. Chemie Int. Ed.* **54**, 12049–12052 (2015).
38. Wilson, I. A., Skehel, J. J. & Wiley, D. C. Structure of the haemagglutinin membrane glycoprotein of influenza virus at 3 Å resolution. *Nature* **289**, 366–373 (1981).
39. Copeland, C. S., Doms, R. W., Bolzau, E. M., Webster, R. G. & Helenius, A. Assembly of influenza hemagglutinin trimers and its role in intracellular transport. *J. Cell Biol.* **103**, 1179–91 (1986).
40. Scolari, S. *et al.* Lateral distribution of the transmembrane domain of influenza virus hemagglutinin revealed by time-resolved fluorescence imaging. *J. Biol. Chem.* **284**, 15708–16 (2009).
41. Shen, Y., Chen, Y., Wu, J., Shaner, N. C. & Campbell, R. E. Engineering of mCherry variants with long Stokes shift, red-shifted fluorescence, and low cytotoxicity. *PLoS One* **12**, e0171257 (2017).
42. Ai, H., Shaner, N. C., Cheng, Z., Tsien, R. Y. & Campbell, R. E. Exploration of New Chromophore Structures Leads to the Identification of Improved Blue Fluorescent Proteins. *Biochemistry* **46**, 5904–5910 (2007).
43. Chu, J. *et al.* Non-invasive intravital imaging of cellular differentiation with a bright red-excitable fluorescent protein. *Nat. Methods* **11**, 572–578 (2014).
44. Bajar, B. T. *et al.* Improving brightness and photostability of green and red fluorescent proteins for live cell imaging and FRET reporting. *Sci. Rep.* **6**, 20889 (2016).
45. Bindels, D. S. *et al.* mScarlet: a bright monomeric red fluorescent protein for cellular imaging. *Nat. Methods* **14**, 53–56 (2017).
46. Dörlich, R. M. *et al.* Dual-color dual-focus line-scanning FCS for quantitative analysis of receptor-ligand interactions in living specimens. *Sci. Rep.* **5**, 10149 (2015).
47. Nagy, P., Claus, J., Jovin, T. M. & Arndt-Jovin, D. J. Distribution of resting and ligand-bound ErbB1 and ErbB2 receptor tyrosine kinases in living cells using number and brightness analysis. *Proc. Natl. Acad. Sci. USA* **107**, 16524–16529 (2010).
48. Hendrix, J. *et al.* Live-cell observation of cytosolic HIV-1 assembly onset reveals RNA-interacting Gag oligomers. *J. Cell Biol.* **210**, 629–46 (2015).
49. Bobone, S. *et al.* Phosphatidylserine Lateral Organization Influences the Interaction of Influenza Virus Matrix Protein 1 with Lipid Membranes. *J. Virol.* **91**, e00267–17 (2017).
50. Dunsing, V., Mayer, M., Liebsch, F., Multhaup, G. & Chiantia, S. Direct evidence of amyloid precursor-like protein 1 trans interactions in cell-cell adhesion platforms investigated via fluorescence fluctuation spectroscopy. *Mol. Biol. Cell* **28**, 3609–3620 (2017).
51. Choi, C. K., Zareno, J., Digman, M. A., Gratton, E. & Horwitz, A. R. Cross-correlated fluctuation analysis reveals phosphorylation-regulated paxillin-FAK complexes in nascent adhesions. *Biophys. J.* **100**, 583–92 (2011).
52. Shcherbakova, D. M. & Verkhusha, V. V. Near-infrared fluorescent proteins for multicolor *in vivo* imaging. *Nat. Methods* **10**, 751–754 (2013).
53. Ries, J., Chiantia, S. & Schwille, P. Accurate Determination of Membrane Dynamics with Line-Scan FCS. *Biophys. J.* **96**, 1999–2008 (2009).
54. Weiss, M., Elsner, M., Kartberg, F. & Nilsson, T. Anomalous subdiffusion is a measure for cytoplasmic crowding in living cells. *Biophys. J.* **87**, 3518–3524 (2004).
55. Wohland, T., Rigler, R. & Vogel, H. The standard deviation in fluorescence correlation spectroscopy. *Biophys. J.* **80**, 2987–99 (2001).
56. Ries, J. & Schwille, P. Studying Slow Membrane Dynamics with Continuous Wave Scanning Fluorescence Correlation Spectroscopy. *Biophys. J.* **91**, 1915–1924 (2006).
57. Digman, M. A., Dalal, R., Horwitz, A. F. & Gratton, E. Mapping the number of molecules and brightness in the laser scanning microscope. *Biophys. J.* **94**, 2320–2332 (2008).
58. Linkert, M. *et al.* Metadata matters: access to image data in the real world. *J. Cell Biol.* **189**, 777–782 (2010).
59. Hellriegel, C., Caiolfa, V. R., Corti, V., Sidenius, N. & Zamai, M. Number and brightness image analysis reveals ATF-induced dimerization kinetics of uPAR in the cell membrane. *FASEB J.* **25**, 2883–2897 (2011).
60. Mayer, M. C. *et al.* Amyloid precursor-like protein 1 (APLP1) exhibits stronger zinc-dependent neuronal adhesion than amyloid precursor protein and APLP2. *J. Neurochem.* **137**, 266–276 (2016).

Acknowledgements

This work was supported by the Deutsche Forschungsgemeinschaft (DFG) grants (254850309 to S.C. and SFB 740, TP C3 to A.H.).

Author Contributions


V.D., M.L. and S.C. conceived the study. V.D., M.L., B.Z. and R.A.P. performed experiments. V.D., M.L. and B.Z. analysed data. V.D., M.L., A.H. and S.C. wrote the manuscript with critical revisions by B.Z. and R.A.P.

Additional Information

Supplementary information accompanies this paper at <https://doi.org/10.1038/s41598-018-28858-0>.

Competing Interests: The authors declare no competing interests.

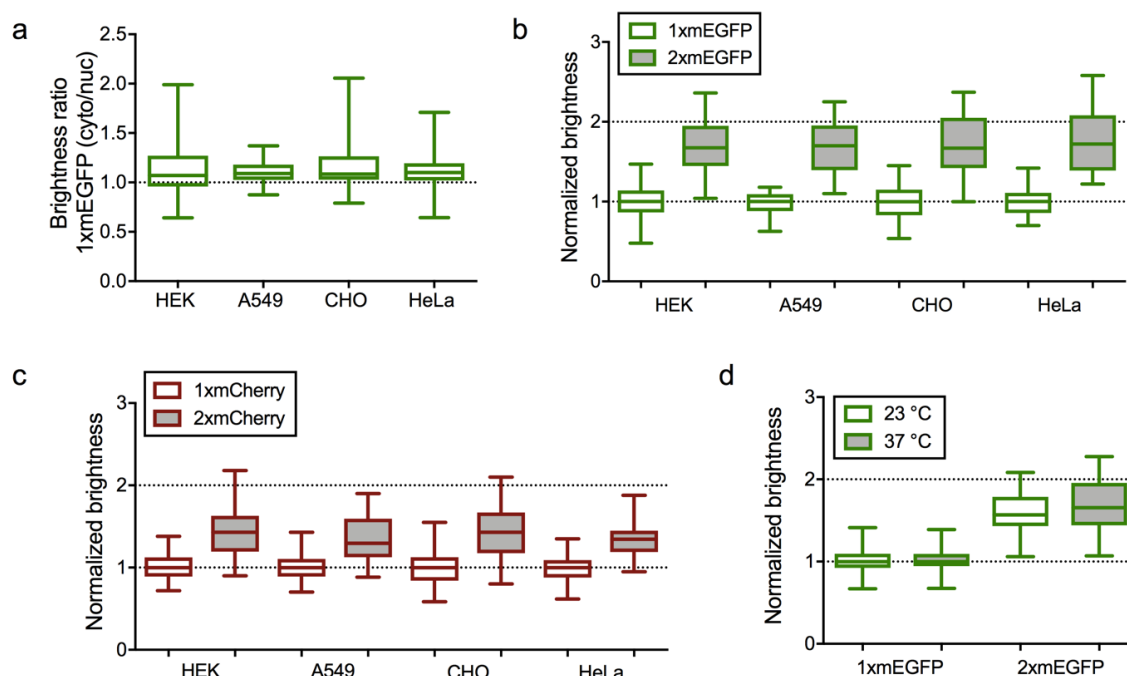
Publisher's note: Springer Nature remains neutral with regard to jurisdictional claims in published maps and institutional affiliations.

 **Open Access** This article is licensed under a Creative Commons Attribution 4.0 International License, which permits use, sharing, adaptation, distribution and reproduction in any medium or format, as long as you give appropriate credit to the original author(s) and the source, provide a link to the Creative Commons license, and indicate if changes were made. The images or other third party material in this article are included in the article's Creative Commons license, unless indicated otherwise in a credit line to the material. If material is not included in the article's Creative Commons license and your intended use is not permitted by statutory regulation or exceeds the permitted use, you will need to obtain permission directly from the copyright holder. To view a copy of this license, visit <http://creativecommons.org/licenses/by/4.0/>.

© The Author(s) 2018

Supplementary Material

Brightness analysis in different cell types and at different temperatures



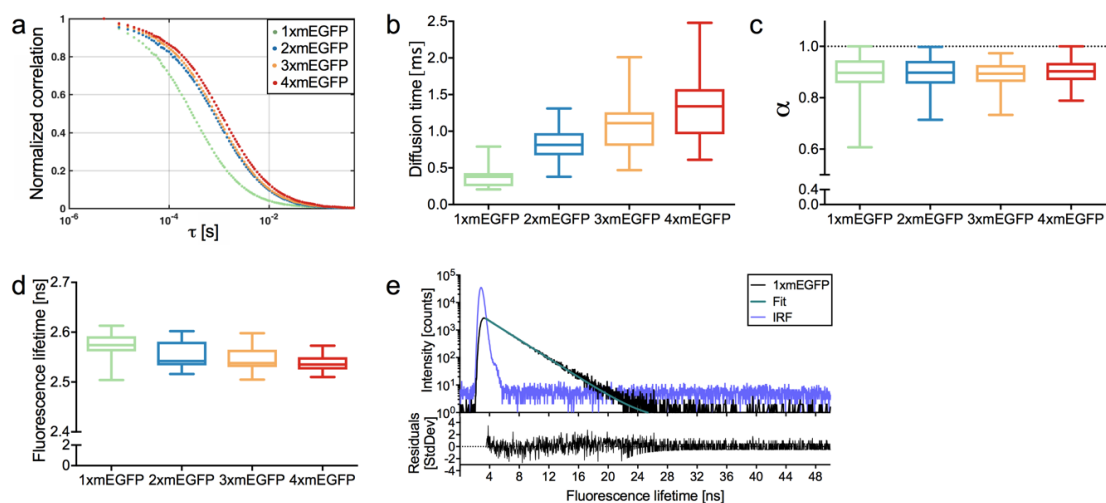
Supplementary Figure S1. Brightness analysis in different cell types and at different temperatures. **a:** Box plots of brightness ratio of mEGFP in cytoplasm and nucleus of HEK 293T, A549, CHO and HeLa cells, measured with N&B. The ratio was calculated for each single cell measurement. Data represent results of at least three independent experiments (HEK: n=47 cells, A549: n=37 cells, CHO: n=34 cells, HeLa: n=38 cells). **b:** Box plots of normalized molecular brightness of mEGFP monomers (white boxes) and homo-dimers (grey boxes) measured with N&B in cytoplasm of HEK 293T, A549, CHO and HeLa cells. Data represent results of at least three independent experiments (1x HEK: n=47 cells, 2x HEK: n=48 cells, 1x A549: n=38 cells, 2x A549: n=33 cells, 1x CHO: n=36 cells, 2x CHO: n=39 cells, 1x HeLa: n=39 cells, 2x HeLa: n=37 cells). **c:** Box plots of normalized molecular brightness of mCherry monomers and homo-dimers measured with N&B in cytoplasm of HEK 293T, A549, CHO and HeLa cells. Data represent results of at least three independent experiments (1x HEK: n=50 cells, 2x HEK: n=53 cells, 1x A549: n=37 cells, 2x A549: n=36 cells, 1x CHO: n=44 cells, 2x CHO: n=41 cells, 1x HeLa: n=35 cells, 2x HeLa: n=36 cells). **d:** Box plots of normalized molecular brightness of mEGFP monomers and homo-dimers at 23°C (white boxes) and 37°C (grey boxes) measured with pFCS in HEK 293T. Data are pooled from at least three independent experiments (1x 23°C: n=39 cells, 2x 23°C: n=38 cells, 1x 37°C: n=64 cells, 2x 37°C: n=63 cells).

Diffusion and FLIM analysis of mEGFP homo-oligomers

In the FCS analysis of the mEGFP homo-oligomer diffusion behavior in cells, introduction of an anomaly parameter α was needed to appropriately fit a 3-D diffusion model (Supplementary Figure S2a). As previously shown¹, we reproducibly observed anomalous subdiffusion in the molecular crowded cytoplasm of cells, indicated by α values lower than one for all investigated mEGFP homo-oligomers (Supplementary Figure S2c). Interestingly, we observed the same average α values for all homo-oligomers. The diffusion times increased for increasing homo-oligomer size (1xmEGFP: 27 kDa, 2xmEGFP: 54 kDa, 3xmEGFP: 81 kDa, 4xmEGFP: 108 kDa) (Supplementary Figure S2c), although with a different scaling than observed *in vitro*², in accordance with previous studies³.

Additionally, we performed fluorescence lifetime imaging measurements (FLIM) in A549 cells, since energy transfer between different mEGFP brightness states or to non-fluorescent subunits could result in a reduction of homo-oligomer brightness values. All lifetime decays

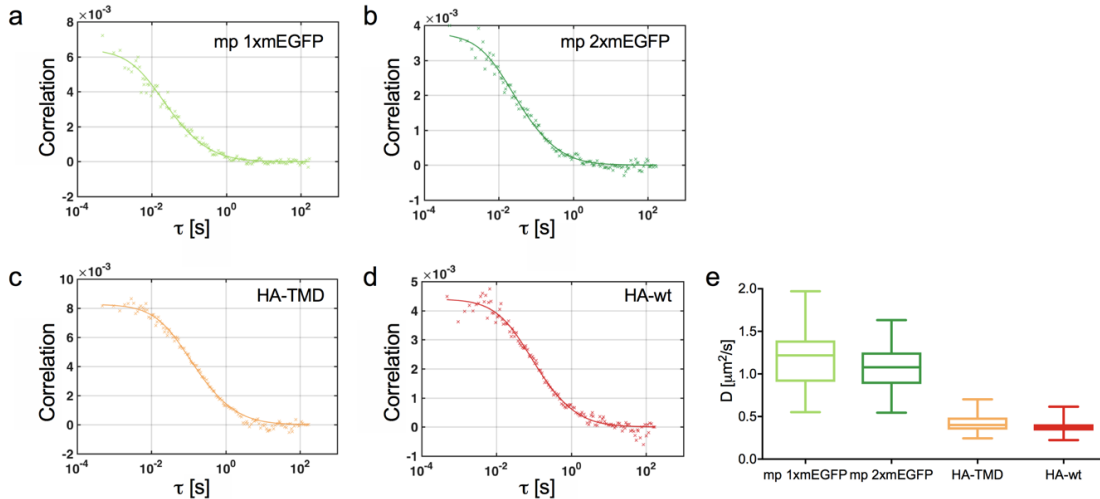
could be fitted by a single exponential component (Supplementary Figure S2e), indicating a single mEGFP brightness state in all mEGFP homo-oligomers. We observed negligible lifetime differences for all the tested homo-oligomers (Supplementary Figure S2e) corresponding to FRET efficiencies of less than 1.5%. Thus, we can exclude energy transfer to non-fluorescent mEGFP states.



Supplementary Figure S2. Diffusion and FLIM analysis of mEGFP homo-oligomers. **a:** Normalized average autocorrelation functions (ACFs) of 1xmEGFP, 2xmEGFP, 3xmEGFP and 4xmEGFP (i.e. monomers to tetramers), obtained by pFCS measurements in the cytoplasm of A549 cells. Average ACFs of all cells, measured in at least three independent experiments (1xmEGFP: n=52 cells, 2xmEGFP: n=39 cells, 3xmEGFP: n=42 cells, 4xmEGFP: n=28 cells) are shown. **b:** Box plots of diffusion times of mEGFP homo-oligomers obtained from fitting a model for three-dimensional anomalous diffusion to the data, pooled from all measured cells. **c:** Box plots of anomaly parameter α obtained from the anomalous diffusion model, pooled from all measured cells. **d:** Box plots of fluorescence lifetime of 1xmEGFP (n=16 cells), 2xmEGFP, (n=20 cells), 3xmEGFP (n=15 cells), 4xmEGFP (n=8 cells) measured in two independent experiments in the cytoplasm of A549 cells. **e:** Representative lifetime histogram for 1xmEGFP fitted with a single exponential component fit. The instrument response function (IRF) was calibrated as described in the methods paragraph.

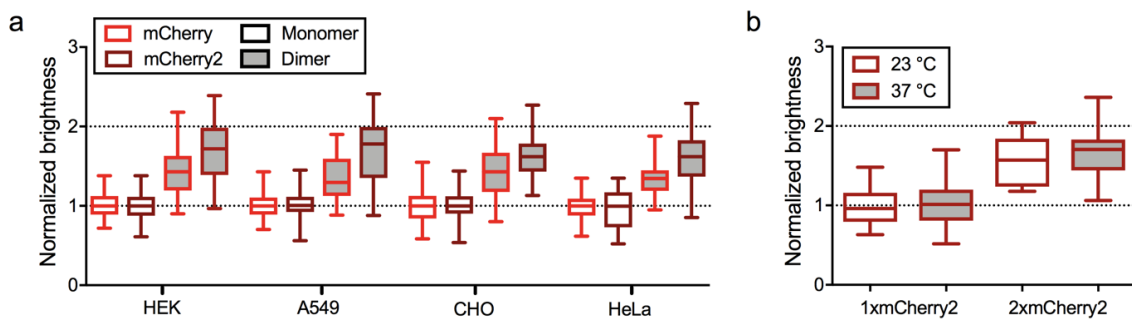
Diffusion analysis of Influenza A virus hemagglutinin (HA) measured with sFCS

From the sFCS auto-correlation functions (Supplementary Figure S3a-d) we also determined the diffusion dynamics of HA-wt-mEGFP (HA-wt) and HA-TMD-mEGFP (HA-TMD). In line with the Saffman-Delbrück model⁴, albeit having a different oligomeric state, both constructs display only slight differences in their diffusion coefficients: $D_{HA}=0.38 \pm 0.01 \mu\text{m}^2/\text{s}$ and $D_{HA-TMD}=0.42 \pm 0.02 \mu\text{m}^2/\text{s}$ (Supplementary Figure S3e).



Supplementary Figure S3. Diffusion analysis of Influenza A virus hemagglutinin (HA) measured with sFCS. a-d: Representative correlation functions and fit curves for sFCS measurements of mp 1xmEGFP (a), mp 2xmEGFP (b), HA-TMD-mEGFP (c) and HA-wt-mEGFP (d) measured in HEK 293T cells. Fit curves (solid lines) were obtained by fitting a two-dimensional diffusion model to the data. **e:** Box plots of diffusion coefficients calculated from sFCS diffusion times, pooled from at least three independent experiments (mp 1xmEGFP: n=55 cells, mp 2xmEGFP: n=54 cells, HA-TMD: n=37 cells, HA-wt: n=36 cells).

Comparison of mCherry2 to mCherry brightness values in different cell types and at different temperatures



Supplementary Figure S4. Comparison of mCherry2 to mCherry brightness values in different cell types and at different temperatures. a: Box plots of normalized molecular brightness of mCherry (light red)/ mCherry2 (dark red) monomers (white boxes) and homo-dimers (grey boxes) measured with N&B in the cytoplasm of HEK 293T, A549, CHO and HeLa cells. Data represent results of at least three independent experiments (mCherry: 1x HEK: n=50 cells, 2x HEK: n=53 cells, 1x A549: n=37 cells, 2x A549: n=36 cells, 1x CHO: n=44 cells, 2x CHO: n=41 cells, 1x HeLa: n=35 cells, 2x HeLa: n=36 cells; mCherry2: 1x HEK: n=49 cells, 2x HEK: n=54 cells, 1x A549: n=38 cells, 2x A549: n=34 cells, 1x CHO: n=43 cells, 2x CHO: n=40 cells, 1x HeLa: n=38 cells, 2x HeLa: n=40 cells). **b:** Box plots of normalized molecular brightness of mCherry2 monomers and homo-dimers at 23°C (white boxes) and 37°C (grey boxes) measured with pFCS in HEK 293T. Data are pooled from at least two independent experiments (1x 23°C: n=18 cells, 2x 23°C: n=20 cells, 1x 37°C: n=34 cells, 2x 37°C: n=33 cells).

Relative cross-correlation of mCherry-/mCherry2-mEGFP hetero-dimers and negative controls

Based on the determined apparent fluorescence probabilities ($p_{f,mEGFP}=0.65$, $p_{f,mCherry}=0.42$, $p_{f,mCherry2}=0.64$), the expected relative populations of fluorescent and non-fluorescent mCherry-/mCherry2-mEGFP hetero-dimers can be calculated. For mCherry-mEGFP, the following relative populations f are expected in the sample: $f_{G-R}=p_{f,mEGFP} \cdot p_{f,mCherry}=27\%$, $f_{g-R}=15\%$, $f_{G-r}=38\%$, $f_{g-r}=20\%$, where G, R denote fluorescent and g, r non-fluorescent mEGFP/mCherry FPs. Thus, the expected relative concentration of fluorescent mCherry hetero-dimer subunits (relative to the concentration of those containing fluorescent mEGFP) is $\frac{f_{G-R}+f_{g-R}}{f_{G-R}+f_{G-r}} = 0.65$, which

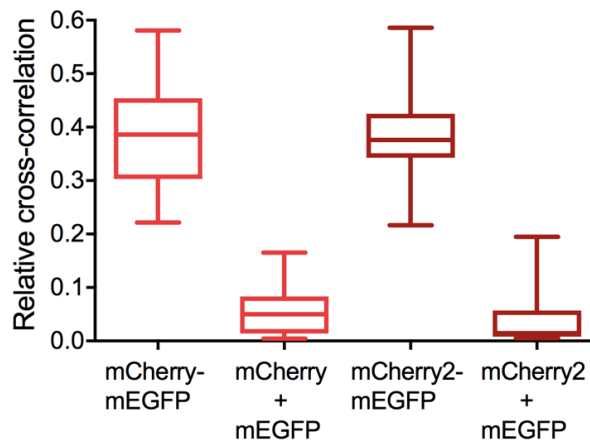
agrees very well with the measured average ratio of the mEGFP and mCherry ACF amplitudes of 0.65 (Figure 5). For mCherry2-mEGFP hetero-dimers, the expected populations are:

$f_{G-R}=p_{f,mEGFP} \cdot p_{f,mCherry2}=42\%$, $f_{g-R}=22\%$, $f_{G-r}=23\%$, $f_{g-r}=12\%$.

Thus, the relative concentration of fluorescent mEGFP and mCherry2 is expected to be $\frac{f_{G-R}+f_{g-R}}{f_{G-R}+f_{G-r}} = 0.98$, which agrees well with the measured value of 0.97 (Figure 5). Based on the p_f values and corresponding populations, it is also expected that the relative cross-correlation (rel.cc.) of mCherry-/ and mCherry2-mEGFP hetero-dimers is similar, since this quantity depends on the relative amount of FPs in a complex, for the less abundant FP species:

$$\frac{rel.cc.mCherry2-mEGFP}{rel.cc.mCherry-mEGFP} = \frac{\max\left\{\frac{f_{G-R}}{f_{G-R}+f_{G-r}}, \frac{f_{g-R}}{f_{G-R}+f_{g-R}}\right\}_{mCherry2}}{\max\left\{\frac{f_{G-R}}{f_{G-R}+f_{G-r}}, \frac{f_{g-R}}{f_{G-R}+f_{g-R}}\right\}_{mCherry}} = 1.02$$

In agreement with this expected ratio, mCherry-/ mCherry2-mEGFP hetero-dimers show the same relative cross-correlation in pFCCS measurements of A549 cells: $rel.cc.mCherry-mEGFP=0.39 \pm 0.02$, $rel.cc.mCherry2-mEGFP=0.39 \pm 0.01$. As a negative control, pFCCS measurements were performed in A549 cells co-expressing mCherry (or mCherry2) and mEGFP. The obtained relative cross-correlation is close to zero ($rel.cc.mCherry+mEGFP=0.06 \pm 0.01$, $rel.cc.mCherry2+mEGFP=0.04 \pm 0.01$). The residual positive cross-correlation is most likely due to minor cross-talk of mEGFP emission into the mCherry/ mCherry2 channel.



Supplementary Figure S5. Relative cross-correlation of mCherry-/mCherry2-mEGFP hetero-dimers and negative controls. Box plots of cross-correlation values measured for mCherry-mEGFP (light red) and mCherry2-mEGFP (dark red) hetero-dimers measured in A549 cells. Negative controls for cross-correlation were obtained by co-expressing mCherry (or mCherry2) together with mEGFP in A549 cells. The relative cross-correlation was calculated for each measurement as described in Methods. Data are pooled from at least two independent experiments (mCherry-mEGFP: n=35 cells, mCherry+mEGFP: n=19 cells, mCherry2-mEGFP: n=32 cells, mCherry2+mEGFP: n=16 cells).

Supplementary Table S1: Apparent fluorescence probabilities (p) determined in this study. Values are given as mean \pm SEM, NA: values were not determined.

Cell type	Localization	Method	mEGFP	mEYFP	mCherry	mCherry2	mCardinal	mRuby3	mScarlet	mScarlet-I
A549	Cytoplasm	N&B	0.68 \pm 0.06	NA	0.36 \pm 0.05	0.69 \pm 0.07	NA	NA	NA	NA
		pFCS	0.65 \pm 0.05	0.47 \pm 0.07	0.42 \pm 0.07	0.64 \pm 0.09	NA	NA	NA	NA
CHO	Cytoplasm	N&B	0.72 \pm 0.06	NA	0.44 \pm 0.05	0.62 \pm 0.04	NA	NA	NA	NA
HEK 293T	Cytoplasm	N&B	0.69 \pm 0.05	0.63 \pm 0.05	0.41 \pm 0.04	0.71 \pm 0.05	0.24 \pm 0.03	0.22 \pm 0.05	0.4 \pm 0.05	0.63 \pm 0.05
		pFCS	0.84 \pm 0.06	0.62 \pm 0.04	0.45 \pm 0.06	NA	NA	NA	NA	NA
	Nucleus	N&B	0.76 \pm 0.06	0.59 \pm 0.07	0.3 \pm 0.03	NA	NA	NA	NA	NA
	Plasma membrane	sFCS	0.67 \pm 0.04	0.44 \pm 0.04	0.43 \pm 0.05	NA	NA	NA	NA	NA
HeLa	Cytoplasm	N&B	0.76 \pm 0.06	NA	0.34 \pm 0.03	0.63 \pm 0.05	NA	NA	NA	NA
U2OS	Cytoplasm	N&B	0.72 \pm 0.05	NA	NA	NA	NA	NA	NA	NA

Supplementary Methods

Fluorescent protein constructs. For the cloning of all following constructs, standard PCRs with custom-designed primers (Supplementary Table S2) were performed to obtain monomeric FP cassettes, followed by digestion with fast digest restriction enzymes and ligation with T4-DNA-Ligase according to the manufacturer's instructions. All enzymes were purchased from Thermo Fisher Scientific, unless specified otherwise.

The constructs 2xmEGFP, 3xmEGFP and 4xmEGFP (i.e. mEGFP homo-dimer, homo-trimer and homo-tetramer) were obtained by step-wise cloning of monomeric mEGFP cassettes amplified from mEGFP-N1, a gift from Michael Davidson (Addgene plasmid #54767). First, 2xmEGFP was generated by ligating a mEGFP cassette into mEGFP-N1 digested with BamHI and AgeI. Subsequently, an additional monomeric mEGFP cassette was ligated into 2xmEGFP by digestion with KpnI and BamHI to generate 3xmEGFP. Finally, 4xmEGFP was obtained by ligation of an additional monomeric mEGFP cassette into 3xmEGFP by digestion with EcoRI and KpnI. All mEGFP subunits are linked by a polypeptide sequence of five amino acids. To ensure purity of mEGFP homo-oligomers, all full-length inserts were subcloned into pcDNATM3.1(+) (Thermo Fisher Scientific) possessing ampicillin instead of kanamycin resistance.

The GlnA-mEGFP plasmid was a kind gift from Ana García Sáez (University of Tübingen) and cloned based on pGlnA-Ypet (gift from Mike Heilemann, Addgene plasmid #98278).

To obtain 2xmEYFP, mEYFP was amplified from mEYFP-N1⁵ and inserted into mEYFP-C1 by digestion with KpnI and BamHI.

The plasmids mCherry-C1 and mCherry2-C1/N1 (gifts from Michael Davidson, Addgene plasmids #54563 and #54517, respectively) were used to generate 2xmCherry and 2xmCherry2, respectively. First, mCherry-C1 was generated by amplification of mCherry from mCherry-pLEXY plasmid (a gift from Barbara Di Ventura & Roland Eils, Addgene plasmid #72656) and inserted into a pBR322 empty vector. A second mCherry cassette was inserted into this vector by digestion with XhoI and BamHI to obtain 2xmCherry (i.e. mCherry homo-dimer). The 2xmCherry2 (mCherry2 homo-dimer) plasmid was generated by amplification of mCherry2 and insertion of this construct into mCherry2-C1 through digestion with XhoI and BamHI. To clone mRuby3-C1, mRuby3 was amplified from the pKanCMV-mClover3-mRuby3 plasmid, a gift from Michael Lin (Addgene plasmid #74252). The obtained PCR product was digested with AgeI and XhoI and exchanged with mEYFP from digested mEYFP-C1 plasmid. For 2xmRuby3 (mRuby3 homo-dimer), mRuby3 was again amplified by PCR and the product inserted into mRuby3-C1 by digestion with KpnI and BamHI. The mCardinal-C1/N1 plasmids were a gift from Michael Davidson (Addgene plasmids #54590 and #54799). To obtain 2xmCardinal (mCardinal homo-dimer), mCardinal was amplified from mCardinal-C1 and the PCR product inserted into mCardinal-C1 by digestion with KpnI and BamHI. The plasmids mScarlet-C1 and mScarlet-I-C1 are gifts from Dorus Gardella (Addgene plasmids #85042 and #85044). 2xmScarlet (mScarlet homo-dimer) and 2xmScarlet-I (mScarlet-I homo-dimer) were generated by amplification of mScarlet and mScarlet-I from the corresponding plasmids and reintegration into mScarlet-C1 and mScarlet-I-C1 by digestion with XhoI and KpnI. To ensure purity of homo-dimers, all full-length homo-dimers were subcloned into pcDNATM3.1(+) (Thermo Fisher Scientific) possessing ampicillin instead of kanamycin resistance.

The hetero-dimers mCherry-mEGFP and mCherry2-mEGFP were generated by amplification of mCherry and mCherry2, respectively, and insertion of the obtained constructs into mEGFP-C1, (Michael Davidson, Addgene plasmid #54759), by digestion with XhoI and BamHI. Both fluorophores are linked by five and seven amino acids, respectively.

The membrane constructs consisting of mEGFP linked to a myristoylated and palmitoylated peptide (mp 1xmEGFP) and its homo-dimer mp 2xmEGFP were kind gifts from Richard J. Ward (University of Glasgow)⁶. The analogue mp 1xmEYFP construct was obtained as described elsewhere⁵. To generate mp 2xmEYFP, the 2xmEYFP cassette described above was transferred into a mp mCardinal vector⁷, by digestion with AgeI and BamHI. The GPI mCherry (glycosylphosphatidylinositol-anchored mCherry) plasmid was a kind gift from Roland Schwarzer (Gladstone Institute, San Francisco). Based on this plasmid, GPI 2xmCherry was generated by amplification of a mCherry cassette and ligation of the obtained insert into GPI mCherry, digested using Sall and BamHI.

The Influenza virus A/chicken/FPV/Rostock/1934 hemagglutinin (HA) constructs HA-wt-mEGFP and HA-TMD-mEGFP were cloned based on the previously described HA-wt-mEYFP⁵ and HA-TMD-mEYFP⁸ plasmids. HA-wt-mEYFP contains full-length HA protein fused to mEYFP at the C-terminus, whereas in HA-TMD-mEYFP a large part of the extracellular domain of HA is replaced by mEYFP. To clone HA-wt-mEGFP, HA-wt-mEYFP was digested using BglII and SacII (New England Biolabs) and the obtained HA insert ligated into mEGFP-N1. For HA-TMD-mEGFP, HA-TMD-mEYFP plasmid and mEGFP-N1 vector were digested with AgeI and BsrGI to replace mEYFP with mEGFP.

Supplementary Table S2: Primer sequences (5'-3' orientation) used for cloning of FP expression plasmids.

Construct	Orientation (restriction enzyme)	Sequence (5'-3')
2xmEGFP	forward (BamHI)	GAGAGGGATCCATGGTGAGCAAGGGCGAGGAG
	reverse (AgeI)	GAGAACCGGTCTCTTGTACAGCTCGTCCATGCC
3xmEGFP	forward (KpnI)	GAGAGGTACCATGGTGAGCAAGGGCGAGGAG
	reverse (BamHI)	GAGAGGATCCCGACGGTCTCTTGTACAGCTCGTCCATGCC
4xmEGFP	forward (EcoRI)	GAGAGAATTCATGGTGAGCAAGGGCGAGGAG
	reverse (KpnI)	GAGAGGTACCGACCGGTCTCTTGTACAGCTCGTCCATGCC
mCherry-C1	forward (NheI)	GTACGGCTAGCATGGTGAGCAAGGGCGAGGAG
	reverse (BglII)	GACAGATCTGAGTCCGGACTTGTACAGCTCGTCCATGC
2xmEYFP, 2xmCardinal	forward (KpnI)	ATATGGTACCATGGTGAGCAAGGGC
	reverse (BamHI)	CGCGGGATCCCTTGTACAGCTCGTCC
2xmCherry, 2xmCherry2, mCherry-mEGFP, mCherry2-mEGFP	forward (XhoI)	GAGACTCGAGGAATGGTGAGCAAGGGCGAGGAG
	reverse (BamHI)	GAGAGGATCCTTACTTGTACAGCTCGTCCATGCC
GPI 2xmCherry	forward (Sall)	GAGAGTCTGACTATGGTGAGCAAGGGCGAGGAG
	reverse (BamHI)	GAGAGGATCCGAAGCTTGTAGCTCGAGATCTAGAAGAACCAGAACCCAGTAG ACCAGTACCATGACCTCCGGACTTGTACAGCTCGTCCATGCCCGCCGGTG
mRuby3-C1	forward (AgeI)	ATATACCGGTCATGGTGAGCAAAGGC
	reverse (XhoI)	CGCGCTCGAGCTTGTACAGCTCGTCC
2xmRuby3	forward (KpnI)	ATATGGTACCCATGGTGAGCAAAGGC
	reverse (BamHI)	CGCGGGATCCCTTGTACAGCTCGTCC
2xmScarlet(-I)	forward (XhoI)	AGAGTCCTCGAGATATGGTGAGCAAGGGCGAGGCAGTGATC
	reverse (KpnI)	CTGCAGGTACCTTACAGCTCGTCCATGCCCGCCGGTG

References

1. Weiss, M., Elsner, M., Kartberg, F. & Nilsson, T. Anomalous subdiffusion is a measure for cytoplasmic crowding in living cells. *Biophys. J.* **87**, 3518–3524 (2004).
2. Vámosi, G. *et al.* EGFP oligomers as natural fluorescence and hydrodynamic standards. *Sci. Rep.* **6**, 33022 (2016).
3. Dross, N. *et al.* Mapping eGFP Oligomer Mobility in Living Cell Nuclei. *PLoS One* **4**, e5041 (2009).
4. Saffman, P. G. & Delbrück, M. Brownian motion in biological membranes. *Proc. Natl. Acad. Sci. U. S. A.* **72**, 3111–3113 (1975).
5. Engel, S. *et al.* FLIM-FRET and FRAP reveal association of influenza virus haemagglutinin with membrane rafts. *Biochem. J.* **425**, 567–573 (2010).
6. Ward, R. J., Pediani, J. D., Godin, A. G. & Milligan, G. Regulation of oligomeric organization of the serotonin 5-hydroxytryptamine 2C (5-HT_{2C}) receptor observed by spatial intensity distribution analysis. *J. Biol. Chem.* **290**, 12844–57 (2015).
7. Dunsing, V., Mayer, M., Liebsch, F., Multhaup, G. & Chiantia, S. Direct evidence of amyloid precursor-like protein 1 trans interactions in cell-cell adhesion platforms investigated via fluorescence fluctuation spectroscopy. *Mol. Biol. Cell* **28**, 3609–3620 (2017).
8. Scolari, S. *et al.* Lateral distribution of the transmembrane domain of influenza virus hemagglutinin revealed by time-resolved fluorescence imaging. *J. Biol. Chem.* **284**, 15708–16 (2009).

2.4 [P4] Purely polysaccharide-based biofilm matrix provides size-selective diffusion barriers for nanoparticles and bacteriophages

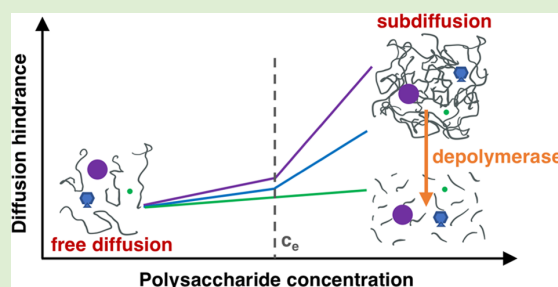
Purely Polysaccharide-Based Biofilm Matrix Provides Size-Selective Diffusion Barriers for Nanoparticles and Bacteriophages

Valentin Dunsing,[†] Tobias Irscher,[‡] Stefanie Barbirz,^{*,‡,†} and Salvatore Chiantia^{*,†,§}

Universität Potsdam,[†]Institut für Biochemie und Biologie, Physikalische Zellbiochemie and [‡]Institut für Biochemie und Biologie, Physikalische Biochemie, Karl-Liebknecht-Str. 24-25, 14476 Potsdam, Germany

Supporting Information

ABSTRACT: Biofilms are complex mixtures of proteins, DNA, and polysaccharides surrounding bacterial communities as protective barriers that can be biochemically modified during the bacterial life cycle. However, their compositional heterogeneity impedes a precise analysis of the contributions of individual matrix components to the biofilm structural organization. To investigate the structural properties of glycan-based biofilms, we analyzed the diffusion dynamics of nanometer-sized objects in matrices of the megadalton-sized anionic polysaccharide, stewartan, the major biofilm component of the plant pathogen, *Pantoea stewartii*. Fluorescence correlation spectroscopy and single-particle tracking of nanobeads and bacteriophages indicated notable subdiffusive dynamics dependent on probe size and stewartan concentration, in contrast to free diffusion of small molecules. Stewartan enzymatic depolymerization by bacteriophage tailspike proteins rapidly restored unhindered diffusion. We, thus, hypothesize that the glycan polymer stewartan determines the major physicochemical properties of the biofilm, which acts as a selective diffusion barrier for nanometer-sized objects and can be controlled by enzymes.



INTRODUCTION

Bacterial biofilms provide strong physicochemical barriers and structural scaffolds to organize surface adherence of bacterial communities and control access of nutrients, antibiotics, or bacteriophages.^{1–3} A major component of bacterial biofilms, contributing up to 90% of the dry weight, is the extracellular polymeric substance (EPS), a multicomponent matrix containing proteins, DNA, and polysaccharides in varying amounts that form complex hydrated polymer networks.^{4–6} Apart from providing mechanical stability for the embedded bacteria, the EPS regulates the selective transport of molecules, similarly to what is observed in other biological hydrogels.^{7,8} More specifically, particle mobility in polymer hydrogels is shown to depend on the volume fraction, dynamics, and interactions of the polymer chains, as well as on the size of the particles themselves.^{8,9} Nonsteric interactions, e.g., electrostatic or hydrophobic, affect the mobility of particles in such systems.⁸ Moreover, salts and divalent cations modulate mechanical and electrostatic properties of biofilms, influencing the diffusion of charged molecules such as antibiotics.^{10–12} As a consequence, each bacterial biofilm has distinct particle transport characteristics that modulate its function and are variable in space and time.^{13–15} The life style and distribution of the bacteria embedded in the EPS matrix can further influence biofilm properties via, e.g., mechanical cell–cell interactions.¹⁶

An effective and noninvasive approach to measure diffusion dynamics through hydrogels on the microscopic scale is

provided by fluorescence techniques,¹⁷ such as fluorescence correlation spectroscopy¹⁸ (FCS) or single-particle tracking¹⁹ (SPT). While FCS reports ensemble properties with a high temporal resolution, i.e., microsecond (μ s) timescale,¹⁸ SPT probes the dynamics of single particles with nanometer (nm) precision.¹⁹ In biofilms, the mobilities of nutrients, bacterial cells, antibiotics, or viral infective particles have a major impact on the embedded microbial communities.^{20–23} FCS revealed that biofilms are heterogeneous with respect to diffusion of latex beads and phage particles.^{13,20,24,25} Moreover, nanoparticles and phages can interact with the cell surface of biofilm-embedded bacteria.^{23,26} So far, most studies have focused on complex mixtures of EPS and bacteria, and the age of a biofilm was considered as the main factor inducing changes in the observed probe diffusion dynamics.¹⁴ Yet, less attention has been paid to the fact that these changes might be linked to variations in the biofilm molecular structure, resulting from the biochemical properties and composition of all biomacromolecules at a given time and location. Proteins, DNA, and glycans can be modified by endogenous or exogenous enzymes during the bacterial life cycle, resulting in spatiotemporal control of the biofilm structure.^{6,27,28}

In this work, we studied one major biofilm component, the pure exopolysaccharide, stewartan, produced by the plant

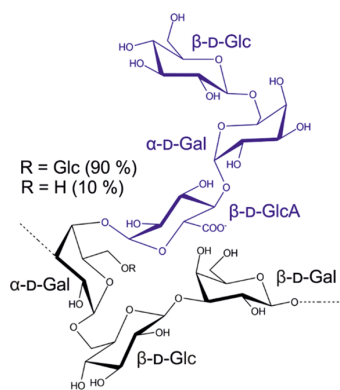
Received: July 6, 2019

Revised: September 3, 2019

Published: September 3, 2019

pathogen *Pantoea stewartii*.²⁹ This biofilm-forming pathogen is responsible for Stewart's wilt, a severe disease of corn and sweet maize. Transmitted by an insect vector, *P. stewartii* bacteria change into a biofilm state when inside the plant, and switch on three gene clusters encoding proteins for the synthesis of the exopolysaccharide, stewartan.³⁰ Consequently, *P. stewartii* becomes embedded in a dense polysaccharide biofilm matrix that blocks water flow in the xylem and leads to wilting and death of the plants.²⁹ Stewartan is an anionic linear heteropolysaccharide with chain lengths of up to 2 MDa. It is polymerized from individual oligosaccharide repeat units consisting of a backbone of alternating Glc and Gal residues, branched with a glucuronic acid-containing side chain (Scheme 1).³¹ We applied a combination of FCS and SPT

Scheme 1. Structure of the Stewartan Repeat Unit (According to Nimtz et al.³¹)^a



^a**3)- α -D-Galp-[(4 \rightarrow 1)- β -D-GlcAp-(4 \rightarrow 1)- α -D-Galp)-(6 \rightarrow 1)- β -D-Glcp]-**(1 \rightarrow 6)- β -D-Glcp-(1 \rightarrow 3)- β -D-Galp-(1 \rightarrow). The oligosaccharide repeat unit backbone structure is shown in black (bold type), and the side chain branch is in blue. About 90% of the backbone α -D-Galp are substituted with (6 \rightarrow 1)- β -D-Glcp. Stewartan repeat units are assembled in polymeric chains with an approximate size of 2 MDa.

to investigate particle mobility in matrices consisting of pure stewartan, as a simplified model for a homogeneous, glycan-based biofilm. We chose this bottom-up approach to quantitatively describe the mobility of different tracers: small molecules, synthetic beads, or bacteriophage particles. From our results, we hypothesize that the physicochemical properties of the stewartan matrix might dominate particle diffusion in a glycan-based biofilm, as a function of polysaccharide concentration, solvent pH, and tracer properties. We, furthermore, show that stewartan degradation by glycan-depolymerizing enzymes [e.g., bacteriophage tailspike proteins (TSPs)] is an important regulatory mechanism that can rapidly modulate particle dynamics within the matrix.

MATERIALS AND METHODS

Materials. *P. stewartii* DSM 30176 was purchased from the German Collection of Microorganisms and Cell Cultures (DSMZ, Braunschweig, Germany). Standard buffers were 50 mM Tris-HCl, pH 8, or 50 mM 2-morpholinoethanesulfonic acid (MES)-NaOH, pH 5, if not indicated otherwise. A complementary DNA containing the coding sequence for bacteriophage ϕ Ea1h TSP depolymerase was a kind gift from K. Geider (Julius Kühn Institut, Dossenheim, Germany).³² Bacteriophage P22 and Φ Ea1h TSP purification and fluorescence labeling are described in the Supporting Information (SI). Nonfunctionalized polystyrene fluorescent microspheres (Drag-

on Green, λ_{ex} 480 nm, λ_{em} 520 nm) were purchased from Bangs Laboratories (Fishers, IN). Effective tracer size and ζ potential measurements are reported in Table S1. All other chemicals used were of analytical grade.

Growth of *P. Stewartii* Biofilm and Purification of Stewartan. Isolation of stewartan from *P. stewartii* has been described.³¹ Briefly, bacteria were plated on a membrane filter (MF-Millipore mixed cellulose ester, 0.45 μ m pore size, Merck, Darmstadt, Germany) placed on CPG agar and incubated at 28 $^{\circ}$ C for 3 days. During this time, the biofilm increased in volume until covering the entire available surface on the disk, while maintaining an almost stable stewartan concentration (see the next paragraph) and, thus, maximizing the amount of stewartan available for purification. Biofilm-embedded cells were suspended in 0.85% (w/v) NaCl and removed by centrifugation. The supernatant stewartan solution was further purified by ultracentrifugation at 160 000g for 3 h. Stewartan concentrations in these crude biofilm solutions were determined by the phenol-sulfuric acid method.³³ Similar stewartan concentrations were found in 21 h and 72 h old biofilms (see the SI).

Stewartan was concentrated by ethanol precipitation (80% v/v) and nucleic acids and proteins were removed by benzonase (50 U/mL, 16 h, 37 $^{\circ}$ C) and proteinase K (15 μ g/mL, 60 h, 65 $^{\circ}$ C) treatments. After three dialyses (acetic acid 100 mM, 50 mM, water) and lyophilization, pure stewartan was obtained with a yield of $\sim 10^{-2}$ g stewartan/g crude biofilm. Sodium dodecyl sulfate-polyacrylamide gel electrophoresis and silver staining could not reveal major amounts of lipopolysaccharide in the purified stewartan preparations (data not shown).

For FCS/SPT experiments, stewartan was dissolved in 50 mM Tris-HCl, pH 8, or 50 mM MES-NaOH, pH 5, at the indicated concentrations and left at room temperature for 1 h before starting the measurements.

Confocal Microscopy System. SPT and FCS measurements were performed on a Zeiss LSM780 system (Carl Zeiss, Oberkochen, Germany) using a 40 \times , 1.2 NA water immersion objective. Samples were excited with a 488 nm argon laser. Excitation and detection light were separated by a 488 nm dichroic mirror. Fluorescence was detected between 500 and 600 nm, using a GaAsP detector in photon counting mode.

Fluorescence Correlation Spectroscopy. FCS measurements were performed in spot acquisition mode for at least 30 s (up to 10 min for more viscous samples) with a time resolution of 1.53 or 7.56 μ s. To minimize potential distortions of the focal volume by the refractive index mismatch between water immersion medium, glass slide, and stewartan/sucrose solutions, all measurements were performed at a depth of 10 μ m, and the collar ring of the objective was adjusted by maximizing the signal in Alexa Fluor 488 (AF488) containing stewartan/sucrose solutions at each concentration. Laser powers were chosen to keep the photon count rate below 2 MHz to avoid detector saturation. Typical values were ~ 2 μ W for AF488, ~ 0.2 μ W for 60 nm beads, ~ 0.05 μ W for 200 nm beads, and ~ 2 μ W for P22 bacteriophages. In all cases, no noticeable photobleaching was observed. The pinhole was set to one Airy Unit. Acquired data were exported as TIFF files, imported, and analyzed in MATLAB (The MathWorks, Natick, MA) using a custom-written code. First, the autocorrelation function (ACF) was calculated as follows, using a multiple τ algorithm:

$$G(\tau) = \frac{\langle \delta F(t) \delta F(t + \tau) \rangle_t}{\langle F(t) \rangle_t^2} \quad (1)$$

where $\delta F(t) = F(t) - \langle F(t) \rangle_t$.

To avoid artifacts caused by rarely occurring aggregates of particles inducing single bright events, ACFs were calculated segment-wise (4–10 segments) and then averaged. Segments showing clear distortions were manually removed from the analysis. Next, a model for three-dimensional anomalous diffusion and a Gaussian focal volume geometry³⁴

$$G(\tau) = \frac{1}{N} \left(1 + \frac{T}{1-T} e^{-\tau/\tau_b} \right) \left(1 + \left(\frac{\tau}{\tau_d} \right)^\alpha \right)^{-1} \left(1 + \frac{1}{S^2} \left(\frac{\tau}{\tau_d} \right)^\alpha \right)^{-1/2} \quad (2)$$

was fitted to the ACFs, resulting in parameter estimates of the diffusion time τ_d , number of particles N , and anomaly exponent α . The exponential term accounts for photophysical transitions, e.g., to a triplet state, of an average fraction T ($0 \leq T \leq 1$) of particles with a time constant τ_b . The structure parameter S was fixed to the value (typically around 5–9) obtained from daily calibration measurements of AF488 in water or stewartan/sucrose solutions. Using the determined diffusion times in buffer, $\tau_{d,\text{buffer}}$ and stewartan/sucrose solutions, τ_d , relative diffusion times $\frac{\tau_d}{\tau_{d,\text{buffer}}}$ were calculated. From the diffusion time, τ_d , the diffusion coefficient, D , can be determined: $D = \frac{\omega_0^2}{4\tau_d}$. Here, ω_0 denotes the waist of the focal volume. Of note, this relation is strictly valid only for normal Brownian diffusion, i.e., $\alpha = 1$. Therefore, calculated diffusion coefficients for $\alpha < 1$ have to be considered as approximate values, denoted as D_{app} describing diffusion at the length scale set by ω_0 .³⁵ The waist ω_0 was determined from calibration measurements of AF488 in water, using the previously determined diffusion coefficient³⁶ of $D_{\text{AF488}} = 435 \mu\text{m}^2/\text{s}$. Based on control measurements with sucrose solutions, i.e., correct determination of their relative viscosity up to 40% (w/v) (Figure S1) calculated by measured diffusion times, it was concluded that distortions of the focal volume due to changes in refractive index are minimal and the calibrated waist ω_0 can be assumed to be constant under all conditions. To further assess potential particle aggregation, the molecular brightness, $\frac{\langle F(t) \rangle_t}{N}$ (i.e., the average photon count rate emitted by each diffusing entity), was compared for different measurement conditions. All measurements were performed at room temperature. Fluorescent tracer particles were used at the following concentrations: ~ 20 nM for AF488, ~ 5 nM for 60 nm beads, and ~ 0.2 nM for 200 nm beads.

Single-Particle Tracking. For SPT, 1000–2000 images were acquired in a fixed plane in an area of $\sim 180 \mu\text{m}^2$ as 128×128 or 256×256 pixels of $0.104 \mu\text{m}$ or $0.052 \mu\text{m}$ size, using a pixel dwell time of 1.58 or 0.79 μs , in photon counting mode. This resulted in a frame time of 62 or 122 ms. Laser powers were adjusted to maximize the signal, while keeping the photon count rate below 2 MHz, i.e., $\sim 2 \mu\text{W}$ for P22 bacteriophages and 0.05 μW for 200 nm fluorescent polystyrene beads. All measurements were performed at room temperature. CZI image stacks were imported in Fiji³⁷ and analyzed using the TrackMate v3.8.0 plugin.³⁸ Particles were localized with subpixel resolution using a Laplacian of Gaussian filter with a blob diameter of $0.4 \mu\text{m}$ and a quality threshold³⁸ of 1 for P22 bacteriophages and 0.15 for 200 nm beads. Particle positions within four pixels from the frame edges were neglected to exclude partial presence of particles in the images and related localization artifacts. Tracking, i.e., connecting individual particle positions to trajectories, was performed using a simple linear assignment problem tracker³⁸ allowing a maximum distance of 0.5–1.5 μm between positions in subsequent frames, a maximum gap of two frames, and no splitting or merging events. Trajectories corresponding to rarely occurring aggregates of particles were identified by unusually high spot intensities and removed manually. Trajectories were saved as TrackMate XML files and imported in MATLAB (The MathWorks, Natick, MA) using the `importTrackMateTracks` script for further analysis with a custom-written code. Only trajectories extracted from at least 20 frames were considered.

First, individual time-averaged mean-square displacements (taMSDs) were calculated:³⁹

$$\text{taMSD} = \langle r^2(\tau) \rangle_t = \frac{1}{N-k} \sum_{i=1}^{N-k} \{ \mathbf{r}((i+k)\Delta t) - \mathbf{r}(i\Delta t) \}^2 \quad (3)$$

where N denotes the number of particle positions in the track, Δt the frame time of 62 or 122 ms, and $\tau = k\Delta t$ the lag time between positions in frames i and $i+k$. Here, $\mathbf{r}(t)$ is a two-dimensional vector denoting the position of a particle at time point t , $\mathbf{r}(t) = (x(t), y(t))$. Ensemble-averaged taMSDs were obtained by averaging taMSDs of all trajectories. Apparent diffusion coefficients D_{app} were determined by fitting a linear function that is expected for normal Brownian motion to the first 10 points ($\Delta t \leq \tau \leq 10\Delta t$) of individual taMSDs:

$$\text{taMSD}(\tau) = 4D_{\text{app}}\tau + c \quad (4)$$

where c is a free fit parameter that accounts for static and dynamic errors due to the finite localization precision and acquisition speed. Typical values of c were $\sim 0.005 \mu\text{m}^2$, i.e., corresponding at maximum to a ~ 50 – 100 nm localization error. To account for the different statistical weights of each point in the taMSD, a weighted fit was performed according to the factor $N-k$, i.e., the number of squared differences that are used to calculate the mean in eq 3 for each taMSD point. The quantity D_{app} characterizes diffusion dynamics on a small scale and can, therefore, be used for comparison with D_{app} determined via FCS. Also, D_{app} was used to calculate an approximate specific diffusion hindrance $\tau_{d,\text{sp}} = (D_{\text{app}} - D_{\text{app,buffer}})/D_{\text{app,buffer}}$ for a more direct comparison with FCS data.

Second, the anomaly exponent α characterizing anomalous diffusion behavior^{19,39} was determined by performing a weighted fit of a power law to individual taMSDs for $\Delta t \leq \tau \leq n\Delta t$ ($n = 20$ – 40 depending on the sample, i.e., \sim one-fourth of the typical length of trajectories):

$$\text{taMSD}(\tau) = 4D_a\tau^\alpha + d \quad (5)$$

where D_a is the anomalous transport coefficient and d a free fit parameter accounting for the localization error. Here, only trajectories with a minimum length of 40 frames were considered. In the fit routine, d was restricted to values between 0 and the value of the offset parameter c obtained from the linear fit model. In practice, correcting for an MSD offset using d had a negligible effect on the values obtained for α .

Third, the distribution of angles between successive steps taken in an interval δt and separated by a lag time τ was calculated according to

$$\theta = \cos^{-1} \left(\frac{[\mathbf{r}(t+\delta t) - \mathbf{r}(t)] \cdot [\mathbf{r}(t+\delta t + \tau) - \mathbf{r}(t + \tau)]}{|\mathbf{r}(t+\delta t) - \mathbf{r}(t)| \cdot |\mathbf{r}(t+\delta t + \tau) - \mathbf{r}(t + \tau)|} \right) \quad (6)$$

Here, \cdot denotes the dot product of the vectors.

Finally, the ensemble average of the time-averaged velocity autocorrelation^{40,41} of individual trajectories was determined for steps taken in an interval δt , separated by the lag time, τ :

$$C_v(\tau) = \frac{1}{\delta t^2} \langle [\mathbf{r}(t+\delta t) - \mathbf{r}(t)] \cdot [\mathbf{r}(t+\delta t + \tau) - \mathbf{r}(t + \tau)] \rangle_t \quad (7)$$

Of note, the distributions obtained for D_{app} and α based on fitting to individual taMSDs according to eqs 4 and 5 were fairly broad due to the limited statistics of single trajectories, similar to previous studies analyzing anomalous diffusion dynamics using SPT.^{42,43} Generally, statistics could be improved by additional ensemble-averaging of taMSDs before fitting,⁴² but this may lead to artifacts (e.g., apparent subdiffusive dynamics for freely diffusing particles) when taMSDs for trajectories of different lengths are averaged.⁴⁴ All measurements were performed at room temperature. Fluorescent tracer particles were used at the following concentrations: ~ 20 nM for AF488, ~ 5 nM for 60 nm beads, and ~ 0.2 nM for 200 nm beads.

Viscosimetry. Bulk viscosity measurements were performed on an AMVn Automated Micro Viscometer (Anton Paar, Graz, Austria), based on the falling ball principle, at a 70° angle. Per sample, six runs were acquired.

Statistical Analyses. All data are displayed as box plots indicating the median values and whiskers ranging from minimum to maximum values. Quantities in the main text are given as mean \pm standard

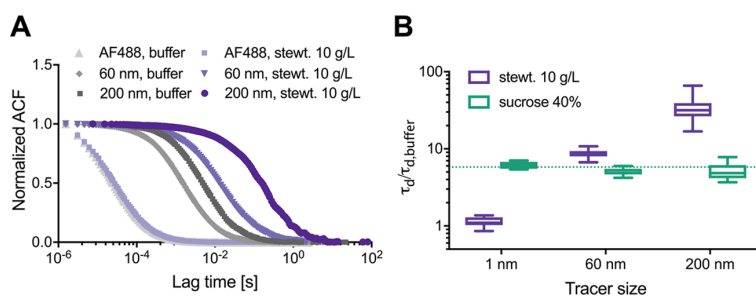


Figure 1. FCS analysis of fluorescent tracer particles of different sizes in stewartan, sucrose and buffer solutions. (A) Normalized ACFs calculated from FCS measurements for AF488 (~1 nm) or Dragon Green-labeled polystyrene beads (60, 200 nm) in 10 g/L stewartan (stewt.) and 50 mM Tris-HCl pH 8 buffer. The ACFs shown here were averaged from at least 12 measurements each. (B) Box plots of the hindrance factor ($\tau_d/\tau_{d,\text{buffer}}$) in 10 g/L stewartan or 40% (w/v) sucrose solutions, measured with the fluorescent tracers described in (A). Diffusion times were obtained by fitting a three-dimensional anomalous diffusion model (eq 2) to individual ACFs. The dashed line shows the expected relative diffusion time in 40% (w/v) sucrose at 25 °C, which is equal to the viscosity ratio of 40% (w/v) sucrose solution and water ($\eta/\eta_{\text{water}} = 5.80$), measured by rotational rheometry.⁴⁷

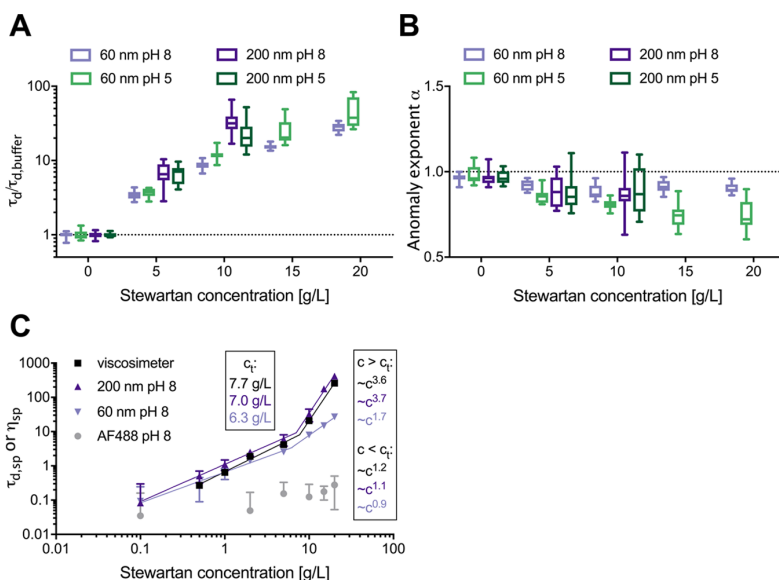


Figure 2. FCS analysis of fluorescent tracer particles in stewartan solutions of varying concentrations and pH values. (A) Box plots of hindrance factors $\tau_d/\tau_{d,\text{buffer}}$ in 5–20 g/L stewartan solutions at pH 5 and 8, calculated by normalizing diffusion times to the average values obtained in pure 50 mM Tris-HCl, pH 8, or 50 mM MES-NaOH, pH 5, buffer solutions, measured by FCS on 60 and 200 nm fluorescent polystyrene bead suspensions. Data are pooled from at least 12 measurements in two independent experiments. (B) Box plots of anomaly exponent α obtained by fitting an anomalous diffusion model (eq 2) to the ACFs of FCS measurements described in (A). (C) Specific viscosity, $\eta_{\text{sp}} = (\eta_{\text{stewartan}} - \eta_{\text{buffer}})/\eta_{\text{buffer}}$, obtained from falling ball viscosimeter measurements of 0.5–20 g/L stewartan solutions, or specific diffusion hindrance, $\tau_{d,\text{sp}} = (\tau_d - \tau_{d,\text{buffer}})/\tau_{d,\text{buffer}}$, calculated from FCS measurements on AF488, and 60 and 200 nm polystyrene beads in 0.1–20 g/L stewartan solutions in 50 mM Tris-HCl pH 8 buffer. Error bars show SD from 6 (viscosimeter) or at least 12 (FCS, from two independent experiments) measurements. Solid lines indicate separate fits to a power-law model in the ranges of 0.1–5 and 10–20 g/L, yielding the exponents reported in the box. Transition concentrations c_t , defined as the intersection points of the two power-law curves obtained for each sample, are reported in the box on the left. The data points for 200 nm beads at 15 and 20 g/L were calculated from the SPT data presented in Figure 3, based on average diffusion coefficients reported in Table S2 (see Materials and Methods).

deviation (SD) (SPT) or median \pm SD (FCS). Sample sizes are given in figure captions.

RESULTS

Diffusion Hindrance in the Stewartan Anionic Glycan Polymer Matrix Is Probe-Size-Dependent.

In simple fluids, diffusion times of freely diffusing spherical particles are directly proportional to the particle size. In a hydrogel, in contrast, the diffusivity of particles might show a more complex relationship, depending not only on particle size, but also on

several other parameters, including gel porosity and cross-linking of matrix components.^{8,9} As bacterial biofilms are complex, multisubstance mixtures, we chose the major *P. stewartii* biofilm EPS component, stewartan,³¹ to set up a simplified model biofilm and study particle diffusion in this matrix system. We purified stewartan from 72 h old biofilms and prepared viscous matrices by reconstitution in buffer. We then quantified the mobility of fluorescent tracers of different sizes (1, 60, and 200 nm) via FCS measurements. We first analyzed the ACFs in stewartan and pure buffer with a three-

dimensional anomalous diffusion model. The obtained diffusion times allowed us to determine the relative diffusion time ($\tau_d/\tau_{d,\text{buffer}}$), which we will refer to as the “diffusion hindrance factor” in what follows. This parameter provides a relative measure of tracer diffusion dynamics in stewartan matrices compared to aqueous buffer solutions. A similar approach was applied in recent studies^{13,45,46} reporting the relative diffusion coefficient $D_{\text{gel}}/D_{\text{buffer}} = \tau_{d,\text{buffer}}/\tau_{d,\text{gel}}$ to characterize diffusion in hydrogels. The effective sizes of tracers examined in this work were confirmed by dynamic light scattering (DLS) (see Table S1 in the SI). In a simple fluid, the hindrance factor is expected to be constant, i.e., independent of tracer size, thus reporting on the relative viscosity of the examined fluid. In stewartan matrices, however, we observed a strong dependence of the hindrance on tracer size. While small AF488 molecules diffused with a similar mobility as in pure buffer ($\tau_d/\tau_{d,\text{buffer}} = 1.1 \pm 0.2$, also indicated by nearly overlapping ACFs in Figure 1A), larger particles such as 60 nm polystyrene beads showed a higher relative diffusion time within the stewartan matrix ($\tau_d/\tau_{d,\text{buffer}} = 8.6 \pm 1.2$), as evident by a shift of the ACFs toward larger lag times (Figure 1A). For the largest polystyrene beads (200 nm diameter), we measured a ~ 30 -fold slower diffusion in stewartan compared to pure buffer (Figure 1B). In contrast, probing the diffusion of the same set of tracer particles in 40% (w/v) sucrose solutions resulted in a constant relative diffusion time, independent of the tracer size and matching the expected ~ 6 -fold larger viscosity compared to water.⁴⁷ This indicates that the varying hindrance factor reported by particles with different sizes is in fact a specific feature of the stewartan glycan matrix.

Stewartan Matrix Hinders the Diffusion of Fluorescent Tracer Particles in a Concentration-Dependent Manner. Bacterial biofilms are heterogeneous environments, in which the concentration of EPS was shown to vary in space (e.g., arrangement of EPS in multiple zones inside and around microcolonies)⁴⁸ and time (e.g., older, more mature biofilms were shown to have higher EPS content).⁴⁹ Therefore, we performed FCS measurements for differently sized fluorescent tracer particles in stewartan solutions of several concentrations ranging from 5 to 20 g/L. Furthermore, given the overall negative charge of stewartan,³¹ the negative ζ potential of the fluorescent beads (Table S1), and putative heterogeneities of local pH in biofilms,³ we reconstituted stewartan EPS at pH 5 and 8, to investigate the influence of solvent pH on stewartan matrix organization. Under all conditions, the diffusion times of small AF488 molecules were only slightly higher than those in free buffer (e.g., $\tau_d/\tau_{d,\text{buffer}} = 1.3 \pm 0.4$ at pH 5 in 20 g/L stewartan, Figure S2). The anomaly exponent α , obtained from fitting an anomalous diffusion model to the ACFs, was close to 1 in all cases (Figure S2), corresponding to free, unhindered diffusion.

For 60 nm beads, in contrast, we observed a pronounced increase of the hindrance factor at higher stewartan concentrations, with slightly larger values at lower pH (Figure 2A). The anomaly exponent decreased with increasing stewartan concentration to values lower than 1 and was significantly lower than that in aqueous buffer solution (e.g., $\alpha = 0.72 \pm 0.08$ for 60 nm beads in 20 g/L stewartan at pH 5, Figure 2B and Table S2), indicating subdiffusive dynamics of the beads. Interestingly, the anomaly exponent correlated with pH, i.e., it showed consistently lower values at pH 5 compared to those at pH 8. To ensure that the observed differences were not caused by particle aggregation, the average molecular

brightness in FCS was analyzed at different pH values, showing no significant variations (data not shown), in agreement with DLS measurements of particle sizes in pure buffer solutions (Table S1).

For 200 nm beads, FCS analysis showed a similar general dependence, i.e., increase of the hindrance factor and decrease of the anomaly exponent with increasing stewartan concentration, but no systematic differences with pH at the probed concentrations of 5 and 10 g/L stewartan.

Furthermore, FCS in diluted stewartan solutions from 0.1 to 2 g/L showed similar general trends of probe-size-dependent diffusion hindrance and weakly subdiffusive dynamics (Figure S2C,D). In analogy to previous studies,^{50–52} we determined the specific viscosity [$\eta_{\text{sp}} = (\eta_{\text{stewartan}} - \eta_{\text{buffer}})/\eta_{\text{buffer}}$] obtained from viscosimetric measurements in the same stewartan solutions. To compare these data with those obtained from FCS of beads and AF488, we defined a specific diffusion hindrance $\tau_{d,\text{sp}} = (\tau_d - \tau_{d,\text{buffer}})/\tau_{d,\text{buffer}}$. Note that $\tau_{d,\text{sp}}$ and a macroscopically determined η_{sp} are equivalent in the continuum limit, i.e., for particles that experience the full macroscopic viscosity, according to the Stokes–Einstein relation. All data were then pooled in a single log–log plot, evidencing two distinct regimes, i.e., 0.1–5 and 10–20 g/L (Figure 2C). Each group of data points was separately analyzed using a power-law fit ($\tau_{d,\text{sp}}$ or $\eta_{\text{sp}} \propto c^x$). We thus identified a transition concentration c_t (~ 7 g/L stewartan for all samples), defined as the intersection between the two fit curves within each sample. Below c_t , $\tau_{d,\text{sp}}$ for beads and η_{sp} scale with similar exponents in the range 0.9–1.2. Above c_t , similar exponents (3.7 and 3.6) are obtained for 200 nm beads and viscosimeter data, whereas 60 nm beads’ diffusion is characterized by a lower exponent of 1.7. It is worth noting that the presence of such different regimes could not be univocally identified in the case of AF488 diffusion data which were, therefore, not further analyzed.

Single-Particle Tracking Experiments Quantify Slow, Subdiffusive Dynamics of Larger Probes in Stewartan. FCS experiments with 200 nm beads could not be performed above 10 g/L stewartan due to the significantly slow dynamics, with diffusion times above several hundred milliseconds (ms). In this slow regime, we therefore used single-particle tracking (SPT) to analyze the dynamics of 200 nm beads also at high stewartan matrix concentrations. From the trajectories of individual particles (Figure 3A), we calculated tAMSDs (eq 3). As shown in Figure 3B, the ensemble-averaged tAMSD values clearly decreased with increasing stewartan concentration, in general agreement with the FCS results. We then fitted a linear model (eq 4) and an anomalous diffusion model (eq 5) to individual tAMSDs to obtain an approximate diffusion coefficient D_{app} from the first 10 points of tAMSDs ($\Delta t \leq 10\Delta t$ with $\Delta t = 31, 62,$ and 122 ms for experiments in pure buffer, sucrose, and stewartan, respectively) and the anomaly exponent α from the behavior of tAMSDs at longer times ($\Delta t \leq \tau \leq N\Delta t$ with $N = 20$ for sucrose, 30 for 5–15 g/L and 40 for 20 g/L stewartan). Due to the fast diffusion dynamics in pure buffer, the anomaly exponent and further parameters were not analyzed for this sample because of the short lengths of trajectories resulting in poor statistics. We observed strongly reduced dynamics in the stewartan matrix by almost three orders of magnitude under both pH conditions (e.g., $D_{\text{app}} = 2.5 \pm 1.8 \mu\text{m}^2/\text{s}$ in buffer to $0.006 \pm 0.003 \mu\text{m}^2/\text{s}$ in 20 g/L at pH 8, Figures 3C and S3A for pH 5 and Table S2).

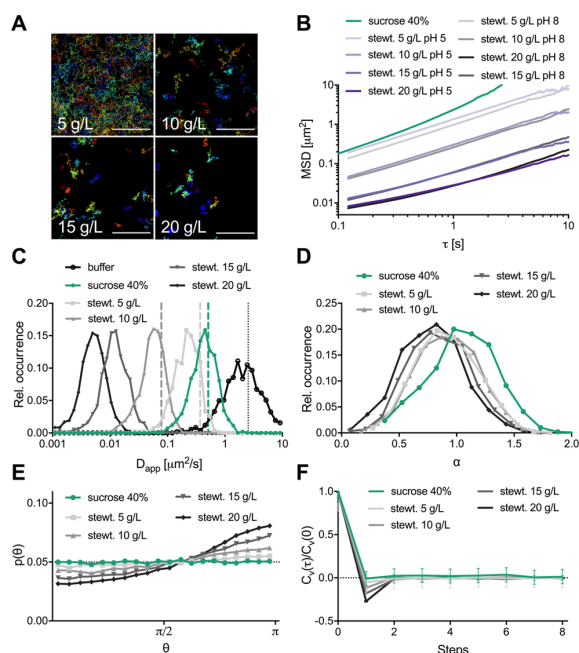


Figure 3. SPT analysis of polystyrene beads in stewartan matrices. (A) Image of trajectories from SPT measurements of 200 nm polystyrene beads in 5, 10, 15, and 20 g/L stewartan solutions at pH 8. The panel shows all trajectories obtained by tracking particles in a single image stack of 1200 frames, i.e., ~ 2.5 min acquisition. Scale bars denote $5 \mu\text{m}$. (B) Ensemble average of tMSDs of 200 nm polystyrene beads in 5–20 g/L stewartan solutions at pH 5, pH 8, and in 40% (w/v) sucrose solutions. (C, D) Distributions of apparent diffusion coefficient D_{app} (C) and anomaly exponent α (D) obtained by fitting of eqs 4 and 5 to individual tMSDs for each sample. Dashed lines in (C) show median D_{app} values from FCS analysis. In (C), also the D_{app} distribution obtained in pure 50 mM Tris–HCl pH 8 buffer is shown. (E) Probability distribution of angle θ (eq 6) between successive steps taken in an interval $\delta t = \Delta t = 62$ ms (sucrose) or 122 ms (stewartan) with lag time $\tau = \delta t$, pooled from all trajectories recorded in each sample. (F) Normalized velocity autocorrelation function of successive steps taken in an interval $\delta t = \Delta t = 62$ ms (sucrose) or 122 ms (stewartan), separated by one to 8 steps ($\Delta t \leq \tau \leq 8\Delta t$), calculated using eq 7. The panel shows the average over all individual trajectories, calculated in segments of 10 steps. Error bars show standard deviations over all segments. All graphs in (C)–(F) represent measurements at pH 8. Corresponding data at pH 5 are shown in Figure S3. The number of trajectories per sample is given in Table S2.

The distributions of the measured anomaly exponents were, similarly to those of D_{app} , fairly broad due to the limited statistics of individual trajectories but showed, on average, subdiffusive dynamics of the beads, i.e., a shift of the distributions to values smaller than 1 (e.g., $\alpha = 0.91 \pm 0.28$ in 5 g/L to $\alpha = 0.64 \pm 0.26$ at pH 5, Figures 3D and S3B for pH 5, and Table S2). In agreement with FCS experiments, the anomaly exponents at pH 5 and 8 were similar at low stewartan concentrations. However, at high stewartan concentrations, anomaly exponents were consistently lower at pH 5, similarly to FCS results obtained for 60 nm beads (Table S2). Moreover, a larger spread of D_{app} values measured for the low-pH sample was observed at high stewartan concentrations, compared to that at pH 8 (Figures 3C and S3A for pH 5).

As a control for normal Brownian motion, we analyzed SPT data acquired in 40% (w/v) sucrose solutions, resulting in an average anomaly exponent close to 1 ($\alpha = 1.04 \pm 0.29$), as shown in Figure 3B–D. We attribute the slightly higher-than-expected slope (see Figure 3B, for $t > \sim 0.5$ s) to the fast diffusion dynamics in this sample, leading in general to short trajectories: this causes poor statistics at large lag times and potential artifacts due to false assignment of the positions of multiple particles to a single trajectory.

To gain further insights into the stochastic process governing diffusion dynamics of beads inside the stewartan matrix, we calculated the distribution of angles between successive steps from all trajectories in the ensemble (eq 6). We observed a clear bias toward angles around π , i.e., a step in an opposite direction was more likely than a step in a similar direction with respect to the previous step (Figures 3E and S3C for pH 5). This bias was more pronounced at higher stewartan concentrations. In contrast, step angles in 40% (w/v) sucrose solutions were uniformly distributed, as expected for normal Brownian motion (Figure 3E). The anti-persistence of subsequent steps was also evident from the velocity autocorrelation (eq 7), showing a characteristic negative dip for successive steps that was absent in the sucrose control (Figures 3F and S3D for pH 5).

In summary, FCS and SPT experiments revealed a probe-size-dependent apparent viscosity within the stewartan matrix, with strong hindrance of large particles and subdiffusive dynamics, particularly pronounced at stewartan concentrations higher than c_t and at low pH.

Bacteriophage Particles Show Hindered Diffusion Dynamics and Trapping at High Stewartan Concentrations. The quantification of diffusive dynamics in stewartan matrices indicated hindered molecular mobility of 50–200 nm sized particles. In a biofilm, this size regime reflects the typical dimensions of tailed bacteriophages⁵³ and may be particularly relevant in the context of bacteriophage attack in which the EPS may provide protection against phages, by forming a diffusion barrier and inhibiting phage transport through the biofilm. To investigate diffusion dynamics of bacteriophages in our reconstituted system, we selected the dsDNA bacteriophage P22, as a model phage particle with a capsid diameter of about 70 nm.⁵⁴ P22 infects *Salmonella enterica* spp. *enterica* serovar Typhimurium (*S. Typhimurium*) and cannot enzymatically modify stewartan.⁵⁵ DNA inside the P22 capsid was fluorescently labeled and phage size was confirmed by DLS and FCS in pure buffer (see Table S1 in the SI). In addition, we found an overall negative ζ potential for P22 phages, similar to that of the 60 nm polystyrene beads (see the SI). Then, we performed FCS measurements in 10 and 20 g/L stewartan matrices at pH 5. Similarly to experiments with beads, we observed reduced diffusion dynamics of phage particles, with ~ 20 -fold higher diffusion times in 20 g/L stewartan compared to those in pure buffer ($\tau_d/\tau_{d,\text{buffer}} = 16 \pm 11$ in 20 g/L, see Figure 4A), and anomaly exponents lower than 1 ($\alpha = 0.78 \pm 0.12$ in 20 g/L, see Figure 4B). However, in comparison to 60 nm beads, the phage diffusion dynamics were ca. 3 times faster and less subdiffusive. In contrast, in 40% (w/v) sucrose solutions, phage particles and beads showed equally reduced dynamics, matching the expected value of around 6-fold reduction, and anomaly exponents around 1, indicating normal Brownian motion.

Interestingly, SPT at 20 g/L stewartan revealed that some phages appeared to be strongly confined, i.e., the trajectories

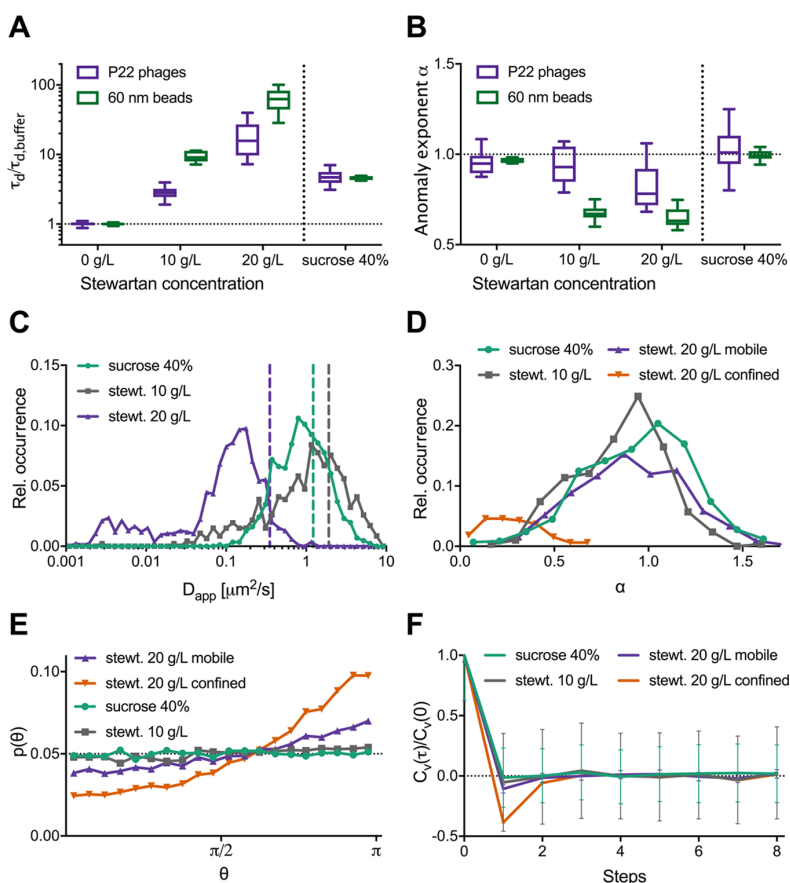


Figure 4. Bacteriophage diffusion dynamics in stewartan matrices measured with FCS and SPT. (A) Box plots of hindrance factor $\tau_d/\tau_{d,\text{buffer}}$ of fluorescently labeled P22 bacteriophage particles and 60 nm polystyrene beads in 10 or 20 g/L stewartan and 40% (w/v) sucrose solution, calculated by normalization of diffusion times to the average values obtained in 50 mM MES–NaOH pH 5 buffer. Data were obtained from at least 14 FCS measurements for each condition in at least two independent experiments. (B) Box plots of anomaly exponent α values obtained from FCS analysis of the measurements described in (A), by fitting a three-dimensional anomalous diffusion model to individual ACFs. (C–F) SPT analysis of P22 bacteriophage particles in 10 or 20 g/L stewartan and 40% (w/v) sucrose solution. The number of trajectories per sample is given in Table S3. Apparent diffusion coefficients D_{app} (C) were obtained by fitting a linear function (eq 4) to the first 10 points of individual taMSDs. (D) Histogram of anomaly exponent α obtained by fitting an anomalous diffusion model (eq 5) to individual taMSDs. Trajectories of measurements in 20 g/L stewartan were classified as mobile ($D_{\text{app}} > 0.01 \mu\text{m}^2/\text{s}$) or confined ($D_{\text{app}} < 0.01 \mu\text{m}^2/\text{s}$) subpopulations. An image of exemplary trajectories is shown in Figure S4. (E) Probability distribution of angle θ (eq 6) between successive steps taken in an interval $\delta t = \Delta t = 62$ ms with lag time $\tau = \delta t$ between the two steps, pooled from all trajectories under each condition. (F) Normalized velocity autocorrelation function of successive steps taken in an interval $\delta t = \Delta t = 62$ ms, separated by one to 8 steps ($\Delta t \leq \tau \leq 8\Delta t$), calculated using eq 7. The panel shows the average over all individual trajectories, calculated in segments of 10 steps. Error bars show standard deviations over all segments.

were restricted in a small area throughout the entire measurement (see Figure S4). Correspondingly, we found a population (~15% of all tracked phages in 20 g/L stewartan) of very slow phage particles in the D_{app} distribution determined from the first 10 points of individual taMSDs. This subset of phage particles is characterized by D_{app} values of $\sim 10^{-3}$ – $10^{-2} \mu\text{m}^2/\text{s}$ (Figure 4C), i.e., a more than 500-fold reduction compared to dynamics in buffer solution.

We used this quantity to group particles in 20 g/L stewartan samples into mobile ($D_{\text{app}} > 10^{-2} \mu\text{m}^2/\text{s}$) and confined ($D_{\text{app}} \leq 10^{-2} \mu\text{m}^2/\text{s}$) subpopulations. We then determined the distribution of the anomaly exponent α , the step angle distribution, and the velocity autocorrelation separately for particle trajectories in 10 g/L stewartan solutions, 40% (w/v) sucrose solutions, and for both populations (i.e., mobile and confined) in 20 g/L stewartan solutions. The distribution of

the anomaly exponent (Figure 4D), obtained by fitting a power law to the individual taMSDs ($\Delta t \leq \tau \leq N\Delta t$ with $N = 20$ for 10 g/L stewartan or 40% (w/v) sucrose and $N = 40$ for 20 g/L stewartan), revealed, at most, weakly subdiffusive dynamics at 10 g/L and for the mobile fraction at 20 g/L, whereas the distribution measured in sucrose solution was centered around 1 (see also Table S3). The confined population, however, appeared strongly subdiffusive ($\alpha = 0.28 \pm 0.15$). Similar to the SPT results observed for 200 nm beads, the angle distribution between successive steps of all trajectories in the ensemble showed a bias toward π (Figure 4E), which increased with stewartan concentration and was very pronounced for the confined phage particles. The probability $p(\theta)$ of observing angle values close to π observed for confined phages was even higher than that for 200 nm beads in 20 g/L stewartan. This feature indicates a strong anti-persistence of the underlying

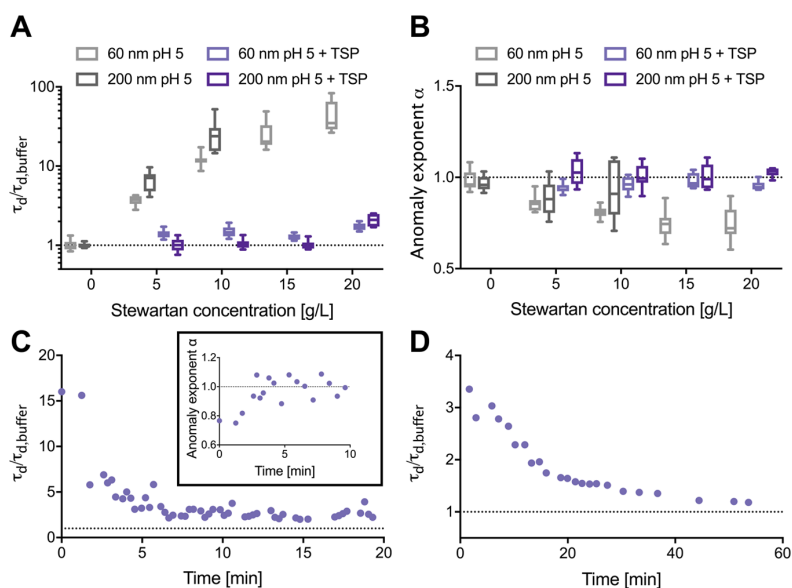


Figure 5. FCS analysis of fluorescent tracers in stewartan matrices in the presence of Φ Ea1h TSP stewartan depolymerase. (A) Box plots of hindrance factor $\tau_d/\tau_{d,buffer}$ in stewartan samples, calculated by normalization of diffusion times to the average values in pure 50 mM MES–NaOH pH 5 buffer, before and 1 h after incubation with 140 nM Φ Ea1h TSP, obtained from FCS analysis of measurements on 60 and 200 nm fluorescent polystyrene beads. Data were pooled from at least 12 measurements each in two independent experiments. (B) Box plots of anomaly exponent α obtained from FCS analysis of the measurements described in (A), by fitting a three-dimensional anomalous diffusion model to individual ACFs. Corresponding data at pH 8 are shown in Figure S5. (C) Hindrance factor in 10 g/L stewartan matrix at pH 5, obtained from consecutive FCS measurements on 60 nm fluorescent polystyrene beads during incubation with Φ Ea1h TSP (140 nM), started at $t = 0$ min. The inset shows anomaly parameter α values obtained for the first 10 min. (D) Hindrance factor of 140 nM Atto488-labeled Φ Ea1h TSP during depolymerization of a 10 g/L stewartan matrix at pH 5, measured in 50 mM MES–NaOH pH 5 buffer. Diffusion times were obtained from FCS analysis of consecutive measurements, by fitting a three-dimensional anomalous (C) or normal (D, $\alpha = 1$) diffusion model to individual ACFs.

random walk that also appears in the velocity autocorrelation as a characteristic negative dip for the subsequent step (Figure 4F). Of note, the anti-persistence relaxed after the second subsequent step. In contrast, trajectories of phage particles in sucrose solution are characterized by a uniform angle distribution and uncorrelated velocities between subsequent steps, indicative of unconstrained Brownian motion.

In summary, FCS and SPT analyses revealed significant hindrance of bacteriophage mobility in the stewartan matrix, subdiffusive dynamics at high concentrations and, additionally, trapping of a substantial fraction of phage particles.

Treatment of Stewartan Matrix by Bacteriophage Tailspike Enzymes Rapidly Restores Free Diffusion. To overcome glycan-based barriers within bacterial biofilms and on the surface of bacterial cells during phage infection, many bacteriophages are equipped with tailspike depolymerases, which specifically degrade extracellular glycan structures.^{28,56–58}

Bacteriophage Φ Ea1h infects *P. stewartii* and related species⁵⁹ and uses its TSP depolymerase of about 233 kDa to specifically depolymerize stewartan into single repeat unit oligosaccharides of 1163 Da molecular mass (cf. Scheme 1).³¹ We added Φ Ea1h TSP (140 nM) to stewartan solutions and measured particle diffusion dynamics to analyze how a bacteriophage depolymerase enzyme affects the polysaccharide glycan matrix structural organization. Φ Ea1h TSP treatment resulted in a significant reduction of the hindrance factor in stewartan solutions, for both 60 and 200 nm beads, under all tested conditions (Figures 5A and S5). After TSP treatment of the stewartan matrix, the resulting diffusion times were close to

those in water and the anomaly exponent approached values around 1 (Figure 5B), indicating a transition from subdiffusive dynamics to free diffusion. Only in 20 g/L stewartan samples was a ~ 2 -fold hindrance still observed.

To gain further insights into the dynamic changes of stewartan matrix organization in the presence of matrix degrading enzymes, we performed a series of FCS measurements with 60 nm beads in the presence of TSP in a 10 g/L stewartan sample. We observed a rapid decrease of the hindrance factor in the stewartan matrix from ~ 15 to ~ 2 within the first 10 min (Figure 5C) and an increase of the related anomaly exponent to ~ 1 within a few minutes (Figure 5C, inset). Φ Ea1h TSP depolymerase activity on the stewartan matrix requires rapid access to the substrate, which might initially be hindered by the high viscosity of the system. We, therefore, analyzed the diffusion of fluorescently labeled TSP during the enzyme action. While diffusion of TSP was initially around three times slower than that in buffer solution, it approached values close to that in buffer within ~ 45 min (Figure 5D). Biochemical analysis of stewartan depolymerization revealed similar activities of labeled and unlabeled TSP (Figure S6).

Taken together, these experiments demonstrate that degradation of the stewartan matrix by specific TSP enzymes drastically changes its structural organization and efficiently restores free, unhindered diffusion of particles on the \sim minute timescale.

DISCUSSION

In this work, we have applied FCS and SPT to analyze the size-dependent diffusion dynamics of fluorescent tracer particles in a pure stewartan biofilm matrix model. Compared to bulk diffusion assays that are commonly applied in biofilm research,^{60,61} these methods provide information with high temporal and spatial resolution.^{15,17} According to our results, the polysaccharide stewartan forms a glycan-polymer-based matrix, leading to subdiffusive particle mobility dynamics and strong hindrance of large particles at high polysaccharide concentrations. More specifically, diffusion and viscosity analysis as a function of stewartan concentration shows two characteristic scaling regimes, similar to the characteristic behavior reported for other polysaccharide and polymer systems.^{50–52,62} The observed power-law scaling of the specific diffusion hindrance (or specific viscosity) with exponents around 1 in the low-concentration regime and 3.5–4 in the high-concentration regime is consistent with a transition from a semidilute nonentangled polymer solution to a semidilute entangled system.^{52,63} We therefore assume that the transition concentration c_t (~ 7 g/L) likely represents the entanglement concentration c_e as an individual polymer material constant which has also been described for other glycan polymers.⁵² This conclusion is also in agreement with the estimated stewartan critical overlap concentration⁶⁴ (~ 1 g/L, see DLS measurements in the SI) being significantly lower than the estimated c_e .⁶⁵

At concentrations below c_t , we observed similar scaling exponents for both fluorescent bead diffusion and macroscopic viscosity, in agreement with the Rouse model prediction of 1.25.⁵² In the high-concentration regime (stewartan concentration $> c_t$), scaling exponents depended on probe size. The fact that the dynamics observed for both 200 nm beads and the specific viscosity exhibit similar variations with stewartan concentration (Figure 2C) suggests that beads of such size experience already the full macroscopic viscosity of the matrix, above the continuum limit. In contrast, 60 nm beads show a significantly lower scaling exponent and diffuse faster than the Stokes–Einstein relation would predict, based on the measured macroscopic viscosity. This indicates that the characteristic mesh size of the stewartan matrix is much closer to (and, possibly, slightly above) 60 nm than 200 nm.⁶⁶ This estimate is also supported by a recent study, reporting unexpectedly fast diffusion dynamics for particles with diameters smaller than the mesh size and radius of gyration (~ 75 nm for stewartan, see DLS measurements in the SI) of the polymer constituting the matrix.⁶⁷ Correspondingly, it is expected that much smaller particles (e.g., AF488) diffuse almost exclusively in the interstitial space and, thus, do not experience a significant viscous drag,⁶⁶ in very good agreement with our data.

However, diffusing particles will not only be affected by the stewartan mesh size. In addition, noncovalent interactions with the matrix might occur. Stewartan contains a negatively charged glucuronic acid building block, with an estimated pK_a of about 3 when within the stewartan polymer.⁶⁸ The overall negative charge accounts for strong water association, and it may affect interactions among stewartan chains and the penetration of other charged molecules. For example, it was shown that the matrix charge had an important influence on the ability of antibiotics to penetrate bacterial biofilms.^{11,21,69} The higher, more heterogeneous diffusion hindrance and more

pronounced subdiffusion that we observed at lower pH indeed suggest an important role of charge–charge interactions in this context. This might be a consequence of reduced electrostatic repulsion between the negatively charged polystyrene beads and stewartan at low pH. On the other hand, the solvent pH could directly affect stewartan matrix organization, by modulating the association or the entanglement of the polysaccharide chains. Further evidence that the transport of particles in the EPS might, at least, be modulated by properties such as charge or surface chemistry is provided by the comparison of diffusion dynamics of 60 nm polystyrene beads and P22 bacteriophages. These particles are similar in size and yet show a ca. 3-fold difference in mobility. Nevertheless, these differences were only minor compared to the variations in the diffusion hindrance reported by probes with different sizes. This indicates that the molecular size may still be the major factor determining diffusion dynamics in stewartan EPS.

We, therefore, conclude that the stewartan EPS is probably not a fully inert meshwork but rather acts as a reactive molecular sieve, likely allowing selective transport of particles. Similar characteristics were previously observed for mucin, i.e., glycosylated protein hydrogels.⁷⁰ Future studies are needed to more specifically investigate the role of salts, divalent ions, and pH, since these factors were recently shown to modulate the mechanical properties of reconstituted mucin¹² and alginate¹⁰ hydrogels. Diffusion of charged molecules through charged hydrogel networks has also been addressed by theoretical work in recent years,^{71,72} although most studies have focused on tracer particles much smaller than those present in our system.

The observation of a strong concentration dependence of diffusion hindrance in stewartan matrices could be very relevant in the context of actual biofilms that are characterized by heterogeneous EPS densities in space and time.^{48,49,73} We have estimated the physiological concentration of stewartan EPS in 65 h old *P. stewartii* biofilms to be, on average, ~ 15 g/L, i.e., ca. 2-fold higher than the identified entanglement concentration. Previous studies on other extracellular biofilm polysaccharides report lower concentrations, below their entanglement concentration.⁶⁴ This emphasizes that biofilm polysaccharides from different bacteria and microbiological contexts may feature diverse modes of structural organization. Our results indicate that stewartan EPS still provides unrestrained transport for small molecules, such as water and nutrients, but significant hindrance for larger particles with sizes around or above the mesh size. This implies that, for example, *P. stewartii* bacteria will remain immobile in an intact stewartan matrix, and this might be important for immobilization in the plant xylem water flow. Compared to the case of a complete biofilm, our diffusion data can be most likely considered as an upper estimate for transport dynamics, since the presence of other macromolecules and bacteria might further slow diffusion down.

Another very important aspect of biofilm EPS function is protection against phages. The EPS matrix is hypothesized to form a diffusion barrier, inhibiting phage movement through biofilms.^{20,23,74} The model phage P22 used in this work has a similar morphology and size, compared to native phages infecting *P. stewartii*, such as Φ Ea1h.⁵⁹ However, in the presence of P22, the stewartan matrix remains intact because the P22 TSP depolymerase is not active on this polysaccharide.⁵⁵ Based on FCS and SPT investigations, we report a stewartan-concentration-dependent mobility of P22 bacteriophage particles. The two techniques provide similar results

regarding the dynamics of the mobile bead and phage populations, in agreement with recent studies.^{42,75} Compared to previously reported FCS-based studies of bacteriophage diffusion in biofilms,²⁰ we observe a stronger diffusion hindrance of phage particles in our system. It is worth noting that FCS cannot quantitatively detect immobile particles and, therefore, is not the technique of choice for the study of strongly confined dynamics. Our observation of substantially lower phage mobility and even trapping in concentrated stewartan matrices may be relevant also for actual biofilms: higher bacteriophage infection rates have been found in fact in less mature or less dense areas of biofilms (e.g., bacteria on the edge of colonies), which may have lower local EPS densities.^{23,76,77} Apart from indicating a low phage mobility, our measurements quantify the presence of anomalous subdiffusion, which hinders long-range transport and has been frequently observed in crowded biomacromolecule solutions, for example the cytoplasm of living cells.^{34,44,78} Considering the diffusion coefficient and anomaly exponent estimated for the mobile fraction of phages in 20 g/L stewartan, a phage particle would take, on average, around 15 h to diffuse through a 100 μm thick biofilm matrix, compared to ~ 1.3 h if the diffusion were not anomalous. Furthermore, our SPT data provide insights into the stochastic process underlying bead and phage diffusion in stewartan, by evidencing a random walk characterized by anti-persistence of subsequent steps, most likely due to encounters with the dense, putatively viscoelastic stewartan matrix. In this context, the observed trapping of phage particles is in agreement with the hypothesized stewartan matrix mesh size in the range ~ 50 – 100 nm, potentially halting phage particles in some meshes that are (transiently) smaller than the average. Similar characteristics have recently been reported for the diffusion of micron-sized particles through mucus biofilms.⁷⁹ It is important to note, however, that trapping might also be related to the presence of noncontact phage particles under these conditions,⁵⁸ although no difference in average particle size was observed at pH 5 compared to phage buffer (Table S1). Furthermore, the fluorescence intensity signal originating from trapped phages was generally not higher than the signal from mobile particles, thus excluding the possibility of significant phage aggregation. Recent work on modeling of population dynamics in biofilms containing bacteria and phages suggests that the mobility of phages is an important parameter for the coexistence of phages and bacteria or successful killing.²² In this regard, our quantification provides experimental estimates that could help refine such models with reasonable parameter values.

Finally, we show that depolymerization of stewartan by bacteriophage tailspike enzymes rapidly reduces the hindrance of diffusion within the matrix, resulting in free diffusion with dynamics similar to those in pure buffer. Interestingly, we found a delay between the decrease of the diffusion hindrance of beads (occurring after ca. 2 min) and that of labeled tailspike enzyme (occurring after ca. 15 min). We suppose that the persistently reduced mobility of the enzyme is likely due to specific substrate-binding interactions with the slowly diffusing polysaccharide chains. Furthermore, this result suggests a sensitive dependence of the diffusion hindrance on stewartan chain length: a few initial cleavages of long, entangled chains appear sufficient for strong hindrance reduction of tracer particles, within the first few minutes of the reaction. This might be due to a transition from an entangled polymer

network to a solution of unentangled chains (in other words, the reduction in molecular size causes an increase of c_e). Afterward, the enzyme appears to still interact with the residual, slowly diffusing, medium-length polysaccharide chains, probably working in processive enzymatic mode, as often found for TSP depolymerases.⁸⁰ This has, however, only minor additional impact on the diffusion dynamics of particles.

Our data show the high efficacy of tailspike enzymes, which have come into focus in recent years as potential novel antimicrobial substances.^{27,28} Reconstituted systems such as our stewartan polysaccharide EPS model, combined with FCS/SPT measurements, could help to further optimize these enzymes, e.g., by introducing and testing mutations that provide even more efficient cleavage^{81,82} or promote recognition of multiple polysaccharide substrates. An exciting application of such enzymes is phage engineering, allowing enhancement of host specificity or killing efficiency of bacteriophages in biofilms.⁸³ During infection, glycan depolymerases may clearly provide a fitness advantage for phages to evade trapping inside dense biofilm regions or accelerate target search. The presented approach provides a promising experimental strategy to explore dynamic changes of bacterial biofilm EPS in the context of bacteriophage infections.

An underlying assumption in our study is that alterations in the extracellular glycan organization are needed to modulate dynamics within the biofilm. This hypothesis is supported by the fact that a large number of carbohydrate active enzymes exist in bacteria and bacteriophages.⁸⁴ Furthermore, gene clusters switched on in *P. stewartii* during biofilm production mainly code for polysaccharide synthesis, polymerization, and export proteins.³⁰ Therefore, at least for plant pathogens such as *P. stewartii*, the exopolysaccharide might play a fundamental role in the modulation of macromolecule dynamics in the biofilm. We, thus, propose that the pure stewartan matrix examined in this work provides a simplified model to study relevant physical properties of more complex biofilms. Previous work indicated similar characteristics of intact bacterial biofilms when compared to our analyses of stewartan.^{13,14,24,25} However, these studies did not focus specifically on the chemical or biophysical properties and density of EPS. We emphasize that it is important to take into account the biofilm molecular composition, in this case, pure polysaccharide, to increase our understanding of the extent to which individual physicochemical properties of all molecules in the EPS will govern the overall biofilm characteristics and their regulation in space and time.

CONCLUSIONS

Overall, our results suggest that the glycan matrix of bacterial biofilms acts as a selective sieve of entangled polymer strands, allowing modulated transport of molecules and pathogens based on their size and surface properties. Our investigations also demonstrate the high efficacy of EPS-depolymerizing enzymes in modifying the biofilm-matrix structure. These findings may have important implications in the context of bacteriophage infections, affecting bacteriophage mobility in biofilms.^{22,25} Future studies are needed to further explore the molecular details of the EPS structural organization and matrix-particle interactions. In conclusion, our reconstituted approach highlights the connection between the biophysical characteristics of a biofilm and the specific properties and composition of its exopolysaccharide matrix. This provides a

promising starting point for more complex biofilm-matrix models, which will also include other macromolecules such as extracellular proteins and DNA.

■ ASSOCIATED CONTENT

Supporting Information

The Supporting Information is available free of charge on the ACS Publications website at DOI: [10.1021/acs.biomac.9b00938](https://doi.org/10.1021/acs.biomac.9b00938).

Supporting methods (stewartan concentration determination, P22 phage labeling, purification and labeling of TSP, description of DLS); tables listing the properties of tracer particles and average diffusion coefficients of FCS/SPT measurements on beads; viscosity measurements of sucrose solutions; FCS analysis of AF488 diffusion and beads at low stewartan concentrations; SPT analysis at pH 5; SPT analysis of phages; FCS analysis with TSP at pH 8, biochemical assay of TSP activity (Figures S1–S6) (PDF)

■ AUTHOR INFORMATION

Corresponding Authors

*E-mail: barbirz@uni-potsdam.de (S.B.).

*E-mail: chiantia@uni-potsdam.de (S.C.).

ORCID

Stefanie Barbirz: 0000-0001-6101-9862

Salvatore Chiantia: 0000-0003-0791-967X

Author Contributions

V.D. contributed with conceptualization, methodology, experiments, analysis, writing of the manuscript, visualization, and software. T.I. was involved in conceptualization, methodology, experiments, and editing the manuscript. S.B. and S.C. contributed with conceptualization, methodology, writing the manuscript, supervision, and funding acquisition.

Funding

S.B. was funded by the Deutsche Forschungsgemeinschaft (grant number BA 4046/1-2). T.I. received a Max Planck Society grant (IMPRS Multiscale Bio-Systems).

Notes

The authors declare no competing financial interest.

■ ACKNOWLEDGMENTS

The authors thank Mandy Schietke for technical assistance, Ismail Dahmani and Martin Wolff for support with DLS, and Antje Voelkel for support with viscosimeter measurements.

■ ABBREVIATIONS

ACF, autocorrelation function; AF488, Alexa Fluor 488; DLS, dynamic light scattering; EPS, extrapolymeric substance; FCS, fluorescence correlation spectroscopy; MSD, mean-square displacement; SPT, single-particle tracking; taMSD, time-averaged mean-square displacement; TSP, tailspike protein

■ REFERENCES

- Hall-Stoodley, L.; Costerton, J. W.; Stoodley, P. Bacterial Biofilms: From the Natural Environment to Infectious Diseases. *Nat. Rev. Microbiol.* **2004**, *2*, 95–108.
- Stewart, P. S.; Franklin, M. J. Physiological Heterogeneity in Biofilms. *Nat. Rev. Microbiol.* **2008**, *6*, 199–210.

- Flemming, H.-C.; Wingender, J.; Szewzyk, U.; Steinberg, P.; Rice, S. A.; Kjelleberg, S. Biofilms: An Emergent Form of Bacterial Life. *Nat. Rev. Microbiol.* **2016**, *14*, 563–575.

- Sutherland, I. W. The Biofilm Matrix—an Immobilized but Dynamic Microbial Environment. *Trends Microbiol.* **2001**, *9*, 222–227.

- Branda, S. S.; Vik, S.; Friedman, L.; Kolter, R. Biofilms: The Matrix Revisited. *Trends Microbiol.* **2005**, *13*, 20–26.

- Flemming, H.-C.; Wingender, J. The Biofilm Matrix. *Nat. Rev. Microbiol.* **2010**, *8*, 623–633.

- Lieleg, O.; Ribbeck, K. Biological Hydrogels as Selective Diffusion Barriers. *Trends Cell Biol.* **2011**, *21*, 543–551.

- Witten, J.; Ribbeck, K. The Particle in the Spider's Web: Transport through Biological Hydrogels. *Nanoscale* **2017**, *9*, No. 8080.

- Amsden, B. Solute Diffusion within Hydrogels. Mechanisms and Models. *Macromolecules* **1998**, *31*, 8382–8395.

- Körstgens, V.; Flemming, H.-C.; Wingender, J.; Borchard, W. Influence of Calcium Ions on the Mechanical Properties of a Model Biofilm of Mucoid *Pseudomonas aeruginosa*. *Water Sci. Technol.* **2001**, *43*, 49–57.

- Singh, R.; Sahore, S.; Kaur, P.; Rani, A.; Ray, P. Penetration Barrier Contributes to Bacterial Biofilm-Associated Resistance against Only Select Antibiotics, and Exhibits Genus-, Strain- and Antibiotic-Specific Differences. *Pathog. Dis.* **2016**, *74*, No. ftw056.

- Wagner, C. E.; Turner, B. S.; Rubinstein, M.; McKinley, G. H.; Ribbeck, K. A Rheological Study of the Association and Dynamics of MUC5AC Gels. *Biomacromolecules* **2017**, *18*, 3654–3664.

- Peulen, T.-O.; Wilkinson, K. J. Diffusion of Nanoparticles in a Biofilm. *Environ. Sci. Technol.* **2011**, *45*, 3367–3373.

- Birjiniuk, A.; Billings, N.; Nance, E.; Hanes, J.; Ribbeck, K.; Doyle, P. S. Single Particle Tracking Reveals Spatial and Dynamic Organization of the *Escherichia Coli* Biofilm Matrix. *New J. Phys.* **2014**, *16*, No. 085014.

- Billings, N.; Birjiniuk, A.; Samad, T. S.; Doyle, P. S.; Ribbeck, K. Material Properties of Biofilms—a Review of Methods for Understanding Permeability and Mechanics. *Rep. Prog. Phys.* **2015**, *78*, No. 036601.

- Hartmann, R.; Singh, P. K.; Pearce, P.; Mok, R.; Song, B.; Díaz-Pascual, F.; Dunkel, J.; Drescher, K. Emergence of Three-Dimensional Order and Structure in Growing Biofilms. *Nat. Phys.* **2019**, *15*, 251–256.

- Sankaran, J.; Karampatzakis, A.; Rice, S. A.; Wohland, T. Quantitative Imaging and Spectroscopic Technologies for Microbiology. *FEMS Microbiol. Lett.* **2018**, *365*, No. fny075.

- Elson, E. L.; Magde, D. Fluorescence Correlation Spectroscopy. I. Conceptual Basis and Theory. *Biopolymers* **1974**, *13*, 1–27.

- Saxton, M. J.; Jacobson, K. SINGLE-PARTICLE TRACKING: Applications to Membrane Dynamics. *Annu. Rev. Biophys. Biomol. Struct.* **1997**, *26*, 373–399.

- Briandet, R.; Lacroix-Gueu, P.; Renault, M.; Lecart, S.; Meylheuc, T.; Bidnenko, E.; Steenkeste, K.; Bellon-Fontaine, M.-N.; Fontaine-Aupart, M.-P. Fluorescence Correlation Spectroscopy to Study Diffusion and Reaction of Bacteriophages inside Biofilms. *Appl. Environ. Microbiol.* **2008**, *74*, 2135–2143.

- Tseng, B. S.; Zhang, W.; Harrison, J. J.; Quach, T. P.; Song, J. L.; Penterman, J.; Singh, P. K.; Chopp, D. L.; Packman, A. I.; Parsek, M. R. The Extracellular Matrix Protects *Pseudomonas aeruginosa* Biofilms by Limiting the Penetration of Tobramycin. *Environ. Microbiol.* **2013**, *15*, 2865–2878.

- Simmons, M.; Drescher, K.; Nadell, C. D.; Bucci, V. Phage Mobility Is a Core Determinant of Phage-Bacteria Coexistence in Biofilms. *ISME J.* **2018**, *12*, 531–543.

- Vidakovic, L.; Singh, P. K.; Hartmann, R.; Nadell, C. D.; Drescher, K. Dynamic Biofilm Architecture Confers Individual and Collective Mechanisms of Viral Protection. *Nat. Microbiol.* **2018**, *3*, 26–31.

- Guiot, E.; Georges, P.; Brun, A.; Fontaine-Aupart, M. P.; Bellon-Fontaine, M. N.; Briandet, R. Heterogeneity of Diffusion

Inside Microbial Biofilms Determined by Fluorescence Correlation Spectroscopy Under Two-Photon Excitation. *Photochem. Photobiol.* **2007**, *75*, 570–578.

(25) Aldeek, F.; Schneider, R.; Fontaine-Aupart, M.-P.; Mustin, C.; Lécart, S.; Merlin, C.; Block, J.-C. Patterned Hydrophobic Domains in the Exopolymer Matrix of *Shewanella oneidensis* MR-1 Biofilms. *Appl. Environ. Microbiol.* **2013**, *79*, 1400–1402.

(26) Habimana, O.; Steenkeste, K.; Fontaine-Aupart, M.-P.; Bellon-Fontaine, M.-N.; Kulakauskas, S.; Briand, R. Diffusion of Nanoparticles in Biofilms Is Altered by Bacterial Cell Wall Hydrophobicity. *Appl. Environ. Microbiol.* **2011**, *77*, 367–368.

(27) Chan, B.; Abedon, S. Bacteriophages and Their Enzymes in Biofilm Control. *Curr. Pharm. Des.* **2014**, *21*, 85–99.

(28) Pires, D. P.; Oliveira, H.; Melo, L. D. R.; Sillankorva, S.; Azeredo, J. Bacteriophage-Encoded Depolymerases: Their Diversity and Biotechnological Applications. *Appl. Microbiol. Biotechnol.* **2016**, *100*, 2141–2151.

(29) Roper, M. C. *Pantoea Stewartii* Subsp. *Stewartii*: Lessons Learned from a Xylem-Dwelling Pathogen of Sweet Corn. *Mol. Plant Pathol.* **2011**, *12*, 628–637.

(30) Wang, X.; Yang, F.; von Bodman, S. B. The Genetic and Structural Basis of Two Distinct Terminal Side Branch Residues in Stewartan and Amylovoran Exopolysaccharides and Their Potential Role in Host Adaptation. *Mol. Microbiol.* **2012**, *83*, 195–207.

(31) Nimtz, M.; Mort, A.; Wray, V.; Domke, T.; Zhang, Y.; Coplin, D. L.; Geider, K. Structure of *Stewartia*, the Capsular Exopolysaccharide from the Corn Pathogen *Erwinia Stewartii*. *Carbohydr. Res.* **1996**, *288*, 189–201.

(32) Hartung, J. S.; Fulbright, D. W.; Klos, E. J. Cloning of a Bacteriophage Polysaccharide Depolymerase Gene and Its Expression in *Erwinia Amylovora*. *Mol. Plant-Microbe Interact.* **1988**, *1*, 87–93.

(33) Masuko, T.; Minami, A.; Iwasaki, N.; Majima, T.; Nishimura, S.-I.; Lee, Y. C. Carbohydrate Analysis by a Phenol–Sulfuric Acid Method in Microplate Format. *Anal. Biochem.* **2005**, *339*, 69–72.

(34) Weiss, M.; Elsner, M.; Kartberg, F.; Nilsson, T. Anomalous Subdiffusion Is a Measure for Cytoplasmic Crowding in Living Cells. *Biophys. J.* **2004**, *87*, 3518–3524.

(35) Banks, D. S.; Fradin, C. Anomalous Diffusion of Proteins Due to Molecular Crowding. *Biophys. J.* **2005**, *89*, 2960–2971.

(36) Petrásek, Z.; Schwill, P. Precise Measurement of Diffusion Coefficients Using Scanning Fluorescence Correlation Spectroscopy. *Biophys. J.* **2008**, *94*, 1437–1448.

(37) Schindelin, J.; Arganda-Carreras, I.; Frise, E.; Kaynig, V.; Longair, M.; Pietzsch, T.; Preibisch, S.; Rueden, C.; Saalfeld, S.; Schmid, B.; Tinevez, J.-Y.; White, D. J.; Hartenstein, V.; Eliceiri, K.; Tomancak, P.; Cardona, A. Fiji: An Open-Source Platform for Biological-Image Analysis. *Nat. Methods* **2012**, *9*, 676–682.

(38) Tinevez, J.-Y.; Perry, N.; Schindelin, J.; Hoopes, G. M.; Reynolds, G. D.; Laplantine, E.; Bednarek, S. Y.; Shorte, S. L.; Eliceiri, K. W. TrackMate: An Open and Extensible Platform for Single-Particle Tracking. *Methods* **2017**, *115*, 80–90.

(39) Metzler, R.; Jeon, J.-H.; Cherstvy, A. G.; Barkai, E. Anomalous Diffusion Models and Their Properties: Non-Stationarity, Non-Ergodicity, and Ageing at the Centenary of Single Particle Tracking. *Phys. Chem. Chem. Phys.* **2014**, *16*, 24128–24164.

(40) Weber, S. C.; Thompson, M. A.; Moerner, W. E.; Spakowitz, A. J.; Theriot, J. A. Analytical Tools To Distinguish the Effects of Localization Error, Confinement, and Medium Elasticity on the Velocity Autocorrelation Function. *Biophys. J.* **2012**, *102*, 2443–2450.

(41) Weiss, M. Single-Particle Tracking Data Reveal Anticorrelated Fractional Brownian Motion in Crowded Fluids. *Phys. Rev. E* **2013**, *88*, No. 010101.

(42) Struntz, P.; Weiss, M. The Hitchhiker's Guide to Quantitative Diffusion Measurements. *Phys. Chem. Chem. Phys.* **2018**, *20*, 28910–28919.

(43) Speckner, K.; Stadler, L.; Weiss, M. Anomalous Dynamics of the Endoplasmic Reticulum Network. *Phys. Rev. E* **2018**, *98*, No. 012406.

(44) Etoc, F.; Balloul, E.; Vicario, C.; Normanno, D.; Liße, D.; Sittner, A.; Piehler, J.; Dahan, M.; Coppey, M. Non-Specific Interactions Govern Cytosolic Diffusion of Nanosized Objects in Mammalian Cells. *Nat. Mater.* **2018**, *17*, 740–746.

(45) Zhang, Z.; Nadezhina, E.; Wilkinson, K. J. Quantifying Diffusion in a Biofilm of *Streptococcus mutans*. *Antimicrob. Agents Chemother.* **2011**, *55*, 1075–1081.

(46) Sandrin, D.; Wagner, D.; Sitta, C. E.; Thoma, R.; Felekyan, S.; Hermes, H. E.; Janiak, C.; de Sousa Amadeu, N.; Kühnemuth, R.; Löwen, H.; Egelhaaf, S. U.; Seidel, C. A. M. Diffusion of Macromolecules in a Polymer Hydrogel: From Microscopic to Macroscopic Scales. *Phys. Chem. Chem. Phys.* **2016**, *18*, 12860–12876.

(47) Telis, V. R. N.; Telis-Romero, J.; Mazzotti, H. B.; Gabas, A. L. Viscosity of Aqueous Carbohydrate Solutions at Different Temperatures and Concentrations. *Int. J. Food Prop.* **2007**, *10*, 185–195.

(48) Lawrence, J. R.; Swerhone, G. D. W.; Kuhlicke, U.; Neu, T. R. In Situ Evidence for Microdomains in the Polymer Matrix of Bacterial Microcolonies. *Can. J. Microbiol.* **2007**, *53*, 450–458.

(49) Xiao, J.; Koo, H. Structural Organization and Dynamics of Exopolysaccharide Matrix and Microcolonies Formation by *Streptococcus mutans* in Biofilms. *J. Appl. Microbiol.* **2009**, *108*, 2103–2113.

(50) Krause, W. E.; Bellomo, E. G.; Colby, R. H. Rheology of Sodium Hyaluronate under Physiological Conditions. *Biomacromolecules* **2001**, *2*, 65–69.

(51) Ren, Y.; Ellis, P. R.; Sutherland, I. W.; Ross-Murphy, S. B. Dilute and Semi-Dilute Solution Properties of an Exopolysaccharide from *Escherichia coli* Strain S61. *Carbohydr. Polym.* **2003**, *52*, 189–195.

(52) Ganesan, M.; Knier, S.; Younger, J. G.; Solomon, M. J. Associative and Entanglement Contributions to the Solution Rheology of a Bacterial Polysaccharide. *Macromolecules* **2016**, *49*, 8313–8321.

(53) Ackermann, H.-W.; Prangishvili, D. Prokaryotic Viruses Studied by Electron Microscopy. *Arch. Virol.* **2012**, *157*, 1843–1849.

(54) Chang, J.; Weigele, P.; King, J.; Chiu, W.; Jiang, W. Cryo-EM Asymmetric Reconstruction of Bacteriophage P22 Reveals Organization of Its DNA Packaging and Infecting Machinery. *Structure* **2006**, *14*, 1073–1082.

(55) Steinbacher, S.; Baxa, U.; Miller, S.; Weintraub, A.; Seckler, R.; Huber, R. Crystal Structure of Phage P22 Tailspike Protein Complexed with Salmonella Sp. O-Antigen Receptors. *Proc. Natl. Acad. Sci. U.S.A.* **1996**, *93*, 10584–10588.

(56) Andres, D.; Hanke, C.; Baxa, U.; Seul, A.; Barbirz, S.; Seckler, R. Tailspike Interactions with Lipopolysaccharide Effect DNA Ejection from Phage P22 Particles *in Vitro*. *J. Biol. Chem.* **2010**, *285*, 36768–36775.

(57) Barbirz, S.; Müller, J. J.; Uetrecht, C.; Clark, A. J.; Heinemann, U.; Seckler, R. Crystal Structure of *Escherichia coli* Phage HK620 Tailspike: Podoviral Tailspike Endoglycosidase Modules Are Evolutionarily Related. *Mol. Microbiol.* **2008**, *69*, 303–316.

(58) Broeker, N. K.; Roske, Y.; Valleriani, A.; Stephan, M. S.; Andres, D.; Koetz, J.; Heinemann, U.; Barbirz, S. Time-Resolved DNA Release from an O-Antigen-Specific Salmonella Bacteriophage with a Contractile Tail. *J. Biol. Chem.* **2019**, *294*, 11751–11761.

(59) Müller, I.; Lurz, R.; Kube, M.; Quedenau, C.; Jelkmann, W.; Geider, K. Molecular and Physiological Properties of Bacteriophages from North America and Germany Affecting the Fire Blight Pathogen *Erwinia Amylovora*. *Microb. Biotechnol.* **2011**, *4*, 735–745.

(60) González, S.; Fernández, L.; Gutiérrez, D.; Campelo, A. B.; Rodríguez, A.; García, P. Analysis of Different Parameters Affecting Diffusion, Propagation and Survival of Staphylophages in Bacterial Biofilms. *Front. Microbiol.* **2018**, *9*, No. 2348.

(61) Kumon, H.; Tomochika, K.; Matunaga, T.; Ogawa, M.; Ohmori, H. A Sandwich Cup Method for the Penetration Assay of Antimicrobial Agents through *Pseudomonas* Exopolysaccharides. *Microbiol. Immunol.* **1994**, *38*, 615–619.

(62) Roger, S.; Sang, Y. Y. C.; Bee, A.; Perzynski, R.; Di Meglio, J. M.; Ponton, A. Structural and Multi-Scale Rheophysical Investigation

of Diphasic Magneto-Sensitive Materials Based on Biopolymers. *Eur. Phys. J. E: Soft Matter Biol. Phys.* **2015**, *38*, No. 88.

(63) Heo, Y.; Larson, R. G. The Scaling of Zero-Shear Viscosities of Semidilute Polymer Solutions with Concentration. *J. Rheol.* **2005**, *49*, 1117–1128.

(64) Ganesan, M.; Stewart, E. J.; Szafranski, J.; Satorius, A. E.; Younger, J. G.; Solomon, M. J. Molar Mass, Entanglement, and Associations of the Biofilm Polysaccharide of *Staphylococcus epidermidis*. *Biomacromolecules* **2013**, *14*, 1474–1481.

(65) Colby, R. H. Structure and Linear Viscoelasticity of Flexible Polymer Solutions: Comparison of Polyelectrolyte and Neutral Polymer Solutions. *Rheol. Acta* **2010**, *49*, 425–442.

(66) Cai, L.-H.; Panyukov, S.; Rubinstein, M. Mobility of Nonsticky Nanoparticles in Polymer Liquids. *Macromolecules* **2011**, *44*, 7853–7863.

(67) Nath, P.; Mangal, R.; Kohle, F.; Choudhury, S.; Narayanan, S.; Wiesner, U.; Archer, L. A. Dynamics of Nanoparticles in Entangled Polymer Solutions. *Langmuir* **2018**, *34*, 241–249.

(68) Wang, H. M.; Loganathan, D.; Linhardt, R. J. Determination of the PKa of Glucuronic Acid and the Carboxy Groups of Heparin by ¹³C-Nuclear-Magnetic-Resonance Spectroscopy. *Biochem. J.* **1991**, *278*, 689–695.

(69) Daddi Oubekka, S.; Briandet, R.; Fontaine-Aupart, M.-P.; Steenkeste, K. Correlative Time-Resolved Fluorescence Microscopy to Assess Antibiotic Diffusion-Reaction in Biofilms. *Antimicrob. Agents Chemother.* **2012**, *56*, 3349–3358.

(70) Lieleg, O.; Vladescu, I.; Ribbeck, K. Characterization of Particle Translocation through Mucin Hydrogels. *Biophys. J.* **2010**, *98*, 1782–1789.

(71) Zhang, X.; Hansing, J.; Netz, R. R.; DeRouchey, J. E. Particle Transport through Hydrogels Is Charge Asymmetric. *Biophys. J.* **2015**, *108*, 530–539.

(72) Hansing, J.; Duke, J. R.; Fryman, E. B.; DeRouchey, J. E.; Netz, R. R. Particle Diffusion in Polymeric Hydrogels with Mixed Attractive and Repulsive Interactions. *Nano Lett.* **2018**, *18*, 5248–5256.

(73) Lawrence, J.; Neu, T.; Swerhone, G. D. Application of Multiple Parameter Imaging for the Quantification of Algal, Bacterial and Exopolymer Components of Microbial Biofilms. *J. Microbiol. Methods* **1998**, *32*, 253–261.

(74) Sutherland, I. W.; Hughes, K. A.; Skillman, L. C.; Tait, K. The Interaction of Phage and Biofilms. *FEMS Microbiol. Lett.* **2004**, *232*, 1–6.

(75) Harwardt, M.-L. I. E.; Dietz, M. S.; Heilemann, M.; Wohland, T. SPT and Imaging FCS Provide Complementary Information on the Dynamics of Plasma Membrane Molecules. *Biophys. J.* **2018**, *114*, 2432–2443.

(76) Abedon, S. T. Bacteriophage Exploitation of Bacterial Biofilms: Phage Preference for Less Mature Targets? *FEMS Microbiol. Lett.* **2016**, *363*, No. fnv246.

(77) Hansen, M. F.; Svenningsen, S. L.; Røder, H. L.; Middelboe, M.; Burmølle, M. Big Impact of the Tiny: Bacteriophage–Bacteria Interactions in Biofilms. *Trends Microbiol.* **2019**, *27*, 739–752.

(78) Dunsing, V.; Luckner, M.; Zühlke, B.; Petazzi, R. A.; Herrmann, A.; Chiantia, S. Optimal Fluorescent Protein Tags for Quantifying Protein Oligomerization in Living Cells. *Sci. Rep.* **2018**, *8*, No. 10634.

(79) Cherstvy, A. G.; Thapa, S.; Wagner, C. E.; Metzler, R. Non-Gaussian, Non-Ergodic, and Non-Fickian Diffusion of Tracers in Mucin Hydrogels. *Soft Matter* **2019**, *15*, 2526–2551.

(80) Schwarzer, D.; Stummeyer, K.; Haselhorst, T.; Freiberger, F.; Rode, B.; Grove, M.; Scheper, T.; von Itzstein, M.; Mühlhoff, M.; Gerardy-Schahn, R. Proteolytic Release of the Intramolecular Chaperone Domain Confers Processivity to Endosialidase F. *J. Biol. Chem.* **2009**, *284*, 9465–9474.

(81) Broeker, N. K.; Gohlke, U.; Müller, J. J.; Utrecht, C.; Heinemann, U.; Seckler, R.; Barbirz, S. Single Amino Acid Exchange in Bacteriophage HK620 Tailspike Protein Results in Thousand-Fold Increase of Its Oligosaccharide Affinity. *Glycobiology* **2013**, *23*, 59–68.

(82) Kunstmann, S.; Scheidt, T.; Buchwald, S.; Helm, A.; Mulard, L.; Fruth, A.; Barbirz, S. Bacteriophage Sf6 Tailspike Protein for Detection of *Shigella flexneri* Pathogens. *Viruses* **2018**, *10*, No. 431.

(83) Ryan, E. M.; Gorman, S. P.; Donnelly, R. F.; Gilmore, B. F. Recent Advances in Bacteriophage Therapy: How Delivery Routes, Formulation, Concentration and Timing Influence the Success of Phage Therapy. *J. Pharm. Pharmacol.* **2011**, *63*, 1253–1264.

(84) Lombard, V.; Golaconda Ramulu, H.; Drula, E.; Coutinho, P. M.; Henrissat, B. The Carbohydrate-Active Enzymes Database (CAZy) in 2013. *Nucleic Acids Res.* **2014**, *42*, D490–D495.

■ NOTE ADDED AFTER ASAP PUBLICATION

This paper was published ASAP on September 16, 2019, with errors in equations 1 and 3. The corrected version was reposted on September 17, 2019.

SUPPLEMENTARY INFORMATION

Supplementary Methods

Stewartan biofilm concentration determination with the phenol-sulfuric acid method

To estimate the average stewartan concentration in a *P. stewartii* biofilm, biofilms were centrifuged at 17,000g for 1 h and the supernatant analyzed by the phenol-sulfuric acid method,¹ a colorimetric method to determine the carbohydrate content in a sample. In brief, 50 μ l of the sample (25x diluted in 100 mM NaCl) were mixed with 150 μ l concentrated sulfuric acid and 30 μ l 5 % (v/v) phenol. The reaction was carried out at 90 °C for 5 min and absorption detected at 490 nm. In parallel, a calibration curve of previously isolated stewartan ranging from 0 to 1 g/L stewartan was determined. The estimated average biofilm stewartan concentrations were 13.5 \pm 2.0 g/L in 21 h, and 15.3 \pm 1.3 g/L in 65 h old biofilms (mean \pm SD from multiple aliquots of the same biofilm). In the same time window, we observed only a marginal increase in bacteria concentration, in agreement with previous analyses reporting a stable stewartan amount per *P. stewartii* cell.² It is worth noting that the obtained concentrations might be slightly underestimated, since the volume occupied by the bacteria in the intact biofilm was not explicitly taken into account.

Preparation and labelling of P22 bacteriophages

P22 phages were purified as described previously.³ To label P22 phages, 2.15 x 10¹² particles/ml were incubated with 1 μ M YO-PRO-1 Iodide (491/509) (Thermo Scientific) in phage buffer containing 50 mM Tris-HCl and 4 mM MgCl₂ at pH 7.6 for 2 h at room temperature. Labeled phages were purified using Sephadex G-25 in prepacked PD-10 Desalting Columns (GE Healthcare) according to standard protocols. Absorbance at 260 nm was used to determine elution fractions containing labeled phages which were afterwards concentrated to 1.63 x 10¹² particles/ml (Amicon® Ultra-15, MW: 10 kDa).

Expression, purification and labelling of tailspike enzyme

A cDNA containing the coding sequence for bacteriophage ϕ Ea1h TSP depolymerase was a kind gift from K. Geider (Julius Kühn Institut, Dossenheim, Germany).⁴

The ϕ Ea1hTSP coding sequence was amplified from cDNA with forward primer 5'-CGATATCCCAACGACCGAAAACCTGTATTTTCAGGGCATGCCGAAACTAAGATTAAAG and reverse primer 5'-GCCGCGAAGCTTTACGTGTTAGATAC. A His₆ tag followed by a TEV-protease cleavage site was introduced in the construct using the 5'-CGCGCATATGCATCACCATCACCATCACGATTACGATATCCCAACGACCGAAAACC forward primer and the same reverse primer as above. The construct was then inserted into a pET23a+ vector (Novagen) at NdeI and HindIII restriction sites. The protein was expressed in *E. coli* BL21(DE3), cells were disrupted with French press and cell lysates were purified using immobilized metal affinity chromatography (IMAC). The His₆ tag was cleaved off with His₆-TEV protease and tag-free proteins collected in the flow-through of a second IMAC chromatography.

For fluorescence labeling, Φ Ea1h TSP was dialyzed in phosphate-buffered saline (13.7 mM NaCl, 2.7 mM KCl, 10 mM Na₂PO₄, 2 mM KH₂PO₄, pH 7.4) and incubated with 0.5 mM ATTO 488 NHS-Ester according to manufacturer's protocol (ATTO-Tec, Siegen, Germany). The reaction was carried out at pH 8.4 and room temperature for 1 h and stopped by performing size-exclusion chromatography using the SuperdexTM S200 10/300. Based on the absorption

detected at 280 nm and 550 nm, the protein and dye concentrations were determined, resulting in an average labeling ratio of 1.67 dye molecules per TSP.

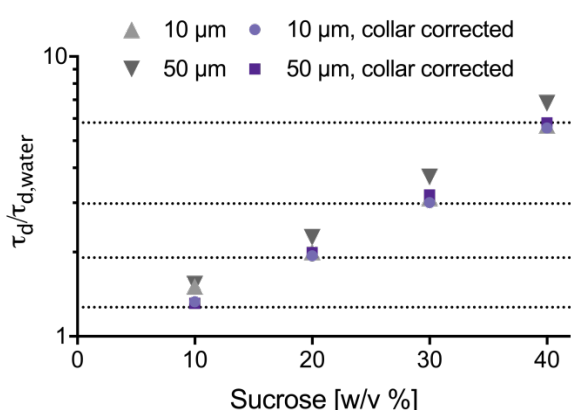
Dynamic light scattering and Zeta potential analyses of tracer particles

Size and zeta potential of 60 nm (40-60 nm, according to manufacturer specification) and 200 nm (190-210 nm, according to manufacturer specification) Dragon Green fluorescent polystyrene beads and YO-PRO-1 labelled P22 bacteriophages were determined by DLS and laser Doppler micro-electrophoresis using a Zetasizer Nano ZS (Malvern Pananalytical Ltd, Malvern, UK). For comparison, particle diameters were calculated from diffusion coefficients D determined in FCS measurements using the Stokes-Einstein relation, $R_h = \frac{k_B T}{6\pi\eta D}$, where R_h is the average hydrodynamic radius of the particles, k_B the Boltzmann constant, T and η the solvent temperature and viscosity.

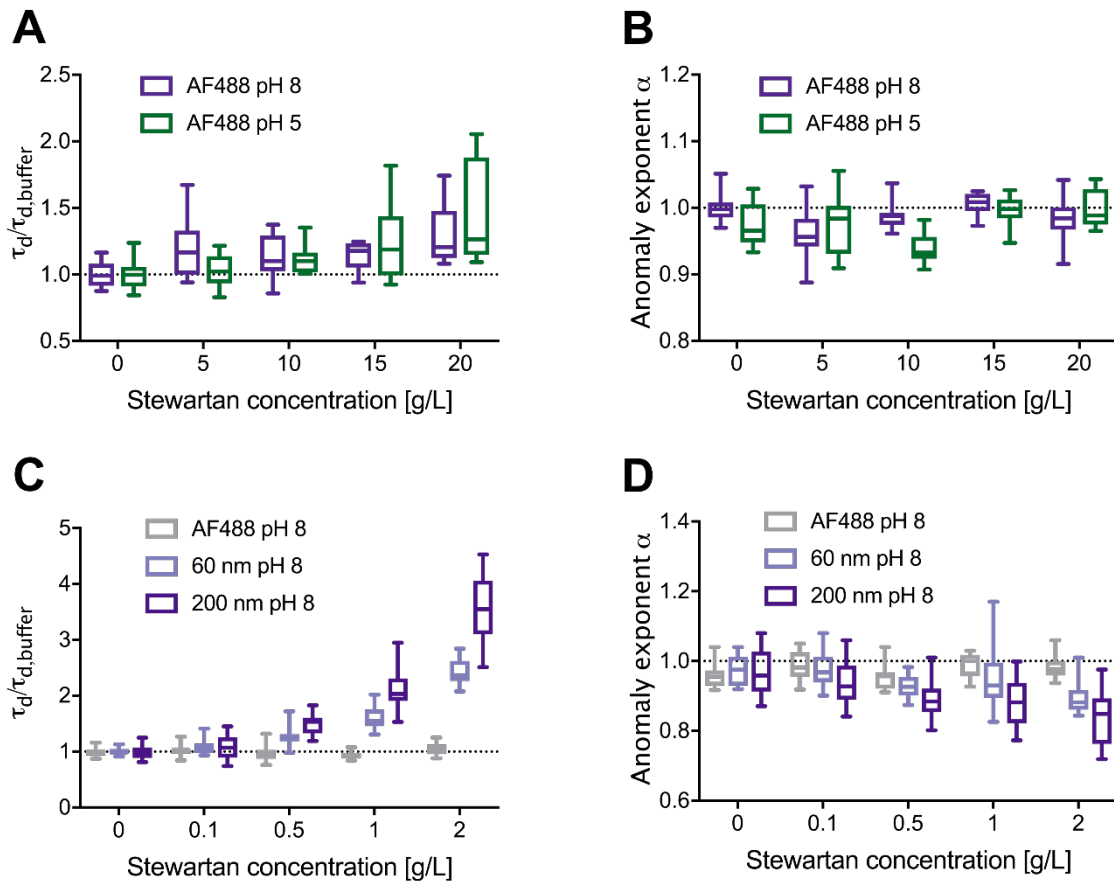
Dynamic light scattering on stewartan solutions

To estimate the radius of gyration and critical overlap concentration of stewartan, we performed dynamic light scattering measurements at 90° angle on highly diluted stewartan solutions, and determined the molecular weight MW (using $dn/dc=0.162$ mL/g) and hydrodynamic radius R_h by linear interpolation of these quantities to zero stewartan concentration. From the obtained values, MW=1.1 MDa and $R_h=50$ nm, we estimated a radius of gyration $R_g=75$ nm, using $R_g=1.505 R_h$ (random polymer coil, from Schärftl, Springer 2007), as an approximation. We did not observe significant variations when changing the pH between 8 and 5. Then, we obtained $c_{\text{overlap}} = 3MW/(4\pi R_g^3 N_A) \approx 1$ g/L as an estimate for the critical overlap concentration. The determined quantities have to be considered as approximate values. A more accurate quantification would require multi-angle light scattering measurements.

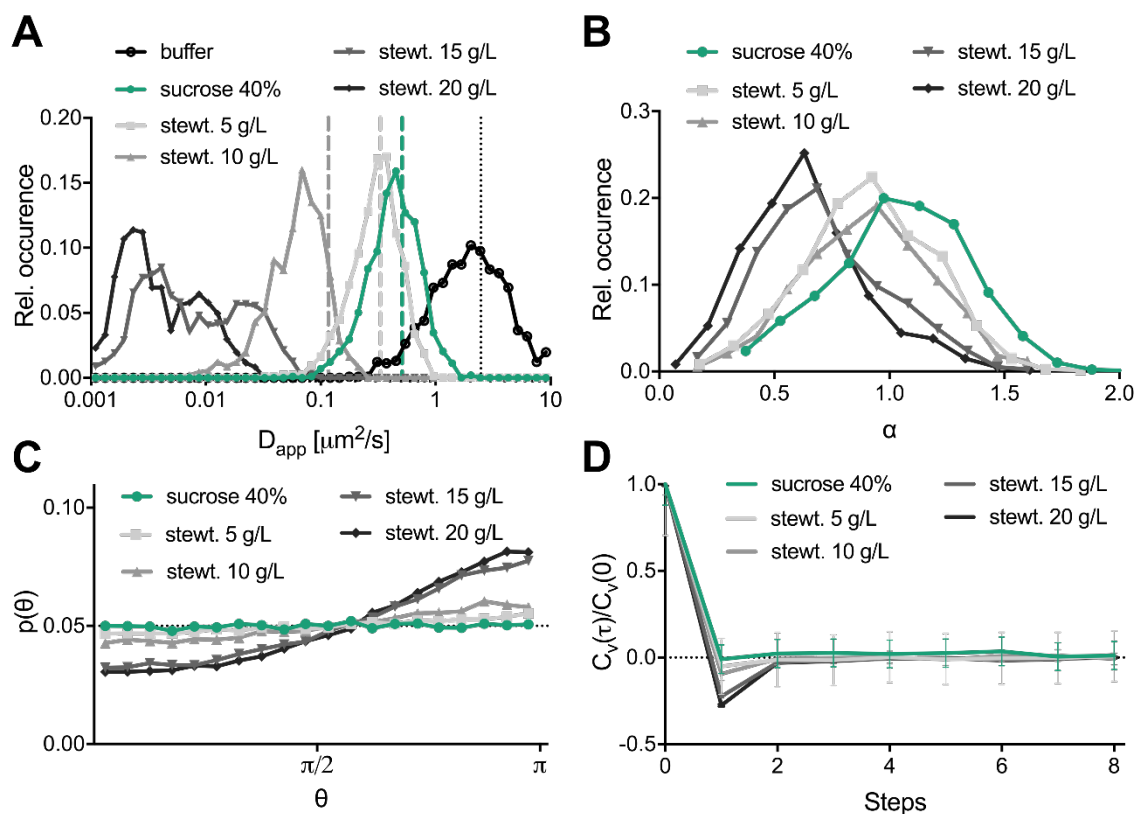
Supplementary Data



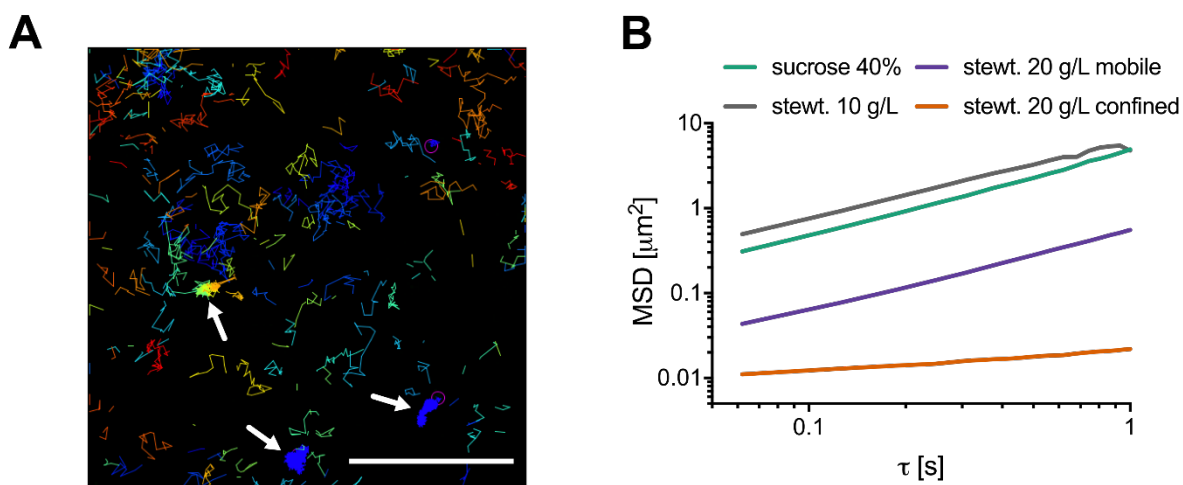
Supplementary Figure S1. Viscosity measurements of sucrose solutions using FCS. Relative diffusion times in 10%-40% (w/v) sucrose solutions, obtained by calculating the ratio of average diffusion times of AF488 molecules in sucrose solutions and water, measured by FCS. At each concentration, 6 measurements were performed at 10 μm and 50 μm above the coverslip, with and without adjustment of the objective collar ring. Dashed lines show the expected relative viscosity values ($\eta_{10\%}/\eta_{\text{water}}=1.27$, $\eta_{20\%}/\eta_{\text{water}}=1.91$, $\eta_{30\%}/\eta_{\text{water}}=2.97$, $\eta_{40\%}/\eta_{\text{water}}=5.80$) at 25°C , measured by rotational rheometry⁵. All measurements were performed at $24\pm 1^\circ\text{C}$.



Supplementary Figure S2. FCS analysis of AF488 in stewartan solutions of varying concentration/ pH, and FCS analysis of all tracer particles at low stewartan concentrations. (A) Box plots of relative diffusion times of AF488 in 5-20 g/L stewartan solutions at pH 5 and 8, calculated by normalizing diffusion times to the average values obtained in pure 50 mM Tris-HCl, pH 8, or 50 mM MES-NaOH, pH 5, buffer solutions, as measured by FCS. Data are pooled from at least 12 measurements in two independent experiments. (B) Box plots of anomaly exponent α obtained by fitting an anomalous diffusion model (eq. 2) to the ACFs of FCS measurements described in (A). (C) Box plots of hindrance factors $\tau_d/\tau_{d,buffer}$ in 0.1-2 g/L stewartan solutions at pH 8, calculated by normalizing diffusion times to the average values obtained in pure 50 mM Tris-HCl, pH 8, buffer solutions, measured by FCS on AF488 molecules, 60 and 200 nm fluorescent polystyrene beads suspensions. Data are pooled from 12 measurements in two independent experiments. (D) Box plots of anomaly exponent α obtained by fitting an anomalous diffusion model (eq. 2) to the ACFs of FCS measurements represented in (C).

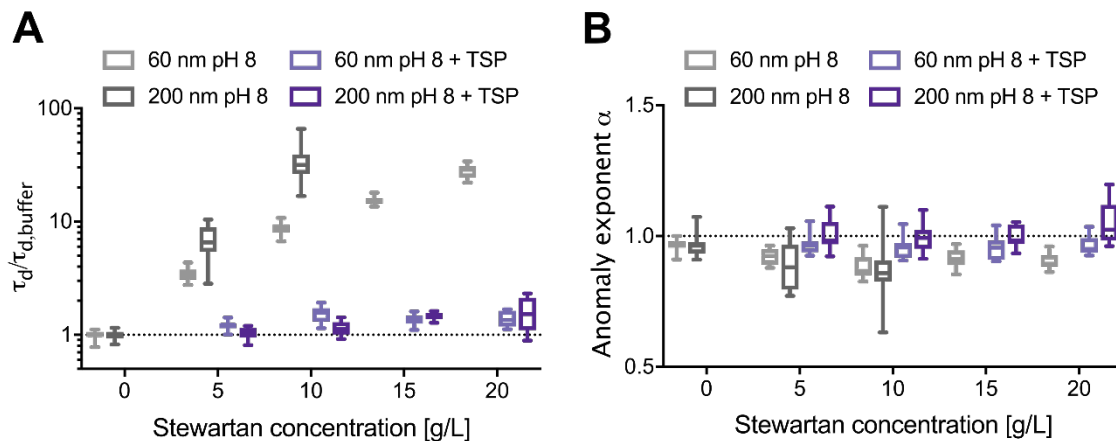


Supplementary Figure S3. SPT analysis of polystyrene beads in stewartan matrices at pH 5. (A-B) Distributions of apparent diffusion coefficient D_{app} (A) and anomaly exponent α (B) obtained by fitting of eqs. 4 and 5 to individual taMSDs of 200 nm polystyrene beads in 5-20 g/L stewartan solutions at pH 5 and in 40% (w/v) sucrose solutions. Dashed lines in (A) show median D_{app} values from FCS analysis. In (A) also the D_{app} distribution obtained in pure 50 mM MES-NaOH pH 5 buffer is shown. **(C)** Probability distribution of angle θ (eq. 6) between successive steps taken in an interval $\delta t = \Delta t = 62$ ms (sucrose) or 122 ms (stewartan) with lag time $\tau = \delta t$, pooled from all trajectories recorded in each sample. **(D)** Normalized velocity autocorrelation function of successive steps taken in an interval $\delta t = \Delta t = 62$ ms (sucrose) or 122 ms (stewartan), separated by one to 8 steps ($\Delta t \leq \tau \leq 8\Delta t$), calculated using eq. 7. The panel shows the average over all individual trajectories, calculated in segments of 10 steps. Error bars show standard deviations over all segments. The number of trajectories per sample is given in Table 1. Corresponding data at pH 8 are shown in Figure 5.

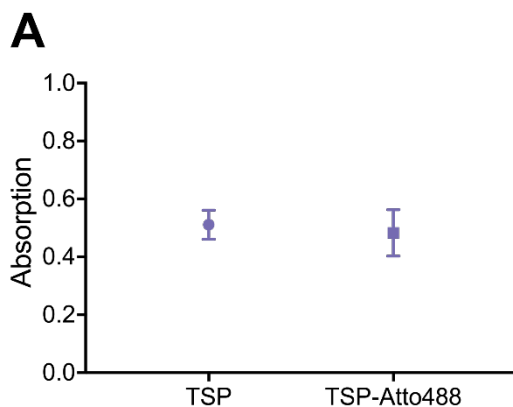


Supplementary Figure S4. SPT analysis of bacteriophage diffusion in stewartan matrices. (A) Image of SPT analysis of fluorescently labeled P22 bacteriophage particles in 20 g/L stewartan solution. The panel shows all individual trajectories obtained by tracking particles in a single image stack of 2000 frames, i.e. ~ 2 min acquisition.

White arrows highlight trajectories of confined particles. Scale bar is 5 μm . **(B)** Ensemble average of taMSDs of fluorescently labeled P22 bacteriophage particles in 10 or 20 g/L stewartan solution and 40% (w/v) sucrose solution. Trajectories of measurements in 20 g/L stewartan were arbitrarily split into mobile ($D_{\text{app}} > 0.01 \mu\text{m}^2/\text{s}$) and confined ($D_{\text{app}} < 0.01 \mu\text{m}^2/\text{s}$) subpopulations and the respective taMSDs averaged separately.



Supplementary Figure S5. FCS analysis of fluorescent tracers in stewartan matrices at pH 8 upon digestion by bacteriophage tailspike enzyme. (A) Box plots of relative diffusion times in stewartan samples, calculated by normalizing diffusion times to the average values in pure 50 mM Tris-HCl pH 8 buffer, before and 1 h after incubation with 140 nM purified bacteriophage TSP, obtained from FCS analysis of measurements on 60 and 200 nm fluorescent polystyrene beads. Data are pooled from at least 12 measurements each in two independent experiments. **(B)** Box plots of anomaly exponent α obtained from FCS analysis of the measurements described in (A), by fitting a three-dimensional anomalous diffusion model to individual ACFs. Corresponding data at pH 5 are shown in Figure 5.



Supplementary Figure S6. Biochemical assay of ΦEa1h TSP stewartan depolymerase activity. (A) Absorption values at 655 nm in 3-Methyl-2-benzothiazolinon-hydrizon (MBTH) reducing ends test after 30 min incubation of 10 g/L stewartan in 50 mM MES-NaOH pH 5 buffer with 140 nM unlabeled or Atto488 labeled TSP enzyme. Data are presented as mean \pm SD from three replicates.

Table S1. Properties of fluorescent polystyrene beads and bacteriophages. Zeta potential and size of particles, measured by laser Doppler micro-electrophoresis, DLS or FCS in the specified buffer solutions. For measurements performed multiple times, numbers are given as mean±SD.

Sample	Buffer	Zeta potential [mV]	Diameter DLS [nm]	Diameter FCS [nm]
60 nm beads	50 mM MES-NaOH, pH 5	-19.9±0.5	64.1±0.5	61.3±3.1
	50 mM Tris-HCl, pH 8	-33.4±1.1	64.1±0.1	61.5±4.5
200 nm beads	50 mM MES-NaOH, pH 5	-12.1±2.2	193±3	202±2
	50 mM Tris-HCl, pH 8	-25.3±2.7	193±1	198±7
P22 phages	50 mM MES-NaOH, pH 5	-7.5±0.3	70.9±1.0	89.2±8.5
	50 mM Tris-HCl, 4 mM MgCl ₂ , pH 7.6 ("phage buffer")	-13.6±1.8	72.9±0.7	78.0±8.8

Table S2. Diffusion analysis of fluorescent beads using FCS and SPT. Average values of the diffusion coefficient D_{app} and anomaly exponent α , obtained from FCS or SPT analysis of measurements on 60 nm (only FCS) and 200 nm polystyrene beads in buffer, 5-20 g/L stewartan at pH 5 and 8 or 40% (w/v) sucrose solutions. Values are given as median±SD (FCS) or mean±SD (SPT). FCS analysis on 200 nm beads could not be performed above 10 g/L stewartan due to the slow dynamics at higher stewartan concentrations. In the SPT analysis, reliable α values could not be determined for measurements in pure buffer due to the fast dynamics and short lengths of individual trajectories resulting in poor statistics. The last column for SPT analysis shows the number of trajectories that were analyzed for each condition.

Sample	60 nm FCS		200 nm FCS		200 nm SPT		
	D_{app} [$\mu\text{m}^2/\text{s}$]	α	D_{app} [$\mu\text{m}^2/\text{s}$]	α	D_{app} [$\mu\text{m}^2/\text{s}$]	α	# of trajectories
0 g/L pH 5 pH 8	7.7±1.0	0.96±0.05	2.5±0.2	0.96±0.04	2.5±1.8	NA	671
	7.8±0.8	0.96±0.02	2.5±0.3	0.96±0.04	2.5±1.8	NA	706
5 g/L pH 5 pH 8	2.1±0.4	0.85±0.04	0.33±0.13	0.85±0.10	0.33±0.15	0.91±0.28	738
	2.1±0.3	0.92±0.03	0.37±0.17	0.88±0.09	0.24±0.11	0.91±0.27	811
10 g/L pH 5 pH 8	0.66±0.11	0.81±0.03	0.12±0.05	0.87±0.13	0.07±0.04	0.90±0.28	907
	0.88±0.11	0.87±0.05	0.08±0.03	0.86±0.12	0.06±0.03	0.92±0.27	965
15 g/L pH 5 pH 8	0.40±0.11	0.74±0.07	NA	NA	0.013±0.013	0.71±0.27	792
	0.50±0.05	0.91±0.03	NA	NA	0.014±0.007	0.85±0.27	999
20 g/L pH 5 pH 8	0.21±0.09	0.72±0.09	NA	NA	0.005±0.005	0.64±0.26	607
	0.29±0.06	0.89±0.03	NA	NA	0.006±0.003	0.78±0.29	839
40% Sucrose	1.6±0.2	0.99±0.06	0.51±0.13	1.07±0.08	0.49±0.25	1.04±0.29	976

Table S3. Diffusion analysis of P22 bacteriophages using FCS and SPT. Average values of the diffusion coefficient D_{app} and anomaly exponent α , obtained from FCS and SPT analyses of P22 bacteriophage diffusion in 50 mM MES-NaOH pH 5 buffer (0 g/L), 10 or 20 g/L stewartan and 40% (w/v) sucrose solutions. Values are given as median±SD (FCS) or mean±SD (SPT). SPT data in 20 g/L stewartan solution were arbitrarily split into a mobile ($D_{app} > 0.01\mu\text{m}^2/\text{s}$) and confined ($D_{app} < 0.01\mu\text{m}^2/\text{s}$) population. The last column shows the number of trajectories that were analyzed in SPT for each condition. In pure buffer, diffusion dynamics of P22 particles were too fast to perform reliable SPT analysis on the used experimental setup.

Sample	D_{app} [$\mu\text{m}^2/\text{s}$]	α	D_{app} [$\mu\text{m}^2/\text{s}$]	α	# of trajectories
	FCS	FCS	SPT	SPT	
0 g/L	5.6±0.7	0.95±0.05	NA	NA	NA
10 g/L	1.9±0.4	0.93±0.10	1.6±1.4	0.84±0.24	297
20 g/L mobile	0.35±0.22	0.78±0.12	0.13±0.08	0.91±0.29	255
20 g/L confined	NA	NA	0.003±0.002	0.28±0.15	71
40% Sucrose	1.2±0.3	0.98±0.13	1.1±0.9	0.94±0.28	578

Supplementary References

- (1) Masuko, T.; Minami, A.; Iwasaki, N.; Majima, T.; Nishimura, S.-I.; Lee, Y. C. Carbohydrate Analysis by a Phenol–Sulfuric Acid Method in Microplate Format. *Anal. Biochem.* **2005**, *339*, 69–72. <https://doi.org/10.1016/J.AB.2004.12.001>.
- (2) Bodman, S. B. von; Majerczak, D. R.; Coplin, D. L. A Negative Regulator Mediates Quorum-Sensing Control of Exopolysaccharide Production in *Pantoea Stewartii* Subsp. *Stewartii*. *Proc. Natl. Acad. Sci.* **1998**, *95*, 7687–7692. <https://doi.org/10.1073/PNAS.95.13.7687>.
- (3) Andres, D.; Hanke, C.; Baxa, U.; Seul, A.; Barbirz, S.; Seckler, R. Tailspike Interactions with Lipopolysaccharide Effect DNA Ejection from Phage P22 Particles *in Vitro*. *J. Biol. Chem.* **2010**, *285*, 36768–36775. <https://doi.org/10.1074/jbc.M110.169003>.
- (4) Hartung, J. S., Fulbright, D. W., and Klos, E. J. Cloning of a Bacteriophage Polysaccharide Depolymerase Gene and Its Expression in *Erwinia Amylovora*. *Mol. Plant. Microbe* **1988**, No. In. 1, 87–93.
- (5) Telis, V. R. N.; Telis-Romero, J.; Mazzotti, H. B.; Gabas, A. L. Viscosity of Aqueous Carbohydrate Solutions at Different Temperatures and Concentrations. *Int. J. Food Prop.* **2007**, *10*, 185–195. <https://doi.org/10.1080/10942910600673636>.

3 Discussion and Outlook

In this thesis FFS techniques were implemented and applied to quantify biomolecular interactions and dynamics in several biological systems. The first part of the investigations focused on protein interactions at contact sites of living cells. It is demonstrated that FFS allows to probe specific interactions of the neuronal transmembrane protein APLP1 at cell-cell contacts, providing evidence that it mediates adhesion of cells and is regulated by metal ions such as zinc. In the second part of the thesis, FP tags were systematically evaluated. The investigation reveals that FP properties can severely bias the quantification of protein interactions via FFS and have to be taken into account to obtain correct results. Finally, diffusion dynamics of particles in bacterial biofilm matrix were investigated. It is shown that biofilm polysaccharides form an entangled meshwork that provides size selective barriers for particle diffusion. The following sections provide a comprehensive discussion of the performed FFS studies and address the advantages and limitations of applied FFS techniques in the context of the biological findings.

3.1 Fluorescence fluctuation spectroscopy is suitable to detect protein interactions at cell-cell contacts

Cell-cell contacts are important interfaces in multicellular systems: in immune response recognition of antigen presenting cells by lymphocytes at immunological synapses plays a key role (Huppa and Davis, 2003). In the nervous system chemical or electrical signals are transmitted between neurons at neuronal synapses (Südhof, 2018). In addition, adhesion of cells at cell-cell junctions is of fundamental importance in tissues, providing structural integrity under mechanical stress and deformation (Harris and Tepass, 2010, Tepass et al., 2000).

For investigations on the molecular level, cell-cell contact sites pose a challenge due to their small spatial dimensions. Immunological synapses extend over few microns along

the interface, but the separation between the two cells is only tens of nanometers (Cartwright et al., 2014). Similar dimensions are reported for adherens junctions (Tepass et al., 2000). In contrast, neuronal synapses are much smaller interfaces with contact areas of less than $0.2 \mu\text{m}^2$ (Santuy et al., 2018). The width of the synaptic cleft is around 20-40 nm and thus similar to the other systems (Savtchenko and Rusakov, 2007).

Such small distances are commonly determined from EM images. Although EM provides spatial resolution on the \sim nm scale, it requires cell fixation and lacks molecular specificity. Therefore, only very abundant protein complexes can be resolved, e.g. the lattice organization of E-cadherin ectodomains in liposome junctions (Harrison et al., 2011). Optical microscopy, on the contrary, reaches molecular specificity at the single molecule level via fluorescence labeling, but has a much lower resolution. At best, most novel super resolution (SR) techniques achieve a resolution of 10-50 nm in living cells (Schermele et al., 2019). In two recent studies, stochastic optical reconstruction microscopy (STORM) and photo activated localization microscopy (PALM) were used to investigate the molecular organization of E-cadherin at adherens junctions (Indra et al., 2018, Wu et al., 2015). In a cell co-culture assay E-cadherin *cis* and *trans* interactions were discriminated by the presence or absence of proximal E-cadherin nanoclusters at PMs of neighboring cells.

The approach presented in this work is based on a different principle. Instead of resolving protein *trans* interactions via spatial co-localization or proximity, sFCCS detects correlated number fluctuations caused by co-diffusion of protein complexes at cell-cell contact sites through a diffraction limited focal volume. In this way, it is also suitable to investigate (transient) interactions of proteins that are homogeneously distributed at contact sites and do not localize in spatially resolvable clusters. Thus, the small distance of proteins in the PMs of neighboring cells does not impose a limitation on the detectability of *trans* complexes. On the other hand, typical distances (< 50 nm) are small enough that simultaneous signal fluctuations in both spectral channels, caused by the diffusion of *trans* interacting protein complexes, can be detected in the observation volume. In sFCCS the full membrane signal is sampled along the scanning direction and summed over multiple pixels at each time point. Therefore, even larger distances between fluorophores on both sides or an optical shift of the observation volumes of both channels in scanning direction do not reduce the cross-correlation, as long as diffusion times are much larger than the time it takes to acquire the signal in one line. Hence, for investigations of transmembrane proteins such as APLP1, fluorophores can be placed at the protein's intracellular terminus, which is a strong advantage compared to fluorescence resonance energy

transfer (FRET) based measurements of *trans* interactions (Kim et al., 2011). FRET is strongly distance dependent and requires short distances ($\lesssim 5$ nm) between fluorophores. Thus, labels need to be placed on the extracellular side at or close to *trans* binding protein domains and therefore potentially hinder *trans* interactions. In addition, variations of fluorophore distances and fluorophore orientations may modulate FRET efficiencies.

Interference of fluorophores with protein interactions may be circumvented by replacing FPs with smaller tags, e.g. organic dyes. However, this requires insertion of unnatural amino acids into the protein sequence, presence or insertion of cysteine residues, or usage of alternative tags such as SNAP-tags, which still have a considerable size of around 19 kDa (Cole, 2013). Nevertheless, organic dyes possess a higher brightness and photostability compared to FPs (Grußmayer et al., 2019) and could thus improve the statistics of FFS measurements.

The established FFS assay allowed to investigate APLP1 *cis* and *trans* interactions at cell-cell contacts and to propose a model of zinc ion mediated adhesion. Based on the observation that zinc ions triggered the formation of large APLP1 clusters also outside of contact sites, it is proposed that zinc ions induce mainly *cis* multimerization of APLP1. Such APLP1 clusters then provide a multivalent platform for *trans* interactions between APLP1s of neighboring cells, which were already detected in the absence of zinc ions. Multiple of such (weak) *trans* interactions finally cause the formation of stable adhesion clusters. Notably, this effect is reversible, i.e. depletion of zinc ions causes disassembly of APLP1 clusters (Mayer et al., 2016). Interestingly, APLP1 clusters showed strongly reduced diffusion dynamics compared to small APLP1 oligomers, likely also due to intracellular interactions with the cortical cytoskeleton. This hypothesis is supported by the finding that filamentous actin enriches at the sites of APLP1 clusters. The reduced mobility appears to stabilize and further promote formation of APLP1 *trans* clusters at contacts of opposing membranes. The effect of zinc and other metal ions such as copper on interactions of APP family members is an object of active research. Based on *in vitro* bead aggregation assays, a recent study proposes that zinc ions directly trigger APLP1 *trans* but not *cis* interactions (August et al., 2019). Nevertheless, the authors neither provide an explanation of how zinc ions mediate APLP1 *trans* interactions despite absence of zinc binding to the putative APLP1 E1 *trans* interaction domain, nor a control that bead aggregation is exclusively a measure of *trans*, but not *cis* interactions.

While the presented investigations were performed in HEK 293T cells as a cellular model system, there is strong evidence that the obtained results are transferable

to neurons. For example, zinc ion induced clustering of APLP1 was observed along the soma and dendritic PM of rat hippocampal neurons (Mayer et al., 2014). In addition, zinc ions promoted adhesion of cortical neurons to substrates printed with immobilized APLP1 ectodomain (Mayer et al., 2016). APLP1 mediated adhesion at neuronal synapses could thus be locally regulated by synaptic zinc ion levels.

Several limitations of the presented assay have to be considered. First of all, FFS requires fluctuations of the fluorescence signal caused by diffusion of molecules. Thus, it cannot detect immobile or very slowly diffusing protein complexes which might, however, be present at cell-cell interfaces. For example, Indra et al. (2018) recently reported transient immobilization of E-cadherin molecules at cell-cell junctions for several seconds. In the presented work, this issue has been encountered for APLP1 in the presence of zinc ions, triggering the assembly of large APLP1 clusters. In sFCCS measurements on such clusters, correlation functions (CFs) showed decay times on the \sim s scale and strong noise at large lag times, prohibiting an accurate correlation analysis. In this case, ccN&B analysis may be more appropriate to detect a cross-correlation caused by *trans* interactions. Photobleaching may be reduced by introducing pauses of a few seconds between each ccN&B frame. Nevertheless, the slow dynamics require acquisition times of 5-10 min, which may not be possible in very dynamic systems and are ultimately restricted by cell movement. To correct for lateral cell movement, an image alignment algorithm was applied in this work. Alternatively to FFS, a co-localization analysis may be sufficient to show *trans* binding of proteins that form heterogeneous clusters at contact sites, similar to the spatial distribution of APLP1 after addition of zinc ions or the mentioned clustering of E-cadherin (Indra et al., 2018, Wu et al., 2015).

To estimate the size of protein complexes at cell-cell contacts, molecular brightness analysis was applied. It should be noted that this analysis does not allow to resolve mixtures of different oligomeric states, but rather provides average values of all molecular species present in the observation volume (see discussion in the next section). Therefore, the exact stoichiometry of *cis* and *trans* interactions is generally not accessible. For example, if a protein of interest can either *cis* or *trans* dimerize, an average oligomeric state between 1 and 2 will be determined by brightness analysis because a mixture of protein complexes having a brightness corresponding to either dimers (*cis* dimers) or monomers (*trans* dimers) is present in each channel. For APLP1 in the absence of zinc ions, small oligomers were detected at cell-cell contacts, i.e. brightness values corresponded to dimers/trimers on each side. In a previous study, we observed a protein concentration dependent *cis* dimerization outside junctions (Mayer et al., 2016). These findings indicate that *trans* binding may involve more

than one APLP1 monomer or dimer on each side, e.g. 2 : 2 stoichiometry or higher. Generally, FFS is not suitable in (macroscopically) very dynamic systems, i.e. systems where concentration and localization of the proteins of interest or the cell morphology change on time scales smaller than the acquisition time. For example, immunological synapse formation by cytotoxic T lymphocytes and downstream signaling processes occur within few minutes (Huppa and Davis, 2003). However, accurately measuring the diffusion of transmembrane proteins involved in one of these processes, e.g. diffusing with $\gtrsim 50$ ms diffusion time, would require sFCS acquisition times of $\gtrsim 1$ min (see figs. 4.22, 4.23 in appendix).

A further limitation may be imposed by the geometry of cell-cell contacts: sFCS fit models are based on the assumption that the membrane is a flat non-curved sheet, along the 1-1.5 μm vertical extension of the focal volume. However, for very flat cells (see fig. 4.15 in appendix), small contacts, e.g. neuronal synapses, or highly curved membranes, this assumption may be strongly violated.

For *in vivo* applications of the presented cross-correlation assay, sample preparation may be difficult. While transient transfection and mixing of culture cells are fairly simple, differential expression of tagged proteins in multicellular organisms requires more sophisticated schemes. Here, photoactivatable tags, cell lineage specific, or light-inducible promoters may provide potential solutions (Zhao et al., 2017). Furthermore, non-tagged endogenous proteins may be present depending on the expression system and could potentially reduce the detectable cross-correlation. This can be circumvented by using CRISPR/Cas9 technology, allowing FP tagging of endogenous proteins.

Despite these challenges, successful *in vivo* applications of pFCS (Kaur et al., 2013) and sFCCS (Ries et al., 2009c) indicate the general suitability of such approaches. As proof of concept, sFCS measurements at cell-cell junctions of living *C.elegans* embryos were successfully performed in the context of this thesis (fig. 4.14 in the appendix).

Finally, FFS may be extended to more than two channels by using FPs that can be excited with an additional laser, e.g. 405 nm, long Stokes shift fluorophores, or spectral detection and unmixing of fluorophores with overlapping spectra (Benda et al., 2014) to minimize bleaching, phototoxicity, and chromatic shifts, as described in the appendix (section 4.11). The successful implementation of three-color spectral sFCCS is demonstrated in fig. 4.32. It is shown that differential interactions of mEGFP, mEYFP, and mCherry2 fluorophores can be discriminated. So far, only few realizations of multicolor FFS exist (Heinze et al., 2004, Hwang et al., 2006, Schrimpf et al., 2018). Using suitable organic dyes and two-photon or single wavelength excita-

tion, Heinze et al. (2004) and Hwang et al. (2006) successfully performed three-color FCS *in vitro* with a single laser beam and three photon counting detectors. Recently, Schrimpf et al. (2018) implemented three-color RICS with FPs in the cytoplasm of living cells, following the same approach presented here, i.e. using a single spectral detector. The data provided in this work mark the first successful realization of multi-color FFS on membrane proteins. In the context of cell-cell interactions, spectral sFCCS could allow to investigate more complex scenarios, e.g. competitive binding of two different receptor types on one cell to one receptor species on the neighboring cell or ternary protein interactions. This may also be applied to APLP1 in order to investigate hetero-interactions with the other APP family members APP and APLP2 that are also present (in lower amounts) at the PM (Kaden et al., 2009, Soba et al., 2005).

In the presented work, protein interactions were mainly investigated at contact sites of living cells. Given the limitations of FFS in dynamic cellular systems, it may prove beneficial to use the presented FFS assay in more controllable systems, for example model membrane vesicles such as giant unilamellar vesicles (GUVs) or giant plasma membrane vesicles (GPMVs). As recently shown, biological processes occurring at cell-cell contacts, e.g. T-cell activation, can be successfully reconstituted in such systems, e.g. at GUV-GUV or GUV-cell contacts (Jenkins et al., 2018). Furthermore, GPMVs were shown to lack an organized cytoskeleton (Schneider et al., 2017) and, thus, can serve as a tool to probe the effect of an absent cytoskeleton on protein interactions. For APLP1 no *trans* interactions were detected at cell-GPMV interfaces, again indicating that the cytoskeleton may play a role in APLP1-APLP1 interactions. All together, such systems provide new platforms to study proteins involved in cell-cell interactions using the described FFS assay.

3.2 The choice of fluorescent protein tags affects molecular brightness analysis in living cells

As discussed in the context of APLP1, molecular brightness analysis of FFS data provides a powerful tool to quantify the oligomeric state of protein complexes in living cells. However, while being conceptually simple, the accuracy of this analysis strongly depends on the type of fluorescence labels used to tag proteins of interest and precise estimation of the corresponding labeling efficiency and stoichiometry. For example, an ensemble of dimeric proteins will only emit twice as many photons per

particle as an ensemble of monomers if i) the two subunits of each dimer are labeled with a single fluorophore with 100% efficiency and ii) the fluorophores continuously emit a signal. In this regard, FPs that are genetically fused to a protein of interest in 1:1 stoichiometry appear to be superior to organic dye labeling via specific residues or antibodies. Nevertheless, a comparison of the brightness data obtained for APLP1 tagged with either mEYFP or mCard showed strong differences of APLP1 oligomeric state estimates (e.g. ca. 3-4 times higher normalized brightness with mEYFP, fig. 4.16 in the appendix), questioning whether using genetically encoded FP tags ensures unbiased brightness measurements. Indeed, previous investigations of FP properties showed sensitive dependencies of photostability, photophysical characteristics, and maturation times on buffer or cellular conditions (Balleza et al., 2017, Cranfill et al., 2016, Haupts et al., 1998, Hendrix et al., 2008, Schwille et al., 2000, Vámosi et al., 2016).

By quantifying the relative molecular brightness of artificial homo-oligomers for several FPs using FFS, the work in chapter 2.3 presents a systematic evaluation of commonly used FPs for oligomerization measurements and provides a simple guideline to obtain unbiased results. It is shown that a thorough calibration of the fluorescence probability and a simple correction scheme of raw brightness data lead to correct estimates of the oligomeric state of even larger protein complexes (experimentally verified up to 12mers). In addition, several recently developed red FPs were characterized, confirming suboptimal properties of mCard, but superior performance of mCherry2. Compared to the other tested red FPs, mCard showed high photostability and brightness, but a low fluorescence probability of only 24%, i.e. around 2.5 times lower than the one measured for mEYFP. This observation is in agreement with the ca. 3-fold lower fraction of fluorescent mCard in sFCCS measurements on myristoylated-palmitoylated (mp)-mCard-mEYFP hetero-dimers and the discrepancy of the APLP1 brightness data.

Overall, strong differences of the fluorescence probability were found among different FPs. It is worth noting that this parameter is conceptually empirical, quantifying the apparent fraction of non-fluorescent states. These can be induced by a variety of processes, for example photophysical transitions to long-lived dark states, blinking between *on* and *off* states, photobleaching, slow FP maturation, or incorrect folding. Notably, the presented correction scheme, determining the fluorescence probability from the relative homo-dimer brightness, is also valid for fluorophores that populate different fluorescent states, e.g. a bright and a dim state, rather than an *on* and an *off* state (Wu et al., 2009).

In order to maximize the dynamic range of brightness measurements, a maximal

fluorescence probability is desired. FPs with a low fraction of fluorescent states suffer from the fact that each FP unit only marginally contributes to the molecular brightness of a protein complex. This issue demonstrates a clear advantage of well-performing FPs such as mEGFP, reaching a fluorescence probability of up to 80%, compared to labeling via tags, antibodies, or specific residues that often lead to much lower labeling ratios in suboptimal cellular conditions (Arant and Ulbrich, 2014, Grubmayer et al., 2019, Thevathasan et al., 2019). Furthermore, the exact labeling efficiency and stoichiometry are often difficult to quantify. For mEGFP, on the other hand, it could be shown that the calibrated fluorescence probability indeed led to correct estimates of the oligomeric state of biologically relevant protein complexes such as the influenza virus hemagglutinin glycoprotein. Moreover, the fluorescence probability was independent of the specific expression system, subcellular FP localization, and FFS technique used. Thus, it appears to be a mostly FP inherent property. The comparison of slow and fast maturing FP variants indicated that FP maturation is a major factor determining the fluorescent probability of FPs. Of note, such FP properties also need to be taken into consideration for other quantitative techniques such as FRET (Liu et al., 2018, McCulloch et al., 2019). For example, maturation of donor and acceptor FPs are required for a functional FP FRET pair.

At this point, it should be briefly considered to which extent the observed properties of mEYFP and mCard, in particular the low mCard fluorescence probability, affect the APLP1 results, particularly the relative cross-correlation that was evaluated as a measure of *trans* interactions. For *trans* binding of large protein complexes, e.g. in zinc conditions, the cross-correlation is expected to be only weakly affected by a high fraction of non-fluorescent mCard units, as long as each *trans* complex still carries at least one fluorescent unit on each side. For small oligomers, on the other hand, non-fluorescent FP units are expected to cause a significant reduction of the detectable cross-correlation (Foo et al., 2012). In the analysis of sFCCS measurements on APLP1, this effect could be minimized by determining the maximum relative cross-correlation, i.e. calculating two relative cross-correlation values by normalizing the amplitude of the cross-correlation function (CCF) with respect to the ACF amplitudes in each channel, and defining the maximum of these two values as a quantitative measure for *trans* binding. This definition is motivated by the fact that the maximum detectable relative cross-correlation in this system is limited by the number of APLP1s in the cell with lower expression levels (of the two cells forming the junction). For example, if 50 proteins are present on one and 100 proteins on the other side, those 50 will (assuming a 1:1 stoichiometry with 100% binding affinity) all have a binding partner, whereas the 50 proteins that are left on the other side

remain unbound (thus limiting the measured cross-correlation). The same logic applies to the bias induced by the different fluorescence probabilities of mEYFP and mCard. Due to the higher fluorescence probability of mEYFP, it is likely that fluorescent APLP1-mCard is bound to a fluorescent APLP1-mEYFP in a *trans* complex. In contrast, many fluorescent APLP1-mEYFPs likely interact with non-fluorescent APLP1-mCards. Hence, a higher relative cross-correlation is expected when normalizing the CCF amplitude to the ACF amplitude of the mEYFP channel (this ratio being a measure of the fraction of fluorescent APLP1-mCard bound to APLP1-mEYFP), in agreement with the results of the sFCCS measurements. In this way, the described analysis minimizes the reduction of the cross-correlation due to non-fluorescent FPs. Nevertheless, the obtained sFCCS relative cross-correlation values in the absence of zinc ions and the cross-correlation brightness of the ccN&B analysis may still underestimate the actual degree of *trans* interactions.

Molecular brightness analysis using FCS or N&B is based on the first and second moment, i.e. mean and variance, of the photon count distribution. Thus, it allows calculating two independent parameters: the average number of particles and their average molecular brightness. This information is sufficient to characterize a homogeneous ensemble of particles that all have the same brightness. However, more complex scenarios, for example mixtures of a single particle species having different oligomeric states, cannot be resolved *per se*. Making *a priori* assumptions such as the binomial model applied to calculate the fluorescence probability, nevertheless, allows to resolve binary mixtures from the average molecular brightness. In this context, evaluation of the concentration dependence of molecular brightness values may help to formulate suitable models. As shown in the appendix (fig. 4.30), an equilibrium between two oligomeric states (e.g. monomers at low concentrations and trimers at high concentrations) is often observed. This information can be used to calculate the monomer/trimer ratio at a certain protein concentration or to determine association constants via fitting of equilibrium models to the brightness measured as a function of concentration. Higher order mixtures, however, cannot be resolved.

To overcome this limitation, several techniques involving more sophisticated statistical analysis have been developed. These methods are based on fitting the photon counting histogram of a temporal (PCH) or spatial (spiDA) measurement, or analyze higher order moments of the photon count distribution (FCA/TIFCA) (Chen et al., 1999, Godin et al., 2011, Müller, 2004, Wu and Müller, 2005). In this work, FCA and TIFCA were explored, as described in the appendix (section 4.10). While working successfully on simulated sFCS data (fig. 4.26), application on membrane proteins in living cells suffered from limited statistics (fig. 4.29).

Generally, the signal-to-noise ratio (SNR) in FFS is directly proportional to the brightness of fluorophores and scales with the square root of the measurement time (figs. 4.6, 4.7). The molecular brightness can principally be increased by the excitation laser power, but photobleaching limits the available brightness in practical cases. Hence, in particular small oligomers suffer from low SNR in FFS measurements. In addition, PCH and FCA/TIFCA require low particle numbers, ideally around 1 (Müller et al., 2000), that are not feasible in sFCS geometry for overexpressing cells, typically showing 100 particles or more in the focal volume. Lastly, higher moment analysis requires careful calibration of the focal volume geometry and the detector noise characteristics. While the detector variance can be determined by calibration measurements (e.g. for N&B, chapter 2.2 and section 4.2.3 in appendix), the detector contribution to higher moments of the photon count distribution is not easily accessible and varies strongly among different microscopes (fig. 4.27). Two recent studies therefore present a time-shifted analysis, using the fact that detector noise contributions are practically not correlated in time (Hennen et al., 2019a,b). In conclusion, a successful application of advanced techniques to resolve higher order mixtures of protein complexes at the PM could not be achieved yet due to the mentioned limitations. Nevertheless, a microscope with higher detection efficiency that only recently became available (fig. 4.29) may help to successfully apply such techniques to sFCS data. This microscope may also enable to multiplex brightness measurements of differently tagged protein species via spectral detection, as discussed in the previous section.

As already mentioned for APLP1 experiments, it is important to consider that FFS *per se* and, hence, brightness analysis is based on detecting fluorescence fluctuations. More specifically, it requires fluctuations of the number of particles present in the focal volume, for example via diffusive transport. As shown in the appendix (fig. 4.6), the molecular brightness is underestimated when particle diffusion is too slow with respect to the total acquisition time of a measurement. The fluorescence signal detected from immobile complexes will only fluctuate due to detector shot noise (and potentially photobleaching), but will not exhibit a contribution from number fluctuations. In the cellular context, this limitation applies to very large membrane protein complexes showing diffusion coefficients of $0.1 \mu\text{m}^2/\text{s}$ and lower. On the other hand, for fast diffusion the temporal resolution of the acquisition needs to be high enough that number fluctuations do not average out during the accumulation of the fluorescence signal in a single pixel or time interval. Therefore, acquisition schemes should be carefully selected and adjusted to match the diffusion dynamics present in the system under investigation.

Compared to other counting techniques, FFS brightness analysis has the advantage that it is live cell compatible due to its dynamic nature. Alternative techniques such as subunit counting via stepwise photobleaching or via photon statistics, intensity or SR based counting require extended acquisition times on single molecule complexes, required to be static during the measurement (Grußmayer et al., 2019). This is often achieved by sample fixation. Similarly to the approach in this work, reference standards such as artificial FP homo-oligomers or protein complexes of known stoichiometry are used to calibrate the quantification in most of these techniques (Finan et al., 2015, Fricke et al., 2015, Thevathasan et al., 2019). For example, Puchner et al. (2013) reported a detectable fraction of close to 60% for the photoactivatable FP mEos2, thus, a value similar to the fluorescence probabilities determined for conventional FPs described here.

Since fluctuation analysis provides the basis for any FFS technique, external fluctuations, e.g. long-term variations of the average signal due to additional processes besides diffusion of molecules, may severely perturb FFS measurements of diffusion or interactions. This issue is often encountered in cellular systems suffering from depletion of fluorescent molecules or fluctuations induced by the active nature of cells, such as cellular motion or intracellular transport. In the appendix of this work multiple schemes are discussed that circumvent or correct for these perturbations. Extensive simulations of sFCS and N&B were carried out to evaluate the performance of correction schemes for photobleaching, background fluorescence, or for instabilities via Fourier- or segment-wise analysis, and their effect on parameter estimates (sections 4.9.1-4.9.4). Nevertheless, amplitude and frequency of such external perturbations strongly vary in different systems and may, in the worst case, completely impede measurements of molecular transport or interactions via FFS techniques.

Future research may help to better identify or correct signal perturbations, e.g. via (supervised) machine learning approaches. In addition, alternative analysis schemes such as the recently presented Bayesian approach by Jazani et al. (2019) may circumvent the current requirement of acquisition times that are much longer than the dynamics of the microscopic process of interest (figs. 4.22, 4.23 in appendix). This requirement is the main reason why, up to now, measurements often suffer from long-term signal variations due to cellular dynamics. Such alternative analysis frameworks may also provide new opportunities to resolve ensembles with mixed populations of different brightness or diffusion dynamics.

3.3 Bacterial biofilm matrix hinders diffusion probe size dependently

In the last part of this work, diffusive transport in a bacterial biofilm matrix model was investigated. By performing pFCS and SPT in a reconstituted polysaccharide matrix system, a characteristic size dependence of the diffusion hindrance experienced by small molecules, nanoparticles, and bacteriophages was found. In addition, diffusion analysis allowed to infer the concentration dependent structural organization of the polysaccharide matrix, showing characteristics of an entangled polymer network at physiological concentrations.

The main advantage of the presented *in vitro* approach is that key parameters of the system such as molecular composition, polysaccharide concentration, and pH are well controllable and can be therefore investigated systematically. Thus, measured diffusion properties can be linked to the organization of a specific biofilm derived biopolymer. This is in contrast to most previous studies that addressed diffusion directly in bacterial biofilms where the specific macromolecular composition is complex and remains unknown. Nevertheless, the *in vitro* approach carried out in this work has several important limitations. The most striking is that *in vivo* biofilms are complex multicomponent systems, which are frequently composed of multiple bacterial species or matrix components. Hence, many different macromolecules potentially interact with each other and give rise to complex emergent properties (Flemming and Wingender, 2010). Even in systems that predominantly consist of one matrix polymer, the chain lengths, concentration, and solvent conditions (e.g. ions, salts) may vary in space and time (Stewart and Franklin, 2008). Generally, biofilms are strongly heterogeneous systems. Embedded bacteria can control composition and abundance of their extracellular matrix by enzymatic modifications or changes in the rate of production or release of certain matrix components. This complex organization is not properly mimicked by a simple homogeneous one component model. Thus, the here investigated system provides a starting point for more realistic model systems incorporating multiple components. For example, it has recently been hypothesized that fibrillar proteins confine phage mobility in *E. coli* biofilms (Vidakovic et al., 2018). These, on the other hand, also contain polysaccharide matrix components of high abundance (Hufnagel et al., 2015). Therefore, it would be very interesting to set up a matrix model system containing both types of macromolecules. The diffusion properties of the combined system should then be investigated as a function of concentration or enzymatic depolymerization of one or both components. In addition, the role of charges in modulating particle diffusion and biofilm matrix

organization should be systematically explored. In many biofilm systems, major EPS components are charged, affecting both, transport of charged molecules such as antibiotics and the macroscopic rheological properties, which may additionally be altered by ions and salts (Körstgens et al., 2001, Singh et al., 2016, Wagner et al., 2017).

Finally, a direct comparison of particle diffusion dynamics in simplified model systems and intact biofilms should be performed. In this context, it could be beneficial to concurrently monitor the amount of specific EPS components in intact biofilms, for example via fluorescence labeling of sugar residues (Lawrence et al., 2007). Implementation of a quantitative calibration protocol could allow to determine the physical concentration of labeled matrix components from the fluorescence signal. Hence, it may be possible to correlate particle dynamics and, in the context of bacteriophage infections, even local infection rates with physiological EPS densities. In order to explore and map spatial heterogeneities, sFCS, imaging FCS, or SPT, providing the possibility to quantify diffusion dynamics in several locations in parallel, should be used rather than pFCS. A recently published investigation by Sankaran et al. (2019) presents the first application of single plane illumination microscopy (SPIM) FCS to generate spatially resolved maps of diffusion in living biofilms.

When performing FCS on finite-sized particles such as polystyrene beads or bacteriophages, size effects and the spatial distribution of fluorophores on the particles have to be considered. As shown by Wu et al. (2008) and Deptuła et al. (2015), diffusion times may be overestimated when fitting a point model to the ACFs. Assuming a shell particle model, a $< 4\%$ error on diffusion times is expected for 60 nm beads and 75 nm phage particles for one-photon excitation. For 200 nm beads the error would be around 15%. In the presented work, SPT and FCS analysis yielded comparable results. Furthermore, size estimates of particles by Dynamic Light Scattering (DLS) and FCS measurements agreed. Thus, size effects appear to be smaller than the experimental variation of diffusion times obtained within each sample, which was typically around 10-15%.

In the last part of the biofilm investigation, it was shown that enzymatic depolymerization of the polysaccharide matrix by bacteriophage tailspike proteins (TSPs) strongly affects matrix organization and facilitates unhindered diffusion even for larger particles. In future studies the effect of TSPs on intact biofilms will be investigated as a function of enzyme concentration. Furthermore, the role of TSPs will be explored at the level of bacteriophages by comparing transport dynamics of phage particles that possess or lack the capability to degrade EPS in both, model systems

and intact biofilms, at different phage titers. An interesting aspect here is that EPS depolymerization by TSP enzymes may have local and global impacts on biofilm organization. At very low phage titers, phage diffusion and accompanied matrix depolymerization should mainly generate local perturbations of the matrix structure, which might even be repaired by release of newly synthesized matrix material. At high phage titers, on the other hand, many local perturbations may globally change EPS matrix organization and cause strong changes of transport dynamics and overall biofilm mechanical properties.

Ultimately, such experimental investigations will provide a quantification of important mechanistic aspects of bacterial biofilm organization that can be incorporated in mathematic models, e.g of the propagation of bacteriophage infections in biofilms (Simmons et al., 2018). Finally, a fundamental understanding of bacterial biofilm ecology is of vital importance considering the strong emergence of multiresistant bacterial strains. Bacteriophages and TSP enzymes could provide novel antimicrobial strategies acting on specific bacterial targets.

4 Appendix

4.1 Introduction to FCS/sFCS and theoretical background

In the following sections, $\langle x \rangle$ denotes the time average of a quantity x , $\langle x \rangle_t$, unless otherwise noted.

4.1.1 Derivation of the FCS correlation function

As introduced in chapter 1, FCS analyzes fluctuations $\delta F(t)$ of the fluorescence signal $F(t)$, emitted by an ensemble of fluorophores that move (e.g. diffuse) through the observation volume. The fluctuations are analyzed using the ACF:

$$G(\tau) = \frac{\langle \delta F(t) \delta F(t + \tau) \rangle}{\langle F(t) \rangle^2} = \frac{\langle F(t) F(t + \tau) \rangle}{\langle F(t) \rangle^2} - 1. \quad (4.1)$$

In order to derive an explicit model for $G(\tau)$ that can be fitted to experimental data, the detected signal $F(t)$ is modeled as follows. The signal emitted by a single fluorophore located at position \vec{r} is $f(\vec{r}) = \epsilon \text{MDF}(\vec{r})$. Here, ϵ denotes the molecular brightness, which depends on the absorption cross-section σ_{abs} , the fluorophore quantum efficiency q_f and the detection efficiency η_d : $\epsilon = \sigma_{abs} q_f \eta_d$. The molecule detection function (MDF) is the product of the microscope illumination profile $I(\vec{r})$ and the detection probability distribution $\Omega(\vec{r})$:

$$\text{MDF}(\vec{r}) = I(\vec{r}) \Omega(\vec{r}). \quad (4.2)$$

The intensity $F(t)$ is the superposition of the signal contributions of each single fluorophore, integrated over the sample volume:

$$F(t) = \int d^3 \vec{r} \epsilon \text{MDF}(\vec{r}) c(\vec{r}, t), \quad (4.3)$$

where $c(\vec{r}, t)$ is the concentration of fluorophores at position \vec{r} and time t . Note that for multiple species i , the total intensity $F(t)$ is the sum of the contributions of all species, $F(t) = \sum_i F_i(t)$.

Splitting the concentration $c(\vec{r}, t)$ into the time-averaged concentration $\langle c \rangle$ (in the following simply noted as c) and a fluctuating part $\delta c(\vec{r}, t)$, the signal fluctuations can be expressed as

$$\delta F(t) = \int d^3\vec{r} \epsilon \text{MDF}(\vec{r}) \delta c(\vec{r}, t). \quad (4.4)$$

Insertion into eq. 4.1 gives

$$G(\tau) = \frac{\int d^3\vec{r} \int d^3\vec{r}' \epsilon^2 \text{MDF}(\vec{r}) \text{MDF}(\vec{r}') \langle \delta c(\vec{r}, t) \delta c(\vec{r}', t + \tau) \rangle}{\left(\int d^3\vec{r} \epsilon \text{MDF}(\vec{r}) \langle c(\vec{r}, t) \rangle \right)^2}. \quad (4.5)$$

The term $\langle \delta c(\vec{r}, t) \delta c(\vec{r}', t + \tau) \rangle$ is the concentration CF, given by the propagator $P(\vec{r}, \vec{r}', \tau)$ (Green's function) of the partial differential equation (PDE) governing the dynamics of $c(\vec{r}, t)$, i.e. the solution of the PDE for the initial condition $c(\vec{r}, 0) = \delta(\vec{r})$:

$$\langle \delta c(\vec{r}, t) \delta c(\vec{r}', t + \tau) \rangle = c P(\vec{r}, \vec{r}', \tau). \quad (4.6)$$

For a single particle, $P(\vec{r}, \vec{r}', \tau)$ gives the probability of finding the particle at position \vec{r}' after time τ . For normal diffusion, P is obtained by solving the diffusion equation,

$$\frac{\partial}{\partial t} c(\vec{r}, t) = D \vec{\nabla}^2 c(\vec{r}, t), \quad (4.7)$$

and given by

$$P(\vec{r}, \vec{r}', \tau) = \frac{1}{(4\pi D\tau)^{d/2}} \exp\left(-\frac{|\vec{r} - \vec{r}'|^2}{4D\tau}\right), \quad (4.8)$$

for diffusion in d dimensions.

Finally, a model for the MDF of the microscope has to be defined. For confocal setups the MDF is commonly described with the 3D Gauss model:

$$\text{MDF}_{3DG}(\vec{r} = (x, y, z)) = \frac{2^{3/2}}{\pi^{3/2} \omega_0^2 \omega_z} \exp\left(-2\frac{(x^2 + y^2)}{\omega_0^2} - 2\frac{z^2}{\omega_z^2}\right), \quad (4.9)$$

where ω_0 and ω_z are the lateral and axial elongations of the focal volume. The ratio of lateral and axial dimensions defines the structure factor, $S = \omega_z/\omega_0$.

Using eqs. 4.5, 4.6, 4.8, 4.9, the ACF for normal diffusion in 3D can be calculated analytically:

$$G(\tau) = \frac{1}{N} \left(1 + \frac{\tau}{\tau_d}\right)^{-1} \left(1 + \frac{\tau}{S^2 \tau_d}\right)^{-1/2}. \quad (4.10)$$

Here, N denotes the number of particles, $N = cV_{\text{eff}}$, in the effective volume $V_{\text{eff}} = \pi^{3/2}S\omega_0^3$ and $\tau_d = \omega_0^2/4D$ the diffusion time. Note that N is obtained directly from the amplitude of $G(\tau)$, $N = 1/G(0)$, which is further discussed in the next section.

For FCS on particles diffusing in a 2D geometry (e.g. a planar lipid membrane, effectively restricted to the xy -plane), the MDF is approximated by a 2D Gaussian:

$$\text{MDF}_{2DG}(\vec{r} = (x, y)) = \frac{2}{\pi\omega_0^2} \exp\left(-2\frac{(x^2 + y^2)}{\omega_0^2}\right). \quad (4.11)$$

The corresponding ACF is given as

$$G(\tau) = \frac{1}{N} \left(1 + \frac{\tau}{\tau_d}\right)^{-1}, \quad (4.12)$$

with $N = cA_{\text{eff}}$ particles in the effective detection area $A_{\text{eff}} = \pi\omega_0^2$ and $\tau_d = \omega_0^2/4D$.

In the following sections, the MDF is used in a rescaled form, normalized at the origin ($\text{MDF}(\vec{0}) = 1$), hence $f(\vec{0}) = \epsilon$ (Chen et al., 1999).

4.1.2 Particle number, molecular brightness and effective detection volume

To fit experimental data, the FCS correlation function is commonly expressed in the form given in the previous section (eq. 4.10) using the parameters N and τ_d that can be obtained directly from the ACF. Determination of the physical parameters c and D requires knowledge of the physical dimensions of the focal volume. Particle number and concentration are related by the effective detection volume,

$$V_{\text{eff}} = \frac{N}{c} = \frac{1}{G(0)c}. \quad (4.13)$$

More generally, V_{eff} can be defined using eq. 4.5. The particle number/concentration in the focal volume follows Poisson statistics. Hence, the variance of the number/concentration is equal to the mean. Thus,

$$\langle \delta c(\vec{r}, t) \delta c(\vec{r}', t) \rangle = \langle \delta c^2(\vec{r}, t) \rangle \delta(\vec{r} - \vec{r}') = \langle c(\vec{r}, t) \rangle \delta(\vec{r} - \vec{r}'). \quad (4.14)$$

Insertion into eq. 4.5 gives:

$$G(0) = \frac{c \epsilon^2 \int d^3\vec{r} \text{MDF}^2(\vec{r})}{c^2 \epsilon^2 (\int d^3\vec{r} \text{MDF}(\vec{r}))^2} \quad (4.15)$$

$$= \frac{1}{c V_{\text{eff}}} = \frac{1}{N}, \quad (4.16)$$

with

$$V_{\text{eff}} = \frac{\int d^3\vec{r} \text{MDF}^2(\vec{r})}{(\int d^3\vec{r} \text{MDF}(\vec{r}))^2}. \quad (4.17)$$

For the 3D Gaussian MDF model (eq. 4.9), V_{eff} can be calculated analytically, giving $V_{\text{eff}} = \pi^{3/2} S \omega_0^3$.

Similarly, $G(0) = 1/N$ can be derived starting directly from eq. 4.1, by taking $\tau = 0$:

$$G(0) = \frac{\langle \delta^2 F(t) \rangle}{\langle F(t) \rangle^2} = \frac{\text{Var}(\epsilon_{\text{eff}} N)}{\langle \epsilon_{\text{eff}} N \rangle^2} = \frac{\epsilon_{\text{eff}}^2 \text{Var}(N)}{\epsilon_{\text{eff}}^2 \langle N \rangle^2} = \frac{1}{N}, \quad (4.18)$$

where the variance of the particle number $\text{Var}(N)$ was assumed to be equal to the mean particle number. Here, it should be noted that in the FCS analysis, $G(0)$ is obtained by interpolating the lag time τ to zero, i.e. a model G_{fit} (e.g. eq. 4.10) is fitted to the ACF and evaluated at $\tau = 0$. Thereby, the detector shot noise, which is not correlated on the experimentally sampled time scales ($\gtrsim 1 \mu\text{s}$), averages out and can thus be neglected here, in contrast to N&B analysis (see section 4.2.3 for details).

In eq. 4.18, ϵ_{eff} denotes the effective molecular brightness,

$$\epsilon_{\text{eff}} = \frac{\langle F \rangle}{N}, \quad (4.19)$$

of particles diffusing through the focal volume. This average value depends on the shape of the focal volume and the spatial distribution of particles. While particles located in the center emit a brightness equal or close to the maximum count rate per particle, $\epsilon \text{MDF}(\vec{0}) = \epsilon$, particles in the periphery emit a lower signal. Thus, the effective brightness ϵ_{eff} is given by the average brightness over all possible particle positions \vec{r} , contributing a signal $\epsilon \text{MDF}(\vec{r})$,

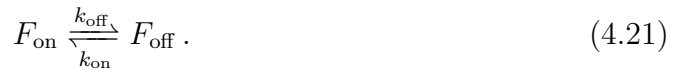
$$\epsilon_{\text{eff}} = \frac{\int d^3\vec{r} (\epsilon \text{MDF}(\vec{r})) \text{MDF}(\vec{r})}{\int d^3\vec{r} \text{MDF}(\vec{r})} = \gamma \epsilon. \quad (4.20)$$

This equation defines the γ -factor, that can be analytically calculated. For the 3D Gaussian model, $\gamma_{3D} = 1/(2\sqrt{2}) \approx 0.35$, for particles distributed in a 2D Gaussian detection area, $\gamma_{2D} = 0.5$. The effect of this geometrical factor can be observed when

comparing FFS brightness values detected on fluorophores distributed in 3D, e.g. the cell cytoplasm, with the values obtained for fluorophores of the same type distributed in 2D, e.g. at the basal membrane, the latter giving significantly higher brightness values due to the axial confinement of fluorophores to the center of the MDF.

4.1.3 Photophysical transition dynamics

Fluorophores that are commonly used in FCS experiments undergo photophysical dynamics, e.g. transition to a triplet state or blinking due to deprotonation/protonation reactions. In the simplest model, these processes are described as transitions between two states, a bright (on) and a dark (off) state:



In equilibrium, the average fraction of particles populating the off state is given by $T = \frac{k_{\text{off}}}{k_{\text{off}} + k_{\text{on}}}$, with an average lifetime $\tau_T = \frac{1}{k_{\text{off}} + k_{\text{on}}}$. The transitions cause additional fluctuations of the fluorescence intensity and contribute to the ACF. Assuming statistical independence of photophysical transitions and particle motions, the CF factorizes in a diffusion and a photophysics term:

$$G(\tau) = G_{\text{diff}}(\tau) \cdot G_T(\tau). \quad (4.22)$$

Solving the corresponding reversible first order equations, the photophysics term follows as

$$G_T(\tau) = \left(1 + \frac{T}{1-T} e^{-\frac{\tau}{\tau_b}}\right). \quad (4.23)$$

Thus, the full ACF model for normal diffusion in 3D, including triplet or blinking dynamics, is given by

$$G(\tau) = \frac{1}{N} \left(1 + \frac{T}{1-T} e^{-\frac{\tau}{\tau_b}}\right) \left(1 + \frac{\tau}{\tau_d}\right)^{-1} \left(1 + \frac{\tau}{S^2 \tau_d}\right)^{-1/2}. \quad (4.24)$$

It has to be noted that diffusion and photophysical dynamics are only statistically independent for transitions that do not depend on the excitation intensity. In contrast, triplet dynamics depend on the excitation power (e.g. increased k_{off} with increased illumination), and thus dependent on the position of particles in the focal volume. Therefore, eq. 4.24 should be considered as an approximation in this case.

4.1.4 FCS correlation function for anomalous diffusion

As mentioned in the introduction (chapter 1), anomalous diffusion dynamics are often encountered in biological systems. They are characterized by a subdiffusive MSD scaling (i.e. $\text{MSD} \sim t^\alpha$) and a deviation of the ACF from a normal diffusion model (see fig. 4.1). To account for such dynamics, a time-dependent diffusion coefficient is assumed, $D(t) = \Gamma t^{\alpha-1}$. From the modified diffusion equation

$$\frac{\partial}{\partial t} c(\vec{r}, t) = D(t) \vec{\nabla} c(\vec{r}, t), \quad (4.25)$$

the propagator

$$P(\vec{r}, \vec{r}', \tau) = \frac{1}{(\sqrt{\pi\Gamma\tau^\alpha})} \exp\left(-\frac{|\vec{r} - \vec{r}'|^2}{\Gamma\tau^\alpha}\right) \quad (4.26)$$

can be derived.

Inserting this expression into eq. 4.5, using a 3D Gaussian MDF model (eq. 4.9) and assuming triplet transitions of a fraction T of particles, the following ACF is obtained (Weiss et al., 2004):

$$G(\tau) = \frac{1}{N} \left(1 + \frac{T}{1-T} e^{-\frac{\tau}{\tau_b}}\right) \left(1 + \left(\frac{\tau}{\tau_d}\right)^\alpha\right)^{-1} \left(1 + \frac{1}{S^2} \left(\frac{\tau}{\tau_d}\right)^\alpha\right)^{-1/2}. \quad (4.27)$$

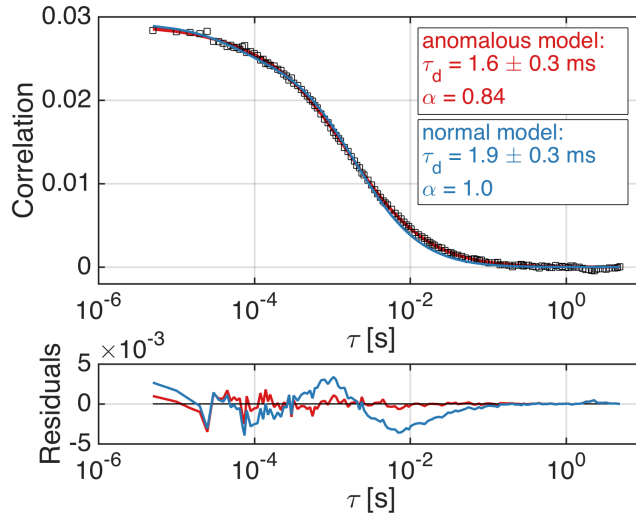


Figure 4.1: Anomalous diffusion in the cell cytoplasm. The top panel shows the ACF (squares) of a pFCS measurement in the cytoplasm of human epithelial lung A549 (A549) cells, expressing mEGFP homo-tetramers. The solid curves are fits of a 3D normal diffusion (blue, eq. 4.24) or anomalous diffusion model (red, eq. 4.27) to the ACF, including a photophysics term. The anomalous diffusion model gives $\alpha = 0.84$, indicating subdiffusive dynamics. The residuals (bottom panel) for the normal diffusion model (blue line) show a systematic deviation of the fit curve from the ACF, particularly at large lag times.

4.1.5 Two-focus FCS

A useful variant of FCS is 2fFCS. In this approach the fluorescence signal is measured in two detection volumes spatially shifted by \vec{d} . Then, ACFs for each detection volume, and the spatial CCF are computed. The latter is defined as

$$G_{\text{cc}}(\tau) = \frac{\langle \delta F(\vec{r}, t) \delta F(\vec{r} + \vec{d}, t + \tau) \rangle}{\langle F(\vec{r}, t) \rangle \langle F(\vec{r} + \vec{d}, t) \rangle}. \quad (4.28)$$

If the two detection volumes can be described by the same MDF, G_{cc} is

$$G_{\text{cc}}(\tau) = \frac{\int d^3\vec{r} \int d^3\vec{r}' \text{MDF}(\vec{r}) \text{MDF}(\vec{r}' + \vec{d}) \langle \delta c(\vec{r}, t) \delta c(\vec{r}' + \vec{d}, t + \tau) \rangle}{\left(\int d^3\vec{r} \text{MDF}(\vec{r}) \langle c(\vec{r}, t) \rangle \right) \left(\int d^3\vec{r}' \text{MDF}(\vec{r}' + \vec{d}) \langle c(\vec{r}' + \vec{d}, t) \rangle \right)}. \quad (4.29)$$

Assuming a lateral shift in one direction, e.g. $\vec{d} = (0, d, 0)$, a 3D Gaussian MDF (eq. 4.9) and normal diffusion, the following CCF is obtained:

$$G_{\text{cc}}(\tau) = G(\tau) \exp\left(-\frac{d^2}{4D\tau + \omega_0^2}\right), \quad (4.30)$$

where $G(\tau)$ is the ACF for pFCS (eq. 4.10).

The advantage of 2fFCS is that it enables calibration-free FCS. Knowing the distance d of the foci, the diffusion coefficient D , the waist ω_0 and thus the average concentration c can be obtained by fitting eq. 4.30 to the measured two-focus CCF. In particular, a global fit of the two ACFs and the two-focus CCF can be performed, leading to more robust and accurate results.

An important issue for the accuracy of 2fFCS is spatial cross-talk, causing leakage of signal emitted by fluorophores in one focus to the second focus. This leads to an autocorrelation contribution to the two-focus CCF at small lag times (Brinkmeier et al., 1999). Sophisticated fit model schemes may be used to correct for this effect. For example, Baum et al. (2014) computationally optimized MDF models for a home-built setup, assuming invariance of the diffusion coefficient of fluorescent particles in water measured for spatial correlations of pixels at multiple distances.

To completely avoid spatial cross-talk, alternated excitation of both foci can be performed. In this case, the time lag Δt between acquisitions of both foci has to be considered:

$$G_{\text{cc}}(\tau) = \frac{\langle \delta F(\vec{r}, t) \delta F(\vec{r} + \vec{d}, t + \tau + \Delta t) \rangle}{\langle F(\vec{r}, t) \rangle \langle F(\vec{r} + \vec{d}, t + \Delta t) \rangle}. \quad (4.31)$$

If Δt is much smaller than the diffusion time, it can be neglected, and eq. 4.28 provides a valid approximation.

An important application of 2fFCS is the investigation of flow (Brinkmeier et al., 1999, Dittrich and Schwille, 2002). If molecular transport is not isotropic, different CCFs will be obtained when correlating the signal in the first focus with the signal in the second focus and vice versa. For normal diffusion with an additional flow of velocity $\vec{v} = (v_x, v_y, v_z)$ and a 3D Gaussian model, the two-focus CCF is

$$G_{\text{cc,flow}}(\tau) = G(\tau) \exp \left(-\frac{(v_x\tau - d_x)^2 + (v_y\tau - d_y)^2}{4D\tau + \omega_0^2} - \frac{(v_z\tau - d_z)^2}{4D\tau + \omega_z^2} \right). \quad (4.32)$$

4.1.6 Dual-color FCCS

A powerful extension of FCS is multiple-color FCCS, in which multiple spectral channels are detected in parallel on a sample containing several fluorescent species with distinct spectral properties (Schwille et al., 1997). In the simplest form (FCCS), two species, named *green* (g) and *red* (r) in the following, are detected. In addition to ACF analysis, the two-color cross-correlation $G_{gr}(\tau)$ is analyzed. This function is a measure of the coincidence of signal fluctuations detected in both channels and thus reports on the degree of co-diffusion of molecules tagged with green or red fluorophores. The CCF is defined as

$$G_{gr}(\tau) = \frac{\langle \delta F_g(t) \delta F_r(t + \tau) \rangle}{\langle F_g(t) \rangle \langle F_r(t + \tau) \rangle}. \quad (4.33)$$

Denoting the MDFs of the two spectral windows MDF_g and MDF_r , the CCF has the form:

$$G_{gr}(\tau) = \frac{\int d^3\vec{r} \int d^3\vec{r}' \text{MDF}_g(\vec{r}) \text{MDF}_r(\vec{r}') \langle \delta c_g(\vec{r}, t) \delta c_r(\vec{r}', t + \tau) \rangle}{\left(\int d^3\vec{r} \text{MDF}_g(\vec{r}) \langle c_g(\vec{r}, t) \rangle \right) \left(\int d^3\vec{r}' \text{MDF}_r(\vec{r}') \langle c_r(\vec{r}', t) \rangle \right)}. \quad (4.34)$$

Using a 3D Gaussian MDF model (eq. 4.9) and assuming normal diffusion, the following CCF is obtained:

$$G_{gr}(\tau) = \frac{c_{gr}}{V_{gr}(c_{gr} + c_g)(c_{gr} + c_r)} \left(1 + \frac{\tau}{\tau_{d,gr}} \right)^{-1} \left(1 + \left(\frac{\omega_{0,gr}}{\omega_{z,gr}} \right)^2 \frac{\tau}{\tau_{d,gr}} \right)^{-1/2}. \quad (4.35)$$

Here, c_{gr} is the concentration of particles carrying both red and green labels, c_g and c_r are the concentrations of free green and red particles, respectively. The parameters $\omega_{0,gr}$ and $\omega_{z,gr}$ are the lateral and axial elongations of the overlap volume V_{gr} , having a structure factor $S = \omega_{z,gr}/\omega_{0,gr}$. The given CCF does not contain a photophysics term. Due to the statistical independence of photophysical transitions of green and

red fluorophores, such fluctuations average out in the CCF. In contrast, eq. 4.24 is usually fitted to the ACFs of an FCCS measurement. Note that for measurements in the cytoplasm, eq. 4.35 can be modified to account for anomalous diffusion, analogous to eq. 4.27.

Generally, the detection volumes V_g , V_r of both spectral channels have different sizes and are shifted with respect to each other (Schwille et al., 1997). When both detection volumes are concentric, the overlap volume is given by the geometric average of the dimensions $\omega_{0,i}$, $\omega_{z,i}$ in each spectral channel ($i = g, r$):

$$V_{gr} = \pi^{3/2} \omega_{0,gr}^2 \omega_{z,gr} = \left(\frac{\pi}{2}\right)^{3/2} (\omega_{0,g}^2 + \omega_{0,r}^2)(\omega_{z,g}^2 + \omega_{z,r}^2)^{1/2}. \quad (4.36)$$

When volumes are shifted by the displacement $\vec{d} = (d_x, d_y, d_z)$, the amplitude of the CCF becomes

$$G_{gr}(0) = \frac{c_{gr}}{V_{gr}(c_{gr} + c_g)(c_{gr} + c_r)} \exp\left(-\frac{d_x^2 + d_y^2}{\omega_{0,gr}^2} - \frac{d_z^2}{\omega_{z,gr}^2}\right). \quad (4.37)$$

The exponential term has the same form as the additional factor in the two-focus CCF (eq. 4.30). Usually, the displacement of the detection volumes is difficult to calibrate and experimental data are therefore fitted without explicit consideration of an optical shift. Then,

$$G_{gr}(0) = \frac{c_{gr}}{V_{gr,\text{eff}}(c_{gr} + c_g)(c_{gr} + c_r)}, \quad (4.38)$$

where $V_{gr,\text{eff}}$ is an effective volume that is generally larger than the actual overlap volume V_{gr} . Hence, the amplitude of the CCF is reduced and higher diffusion times $\tau_{d,gr}$ are obtained (Foo et al., 2012). To account for this effect, the maximum achievable cross-correlation of a setup is calibrated, e.g. using double-labeled DNA strands (Ries et al., 2010b) or FP hetero-dimers (Foo et al., 2012), as a reference for experimentally measured cross-correlation values.

Together with the amplitudes of the channel ACFs,

$$G_g(0) = \frac{1}{V_{gr,\text{eff}}(c_g + c_{gr})}, \quad G_r(0) = \frac{1}{V_{gr,\text{eff}}(c_r + c_{gr})}, \quad (4.39)$$

the approximate relative fractions of bound red (Θ_r) and green molecules (Θ_g) can be calculated:

$$\Theta_g = \frac{c_{rg}}{c_g + c_{rg}} = \frac{G_{gr}(0)}{G_r(0)}, \quad \Theta_r = \frac{c_{rg}}{c_r + c_{rg}} = \frac{G_{gr}(0)}{G_g(0)}. \quad (4.40)$$

Throughout this thesis, the maximum of both relative fractions was used as a measure of hetero-interactions:

$$\text{rel.cc.} = \max\left(\frac{G_{gr}(0)}{G_r(0)}, \frac{G_{gr}(0)}{G_g(0)}\right). \quad (4.41)$$

This definition of the relative cross-correlation is justified by the fact that when the interacting species are present in different numbers, the maximum fraction of bound particles is limited by the species that is present in lower number.

In many systems, red and green particles do not interact in a 1 : 1 stoichiometry. In this case, the molecular brightness of free and bound particles is not the same and the consideration above is not valid anymore (e.g. eqs. 4.40). For more complex interactions, the concentrations can generally not be determined without *a priori* assumptions or a specific model (Kim et al., 2005).

In addition to imperfect overlap, spectral cross-talk limits the accuracy of FCCS. This artifact is caused by leakage of signal emitted from one species into the detection channel of the other. In the common setting, signal from the tail of the emission spectrum of the green species is detected in the red channel. Cross-talk can be reduced by appropriate filter settings, e.g. increasing the lower bound of the red detection window. However, this reduces the brightness and thus the SNR in the red channel. Therefore, a compromise between cross-talk reduction and signal loss has to be found. In FCCS spectral cross-talk induces a false positive cross-correlation. The maximum contribution of cross-talk can be quantified using a negative control, e.g. a sample containing red and green labeled species that are not expected to interact. Alternatively, cross-talk can be corrected by measuring the cross-talk coefficient, i.e. the fraction of green signal that leaks into the red channel in a sample containing only green fluorophores. Using this value, the cross-talk signal can be subtracted from the total red signal measured in the actual sample, thus obtaining a corrected CFs (Bacia et al., 2012). Nevertheless, even with cross-talk correction, the dynamic range of the measurable cross-correlation is reduced, and measurement errors are highly amplified when only a small fraction of red signal comes from red molecules. To overcome these limitations, more sophisticated excitation schemes have been developed based on alternating excitation, e.g. ALEX and pulsed interleaved excitation (PIE) (Kapanidis et al., 2004, Müller et al., 2005). In the absence of cross-excitation, these schemes enable true cross-talk-free FCS measurements and additionally allow to identify FRET between the two species. Alternatively, spectral (see section 4.11) and lifetime detection were recently used to effectively suppress cross-talk using

spectral or lifetime filters (Padilla-Parra et al., 2011, Schrimpf et al., 2018). These procedures, however, might also reduce the SNR of the red ACF.

4.1.7 sFCS perpendicular to the membrane

The major limitations of pFCS on membranes are photobleaching and low stability caused by slow diffusion dynamics and membrane movement. To overcome these limitations, sFCS perpendicular to the membrane was developed by Ries and Schwille (2006). In this variant the detection volume is repeatedly scanned across the membrane with a constant speed v along a line in a time T that is much smaller than the diffusion time of the molecules. For each scanned line, the detected signal emitted by the fluorescent molecules diffusing in the membrane is integrated. To derive the ACF of the integrated signal $F(t)$,

$$G(\tau) = \frac{\langle \delta F(t) \delta F(t + \tau) \rangle}{\langle F(t) \rangle^2}, \quad (4.42)$$

the effective MDF has to be considered. Assuming a scan in x -direction through a plane membrane located at $(x = 0, y, z)$, the MDF is integrated over the scanning period:

$$\text{MDF}_{\text{scan}}(y, z) = \frac{1}{T} \int_{-T/2}^{T/2} dt \text{MDF}(x, y, z) \approx \frac{1}{vT} \int_{-\infty}^{\infty} dx \text{MDF}(x, y, z). \quad (4.43)$$

Using the 3D Gaussian MDF model, the effective MDF is given by

$$\text{MDF}_{\text{scan}}(y, z) = \sqrt{\frac{\pi}{2}} \frac{\omega_0}{vT} \exp\left(-2\frac{y^2}{\omega_0^2} - 2\frac{z^2}{\omega_z^2}\right). \quad (4.44)$$

The ACF can then be derived from ($\vec{r} = (y, z)$):

$$G(\tau) = \frac{\int d^2\vec{r} \int d^2\vec{r}' \epsilon^2 \text{MDF}_{\text{scan}}(\vec{r}) \text{MDF}_{\text{scan}}(\vec{r}') \langle c(\vec{r}, t) c(\vec{r}', t + \tau) \rangle}{\left(\int d^2\vec{r} \epsilon \text{MDF}_{\text{scan}}(\vec{r}) \langle c(\vec{r}, t) \rangle\right)^2}. \quad (4.45)$$

Inserting the concentration CF (eq. 4.6) with the diffusion propagator for 2D diffusion (eq. 4.8 with $d=2$), the final correlation function can be calculated:

$$G(\tau) = \frac{1}{N} \left(1 + \frac{\tau}{\tau_d}\right)^{-1/2} \left(1 + \frac{\tau}{S^2 \tau_d}\right)^{-1/2}. \quad (4.46)$$

Here, $N = c\pi\omega_0\omega_z$ is the mean particle number in the effective detection area $A_{\text{eff}} = \pi\omega_0\omega_z$, $\tau_d = \omega_0^2/4D$ the diffusion time and $S = \omega_z/\omega_0$ the structure parameter.

Eq. 4.46 does not contain a photophysics term, since such transitions usually occur on a time scale (e.g μs) much smaller than the minimal lag time given by scanning period of the microscope (e.g. ms) and, thus, average out.

By scanning two parallel lines across the membrane, two-focus sFCS (2fsFCS) can be easily implemented, offering the possibility to perform calibration-free sFCS measurements. In analogy to eq. 4.30, the following two-focus CCF, expressed in the physical parameters c , D and ω_0 , applies:

$$G_{cc}(\tau) = \frac{1}{c\pi\omega_0^2 S} \left(1 + \frac{4D\tau}{\omega_0^2}\right)^{-1/2} \left(1 + \frac{4D\tau}{\omega_0^2 S^2}\right)^{-1/2} \exp\left(-\frac{d^2}{\omega_0^2 + 4D\tau}\right). \quad (4.47)$$

Eqs. 4.46 and 4.47 can be globally fitted to the ACFs in both lines and the two-focus CCF, taking the temporal shift between both foci, given by one line time, into account. The 2fsFCS variant is particularly useful for fast diffusion dynamics, i.e. diffusion times on the order of the scan time (typically ~ 1 ms for fastest scanning). In this case, an accurate fit to the ACFs is not possible due to the limited time resolution. Nevertheless, the two-focus CCF still allows to capture the fast dynamics by selecting a line separation that shifts the peak (see fig. 4.5) to larger lag times.

In order to investigate hetero-interactions or multiple species in the membrane, sFCS can be extended to multiple colors. In sFCCS the signal is acquired in two spectral channels and the spectral CCF is calculated in addition to two ACFs. By fitting eq. 4.46 to all three CFs, the amplitudes $G_r(0)$, $G_g(0)$, $G_{gr}(0)$ and, following eq. 4.40, the relative fractions of bound and free molecules can be determined. An ALEX acquisition scheme can be easily implemented by alternated scanning in the green and red channel (with only green or red excitation). This procedure is valid as long as diffusion times (usually > 10 ms in cell membranes) are much larger than the scanning period for one line which is fulfilled in most cases. Thus, spectral cross-talk can be circumvented in sFCCS as long as fluorophores do not show cross-excitation.

Finally, sFCCS and 2fsFCS can be combined to dual-color two-focus sFCCS (2fsFCCS) (Dörlich et al., 2015, Ries et al., 2010c), which is typically performed by alternated scanning of two lines and two channels. In this scheme the detected signals are correlated in all combinations resulting in 16 CFs that can be globally fitted. The CCF of both channels and lines is generally given by (Dörlich et al., 2015, Ries et al., 2010c)

$$G_{gr,cc}(\tau) = \frac{1}{cA_{\text{eff}}} \left(1 + \frac{4D\tau}{\omega_{0,\text{eff}}^2}\right)^{-1/2} \left(1 + \frac{4D\tau}{\omega_{z,\text{eff}}^2}\right)^{-1/2} \exp\left(-\frac{d^2}{\omega_{0,\text{eff}}^2 + 4D\tau}\right). \quad (4.48)$$

Here, $A_{\text{eff}} = \pi\omega_{0,\text{eff}}\omega_{z,\text{eff}}$ is the effective detection area, $\omega_{0,\text{eff}} = \sqrt{(\omega_{0,g}^2 + \omega_{0,r}^2)}/2$ the effective waist and $\omega_{z,\text{eff}} = \sqrt{(\omega_{z,g}^2 + \omega_{z,r}^2)}/2$ the axial elongation ($\omega_{z,g} = S\omega_{0,g}$, $\omega_{z,r} = S\omega_{0,r}$). The waists and displacement of the green and red detection volumes can be determined from the global fit, with d , $\omega_{0,g}$ and $\omega_{0,r}$ as free fit parameters (ω_0 replaced by $\omega_{0,\text{eff}}$ in the dual-color CCFs and by $\omega_{0,g}/\omega_{0,r}$ in the single-color CCFs, eqs. 4.46, 4.47). Thereby, artifacts due to imperfect overlap can be corrected.

4.2 N&B analysis

4.2.1 Theoretical background

The previously described FCS variants allow to measure the dynamics and concentration of molecules in a fixed position of a sample, e.g. a small cytoplasmic volume or cross-sectional area of the cell membrane. In order to map concentration and aggregation of particles in space, N&B has been developed (Digman et al., 2008). In this method a pixelwise moment analysis of a stack of confocal images (or of a camera acquired image stack using SPIM or TIRF setups) is performed. The first and second moment of the detected pixel intensity, i.e. mean intensity $\langle I \rangle$ and variance σ^2 , are related to the average particle number n and the average molecular brightness ϵ_{eff} in every pixel:

$$\langle I \rangle = \epsilon_{\text{eff}}n, \quad (4.49)$$

$$\sigma^2 = \epsilon_{\text{eff}}^2n + \epsilon_{\text{eff}}n. \quad (4.50)$$

The variance of the signal has two contributions: i) intensity fluctuations ϵ_{eff}^2n arising from fluctuations of the number of particles (e.g. due to diffusion), ii) photon shot noise which follows Poisson statistics for true photon counting detectors and thus has a variance equal to the average signal $\epsilon_{\text{eff}}n$. The principle of N&B is to explore the Superpoissonian statistics of the signal, i.e. the first contribution, in addition to shot noise. This contribution is usually small (e.g. only 10% of the total variance), requiring a careful calibration of the detector noise characteristics (see section 4.2.3). Inverting eqs. 4.49, 4.50 leads to:

$$\epsilon_{\text{eff}} = \frac{\sigma^2}{\langle I \rangle} - 1, \quad (4.51)$$

$$n = \frac{\langle I \rangle^2}{\sigma^2 - \langle I \rangle}. \quad (4.52)$$

Of note, photon counts in each pixel are integrated over a pixel dwell time τ_p . Thus, the brightness ϵ_{eff} obtained by eq. 4.51 has the unit photon counts per pixel. Division by the pixel dwell time gives the molecular brightness in physical units (counts per molecule and second, i.e. Hz):

$$\epsilon_{\text{eff,t}} = \epsilon_{\text{eff}}/\tau_p. \quad (4.53)$$

Note that in analogy to FCS, ϵ_{eff} is the average brightness over all particle positions, i.e. eq. 4.20 also applies here.

When multiple (independent) brightness species are present, the variance contributions of each species add up and the average brightness is given by:

$$\langle \epsilon_{\text{eff}} \rangle = \frac{\sum_i \epsilon_{\text{eff},i}^2 n_i}{\sum_i \epsilon_{\text{eff},i} n_i}. \quad (4.54)$$

N&B can also be performed on analog detectors or detectors that do not operate in true photon counting, e.g. do not show truly Poissonian shot noise. In this case the following equations apply (Dalal et al., 2008):

$$\epsilon_{\text{eff}} = \frac{\sigma^2 - \sigma_0^2}{S(\langle I \rangle - \text{offset})} - 1, \quad (4.55)$$

$$n = \frac{(\langle I \rangle - \text{offset})^2}{\sigma^2 - \sigma_0^2 - S(\langle I \rangle - \text{offset})}. \quad (4.56)$$

Here S is the conversion factor between detected photons and recorded digital counts, σ_0^2 the readout noise and offset the detector intensity offset. These parameters can be calibrated experimentally by measuring the detector variance as a function of intensity on a sample that does not show number fluctuations, e.g. using constant illumination on a reflective metal surface or dried dye solution as described in chapter 2.2.

An alternative way to quantify the detector noise characteristics based on the ACF amplitude in FCS is presented in section 4.2.3.

4.2.2 Cross-correlation N&B

Similarly to FCCS, the N&B method can be extended to investigate hetero-interactions using multiple labels with distinct spectral properties. For two channels, the cross-

correlation brightness B_{cc} is calculated in addition to the channel brightness values $\epsilon_{\text{eff},i}$ ($i=g,r$):

$$\epsilon_{\text{eff},i} = \frac{\sigma_i^2}{\langle I_i \rangle} - 1, \quad (4.57)$$

$$B_{cc} = \frac{\sigma_{cc}^2}{\sqrt{\langle I_g \rangle \langle I_r \rangle}} = \frac{\langle (I_g - \langle I_g \rangle)(I_r - \langle I_r \rangle) \rangle}{\sqrt{\langle I_g \rangle \langle I_r \rangle}}. \quad (4.58)$$

For two species G , R interacting in unknown stoichiometry,



the average signals and variances can be expressed by molecular parameters:

$$\langle I_i \rangle = \epsilon_{f,i} n_i + \nu_i \epsilon_{f,i} n_{cc}, \quad (4.60)$$

$$\sigma_i^2 = \epsilon_{f,i}^2 n_i + (\nu_i \epsilon_{f,i})^2 n_{cc} + \epsilon_{f,i} n_i + \nu_i \epsilon_{f,i} n_{cc}, \quad (4.61)$$

$$\sigma_{cc}^2 = \nu_g \epsilon_{f,g} \nu_r \epsilon_{f,r} n_{cc}. \quad (4.62)$$

Here, $\epsilon_{f,i}$ is the molecular brightness of the free particles in channel i , n_i their number, and n_{cc} the number of complexes.

Accordingly, the average channel brightness values are apparent brightness values containing contributions from free particles as well as complexes that add up following eq. 4.54:

$$\langle \epsilon_{\text{eff},i} \rangle = \frac{\epsilon_{f,i}^2 n_i + (\nu_i \epsilon_{f,i})^2 n_{cc}}{\epsilon_{f,i} n_i + \nu_i \epsilon_{f,i} n_{cc}}. \quad (4.63)$$

Correspondingly, the apparent particle numbers in each channel, $\langle n_i \rangle = \langle I_i \rangle / \langle \epsilon_{\text{eff},i} \rangle$, do not reflect the true particle numbers.

In equivalence to FCCS, the correct molecular parameters are only obtained for a 1 : 1 stoichiometry. With $\nu_i = 1$, eq. 4.63 simplifies to $\langle \epsilon_{\text{eff},i} \rangle = \epsilon_{f,i}$ and thus

$$\langle n_i \rangle = \frac{\langle I_i \rangle}{\epsilon_{f,i}} = n_i + n_{cc} = n_{\text{total},i}, \quad (4.64)$$

$$n_{cc} = \frac{\sigma_{cc}^2}{\epsilon_{f,g} \epsilon_{f,r}}. \quad (4.65)$$

Experimentally, the limitations mentioned in section 4.1.6 regarding cross-talk and imperfect overlap in FCCS equally apply to ccN&B. Cross-talk may be circumvented by using an ALEX scheme and switching the excitation for each acquired line of the image frames, or pixel-by-pixel PIE if the instrumentation is available (Hendrix

et al., 2013). Furthermore, the consideration above is only valid if all molecules are labeled with a single label and 100% labeling efficiency.

4.2.3 Detector noise characterization

The N&B method requires careful calibration of the detector noise characteristics. Since the contribution of number fluctuations to the total variance of the signal (eq. 4.50) is often only 10% or less, slight deviations of the detector variance from Poissonian statistics can strongly bias the output of N&B measurements. Nevertheless, calibration measurements performed on several microscope setups revealed such deviations. In particular, a larger than expected variance was observed on the mostly used setup (fig. 4.2). In order to calibrate the detector variance, multiple schemes are presented in chapter 2.2. In addition to these approaches, the detector variance can also be calculated from the ACF of FCS measurements. Assuming a detector variance $\sigma_d^2 = K\langle I \rangle$ ($K = 1$ for Poissonian noise), the factor K can be determined using the value of the ACF amplitude calculated at $\tau = 0$, $G(0) = \sigma^2/\langle I \rangle^2$, and the interpolated amplitude that is obtained from FCS analysis, $G_{\text{fit}}(0) = G(\tau \rightarrow 0) = 1/N$. The molecular brightness (eq. 4.51) is now given by $\epsilon_{\text{eff}} = \frac{\sigma^2}{\langle I \rangle} - K$. Thus,

$$K = \frac{\sigma^2}{\langle I \rangle} - \epsilon_{\text{eff}} \quad (4.66)$$

$$= G(0)\langle I \rangle - \frac{\langle I \rangle}{N} \quad (4.67)$$

$$= \langle I \rangle(G(0) - G_{\text{fit}}(0)) \quad (4.68)$$

$$= \langle I \rangle \Delta G. \quad (4.69)$$

Thus, the difference ΔG between the ACF amplitude computed for $\tau = 0$ and the amplitude G_{fit} interpolated by the FCS fit has to be calculated (see fig. 4.2). The latter is dominated by number fluctuations since the detector noise is not correlated on the evaluated time scales.

This procedure gives similar values as the other presented schemes, but has the advantage that it can be easily performed as part of the daily focal volume calibration routine (e.g. FCS on Alexa Fluor 488 (AF488)), with no need for an additional sample or experiment.

It should be noted that a larger than expected variance would also be observed for a detector that does not truly operate in photon counting mode, i.e. for which eqs. 4.55, 4.56 apply. A conversion factor K between detected photons and recorded digital counts (see section 4.2.1 and chapter 2.2) leads to the same higher variance.

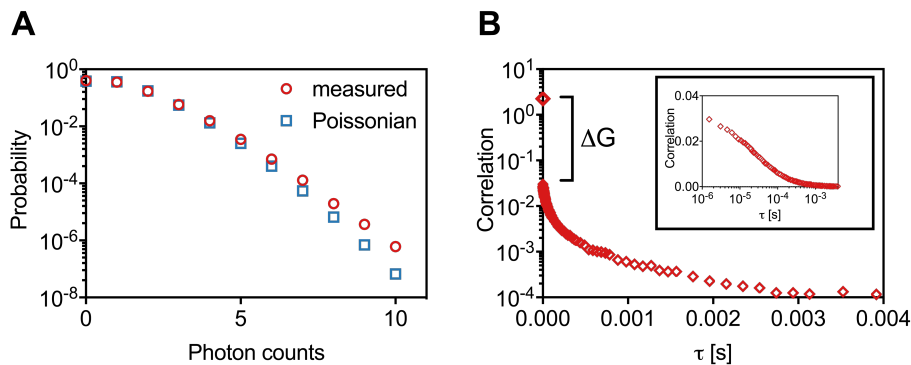


Figure 4.2: Detector noise calibration. **A:** Probability distribution of detector counts measured using constant illumination on a reflective surface on top of the objective. For comparison, the Poissonian probability distribution calculated for the average count rate is plotted, showing a clear deviation in the tail region. **B:** ACF of pFCS measurement on AF488 in water, plotted on a linear time scale. The difference ΔG between the ACF value at $\tau = 0$ (first, upper point) and the interpolated amplitude can be used to calculate the detector noise applying eq. 4.69. For this measurement, $K = 1.08$ is obtained. The inset shows the ACF plotted in conventional form on a logarithmic time scale (i.e without the data point at $\tau = 0$).

4.3 Simulation of sFCS and N&B for 2D diffusion

To test the sFCS and N&B analysis implementations, both methods were validated on Monte Carlo simulations of Brownian diffusion in a 2D plane, using a frame/line scanning acquisition and a Gaussian MDF model. The diffusion simulations were carried out in a $3.6 \mu\text{m} \times 3.6 \mu\text{m}$ (N&B) or $10 \mu\text{m} \times 10 \mu\text{m}$ grid (sFCS) with periodic boundary conditions. Initially, a total number of N particles was placed at random positions drawn from a uniform distribution. The acquisition process was simulated as subsequent frame scans of a central 32×32 pixel region of 50 nm pixel size (N&B) or 50 pixel line scans with 100 nm pixel size perpendicular through the center of the box (sFCS). Each pixel was 'illuminated' for a pixel dwell time $\tau_p = 32 \mu\text{s}$ (N&B) or $\tau_p = 10 \mu\text{s}$ (sFCS). Particles were assigned a molecular brightness ϵ , i.e. a photon count of $\epsilon \tau_p$ per molecule for a particle in the center of the MDF, and a diffusion coefficient D . The simulation was then iterated for a given number of frames (N&B, 20 to 400) or lines (sFCS, 100,000 to 400,000), respectively, with the pixel dwell time as the iteration time step, as follows:

- For a pixel located at $(x_j, y_j, z_j = 0)$ at time t of the scanning process, the photon count I_i contributed from particle i at position $(x_i, y_i, z_i) = (x_i(t), y_i(t), z_i(t))$

is determined by the relative position of the particle to the MDF, centered around $(x_j, y_j, z_j = 0)$ and modeled by a 2D/3D Gaussian function (N&B/sFCS) with structure parameter S . The MDF model takes the geometry of the acquisition relative to the particle plane into account (see fig. 4.3), i.e. diffusion and acquisition in xy -plane ($z_i = z_j = 0$) for N&B, diffusion in yz -plane ($x_i = 0$) and scanning in x -direction ($y_j = y_0, z_j = z_0$) for sFCS,

N&B:

$$I_i(x_j, y_j, 0, t) = \epsilon \tau_p \exp \left(-2 \frac{(x_i - x_j)^2 + (y_i - y_j)^2}{\omega_0^2} \right), \quad (4.70)$$

sFCS:

$$I_i(x_j, y_0, z_0, t) = \epsilon \tau_p \exp \left(-2 \frac{x_j^2 + (z_i - z_0)^2}{\omega_0^2} - 2 \frac{(y_i - y_0)^2}{S^2 \omega_0^2} \right). \quad (4.71)$$

Remark: Instead of further discretizing each pixel and integrating the MDF in scanning direction over the pixel, the intensity I_i is calculated at a fixed position (x_j, y_j, z_j) . This approximation works well for small pixel sizes, i.e sufficient sampling of the MDF.

- The total photon count I in a scanned pixel at (x_j, y_j, z_j) is given by the superposition of the contributions I_i of all particles, drawn from a Poissonian distribution that accounts for the detection shot noise:

$$I(x_j, y_j, z_j, t) = \text{POI} \left(\sum_{i=1}^N I_i(x_j, y_j, z_j) \right). \quad (4.72)$$

- For each particle i , the displacement to the new position $(x_i(t + \tau_p), y_i(t + \tau_p))$ (for N&B, $(y_i(t + \tau_p), z_i(t + \tau_p))$ accordingly for sFCS) is drawn from a standard normal distribution $\text{SND}(\mu, \sigma)$ with mean $\mu = 0$ and standard deviation (SD) $\sigma = \sqrt{2D\tau_p}$:

$$(x_i(t + \tau_p), y_i(t + \tau_p)) = (x_i(t), y_i(t)) + \left(\text{SND} \left(0, \sqrt{2D\tau_p} \right), \text{SND} \left(0, \sqrt{2D\tau_p} \right) \right). \quad (4.73)$$

In addition to single-color implementations, dual-color simulations of ccN&B and sFCCS were implemented containing two optionally binding particle species with total (bound and unbound) particle numbers N_g, N_r and diffusion coefficients D_g, D_r . A number N_{gr} of bound particles diffusing together with diffusion coefficient D_{gr} was set. Furthermore, 2fsFCS and 2fsFCCS were simulated with two parallel lines scanned one after the other in one or two channels with a separation d .

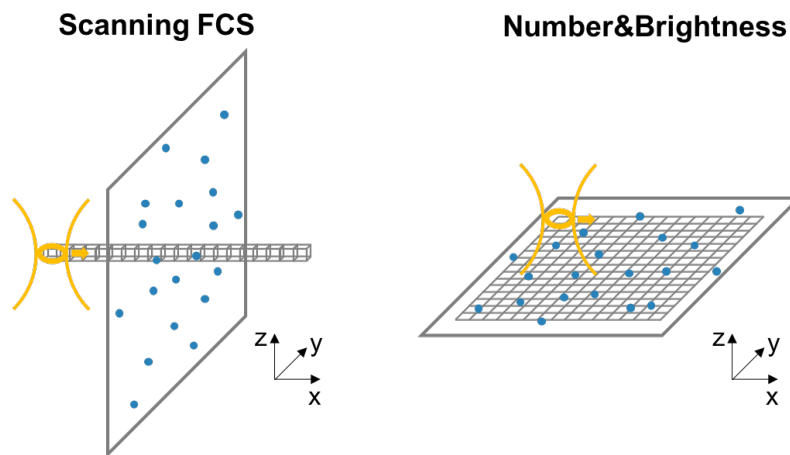


Figure 4.3: Sketch of the acquisition geometry in sFCS and N&B. **A:** In sFCS line scans in x -direction through the center of the yz -plane are acquired. Diffusion is simulated in a 2D plane (yz -plane), the focal volume is elongated in z . For N&B, diffusion and image acquisition are simulated in the xy -plane, the focal volume is elongated in z .

4.4 FFS analysis software

In order to analyze FFS measurements and simulated data, several software packages were implemented in MATLAB for the following methods:

- pFCS and dual-color FCCS
- sFCS, sFCCS, 2fsFCS, and 2fsFCCS perpendicular to the membrane
- spectral sFCCS (see section 4.11)
- N&B, ccN&B and spectral N&B
- FCA/TIFCA (see section 4.10, together with Salvatore Chiantia)
- iMSD for line- and frame acquisition (not part of this thesis)
- SPIM-FCS (not part of this thesis)
- pCF analysis for confocal line scan or light sheet imaging data (not part of this thesis)

Furthermore, a script that calculates statistical properties of SPT trajectories obtained from analysis with the Fiji plugin TrackMate was implemented.

4.5 sFCS simulations

The sFCS analysis code was first tested on simulated data. In all cases, sFCS analysis resulted in correct parameter estimates (figs. 4.4, 4.5). For sFCS (one-focus scanning in one color) (fig. 4.4A) the diffusion coefficient was calculated from the diffusion time determined by fitting the 2D diffusion model eq. 4.46 to the ACF. For 2fsFCS a

global fit to the two ACFs and the two-focus CCF was performed, directly resulting in parameter estimates for the diffusion coefficient, particle concentration, lateral focus waist and structure parameter (fig. 4.4B). The sFCCS diffusion coefficients were calculated from determined diffusion times (fig. 4.5). The relative cross-correlation was calculated from the determined particle numbers according to eqs. 4.40.

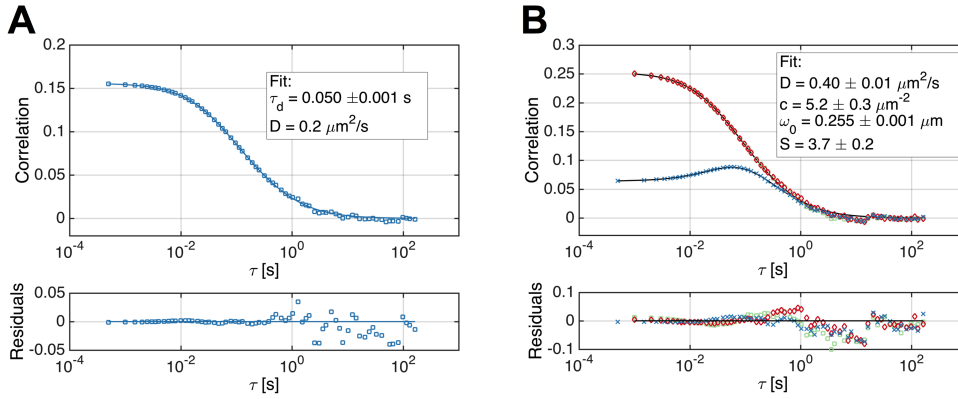


Figure 4.4: Simulation of sFCS and 2fsFCS. **A:** ACF, fit function (solid line), and fit residuals from analysis of an sFCS simulation. The ACF was averaged from four simulations of 400,000 lines each with $D = 0.2 \mu\text{m}^2/\text{s}$, $\omega_0 = 0.2 \mu\text{m}$, $S = 3.5$ and 1000 particles in the simulation box ($10 \mu\text{m} \times 10 \mu\text{m}$). **B:** ACFs and two-focus CCF, fit functions (solid lines) and residuals for 2fsFCS. The CFs were averaged from four simulations of $2 \times 200,000$ lines with $D = 0.4 \mu\text{m}^2/\text{s}$, $\omega_0 = 0.25 \mu\text{m}$, $S = 3.5$, 500 particles in the box, i.e. a concentration of 5 particles/ μm^2 , and line separation $d = 300$ nm. Parameter estimates were correctly obtained from globally fitting eqs. 4.46, 4.47 to the CFs.

To test 2fsFCCS, a simulation with different waists in the green and red channel ($\omega_{0,g} = 0.2 \mu\text{m}$, $\omega_{0,r} = 0.25 \mu\text{m}$) was analyzed, simulated with 80% of bound particles (fig. 4.5B). Due to the larger focal volume in the red channel, the amplitude of the ACF in the red channel was lower than the one in the green channel, i.e. more particles were detected in the red channel on average. A global fit to all 16 CFs resulted in correct estimates of the two waists and diffusion coefficients of all species. The relative cross-correlation differed between both channels. The average amplitude ratio of the red ACFs to the dual-color CCFs, $G_r(0)/G_{gr}(0) = 0.87$, was higher than the ratio calculated with the amplitudes of the green ACFs, $G_g(0)/G_{gr}(0) = 0.71$. This fits the expectation that for a fraction of red particles, a green partner was not detected due to the larger observation volume in the red channel. Thus, the fraction of red particles being in a complex (given by $G_g(0)/G_{gr}(0)$) was lower than the fraction of detected green particles being in a complex with red particles (given by $G_g(0)/G_{gr}(0)$). However, the average relative cross-correlation matched the expected value of 80%.

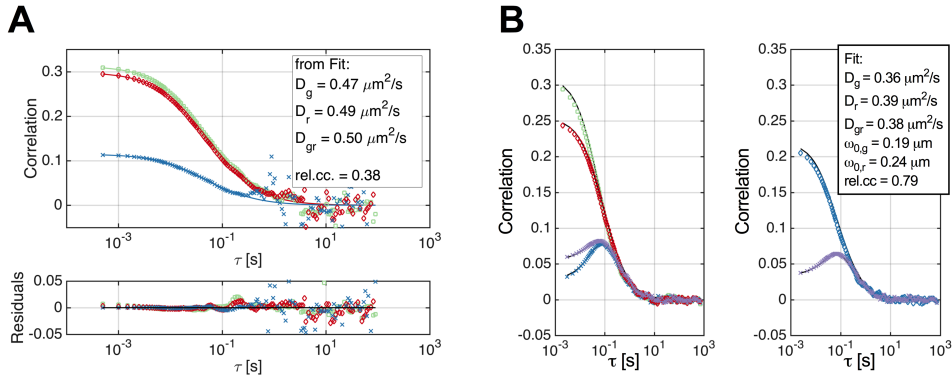


Figure 4.5: Simulation of sFCCS and 2fsFCCS. **A:** Single-channel ACFs (red/green), dual-color CCF (blue), fit functions (solid lines), and residuals for sFCCS. The CFs were obtained from a single simulations of 200,000 lines with $\omega_0 = 0.2 \mu\text{m}$, $S = 3.5$, $D_g = D_r = D_{gr} = 0.5 \mu\text{m}^2/\text{s}$, $N_g = N_r = 500$, and $N_{gr} = 200$ particles in the box. Fitting a 2D diffusion model (eq. 4.46) independently to the CFs resulted in correct estimates of the diffusion coefficients (calculated from diffusion times) and the relative cross-correlation (eq. 4.40). **B:** CFs of 2fsFCCS, averaged from four simulations. $2 \times 200,000$ lines were simulated with $D_g = D_r = D_{gr} = 0.4 \mu\text{m}^2/\text{s}$, $N_g = N_r = 500$ particles in the box of which 400 particles each were bound and $\omega_{0,g} = 0.2 \mu\text{m}$, $\omega_{0,r} = 0.25 \mu\text{m}$. The line separation was $d = 300 \text{ nm}$. Six of the 16 calculated CFs are plotted. Left: Channel ACFs (green/red) in focus one and two-focus CCFs in each channel (blue: channel one, purple: channel two). Right: Dual-color CCF in focus one (blue) and dual-color-two-focus CCF (purple). A global fit model (solid lines) of eqs. 4.46, 4.47, 4.48 was fitted to the CFs with free fit parameters D_g , D_r , D_{gr} , c_g , c_r , c_{gr} , $\omega_{0,g}$, $\omega_{0,r}$.

4.6 N&B simulations

A series of N&B simulations was performed to test the influence of molecular parameters on brightness estimates and their statistical accuracy. N&B analysis of simulated data resulted in correct determination of the molecular brightness (fig. 4.6A), calculated by averaging brightness values of all pixels. Of note, the average brightness values obtained from the analysis were around half of the brightness parameters set in the simulations. This corresponds to a γ -factor of 0.5, as expected for 2D diffusion in the xy -plane of the MDF (see section 4.1.2). Brightness parameters B_{sim} on the x -axis of figs. 4.6, 4.7 were corrected by this factor, i.e. show the MDF averaged brightness that is also obtained by the analysis. To assess the statistical accuracy of determined brightness values B , the SNR was calculated, $\text{SNR} = B/\text{SD}(B)$, where the SD was calculated from brightness values of all pixels. The SNR increased linearly with increasing molecular brightness (fig. 4.6D). Varying the number of particles in the box with fixed brightness parameter resulted in constant brightness and SNR values (fig. 4.6B,E).

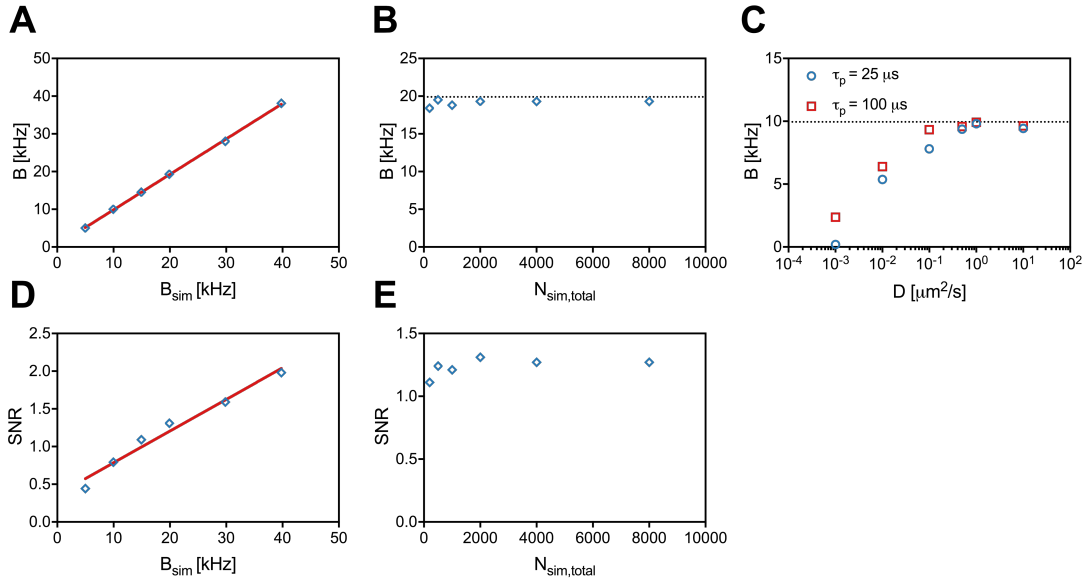


Figure 4.6: Simulation results for N&B with varying molecular parameters. **A,D:** N&B simulation with varying molecular brightness from around 5 – 40 kHz, $D = 1 \mu\text{m}^2/\text{s}$, and 200 particles in the simulation box. The determined brightness values (A, blue points) were close to the expected values (B_{sim}), as shown by the linear fit (red line), giving a slope of 0.94 ± 0.03 (95% confidence intervals (CIs)). The SNR of brightness values (D) shows a linear scaling (linear regression in red) with the molecular brightness. **B,E:** Brightness values (B) and SNR (E) obtained for N&B simulations with particle number $N_{\text{sim,total}}$ in the box varying from 200 to 8000, $D = 1 \mu\text{m}^2/\text{s}$, and a brightness of 20 kHz (dashed line). **C:** Determined brightness values for N&B simulations with varying diffusion coefficients in the range of $10^{-3} - 10 \mu\text{m}^2/\text{s}$, pixel dwell times of 25 μs and 100 μs , 200 particles in the box, and brightness of 10 kHz.

An important parameter when setting up the N&B acquisition experimentally is the diffusion coefficient of the particles. Fig. 4.6C shows the determined brightness values for particle dynamics simulated with diffusion coefficients in the range of 10^{-3} - $10 \mu\text{m}^2/\text{s}$. For slow diffusion dynamics, brightness values were strongly underestimated since the total acquisition time was too short to sample sufficient number fluctuations due to diffusive motion (see also section 4.9.4). For example, for particles diffusing with $D = 0.01 \mu\text{m}^2/\text{s}$ (corresponding to $\tau_d = 1$ s) and acquisition with $\tau_p = 100 \mu\text{s}$ (~ 0.1 s frame time/ ~ 10 s acquisition time for 100 frames, i.e. only 10 times higher than the diffusion time) the brightness was 36% lower than expected. Increasing the acquisition time relative to the diffusion time reduced this bias (e.g. $< 1\%$ error for $D = 1 \mu\text{m}^2/\text{s}$, corresponding to $\tau_d = 10$ ms and thus 1000 times higher acquisition than diffusion time). For a fixed diffusion coefficient, higher acquisition times can be achieved via increasing the pixel dwell time, the number of frames, or by pausing in between frame scans for a few seconds, which was applied in the investigation of APLP1 (chapter 2.1).

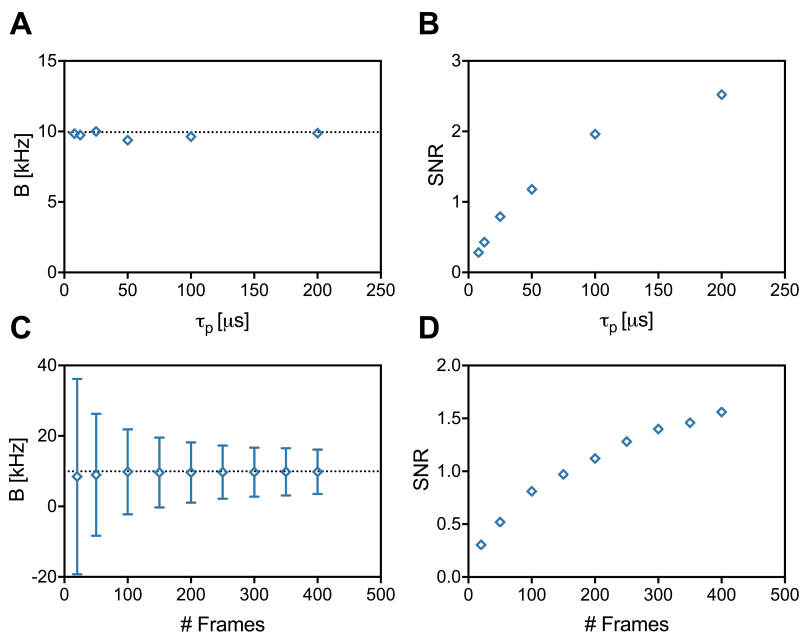


Figure 4.7: Simulation results for N&B with varying acquisition parameters. **A,B:** Brightness values and corresponding SNR values from N&B simulations with varying pixel dwell time τ_p , a brightness of 10 kHz (dashed line in A), 200 particles in the box, and $D = 1 \mu\text{m}^2/\text{s}$. **C,D:** Determined brightness (C) and SNR (D) from N&B simulation as described in (A), analyzed with varying frame number. Error bars show the SD of the pixel brightness distribution.

In order to further investigate the influence of the acquisition settings, additional simulations were performed. Varying the pixel dwell time yielded a constant molecular brightness (fig. 4.7A) for sufficiently fast diffusion dynamics (here $D = 1 \mu\text{m}^2/\text{s}$). Of note, this was obtained after dividing the raw brightness values (in photon counts per molecule and dwell time) by the respective pixel dwell time. The raw brightness values were proportional to the pixel dwell time, as expected from eq. 4.51 since a higher pixel dwell time generates more integrated photon counts from each molecule. For this reason, higher pixel dwell times led to higher SNR, with a square root dependence of the SNR on the dwell time (fig. 4.7B). Similarly, increasing the number of frames improved the accuracy of the brightness quantification. Low frame numbers (i.e. reduced total acquisition time, see also section 4.9.4) led to underestimation of the absolute brightness, e.g. around 10% lower brightness for 50 frames (fig. 4.7C). In addition, the SNR increased with a square root dependence on the frame number (fig. 4.7D), as observed for the pixel dwell time. Hence, the SNR is determined by the total measurement time: e.g. doubling the frame number with half the dwell time does not improve the SNR. Generally the pixel brightness distributions were fairly broad (see fig. 4.7C), showing that N&B is not capable of accurately measuring the brightness in a single pixel, but rather requires averaging over a sufficient number of pixels in a region of interest.

4.7 Experimental test of the sFCS implementation

Throughout this and the following sections, quantities in the text are given as mean \pm SD unless otherwise noted. The number of measurements, e.g. on different cells or GUVs, is given as n . Box plots indicate median values and whiskers ranging from minimum to maximum values.

4.7.1 sFCS on GUVs

In order to test the implementation of the sFCS analysis experimentally, sFCS and pFCS measurements were acquired on the same sample. More in detail, GUVs were produced with a lipid composition that exhibits sufficiently fast diffusion dynamics allowing a direct comparison of sFCS and pFCS parameter estimates on the same GUV. To this aim, pFCS measurements were performed on top of GUVs, followed by sFCS lateral scanning through GUV membranes (fig. 4.8). To test sFCS and 2fsFCS, both acquisition types were carried out at two different sides of the same GUV.

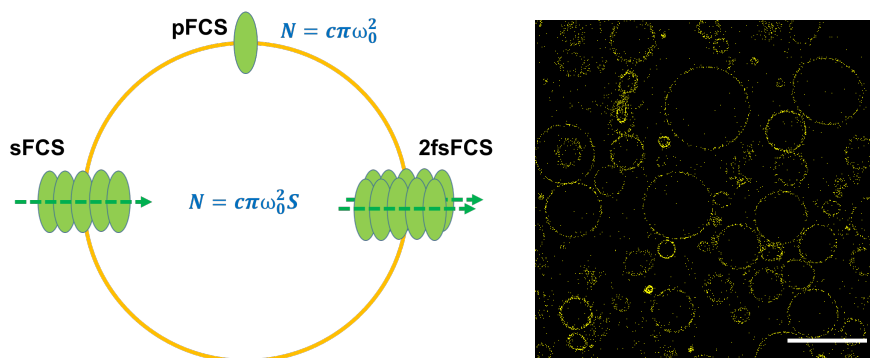


Figure 4.8: Sketch of FCS measurements on GUVs. Schematic of pFCS/sFCS acquisitions performed on GUVs (right-hand side). sFCS and 2fsFCS measurements were acquired laterally across GUV membranes, pFCS measurements on top of GUVs. The image on the right-hand side is a confocal image of GUVs, composed of 30% cholesterol and 70% 1,2-dioleoyl-sn-glycero-3-phosphocholine (DOPC), containing 0.002% Bodipy FL C₁₂-HPC. Scale bar is 50 μm .

Exemplary CFs of sFCS and 2fsFCS measurements are shown in fig. 4.9A,B. By fitting 2D diffusion models (eqs. 4.12, 4.46) to the CFs, the particle number N and diffusion time τ_d were obtained for pFCS and sFCS (fig. 4.9C,D). For 2fsFCS, N and τ_d were calculated from the concentration, diffusion coefficient, and waist obtained from a global fit (eqs. 4.46, 4.47). Due to the different sample orientation relative to the focal volume, the ratio of particle numbers in sFCS (diffusion in yz -plane) relative to pFCS (diffusion in xy -plane) is expected to be equal to the structure factor S for a homogenous dye concentration in the GUV membrane (fig. 4.8A). Indeed, the obtained average ratios of 5.4 ± 1.3 (sFCS, $n = 7$) and 6.3 ± 2.1 (2fsFCS)

were close to the experimental value of $S = 5.0$, calibrated by pFCS measurements on AF488 in water. In contrast, diffusion times from pFCS and sFCS are expected to be comparable. However, obtained sFCS diffusion times, 1.0 ± 0.3 ms, were ca. 30% lower than in pFCS, 1.4 ± 0.1 ms. The difference was most likely caused by the fast diffusion dynamics, i.e. diffusion times that were only 4-5-fold the time resolution of sFCS (sFCS: ca. $236 \mu\text{s}$, 2fsFCS: ca. $473 \mu\text{s}$), precluding an accurate fit of eq. 4.46 to the CFs. For 2fsFCS the situation was improved by the spatial CCF which is governed by the diffusion from one focus to the other causing a peak at larger lag times compared to the decay time of the ACFs. However, 2fsFCS acquisition on the given microscope was restricted to 100,000 frames, limiting the SNR of the CFs and thus the statistical accuracy of the parameter estimates. For comparison to sFCS, an average diffusion time of $\tau_d = 1.4 \pm 0.5$ ms was calculated from the determined 2fsFCS diffusion coefficients and the average waist, $w_0 = 0.21 \pm 0.05 \mu\text{m}$. Overall, given the mentioned limitations, sFCS analysis led to results comparable to pFCS, showing the successful implementation of the sFCS methods.

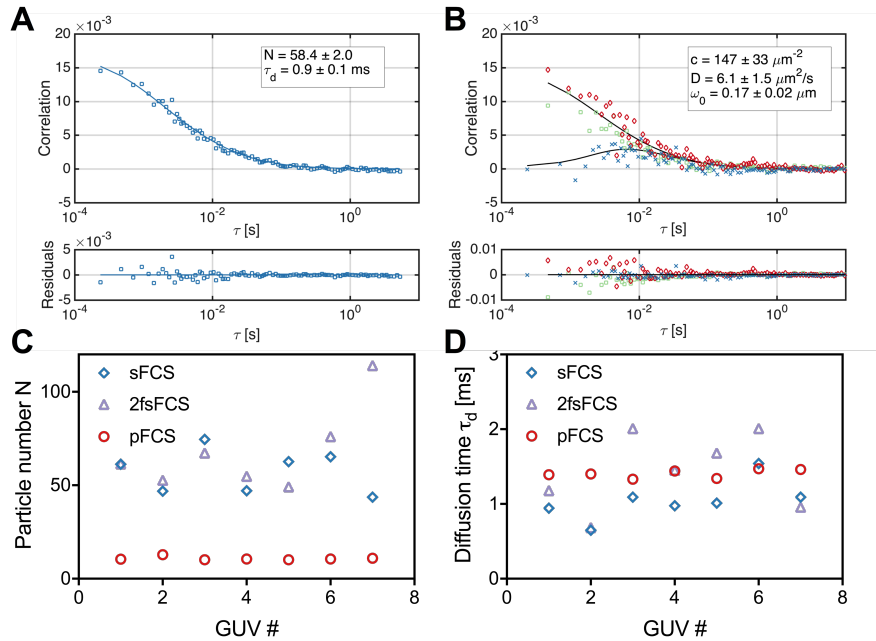


Figure 4.9: FCS measurements on GUVs. **A:** ACF obtained from sFCS measurement across GUVs, as shown in fig. 4.8. 500,000 lines were acquired with a scan time of $236.36 \mu\text{s}$ and 300 nm pixel size. Solid line shows fit of eq. 4.46 to the ACF, resulting in fit parameters given in the box with 95% CIs. **B:** CFs from 2fsFCS measurement of $2 \times 100,000$ lines with scan time of $472.73 \mu\text{s}$ and pixel size of 340 nm . Solid lines show fit curves obtained from a global fit (eqs. 4.46, 4.47) with fit parameters given in the box. The structure factor was fixed to $S = 5$, as obtained from pFCS calibration on AF488. **C, D:** Particle numbers (C) and diffusion times (D) from pFCS, sFCS and 2fsFCS on seven GUVs.

Furthermore, an experimental test of brightness analysis of sFCS data was performed. To this aim, GUVs containing either single- or double-labeled Bodipy FL lipids (Bodipy FL C₁₂-HPC/2xBodipy FL C₁₁-PC) were prepared and sFCS measurements acquired on both samples (fig. 4.10A,B). While similar diffusion times were obtained in both cases (fig. 4.10C), the obtained brightness was significantly higher on the double-labeled GUVs (fig. 4.10D). Nevertheless, the obtained ratio of 1.6 ± 0.2 was lower than the expected value of 2. This indicates suboptimal labeling of the lipids, i.e. not all lipids in the double-labeled sample may have carried two dye labels.

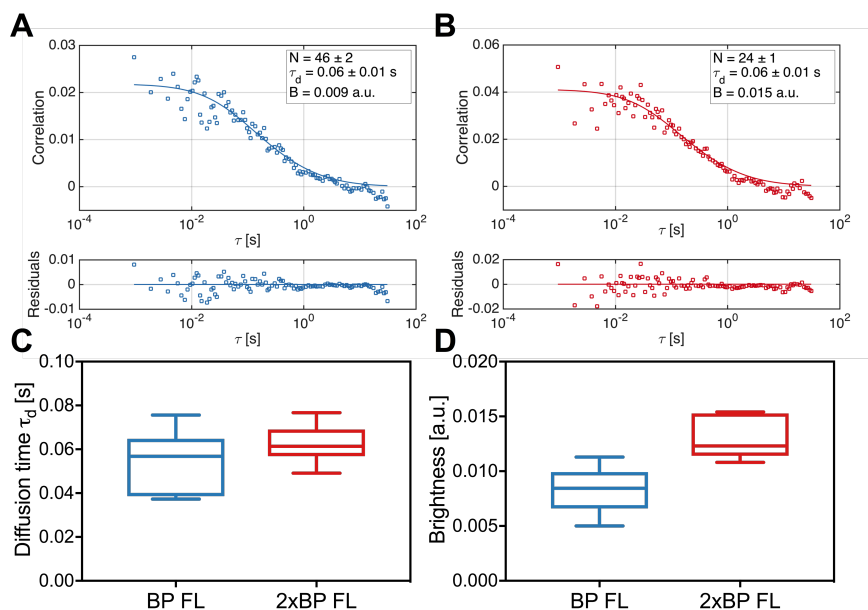


Figure 4.10: Brightness analysis of sFCS measurements on GUVs. A,B: ACFs obtained from sFCS across GUVs containing 32% cholesterol, 68% sphingomyelin and 0.002% Bodipy FL C₁₂-HPC (A) or 2xBodipy FL C₁₁-PC (B). 400,000 lines were acquired with a scan time of 945.54 μ s and 200 nm pixel size. Solid lines show fit curves obtained by fitting eq. 4.46 to the ACFs, resulting in fit parameters given in boxes with 95% CIs. C,D: Diffusion times (C) and brightness values (D) obtained from $n = 10/8$ measurements in each sample. The brightness was obtained by dividing the mean photon count rate by the determined particle number.

4.7.2 sFCS on the plasma membrane of living cells

To check its applicability to living cells sFCS was performed on the PM of HEK 293T cells expressing mp-mEYFP. sFCS and 2fsFCS measurements on the same cell resulted in similar estimates of diffusion coefficient and protein concentration (fig. 4.11). The minor differences (around 25%) were most likely caused by heterogeneities or residual photobleaching.

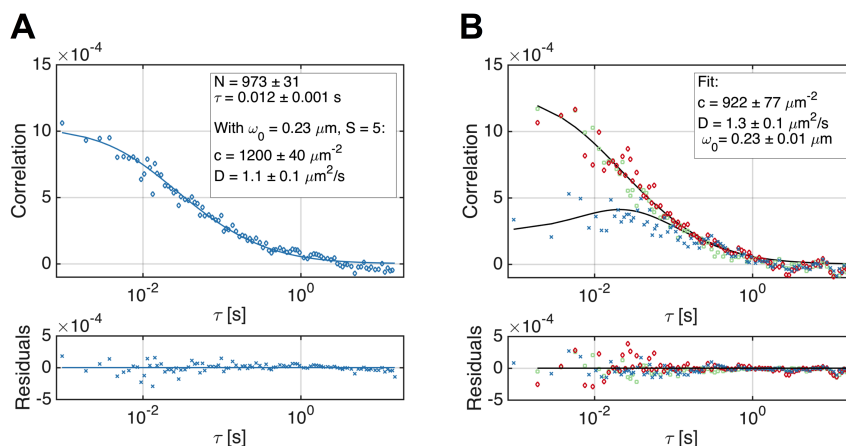


Figure 4.11: sFCS measurements in living cells. A: ACF of sFCS on mp-mEYFP in the PM of HEK 293T cells. 200,000 lines were acquired with a line time of 472.73 μs . Solid line shows fit of eq. 4.46. Fit parameters are given in the box with 95% CIs. Concentration and diffusion coefficient were calculated using ω_0 obtained from 2fsFCS. **B:** CFs of 2fsFCS on the same cell. 100,000 frames were acquired with 945.45 μs frame time. A global fit of eqs. 4.46, 4.47 to the CFs was performed, resulting in parameter estimates given in the box.

In addition, sFCCS was tested on living cells. Therefore, sFCCS was performed on cells co-expressing mp-mEYFP and mp-mCard (negative cross-correlation control) or mp-mCard-mEYFP hetero-dimers (positive cross-correlation control). To avoid spectral cross-talk, an ALEX acquisition scheme was used. From the amplitudes of the obtained CFs (fig. 4.12), the relative cross-correlation was calculated (eq. 4.41). On average, a negligible cross-correlation ($\text{rel.cc} = 0.05 \pm 0.04$, $n = 8$) was obtained in the negative control. In contrast, the positive control showed a high cross-correlation of 0.55 ± 0.11 ($n = 8$). In the latter sample, the same particle numbers would be expected if all hetero-dimers contained fluorescent mEYFP and mCard units. Nevertheless, the amplitude of the ACF in the mCard channel was on average around three times higher than the ACF amplitude in the mEYFP channel. This observation suggests a ca. three-fold lower fraction of fluorescent mCard compared to mEYFP, similar to a previous study investigating hetero-dimers of mEGFP and monomeric red fluorescent protein (mRFP)/-mCherry (Foo et al., 2012), and motivated the work in chapter 2.3. The therein characterized fluorescence probabilities of around 60% for mEYFP and 24% for mCard agree well with the sFCCS results. Nevertheless, the relative cross-correlation calculated using eq. 4.41 was still fairly high, since the majority of fluorescent mCard units were bound to a fluorescent mEYFP, and only few fluorescent mCard units had a non-fluorescent mEYFP partner.

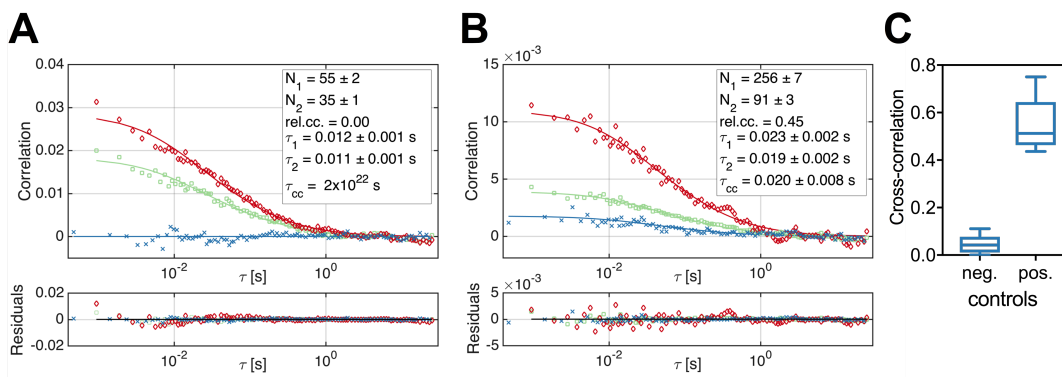


Figure 4.12: sFCCS measurements in living cells. **A:** CFs of sFCCS measurement in PM of HEK 293T cells, co-expressing mp-mEYFP and mp-mCard. 300,000 lines were acquired with alternated excitation of 488 nm and 561 nm lasers and 472.73 μ s line time. Eq. 4.46 was fitted to all CFs (green/red: ACF in mEYFP/mCard channel, blue: CCF). **B:** CFs of sFCCS on HEK 293T cells expressing mp-mCard-mEYFP hetero-dimers, acquired with the same settings. **C:** Box plots of relative cross-correlation values of sFCCS measurements ($n = 8$) on cells expressing mp-mEYFP and mp-mCard (neg.) and mp-mCard-mEYFP hetero-dimers (pos.), calculated according to eq. 4.41.

As shown in chapter 2.3, a larger fraction of fully fluorescent hetero-dimers improves the SNR of the FCCS CCF. Therefore, the identified superior red FP mCherry2 and mCherry were tested in sFCCS measurements on membrane-anchored hetero-dimers with mEGFP. Compared to mCard, both mCherry2 and mCherry showed amplitudes that are closer to the one in the mEGFP channel (fig. 4.13A,B). On average, $G_g(0)/G_r(0)$ ratios of 0.85 ± 0.12 and 0.66 ± 0.12 (median \pm SD, $n = 34/33$) were obtained for mp-mCherry2-mEGFP/mp-mCherry-mEGFP hetero-dimers (fig. 4.13C), in agreement with the detected fluorescence probabilities (mEGFP: $\sim 75\%$, mCherry2: $\sim 65\%$, mCherry: $\sim 45\%$). The relative cross-correlation, however, was similar for mCherry2 and mCherry containing hetero-dimers. While mCherry2 containing hetero-dimers showed a higher fraction ($G_{gr}(0)/G_r(0)$) of mEGFP in fully fluorescent dimers (since more mEGFP units had a fluorescent red partner), mCherry containing hetero-dimers had a higher fraction of red FP units with a fluorescent mEGFP partner (measured by $G_{gr}(0)/G_g(0)$). Due to the higher fluorescence probability of mCherry2, the latter fraction was reduced by the presence of more fluorescent mCherry2 units having no fluorescent mEGFP partner.

The larger diffusion times measured in the red channel (fig. 4.13A,B) suggest a larger red observation volume, which additionally affects the amplitude ratios. As discussed by Foo et al. (2012), this and further factors such as FRET can be taken into account for a more accurate quantification of biomolecular interactions using FCCS.

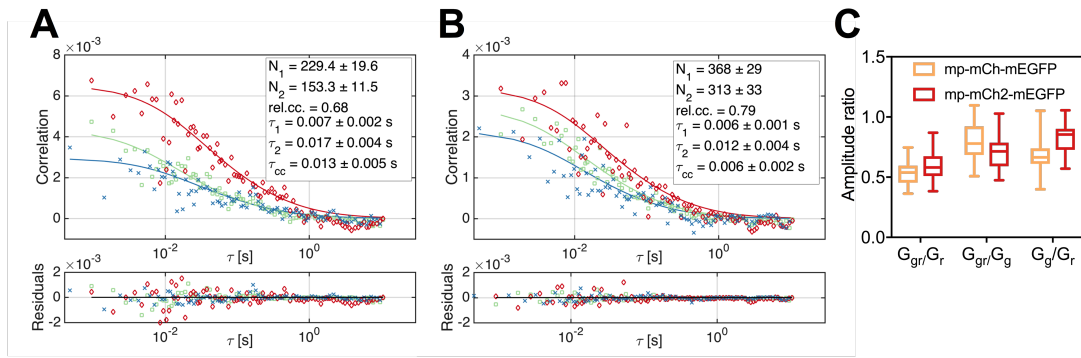


Figure 4.13: sFCCS measurements with mCherry and mCherry2. **A,B:** CFs of sFCCS measurements in PM of HEK 293T cells expressing mp-mCherry-mEGFP (A) or mp-mCherry2-mEGFP hetero-dimers (B). 250,000 lines were acquired with alternated excitation of 488 nm and 561 nm and 472.73 μ s line time. Eq. 4.46 was fitted to all CFs (green/red: ACF in mEGFP/mCherry(2) channel, blue: CCF). **C:** Box plots of amplitude ratios for measurements described in (A)/(B), obtained from 33 (mCherry)/34 (mCherry2) sFCCS measurements in three independent experiments.

It should be emphasized that sFCS is not only applicable to model membranes or culture cells, but can also be used to investigate membrane protein dynamics in living multicellular systems, e.g. living embryos. As an example, sFCS measurements were performed on the peripheral membrane protein Disks large homolog 1 (DLG-1)-1 in the hypodermis of *C.elegans* embryos, around 7 h after fertilization (see fig. 4.14). The measured diffusion time of 80 ms corresponds to a diffusion coefficient of around 0.2 μ m²/s, which is a reasonable value for a membrane protein in a cellular PM. More accurate values could be obtained with 2fsFCS, which was not possible on the given experimental setup.

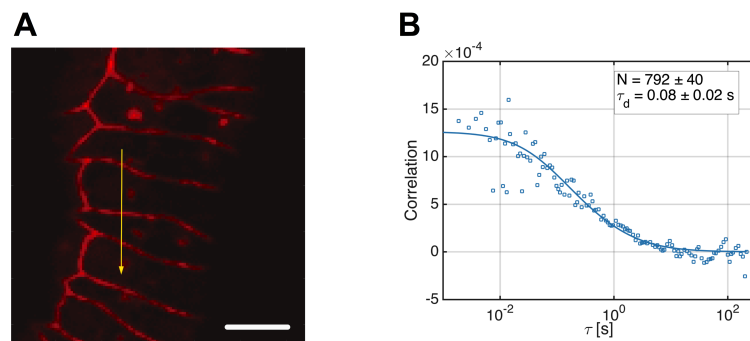


Figure 4.14: sFCS measurements in living *C.elegans* embryo. **A:** Image of DLG-1-mRFP in hypodermis of living *C.elegans* embryo, around 7 h after fertilization. Yellow arrow indicates sFCS line scan of 250,000 lines, acquired with \sim 1 ms line time. Scale bar is 5 μ m. **B:** Corresponding ACF of sFCS measurement. Solid line shows fit of a 2D diffusion model (eq. 4.46).

Generally, sFCS on the PM of living cells has several geometric limitations. In the derivation of the sFCS fit function, eq. 4.46, it is assumed that fluorophores diffuse

in a plane perpendicular to the scan path, i.e. the membrane is modeled as a flat, elongated sheet. This assumption can be challenged by three factors: i) nanoscopic membrane curvature leading to a larger effective area of the (curved) membrane in the focal volume and thus underestimation of diffusion dynamics, ii) microscopic curvature as encountered for very flat cells, iii) tilted membranes, i.e. membranes that appear to be flat but are not perpendicular to the scan path. Such geometric properties are strongly cell type dependent. HEK 293T cells seem to be well suited, showing $\sim 10 \mu\text{m}$ axial elongation of the (sometimes tilted) PM at cell-cell contacts and cell edges (fig. 4.15A,B). In contrast, Madin-Darby canine kidney II (MDCK II) or COS-7 cells are very flat at cell borders (axial elongation of $1 \lesssim \mu\text{m}$ and high curvature) and only appear suitable at cell-cell contacts where the axial height is a few μm (fig. 4.15C,D).

In addition to these constraints, membrane shape fluctuations may contribute to fluorescence intensity fluctuations, causing a displacement (e.g. by 10s of nm) of multiple fluorophores diffusing in the membrane on cell type specific time scales (e.g. $< \text{s}$ -scale) (Monzel et al., 2015).

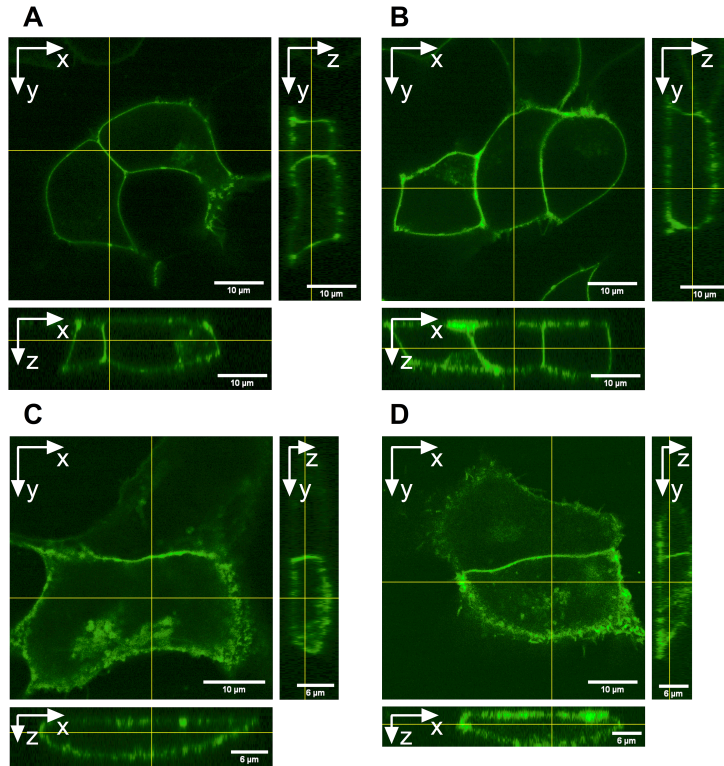


Figure 4.15: Axial elongation of adherent culture cells. A-D: Confocal images (xy) and orthogonal sections (right: yz ; bottom: xz) from z -stacks of HEK 293T (A,B), MDCK II (C) and COS-7 cells (D) expressing mp-mEGFP. Orthogonal cross-sections are plotted along the indicated lines. Image stacks were acquired with $\Delta z = 0.5 \mu\text{m}$ and $0.1 \mu\text{m}$ lateral pixel size. Scale bars are $10 \mu\text{m}$ (A,B) or $10 \mu\text{m}$ (xy) and $6 \mu\text{m}$ (yz/xz) for (C,D).

4.8 Supplementary data related to APLP1

The high fraction of non-fluorescent states for the red FP mCard that was detected in sFCCS measurements on mp-mCard-mEYFP heterodimers was also observed in ccN&B measurements on APLP1 at cell-cell contacts of HEK 293T cells. At these sites, normalized brightness values measured in the mEYFP and mCard channel are expected to be similar due to the symmetry of the system. Nevertheless, brightness distributions of APLP1-mEYFP (fig. 4.16A,C) showed much higher values than the distributions obtained for APLP1-mCard (fig. 4.16B,D) in the absence and presence of zinc ions. The values differed by a factor of ca. 3-4 (e.g. median values of 8.2 and 2.2 for APLP1-mEYFP/-mCard in zinc ion conditions), which is similar to the ca. 3-fold lower fraction of fluorescent states of mCard compared to mEYFP inferred from sFCCS. The even lower fluorescent fraction in the APLP1 experiments indicates that the location of the mCard tag (e.g. C- or N-terminally fused) may affect its folding efficiency.

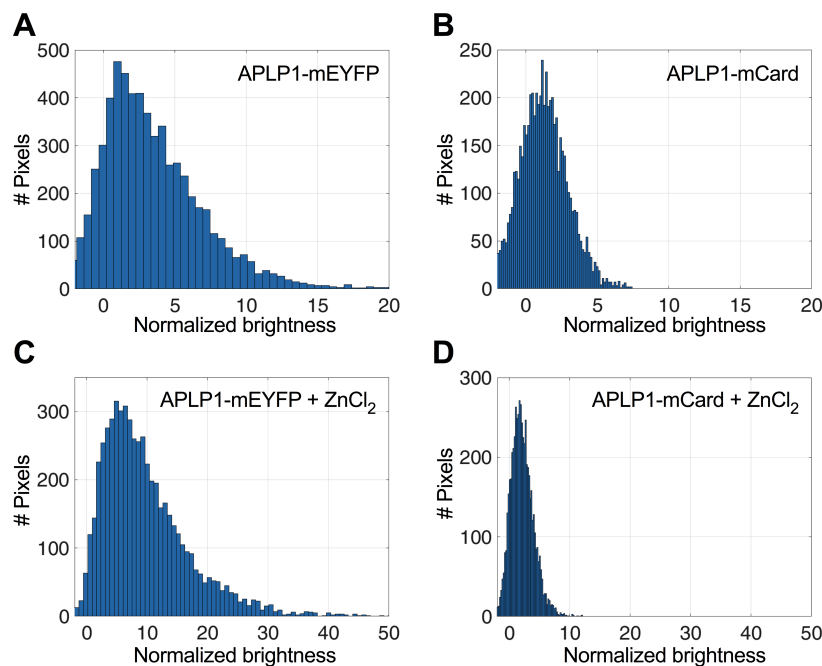


Figure 4.16: Brightness analysis of APLP1-mEYFP and APLP1-mCard clusters. **A,B:** Normalized brightness histograms of APLP1-mEYFP (A) and APLP1-mCard, obtained from ccN&B measurements on cell-cell contacts of HEK 293T cells (see chapter 2.1 for details) in the absence of zinc. Brightness values were normalized to the average brightness obtained from mp-mEYFP/mCard. **C,D:** Normalized brightness histograms obtained from ccN&B measurements on the same samples (C: APLP1-mEYFP, D: APLP1-mCard) after 30 min incubation with 50 μM ZnCl_2 . All data were pooled from 12 measurements in two independent experiments.

4.9 Artifacts in FFS measurements

The following sections discuss a range of artifacts that may occur in any kind of FFS measurement. Potential correction schemes are presented in the context of sFCS and N&B, but equally apply to other FFS techniques.

4.9.1 Photobleaching

A major perturbation in FFS measurements is photobleaching, the irreversible off switching of fluorophores. Photobleaching affects the accuracy of parameters measured by FFS in several ways. At high laser powers, in-focus bleaching can occur, turning off fluorophores before they diffuse out of the focal volume and thus reducing obtained diffusion times. This artifact is usually more pronounced for slowly diffusing molecules, which spend more time in the focal volume and are individually longer exposed to the highest laser power in the center of the focus. At low laser powers and fast dynamics, in-focus bleaching is usually negligible. A useful strategy to check for in-focus bleaching is to measure at different laser powers and compare the obtained diffusion times.

When measuring in confined compartments such as the PM, depletion of fluorophores occurs, causing a long-term decay of the fluorescence signal and severe distortions of the CF (fig. 5 in chapter 2.2, fig. 4.17B). At low laser powers, this effect can be corrected for since each fluorophore diffuses many times through the focal volume before it bleaches. Thus, the short-term fluctuations of the signal are still dominated by diffusion. As proposed by Ries et al. (2009b), the long-term decay of the fluorescence signal $F(t)$ can be fitted with a multi-exponential function,

$$f(t) = \sum_i a_i \exp(b_i t), \quad (4.74)$$

and corrected according to the following transformation:

$$F(t)^c = \frac{F(t)}{\sqrt{f(t)/f(0)}} + f(0)(1 - \sqrt{f(t)/f(0)}). \quad (4.75)$$

As shown by sFCS simulations (fig. 4.17), this procedure correctly recovers the ACF of an unperturbed signal. Most importantly for molecular brightness measurements, the correction also improves the estimate for the number of fluorophores and thus (at least partially) corrects for bleaching of oligomers and the associated decay in variance (fig. 4.17E).

An alternative framework to correct long-term instabilities such as photobleaching or slow oscillations of FCS data was presented by Baum et al. (2014), who proposed to

crop low frequency components of the FCS intensity trace in Fourier space. To this aim, the Fourier spectrum of an unperturbed measurement (e.g. of a dye in solution) is taken as a reference and the Fourier spectrum of a perturbed measurement cropped according to the Fourier envelope of the unperturbed spectrum (see figs. 4.20, 4.21 in section 4.9.3). In more detail, the envelope of the unperturbed spectrum was first calculated with a moving window i along the frequency axis from window mean μ and SD:

$$e_i = \mu_i + 3SD_i. \quad (4.76)$$

Then, an empirical model function given by

$$f_{\text{unperturbed}}(\nu) = a_1 \exp(-k_1 \nu) + a_2 \exp(-k_2 \nu) + a_3 \exp(-k_3 \nu) \quad (4.77)$$

was fitted to this envelope. Afterwards, an envelope function $f(\nu) = b f_{\text{unperturbed}}(\nu)$ proportional to this model function was fitted to the Fourier spectrum of the perturbed measurement. Finally, the amplitudes of this spectrum were cropped to the values of $f(\nu)$ and the spectrum transformed back to time domain for subsequent FCS analysis.

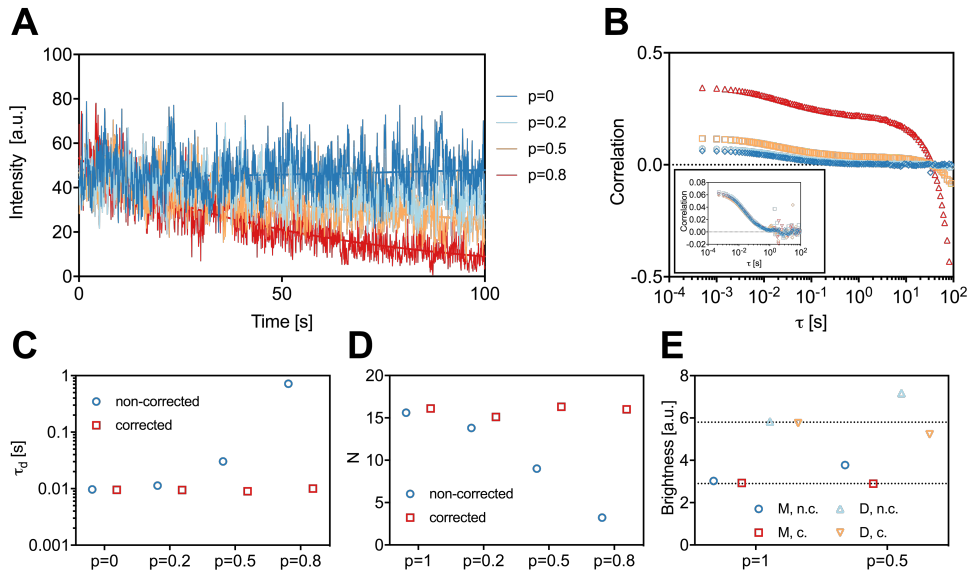


Figure 4.17: Depletion correction of simulated sFCS data. **A:** Intensity traces of sFCS simulations with variable bleaching strength (i.e. bleached fraction at the end of the acquisition) of 0% ($p = 0$) to 80% ($p = 0.8$). Solid lines show double-exponential fit (eq. 4.74 with $i = 2$). **B:** ACFs of sFCS traces shown in A. The inlet shows ACFs of time traces corrected with eq. 4.75. **C,D:** Diffusion time τ_d (C) and particle number N (D) obtained by fitting eq. 4.46 to bleaching corrected and non-corrected ACFs. **E:** Molecular brightness of simulated monomers (M) and dimers (D), obtained by sFCS analysis with (c.) and without (n.c.) bleaching correction for simulations with 50% ($p = 0.5$) or no bleaching ($p = 0$).

To analyze the suitability of the Fourier approach to correct for photobleaching, it was implemented and evaluated at multiple bleaching strengths. As a reference, the Fourier spectrum of a bleaching-free simulation was used. Although Fourier corrected ACFs were much less distorted than non-corrected curves (fig. 4.18), deviations from the non-bleached case were still observed. At 50% bleaching, the diffusion time was overestimated by around 20% (fig. 4.18B) and the number underestimated by around 30% (fig. 4.18C).

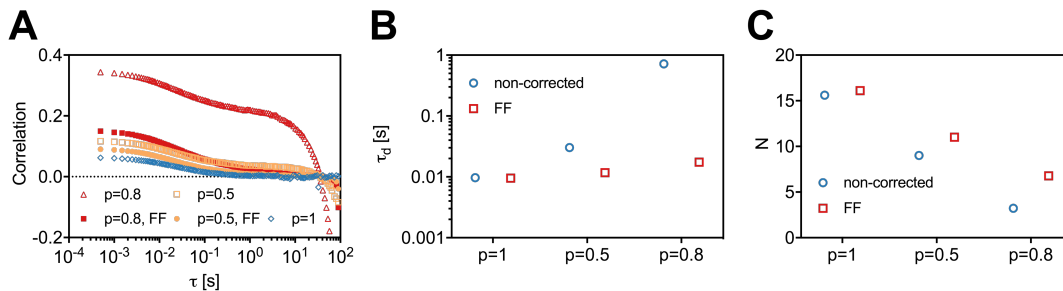


Figure 4.18: Fourier based depletion correction of simulated sFCS data. A: ACFs of Fourier corrected (FF) and non-corrected simulated sFCS measurements at variable bleaching strength of 0% ($p = 0$) to 80% ($p = 0.8$). **B,C:** Diffusion time τ_d and particle number N obtained by fitting eq. 4.46 to the ACFs shown in A.

For N&B, bleaching is more difficult to correct for. The boxcar filter described in chapter 2.2 reduces the additional variance of the signal due to a long-term decay. Thus, as shown by Hellriegel et al. (2011), it can be used to filter bleaching of immobile background. Nevertheless, it does not correct for the decay in variance when higher oligomers are bleached. In contrast to bleaching of monomers, in which the number of molecules that are still detectable decays but their brightness remains constant, the brightness for higher oligomers that are exposed to bleaching decays over time. This can severely bias oligomerization measurements (Hur et al., 2014). Unfortunately, the correction presented above for sFCS is not applicable to moment based methods such as N&B, since it falsely amplifies the detector part of the total variance.

In the presented investigations (chapters 2.1 to 2.3), potential bias by photobleaching was controlled by evaluating the brightness values of the sliding segments of the boxcar filter. If these values decay over time, interpolation of the brightness as a function of segment number can be used to obtain an estimate of the initial brightness before bleaching. However, this procedure only works for low or moderate bleaching strength since the apparent brightness of the first segments may be amplified by a residual decay of signal even within short segments.

4.9.2 Background

In cellular systems background fluorescence is often present and can significantly bias FFS measurements. If background fluorescence is emitted by mobile bright molecules that show fluctuations on a similar time scale as the species of interest, a two-component fit model may be used. On the other hand, if diffusion of background molecules is either much faster (e.g. fluorophores in the cytoplasm for a protein of interest at the membrane) or they are immobile, their fluorescence can be considered as an uncorrelated signal, since corresponding fluctuations average out for the slow sampling of the acquisition or are not present at all. This is typically encountered in sFCS measurements, in which the intracellular background fluorescence contributes an approximately constant offset to the measured fluorescence intensity and thus only to the denominator of eq. 4.42, thereby reducing the ACF amplitude. In this case, the average pixel background signal $\langle F_{bg} \rangle$ can be subtracted from the uncorrected membrane fluorescence $F_u(t)$ (see fig. 4.19):

$$F(t) = F_u(t) - m\langle F_{bg} \rangle/2. \quad (4.78)$$

Here, m is the number of pixels containing membrane signal. The factor $1/2$ takes into account that intracellular background is only present on one side of the PM. If photobleaching is present, the time-dependent background should be subtracted. Immobile background in the membrane is much more difficult to correct for, but is often quickly bleached at the beginning of the sFCS acquisition. For FFS in 3D, an immobile fraction (e.g. a fraction of a cytoplasmic protein of interest binding to a large, immobile structure) may bleach much slower, but can be inferred from the decay kinetics of the signal (Skinner et al., 2008).

As shown in fig. 4.19, intracellular background signal strongly biases the Gaussian fit that is applied in sFCS analysis to identify the pixels containing the membrane fluorescence. This can be compensated by including a sigmoid or step function in the fit model. In the example, an sFCS measurement on a GPMV, around 30% background was present inside the vesicle. This caused a more than 3-fold lower diffusion time, ca. 5-fold higher particle number and around 30% lower molecular brightness compared to the background corrected analysis (sigmoid fit and eq. 4.78). Of note, selection of a smaller region of interest (ROI) containing only few background pixels (ROI 2) only partially improved the analysis.

In many cases background originates rather from the presence of many dim molecules (e.g. autofluorescence), whose contribution to the correlation term can be neglected. This is typically encountered in the cell cytoplasm and may be taken into account by

measuring the average background signal from cells that do not express the protein of interest and subtracting this signal from the fluorescence measured on the protein of interest (in a spot for pFCS or in each pixel for N&B). Alternatively, spectral filtering (see section 4.11) can be used to directly subtract background signals. This is advantageous if background decays due to bleaching or varies from cell to cell. However, a constant background emission spectrum that still has to be measured in a non-expressing sample is required for this approach.

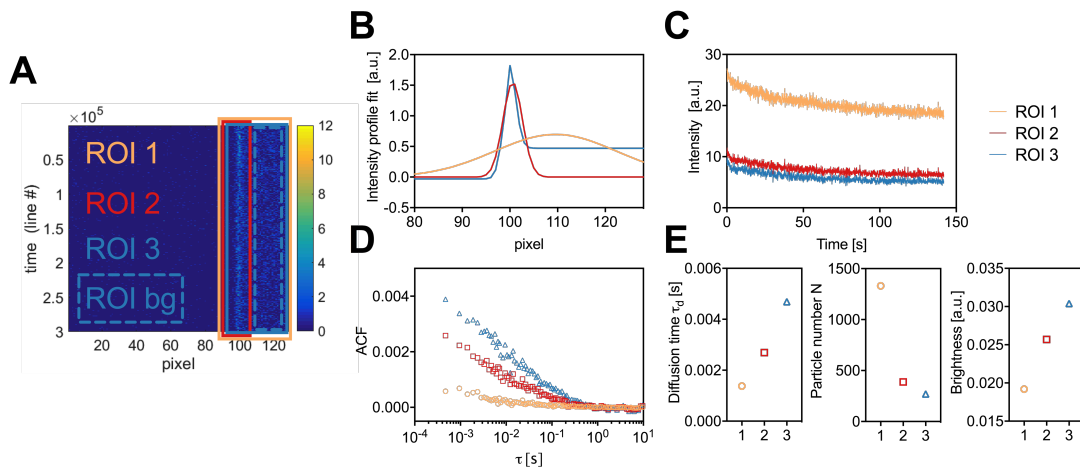


Figure 4.19: Background correction of sFCS measurements. **A:** Kymograph of sFCS on mp-2xmEGFP in a GPMV budding from a living HEK 293T cell. The GPMV membrane is located at pixel 100. Pixels inside the GPMV (right side) show significant background signal. Several ROIs were selected for sFCS analysis: ROI 1 (orange) includes the membrane and background, ROI 2 (red) contains the membrane and only few background pixels, ROI 3 (blue) is the same as ROI 1, but contains a subregion ROI bg (blue, dashed) of background pixels only. **B:** Fits of time-averaged lateral intensity profile for the different ROIs. For ROI 1 and 2, a Gaussian fit was performed, for ROI 3 a sum of a Gaussian and a sigmoid function was fitted to the intensity profile. **C:** Intensity time trace obtained by summation of the pixels within $\pm 2.5SD$ of the Gaussian fit for each ROI. For ROI 3, the background signal of ROI bg was subtracted according to eq. 4.78. **D:** ACFs calculated for the three intensity traces. **E:** Diffusion time (left), particle number (center) and molecular brightness (right), obtained by fitting a 2D diffusion model (eq. 4.46) to the ACFs.

4.9.3 Instabilities

FFS measurements in living cells often suffer from instabilities, caused by movement of the whole cell, sub-cellular structures (e.g. filopodia, intracellular vesicles), or membrane shape fluctuations (e.g. in GPMVs). In most cases, such instabilities appear as a peak or sudden change of the fluorescence intensity, increasing the amplitude of the ACF and/or brightness (e.g. a vesicle containing many fluorophores appears as a single, very bright particle). In more subtle cases, non-fluorescent structures (e.g. organelles not containing fluorophores) may (partially) enter the focal volume,

causing a drop in the fluorescence signal and, depending on its localization relative to the focal volume and dynamics, an increase or decrease of the ACF amplitude. The most common way to deal with such fluctuations is to analyze a measurement in short segments, as discussed in chapter 2.2 for both FCS and N&B (boxcar filter). This allows to i) effectively filter long-term fluctuations causing intensity changes on timescales longer than the segment time and ii) remove segments that show clear instabilities of the intensity and ACFs or brightness values that deviate from the ones obtained for the majority of segments. Nevertheless, segment-wise analysis raises two important issues. First, segments of short size suffer from statistical limitations that can strongly bias parameter estimates (see next section). Second, removing segments manually may be biased by the user. Therefore, more sophisticated filtering schemes have been developed based on automatic segment selection (Ries et al., 2010a) or Fourier filtering (Baum et al., 2014). Generally, segment-wise analysis works well as long as instabilities are sparse. In doubt, unstable measurements should be removed completely from further analysis.

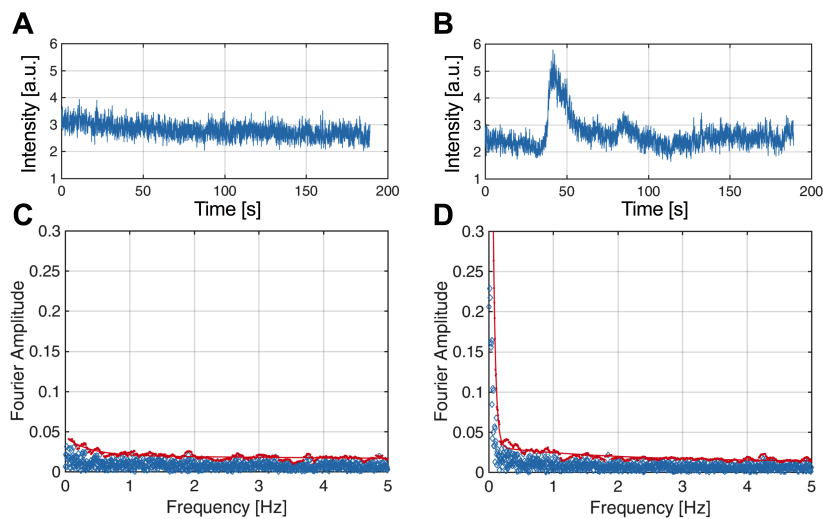


Figure 4.20: Fourier analysis of sFCS intensity traces. **A,B:** Fluorescence time series of two sFCS measurements on mp-mEGFP in HEK 293T cells. **C,D:** Fourier spectra (blue diamonds, shown for frequencies below 5 Hz), Fourier envelopes (red dots, from eq. 4.76) and envelope fit (solid red line, from eq. 4.77) of the fluorescence time series in A/B.

Fourier filtering (see section 4.9.1 for details) is based on the observation that unstable measurements are characterized by higher amplitudes of low frequency components (fig. 4.20). Cropping these amplitudes using Fourier spectra of stable measurements attenuates long-term intensity fluctuations. This procedure was tested on sFCS data acquired on HEK 293T cells expressing mp-mEGFP. Five measurements with visible instabilities were Fourier filtered before sFCS analysis using the Fourier envelope

of stable measurements lacking high Fourier amplitudes at low frequencies (fig. 4.20A). Then, diffusion times and molecular brightness values were compared to estimates without filtering and the values obtained on stable measurements. The filtering successfully removed major distortions of the ACFs (fig. 4.21B) and resulted in strongly reduced diffusion times and brightness values (fig. 4.21C,D). However, compared to parameter estimates from stable measurements, a 40% higher diffusion time (28 ms to 17 ms) and 20% higher brightness were obtained on average. This indicates that the Fourier filter does not fully remove the effect of instabilities and should thus be combined with segment-wise filtering.

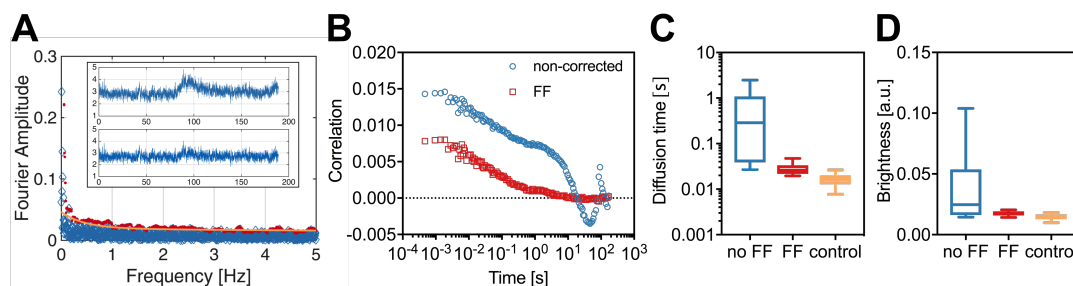


Figure 4.21: Fourier filtering of sFCS measurements. **A:** Fourier spectrum (blue diamonds, shown for frequencies below 5 Hz) of sFCS intensity trace measured on mp-mEGFP. The envelope function (orange solid line) calculated from four stable measurements (by averaging the Fourier envelopes and fitting eq. 4.77) was fitted to the Fourier envelope (red dots). Fourier amplitudes were cropped to the values of the fitted envelope function. The inset shows the intensity time trace before (top) and after Fourier filtering (bottom). **B:** ACFs obtained from sFCS analysis of Fourier filtered (FF) and non-corrected time series (inset in A) for the measurement described in A. **C,D:** Box plots of diffusion times (C) and molecular brightness values (D) from five unstable measurements analyzed with (FF) or without Fourier filtering (no FF) and five stable measurements (control).

A major difficulty of the Fourier approach is that a reference spectrum is always required. To this aim, Baum et al. (2014) used Fourier spectra measured on mEGFP in glycerol solutions with a glycerol concentration adjusted to match the diffusion coefficient of mEGFP in the cytosol of cells. For measurements on membrane proteins, showing much higher diffusion times (e.g. tens of ms rather than a few hundred μ s), this approach is not feasible. Furthermore, diffusion times of a protein of interest are not known *a priori* if no stable measurements are available. As a first approach, Fourier spectra of mp-mEGFP, which is routinely measured as a monomeric reference and usually does not suffer substantially from instabilities, may be used (4.20A). However, this protein is only anchored to one leaflet of the PM and thus diffuses faster than transmembrane proteins. In order to test whether the faster diffusion biases sFCS parameter estimates after Fourier filtering, we compared the diffusion

times of Influenza A virus hemagglutinin (HA) (tagged with mEGFP, see chapter 2.3) obtained with and without mp-mEGFP based Fourier filtering on a measurement lacking visible instabilities. Applying the filtering the diffusion time of HA was 27 ms, compared to 41 ms without filtering. Thus, the potential bias by the faster diffusion of mp-mEGFP ($\tau_d = 17$ ms) appears to be smaller than 30%, considering that the filtering may have also removed minor instabilities that were not visible by eye.

Besides the above-mentioned instabilities, movement of the whole cell may be an issue. Lateral movement in sFCS is effectively corrected. Nevertheless, lateral or vertical cell movement may result in changes of the angle between the membrane and the scan path, which is not taken into account in the sFCS fit model. This geometric constraint likely contributes to the variability of parameters estimated for diffusion or brightness when comparing multiple cells in the same sample. For (cc)N&B, cell movement is not inherently corrected. To overcome this limitation, an image alignment algorithm (described in chapter 2.1) that corrects for lateral shifts of the cell was applied before performing the (cc)N&B calculations. The alignment requires sufficient sampling of the MDF, i.e. pixel sizes below 100 nm, to avoid sudden changes of the intensity in a pixel. Without alignment correction, pixels in the periphery of a structure (e.g. a membrane section) may only contain fluorescence for part of the measurement time and thus give biased brightness values (Trullo et al., 2013).

4.9.4 Statistical Limitations

As described in the previous section, FFS data are often analyzed in segments in order to filter long-term instabilities. However, this procedure can severely bias parameter estimates because of statistical limitations. To obtain correct parameter estimates from an FCS measurement, the total measurement time (or segment length for segment-wise analysis) should be ca. a factor 1000 higher than the diffusion time of the particles. Shorter measurement times (or segment lengths) cause severe distortions of the CF that are recognizable as a characteristic negative dip at large lag times (fig. 4.22A). At a measurement time of $100\tau_d$, the diffusion time from an sFCS simulation was underestimated by ca. 30% (fig. 4.22B) and the number overestimated by around 15% (fig. 4.22C). Generally, the bias was stronger for the diffusion time. Correspondingly, the brightness was underestimated (fig. 4.22D). Nevertheless, relative brightness ratios were preserved (fig. 4.22E), as long as both oligomeric species had the same ratio of total measurement time (or segment length) and diffusion time. Interestingly, experimental data (fig. 4.23) showed a stronger dependence of τ_d on the segment length than simulations (fig. 4.22), probably because analysis with very long segments is additionally biased by long-term fluctuations in

the experimental system.

In the sFCS experiments presented in this thesis, the full sFCS time traces were typically divided in 10-20 segments. For a measurement time of 5 min, a minimum factor of $1000\tau_d$ would be obtained for diffusion times of up to 30 ms (for 10 segments).

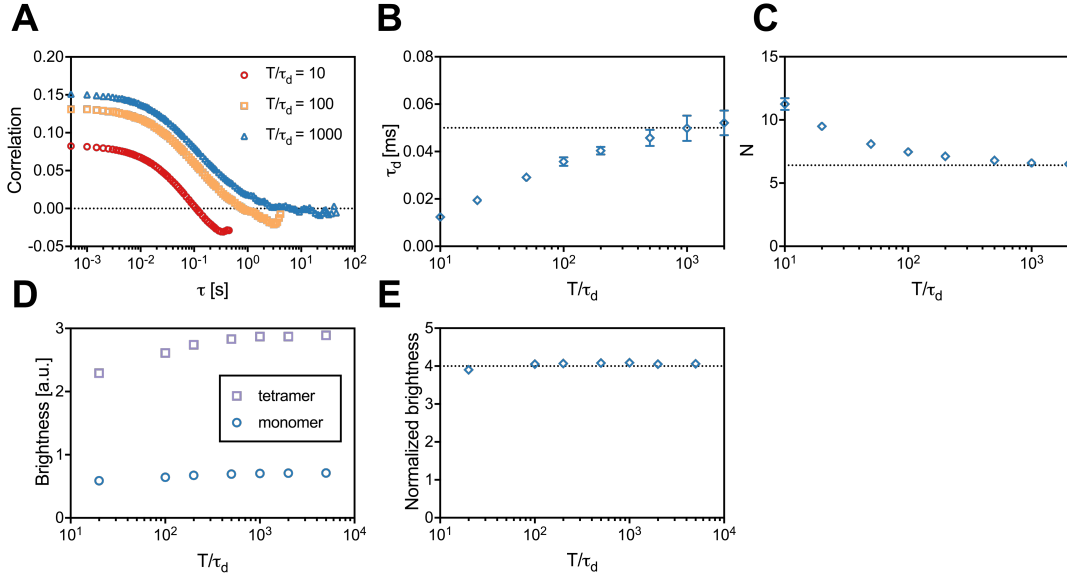


Figure 4.22: Segment-wise analysis of simulated sFCS data. **A:** Average ACFs of sFCS simulation of 400,000 lines with $\omega_0 = 0.2 \mu\text{m}$, $D = 0.2 \mu\text{m}^2/\text{s}$ (i.e. $\tau_d = 0.05 \text{ms}$), $S = 3.5$, and 1000 particles in the box, analyzed in segments of variable length T for $T = 10, 100$ or $1000\tau_d$. **B,C:** Diffusion time τ_d (B) and particle number N (C) obtained from segment-wise analysis ranging from $T = 10\tau_d$ to $T = 2000\tau_d$. Error bars show SDs for four simulations with the same set of parameter. **D,E:** Molecular brightness (D) and brightness ratios (E) from analyzing sFCS simulations as described in (A) run with brightness parameter ϵ (monomer) or 4ϵ (tetramer), in segments of variable length. Brightness ratios were calculated by dividing the determined molecular brightness values of monomer and tetramer for the same segment length.

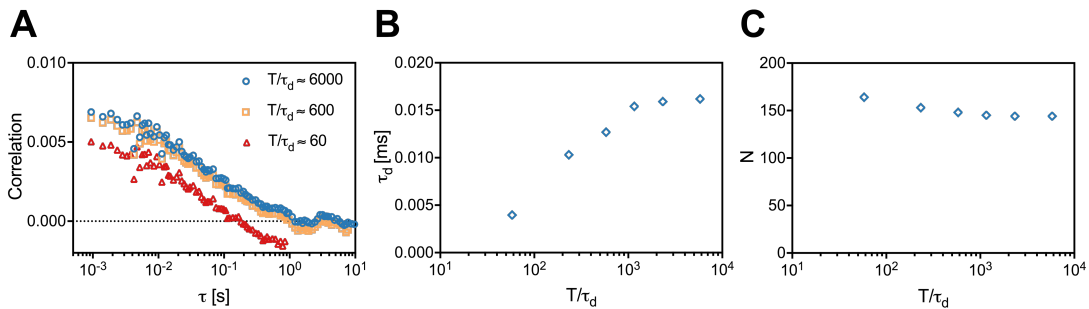


Figure 4.23: Segment-wise analysis of sFCS measurements. **A:** ACFs of sFCS measurement on HEK 293T cells expressing mp-2x-mEGFP, analyzed in 2, 20 or 200 segments, i.e. $T \approx 60, 600$ or $6000\tau_d$. The sFCS acquisition consisted of 400,000 lines, measured with a line time of $472.73 \mu\text{s}$. **B,C:** Diffusion time τ_d (B) and particle number N (C) obtained from sFCS analysis with different segment length T .

Finally, the effect of the boxcar filter (described in chapter 2.2) on the N&B quantification was investigated by simulating N&B measurements on oligomers, i.e. monomers to tetramers, with constant particle number and diffusion coefficient, but brightness proportional to the oligomer size. The simulations revealed that small boxcar sizes (e.g. 5 frames, corresponding to an acquisition time of 0.13 s, i.e. $13\tau_d$) caused up to 25% lower than expected brightness values (fig. 4.24A) due to the insufficient sampling of number fluctuations (i.e. diffusion events) in only a few frames. This statistical effect is equivalent to the bias in segment-wise sFCS analysis (fig. 4.22), where a lower brightness was also obtained for short segments. It has to be considered when determining absolute brightness values and particle concentrations experimentally via N&B: small boxcar sizes will underestimate the brightness and thus overestimate the particle number. In most applications relative brightness ratios are determined as a measure of oligomerization of a protein of interest. As shown in fig. 4.24B, relative brightness ratios were determined correctly even for small boxcar sizes, as long as the size (i.e. the ratio of boxcar time and diffusion time) was kept constant for all samples. Thus, the statistical bias does not effect the quantification of oligomeric states by brightness normalization, as already shown for sFCS (fig. 4.22E).

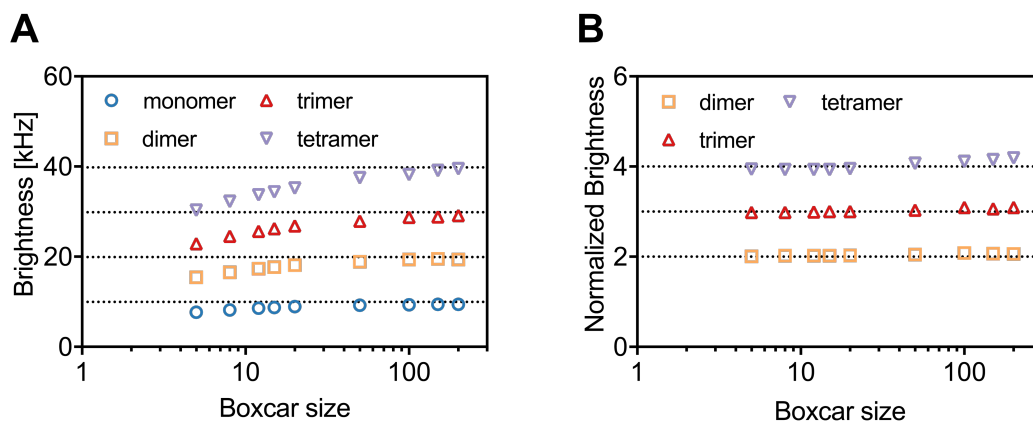


Figure 4.24: Boxcar filter analysis of simulated N&B data. **A:** Brightness from N&B simulations ($N = 200$ particles in the box, $D = 1 \mu\text{m}^2/\text{s}$, i.e. $\tau_d = 0.01$ s, $\tau_p = 32 \mu\text{s}$, i.e. 0.13 s frame time) of oligomers ranging from monomers (brightness 10 kHz) to tetramers (brightness around 40 kHz), analyzed with a boxcar filter of varying boxcar size. **B:** Relative brightness obtained from boxcar filter analysis, calculated by normalizing the brightness values obtained for the oligomers to the monomer brightness value determined with the same boxcar size. Dashed lines show expected (normalized) brightness values.

4.10 FCA and TIFCA

Brightness analysis of N&B data is based on temporal mean and variance of the fluorescence signal, i.e. the first and second moment of the photon count distribution. Thus, two independent parameters can be obtained: the mean number of particles and their average molecular brightness. For a mixture of different oligomeric species, the average brightness obtained by eq. 4.54 does not reflect the true molecular composition of the sample. In order to resolve multiple species, more sophisticated statistical methods have been developed. In the PCH approach (Chen et al., 1999) different models (e.g. monomers and dimers with unknown numbers) are fitted to the photon count distribution and evaluated based on how well they fit the histogram. This method requires a sufficient SNR, i.e. sufficiently long acquisition times, temporal stability, and low particle numbers. Furthermore, the resolvability of a mixture strongly depends on the brightness ratio of the species (Müller et al., 2000). Species with only small differences in brightness are particularly difficult to resolve. A drawback of PCH analysis is the lack of a statistical criterion predicting the number of species that can be resolved. Without any assumption, each species is characterized by two free parameters (particle number and molecular brightness). Resolving two unknown species would thus require to determine four independent parameters reliably.

Such a statistical criterion is provided by the related FCA technique, developed by Müller (2004). This method analyzes factorial cumulants of the photon count distribution. For a species of N fluorophores having a molecular brightness ϵ , the r -th factorial cumulant is given by

$$\kappa_{[r]} = \gamma_r \epsilon^r N, \quad (4.79)$$

where γ_r is the r -th γ -factor of the MDF (e.g. γ_2 in eq. 4.20),

$$\gamma_r = \frac{\int d^3\vec{r} (\text{MDF}(\vec{r}))^r}{\int d^3\vec{r} \text{MDF}(\vec{r})}. \quad (4.80)$$

FCA uses the fact that cumulants of the sum of statistically independent variables are given by the sum of the cumulants of the individual variables. Thus, for a mixture of s species, $\kappa_{[r]}$ is given by

$$\kappa_{[r]} = \gamma_r \sum_{i=1}^s \epsilon_i^r N_i. \quad (4.81)$$

The factorial cumulants of a photon count distribution k can be calculated from its moments (mean $\langle k \rangle$ and higher moments $\langle \Delta k^j \rangle$ for $j \geq 2$), e.g.:

$$\kappa_{[1]} = \langle k \rangle, \quad (4.82)$$

$$\kappa_{[2]} = \langle \Delta k^2 \rangle - \langle k \rangle, \quad (4.83)$$

$$\kappa_{[3]} = \langle \Delta k^3 \rangle - 3\langle \Delta k^2 \rangle + 2\langle k \rangle, \quad (4.84)$$

$$\kappa_{[4]} = \langle \Delta k^4 \rangle - 6\langle \Delta k^3 \rangle - 3\langle \Delta k^2 \rangle^2 + 11\langle \Delta k^2 \rangle - 6\langle k \rangle. \quad (4.85)$$

Notably, Müller (2004) derived a framework to estimate the statistical accuracy of the factorial cumulants. Their variance can be expressed as a function of regular cumulants κ_j . For example, the variance of the first two factorial cumulants, sampled with n data points, reads

$$\text{Var}[\kappa_{[1]}] = \frac{1}{n} \kappa_2, \quad (4.86)$$

$$\text{Var}[\kappa_{[2]}] = \frac{2}{n} (\kappa_2 + 2\kappa_2^2 - 2\kappa_3 + \kappa_4). \quad (4.87)$$

The expressions for the higher order cumulants can be found in Müller (2004). The regular cumulants κ_j are again a function of the moments, e.g.:

$$\kappa_1 = \langle k \rangle, \quad (4.88)$$

$$\kappa_2 = \langle \Delta k^2 \rangle, \quad (4.89)$$

$$\kappa_3 = \langle \Delta k^3 \rangle, \quad (4.90)$$

$$\kappa_4 = \langle \Delta k^4 \rangle - 3\langle \Delta k^2 \rangle^2. \quad (4.91)$$

Finally, the relative error of each factorial cumulant can be calculated:

$$\delta\kappa_{[r]} = \frac{\text{SD}[\kappa_{[r]}]}{\kappa_{[r]}} = \frac{\sqrt{\text{Var}[\kappa_{[r]}]}}{\kappa_{[r]}}. \quad (4.92)$$

The FCA framework allows to determine n independent parameters by fitting a suitable model (generally given by eq. 4.81) to the first n factorial cumulants of the photon count distribution. The number n of statistically reliable cumulants is given by the number of cumulants with a relative error smaller than 1. The quality of the fit is judged by the reduced χ^2 ,

$$\chi^2 = \frac{\sum_{r=1}^{r_0} \frac{(k_{[r]} - \kappa_{[r]})^2}{\text{Var}[\kappa_{[r]}}}{(r_0 - p)}, \quad (4.93)$$

where $k_{[r]}/\kappa_{[r]}$ are the experimental/theoretical cumulants, r_0 the number of cumulants used in the fit and p the number of free fit parameters in the model.

The implementation of the FCA approach was first tested on sFCS simulations. Therefore, two independent simulations of monomers and tetramers were analyzed individually and summed up to simulate a two species mixture of monomers and tetramers. FCA yielded four (monomers) or five (tetramers) statistically reliable factorial cumulants (fig. 4.25C,D). Single species models were fitted to the cumulants, giving a brightness ratio of around 4 and similar particle numbers (fig. 4.25A,B), as expected. To investigate whether the monomer-tetramer mixture can be resolved, several models of putative mixtures (e.g. monomer-dimer, monomer-trimer, monomer-tetramer or dimer-tetramer) were fitted to the cumulants and the reduced χ^2 values evaluated (fig. 4.26). Among all tested models, a monomer-tetramer mixture resulted in the best fit ($\chi^2=1.4$), with similar particle numbers for both species. Of note, models of more than two components collapsed to two species, i.e. the particle number of one species (e.g. dimers in a monomer-dimer-tetramer mixture) was effectively zero.

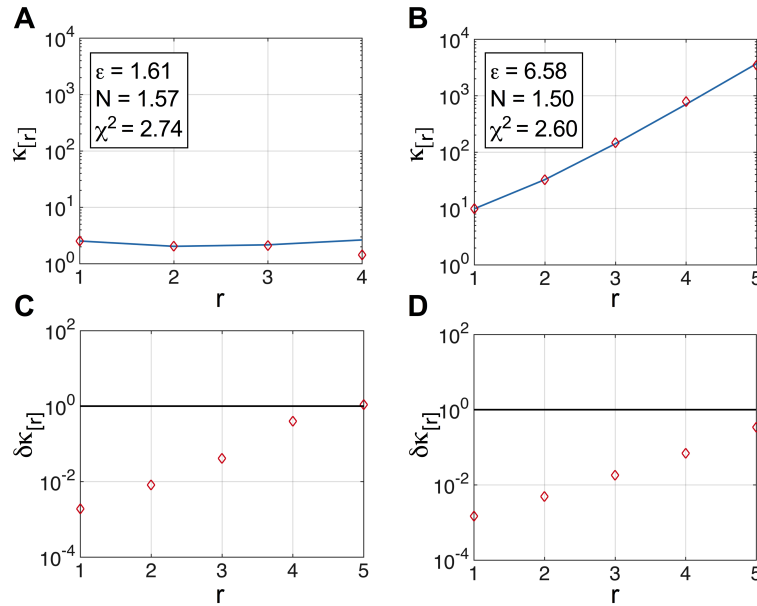


Figure 4.25: Cumulant analysis of simulated sFCS data. **A,B:** Cumulants $\kappa_{[r]}$ (red diamonds) of sFCS simulation of monomers (A) and tetramers (B) diffusing in a 2D plane. Solid blue lines show fit to a single species model resulting in estimates for the particle number N and molecular brightness ϵ , given in arbitrary units. The analysis recovers the expected brightness ratio, $\epsilon_4/\epsilon_1 = 4.09$ and particle number ($N_{\text{simulation}} = 1.57$). **C,D:** Relative errors of cumulants for the described sFCS simulations. The monomer simulation yields four, the tetramer simulation five cumulants with a relative error smaller than 1 (black line).

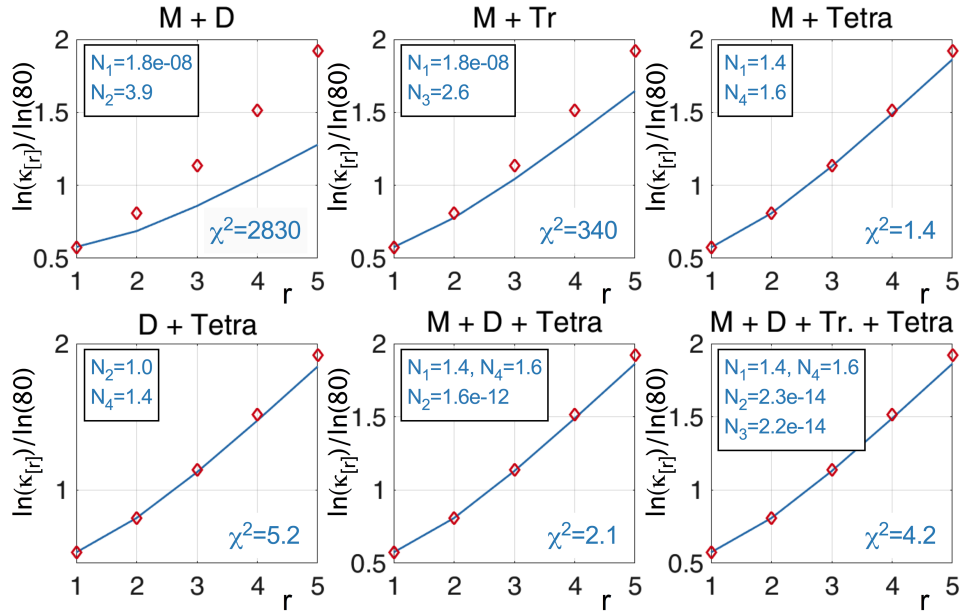


Figure 4.26: Cumulant analysis of simulated oligomer mixture. Cumulants $\kappa_{[r]}$ (red diamonds) of sFCS simulation of mixed monomers and tetramers, fitted with different models (solid blue lines). In the fitting routine, the monomer brightness was fixed to the value obtained for the pure monomer simulation. Fit parameters for the number of monomers (M)/dimers (D)/trimers (Tr) or tetramers (Tetra) are given in boxes. Reduced χ^2 values indicate that a monomer-tetramer model best fits the cumulant data.

In order to perform FCA of experimental data, two issues have to be addressed. First, the detector noise characteristics have to be calibrated. Second, the γ -factors of the experimental MDF need to be calibrated. These often deviate from the theoretical values of a 2D or 3D Gaussian model (Wu et al., 2013).

To calibrate the detector noise, the analysis described in section 4.2.3 has to be extended to characterize higher moments of the detector noise. To this aim, pFCS measurements on AF488 were performed at different laser powers and the offsets of the moments (normalized by the mean) were calculated from a linear interpolation. For truly Poissonian noise, the following moments are expected:

$$\langle \Delta k^3 \rangle_p = \langle \Delta k^2 \rangle_p = \langle k \rangle, \quad (4.94)$$

$$\langle \Delta k^4 \rangle_p = \langle k \rangle (1 + 3\langle k \rangle). \quad (4.95)$$

On different microscope setups, different offset values were calculated, all higher than expected for Poissonian noise (see fig. 4.27). For example, the third moment was 6% (laser scanning microscope (LSM) 880) or 20% (LSM 780) higher than the mean (fig. 4.27B). The same values were obtained by analyzing higher order CFs, in analogy to fig. 4.2B. To correct the FCA calculations, the determined incremental

moments of the detector noise were subtracted from the moments of the photon count distribution when calculating the (factorial) cumulants according to eqs. 4.83-4.85, 4.89-4.91.

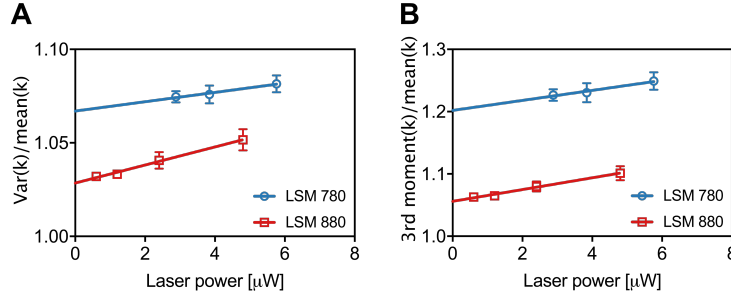


Figure 4.27: Detector calibration for cumulant analysis. A,B: Box plots of relative variance $\langle \Delta k^2 \rangle / \langle k \rangle$ (A) and third moment $\langle \Delta k^3 \rangle / \langle k \rangle$ (B) of photon count distributions obtained from pFCS measurements on AF488 with varying laser powers and on two different microscopes (Zeiss LSM 780/880). Six measurements were performed at each laser power. Solid lines show linear regressions.

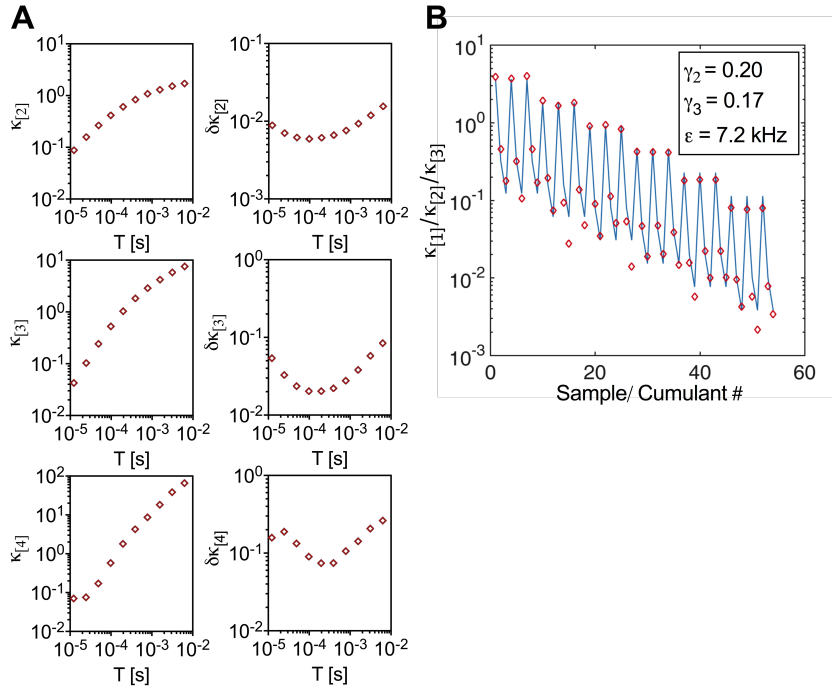


Figure 4.28: Cumulant analysis of pFCS measurements on AF488. A: Factorial cumulants (left column) and relative errors (right column) of 2nd to 4th order as a function of binning time T , obtained from a pFCS measurement on AF488 (FCS: $N = 0.8$, $\tau_d = 29 \mu\text{s}$), acquired for 2.5 min. **B:** First three factorial cumulants (red diamonds) obtained from pFCS measurements in AF488 dilution series. At each concentration three measurements were performed. A single species model (solid line, eq. 4.79) was globally fitted to the cumulants (binned to $T = 12.2 \mu\text{s}$), with γ_2 , γ_3 and molecular brightness as free fit parameters. For the particle number, a single fit parameter was used and the relative concentrations were fixed according to the dilution ratios. Obtained fit parameters are given in the box. For the particle number of the stock solution, $N = 41$ was obtained.

To determine the γ -factors, pFCS measurements on AF488 were performed at different laser powers or concentrations (e.g. in subsequent dilutions of 1:2) and cumulants (up to 3rd or 4th order depending on the relative error) were fitted globally with the γ -factors as free fit parameters (fig. 4.28). To improve the SNR, the time series acquired with a time resolution of $1.53 \mu\text{s}$ were binned by a factor of 4-8, i.e. keeping the binning time T still below the diffusion time of around 30-40 μs . Depending on the concentration of AF488, three (for $N \gg 1$) or four (for $N \approx 1$) factorial cumulants were obtained with a relative error smaller than 1, in line with previous studies (Müller, 2004). The results of a single dilution series fitted to third order (for $T = 12.2 \mu\text{s}$) are shown in fig. 4.28B. From multiple dilution experiments, $\gamma_2 = 0.22$ and $\gamma_3 = 0.18$ were determined on average. The γ_2 value differs from the theoretical value of a 3D Gaussian MDF ($\gamma_{2,3DG} \approx 0.35$, $\gamma_{3,3DG} \approx 0.19$). The resulting particle number (renormalized by respective dilution factors) and molecular brightness ($N = 41$, $\epsilon = 7.2 \text{ kHz}$) agreed well with the parameters obtained from pFCS ($N = 40$, $\epsilon = 7.3 \text{ kHz}$) in the undiluted solution.

Finally, the applicability of FCA to experimental sFCS data was explored. To this aim, factorial cumulants were calculated for sFCS measurements performed on mp-mEGFP or mp-2x-mEGFP in the PM of living HEK 293T cells, on two different microscopes (LSM 780/880). The two microscopes differed in the detector noise characteristics (see fig. 4.27) and detection efficiency (ca. two-fold higher molecular brightness of AF488 on LSM 880 compared to 780 at the same excitation power). To filter instabilities or long-term intensity fluctuations (e.g. due to photobleaching), FCA calculations were performed segment-wise. Segments were manually evaluated based on the ACFs and cumulants of all clean segments were averaged. Laser powers were chosen to keep photobleaching below 25%. For all measurements maximally three factorial cumulants with relative error < 1 were obtained (fig. 4.29B,D). On the LSM 780 time binning was required and three reliable cumulants were never observed for mp-mEGFP (data not shown), i.e. a monomeric FP at the PM, in contrast to the LSM 880 that showed lower relative errors. Overall, the relative errors were around one order of magnitude higher than the values for *in vitro* measurements on AF488 under ideal conditions, i.e. $N \approx 1$ (see fig. 4.28A, measured on LSM 780). This is likely due to the different geometry in sFCS, causing higher particle numbers, and the limited available molecular brightness, since photobleaching restricts the excitation power. Unfortunately, the superiorly performing LSM 880 instrument only recently became available. Therefore, a quantitative cumulant analysis of sFCS could not be realized yet. The high relative errors indicate that meaningful fitting to the third factorial cumulant of live cell data requires a model that includes time binning. For

point measurements, such an extension, TIFCA, was presented by Wu and Müller (2005). It benefits from the fact that the relative errors of factorial cumulants show a minimum for binning times larger than the diffusion time of the particles. In order to apply TIFCA to sFCS, higher order binning functions will have to be derived for the particular sFCS geometry. In addition, elimination of the detector noise correction by time-shifted analysis may improve the precision of the analysis (Hennen et al., 2019a,b) and reduce relative errors.

In principle, three cumulants will be sufficient to resolve a two species mixture at the PM if one parameter, e.g. the monomer brightness or the fluorescence probability, is fixed by additional measurements. Once the theoretical framework is formulated, further experiments containing controllable mixtures (e.g. single- and double-labeled lipids in GUVs) will be required to evaluate the ability to determine two mixed species experimentally, e.g. by fitting different models as shown for simulated sFCS data (fig. 4.26). The presence of oligomeric species showing a higher molecular brightness than monomeric FPs may further improve the SNR.

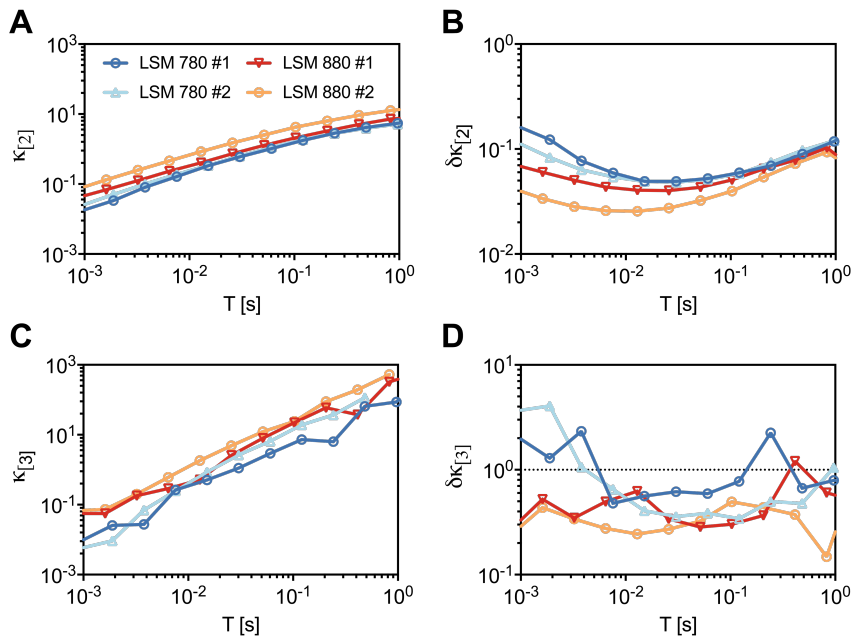


Figure 4.29: Cumulant analysis of sFCS measurements in living cells. **A,C:** Second (A) and third (C) factorial cumulants as a function of binning time T , obtained from two sFCS measurements each in living HEK 293T cells expressing mp-mEGFP (880 #1/2) or mp-2x-mEGFP (780 #1/2) at two different microscopes (Zeiss LSM 780/880). Measurements were acquired for ~ 4 min with $403.2 \mu\text{s}$ (880) or $472.73 \mu\text{s}$ (780) line time at the same laser power. Data points are connected by lines for better visibility. **B,D:** Relative error of second (B) and third (D) factorial cumulant for described sFCS measurements as a function of binning time T .

4.10.1 Distinguishing oligomeric species via protein concentration

In some cases, different oligomeric species of a protein can be resolved by evaluating the molecular brightness as a function of protein concentration (or number). The concentration can be calculated from the mean intensity of an FCS or N&B measurement and the calibrated monomer brightness, giving the number of monomers corresponding to the number of proteins present. Normalization by the focal volume allows to calculate the concentration in physical units. In fig. 4.30A the oligomeric state of eukaryotic fusion failure protein 1 (EFF-1), a transmembrane glycoprotein, is shown as a function of monomer number, measured via sFCS in GPMVs. The oligomeric state depended on the local protein concentration, with monomers at low numbers ($N \lesssim 50$) and trimers at high numbers ($N \gtrsim 500$). At intermediate concentrations brightness values were between 1 and 3, indicating the presence of multiple species, e.g. a monomer-trimer mixture. Although this mixture cannot be specified *per se*, the fraction of monomers and trimers can be calculated assuming a mixture of only monomers and trimers. This generally allows to determine the dissociation constant k_d of an equilibrium model.

The average brightness of a monomer- j -mer mixture is according to eq. 4.54:

$$\langle \epsilon \rangle = \frac{\epsilon_1^2[M] + \epsilon_j^2[J]}{\epsilon_1[M] + \epsilon_j[J]}. \quad (4.96)$$

The fraction of proteins (in units of monomers) that are bound in j -mers is

$$\theta = \frac{[M_j]}{[M_{\text{tot}}]} = \frac{j[J]}{[M] + j[J]}. \quad (4.97)$$

For simplicity, the empirical model

$$\theta([M_{\text{tot}}]) = \frac{1}{1 + \frac{k}{[M_{\text{tot}}]}}, \quad (4.98)$$

containing a single parameter k is used. At a concentration $[M_{\text{tot}}] = k$, half of all monomers that are present would be bound in trimers, the other half would be free monomers. Combining eqs. 4.96-4.98 leads to

$$\langle \epsilon \rangle = \frac{\epsilon_1^2 + \epsilon_j^2 \frac{[M_{\text{tot}}]}{jk}}{\epsilon_1 + \epsilon_j \frac{[M_{\text{tot}}]}{jk}}, \quad (4.99)$$

which can be directly fitted to experimental brightness data. For EFF-1 $k = 103 \mu\text{m}^{-2}$ was obtained after normalization by the effective area $A_{\text{eff}} = \pi\omega_0z_0 \approx 1.1 \mu\text{m}^2$ of the focal volume. Two EFF-1 mutants with a single point mutation in the trimer interface, hypothesized to have a lower oligomerization tendency, resulted in a ca. 10-fold higher k . Of note, the reference proteins mp-mEGFP, mp-2x-mEGFP did not show a concentration dependent brightness (fig. 4.30B), furthermore suggesting that the behavior observed for EFF-1 is protein specific. In order to confirm the monomer-trimer model for EFF-1, e.g. exclude the presence of dimers or higher order oligomers instead of trimers, TIFCA analysis of EFF-1 sFCS data may provide a useful tool.

A more accurate fit model than the empirical model (eq. 4.99) presented here could incorporate such information and can be derived from a third order association equilibrium model.

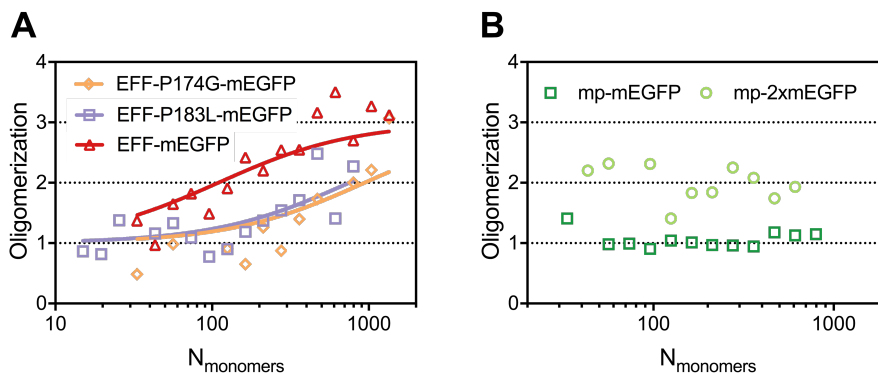


Figure 4.30: Concentration dependence of molecular brightness from sFCS measurements. **A:** Oligomerization of EFF-1-mEGFP (wild type protein) and mutants EFF-1-P174G-mEGFP, EFF-1-P183L-mEGFP as a function of protein number (in units of monomers), measured using sFCS in GPMVs of HEK 293T cells. The oligomerization was calculated from the normalized molecular brightness and the fluorescence probability, calibrated using a monomeric and dimeric reference (mp-mEGFP, mp-2x-mEGFP). Data points were binned in 20 logarithmically spaced bins on the horizontal axis. Solid lines show fits to an empirical monomer-trimer model (eq. 4.99 with $\epsilon_1 = 1$, $j = \epsilon_j = 3$), giving $k_{\text{wt}} = 110$, $k_{\text{P174G}} = 939$, $k_{\text{P183L}} = 749$. **B:** Oligomerization of reference proteins as a function of protein number.

4.11 Spectral sFCCS

Conventionally, the number of different fluorophores that can be detected by FCS is limited by the overlap of their emission and excitation spectra, causing cross-talk or cross-excitation. Furthermore, usage of a wide range of the optical spectrum and

multiple laser lines may induce optical artifacts, e.g. reduced cross-correlation of fluorophores excited in the blue and far red part of the optical spectrum due to chromatic shifts.

An approach which circumvents this limitation is fluorescence lifetime correlation spectroscopy (FLCS), presented by Böhmer et al. (2002). Using time-correlated single photon counting (TCSPC) detection and statistical filtering (Enderlein and Erdmann, 1997), spectrally strongly overlapping fluorophores are discriminated by their different lifetime patterns. This techniques was successfully realized with (mostly) organic dyes to distinguish multiple dye species or detect fast molecular transitions, e.g. on the ns timescale (Ghosh et al., 2018, Kapusta et al., 2012). To separate species their lifetime decays must be sufficiently different, which is often not the case for FPs. Therefore, Benda et al. (2014) recently presented spectral FCS, which combines the mathematical framework of FLCS and hyperspectral detection to discriminate overlapping fluorophores based on their spectral patterns. This method was demonstrated on *in vitro* mixtures of Atto 488 and Oregon Green 488 dyes, and recently implemented with RICS acquisition to perform cross-talk free measurements on FPs in the cytoplasm of living cells (Schrimpf et al., 2018).

The foundation of spectral FCS is the theoretical framework of FLCS (Böhmer et al., 2002):

The fluorescence signal in spectral channels j at time t is a linear combination of the normalized fluorescence spectra p_j^k of the n species:

$$I_j(t) = \sum_{k=1}^n w^k(t) p_j^k, \quad (4.100)$$

where $w^k(t)$ is the contribution of species k at time point t . Eq. 4.100 is a set of linear equations where $I_j(t)$ is measured and the spectra p_j^k calibrated *a priori*. If photon detection in each channel obeys Poissonian statistics, it can be shown (Enderlein and Erdmann, 1997) that the contributions $w^k(t)$ can be calculated by

$$w^k(t) = \sum_{j=1}^N f_j^k I_j(t), \quad (4.101)$$

with the filter functions (or photon weights) f_j^k given by

$$f_j^k = \left(\left[\hat{M}^T D \hat{M} \right]^{-1} \hat{M} D \right)_{jk}. \quad (4.102)$$

Here, the matrix elements are $M_{jk} = p_j^k$ and D is a diagonal matrix: $D = \text{diag}[\langle I_j(t) \rangle^{-1}]$, i.e. diagonal elements $1/\langle I_j(t) \rangle$.

The CFs of the k -th with the l -th species (ACFs: $k = l$, CCFs: $k \neq l$) are then given by

$$G^{kl}(\tau) = \frac{\langle w^k(t)w^l(t+\tau) \rangle}{\langle w^k(t) \rangle \langle w^l(t) \rangle} = \frac{\sum_{i=1}^N \sum_{j=1}^N f_i^k f_j^l \langle I_i(t) I_j(t+\tau) \rangle}{\sum_{i=1}^N \sum_{j=1}^N f_i^k f_j^l \langle I_i(t) \rangle \langle I_j(t) \rangle}. \quad (4.103)$$

In order to apply spectral FCS to membrane proteins in living cells, it is here combined with sFCCS. Therefore, standard sFCCS line acquisition was performed, but the fluorescence signal detected in multiple (up to 32) spectral channels simultaneously using the *Lambda mode* functionality of the Zeiss GaAsP detectors. Spectral patterns of different FPs were measured on cells expressing only one FP (fig. 4.31) using the same excitation and detection settings.

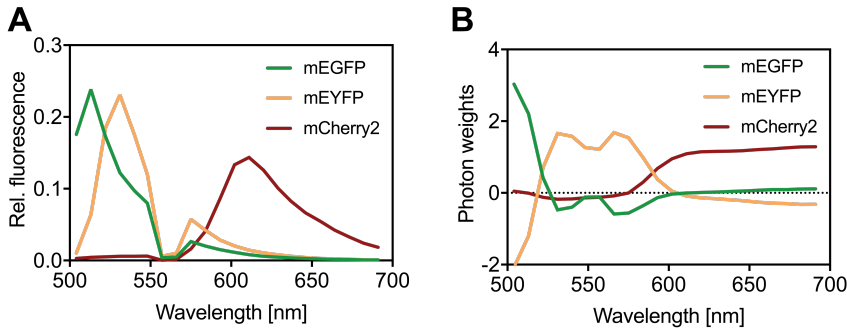


Figure 4.31: Fluorescence spectra and spectral filters in spectral three-species sFCS. **A:** Emission spectra of mEGFP, mEYFP, and mCherry2 measured on HEK 293T cells expressing one of the three FPs anchored to the PM, excited with 488 nm and 561 nm excitation. **B:** Corresponding filter functions calculated from one measurement on cells expressing all three FPs using eq. 4.102.

To demonstrate the feasibility of spectral sFCCS, measurements on cells expressing mEGFP, mEYFP, and mCherry2 independently at the PM and cells expressing mEYFP and mCherry2-mEGFP hetero-dimers, both anchored to the PM (see fig. 4.32), were performed. In the first sample, no cross-correlation is expected for all FP pairs. In the latter sample, a cross-correlation between mEGFP and mCherry2 should appear, while the other pairs should not show cross-correlation. On both samples spectral sFCCS measurements were acquired for ~ 4 min with 488 nm and 561 nm excitation. The fluorescence was detected from 499 to 696 nm in 22 spectral bins of ~ 9 nm width. From the amplitudes of the CFs (fig. 4.32C,D), the relative cross-correlation (eq. 4.41) was calculated (see fig. 4.32E). In the sample containing independently expressed FPs, low average cross-correlation values were obtained for all three FP pairs ($\text{rel.cc}_{G-Y} = 0.08 \pm 0.08$, $\text{rel.cc}_{G-C} = 0.05 \pm 0.08$,

$\text{rel.cc}_{Y-C} = 0.04 \pm 0.05$, $n = 6$). On the other hand, in the cells expressing mp-mCherry2-mEGFP hetero-dimers, a high cross-correlation of 0.51 ± 0.03 was obtained for mEGFP and mCherry2. In contrast, cross-correlation values calculated for the other two pairs were very low ($\text{rel.cc}_{G-Y} = 0.04 \pm 0.04$, $\text{rel.cc}_{Y-C} = 0.07 \pm 0.06$, $n = 6$). The very low cross-correlation measured in the absence of interactions demonstrates the successful decomposition of the fluorescence emitted by the three FPs despite strong spectral overlap (e.g. for mEGFP and mEYFP). The remaining cross-correlation of a few percent is most likely caused by residual membrane dynamics rather than insufficient spectral decomposition. This is indicated by the measured diffusion times. For example, an average diffusion time of ~ 140 ms was obtained from the CCF of mEGFP and mEYFP, i.e. around ten times the diffusion times in the single channels. On the contrary, the diffusion time of the CCF of mp-mCherry2-mEGFP hetero-dimers, $\tau_d = 17 \pm 5$ ms was similar to the diffusion times of the independently expressed FPs at the PM (around 15 ms).

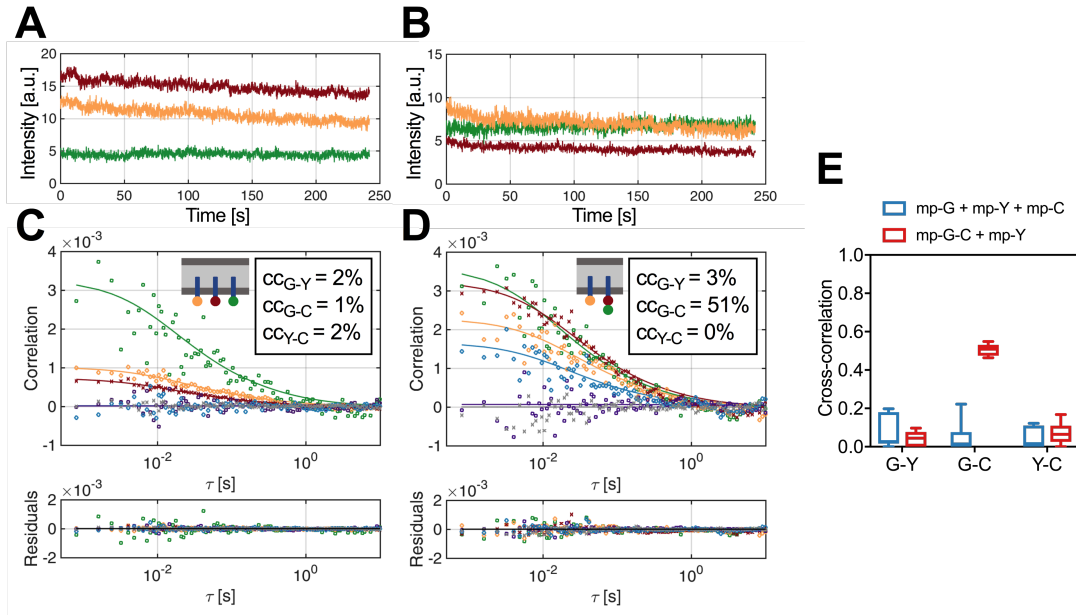


Figure 4.32: Spectral three-species sFCCS in living cells. **A,B:** Decomposed fluorescence signals of spectral sFCCS measurements (300,000 lines with $806.4 \mu\text{s}$ line time) on HEK 293T cells expressing mp-mEGFP, mp-mEYFP, and mp-mCherry2 (A) or mp-mCherry2-mEGFP and mp-mEYFP (B) at the PM. **C,D:** CFs (green/yellow/red: ACFs in mEGFP/mEYFP/mCherry2 channel, purple/blue/grey: CCFs of mEGFP-mEYFP/mEGFP-mCherry2/mEYFP-mCherry2) of spectral sFCCS measurements described in (A)/(B). Solid lines show fits of a 2D diffusion model (eq. 4.46) to the CFs. Bottom panels show fit residuals. The relative cross-correlation (cc) calculated using eq. 4.41 is given in boxes (G=mEGFP, Y=mEYFP, C=mCherry2). **E:** Box plots of relative cross-correlation obtained for six spectral sFCCS measurements in both samples.

As discussed in recent work presenting spectral RICS, the presence of spectrally overlapping fluorophores reduces the SNR of the CFs (Schrimpf et al., 2018). This issue is particularly crucial when the concentrations of two species differ substantially. In future work, the limitations of spectral sFCCS will be further explored, also in the context of multiplexing oligomerization measurements via molecular brightness analysis of decomposed species. In addition, the successful decomposition of three species may allow to detect higher order interactions, e.g. ternary protein interactions, in the PM of living cells via analysis of higher order CFs. So far, such approaches were limited to *in vitro* samples and organic dye labeling (Heinze et al., 2004, Ridgeway et al., 2012a,b). Moreover, four-color sFCCS should become possible by exploring fluorophores that possess suitable spectral properties and fill the gap between mEYFP and mCherry2. Finally, combination of multiple detection schemes (e.g. lifetime and spectral information) may truly enable multicolor FFS investigations.

List of Figures

1.1	Scheme of FCS.	3
1.2	Applications of FCS and FCCS.	4
1.3	Schematic of pFCS/sFCS and imaging FCS modalities.	5
1.4	Time dependence of the MSD for different types of transport in biological systems.	7
1.5	SPT experiments performed by Jean Perrin.	9
1.6	Shape of ACF in FCS for different types of transport in biological systems.	10
1.7	Proposed functions and interactions of APP family members at neuronal synapses.	12
1.8	Effect of non-fluorescent states on molecular brightness analysis.	13
1.9	Bacterial biofilm development and the biofilm EPS matrix.	14
4.1	Anomalous diffusion in the cell cytoplasm.	116
4.2	Detector noise calibration.	127
4.3	Sketch of the acquisition geometry in sFCS and N&B.	129
4.4	Simulation of sFCS and 2fsFCS.	130
4.5	Simulation of sFCCS and 2fsFCCS.	131
4.6	Simulation results for N&B with varying molecular parameters.	132
4.7	Simulation results for N&B with varying acquisition parameters.	133
4.8	Sketch of FCS measurements on GUVs.	134
4.9	FCS measurements on GUVs.	135
4.10	Brightness analysis of sFCS measurements on GUVs.	136
4.11	sFCS measurements in living cells.	137
4.12	sFCCS measurements in living cells.	138
4.13	sFCCS measurements with mCherry and mCherry2.	139
4.14	sFCS measurements in living <i>C.elegans</i> embryo.	139
4.15	Axial elongation of adherent culture cells.	140
4.16	Brightness analysis of APLP1-mEYFP and APLP1-mCard clusters.	141
4.17	Depletion correction of simulated sFCS data.	143
4.18	Fourier based depletion correction of simulated sFCS data.	144

LIST OF FIGURES

4.19	Background correction of sFCS measurements.	146
4.20	Fourier analysis of sFCS intensity traces.	147
4.21	Fourier filtering of sFCS measurements.	148
4.22	Segment-wise analysis of simulated sFCS data.	150
4.23	Segment-wise analysis of sFCS measurements.	150
4.24	Boxcar filter analysis of simulated N&B data.	151
4.25	Cumulant analysis of simulated sFCS data.	154
4.26	Cumulant analysis of simulated oligomer mixture.	155
4.27	Detector calibration for cumulant analysis.	156
4.28	Cumulant analysis of pFCS measurements on AF488.	156
4.29	Cumulant analysis of sFCS measurements in living cells.	158
4.30	Concentration dependency of molecular brightness from sFCS mea- surements.	160
4.31	Fluorescence spectra and filters in spectral three-species sFCCS.	162
4.32	Spectral three-species sFCCS in living cells.	163

Bibliography

- Arant, R. J. and Ulbrich, M. H. 2014. Deciphering the Subunit Composition of Multimeric Proteins by Counting Photobleaching Steps. *ChemPhysChem*, 15(4):600–605.
- August, A., Schmidt, N., Klingler, J., Baumkötter, F., Lechner, M., Klement, J., Eggert, S., Vargas, C., Wild, K., Keller, S., and Kins, S. 2019. Copper and zinc ions govern the trans-directed dimerization of APP family members in multiple ways. *Journal of Neurochemistry*, page jnc.14716.
- Bacia, K., Kim, S. A., and Schwille, P. 2006. Fluorescence cross-correlation spectroscopy in living cells. *Nature methods*, 3(2):83–89.
- Bacia, K., Petrášek, Z., and Schwille, P. 2012. Correcting for spectral cross-talk in dual-color fluorescence cross-correlation spectroscopy. *ChemPhysChem*, 13(5):1221–1231.
- Balleza, E., Kim, J. M., and Cluzel, P. 2017. Systematic characterization of maturation time of fluorescent proteins in living cells. *Nature Methods*, 15(1):47–51.
- Baum, M., Erdel, F., Wachsmuth, M., and Rippe, K. 2014. Retrieving the intracellular topology from multi-scale protein mobility mapping in living cells. *Nature Communications*, 5:4494.
- Benda, A., Kapusta, P., Hof, M., and Gaus, K. 2014. Fluorescence spectral correlation spectroscopy (FSCS) for probes with highly overlapping emission spectra. *Optics Express*, 22(3):2973.
- Billings, N., Birjiniuk, A., Samad, T. S., Doyle, P. S., and Ribbeck, K. 2015. Material properties of biofilms - A review of methods for understanding permeability and mechanics. *Reports on Progress in Physics*, 78(3):036601.
- Böhmer, M., Wahl, M., Rahn, H. J., Erdmann, R., and Enderlein, J. 2002. Time-resolved fluorescence correlation spectroscopy. *Chemical Physics Letters*, 353(5-6):439–445.
- Brinkmeier, M., Dörre, K., Stephan, J., and Eigen, M. 1999. Two-Beam Cross-Correlation: A Method To Characterize Transport Phenomena in Micrometer-Sized Structures. *Analytical Chemistry*, 71(3):609–616.
- Cartwright, A. N. R., Griggs, J., and Davis, D. M. 2014. The immune synapse clears and excludes molecules above a size threshold. *Nature Communications*, 5:5479.

- Chalfie, M., Tu, Y., Euskirchen, G., Ward, W. W., and Prasher, D. C. 1994. Green fluorescent protein as a marker for gene expression. *Science (New York, N.Y.)*, 263(5148):802–5.
- Chen, Y., Müller, J. D., So, P. T., and Gratton, E. 1999. The photon counting histogram in fluorescence fluctuation spectroscopy. *Biophysical journal*, 77(1):553–67.
- Cherstvy, A. G., Nagel, O., Beta, C., and Metzler, R. 2018. Non-Gaussianity, population heterogeneity, and transient superdiffusion in the spreading dynamics of amoeboid cells. *Physical Chemistry Chemical Physics*, 20(35):23034–23054.
- Chiantia, S., Ries, J., and Schwille, P. 2009. Fluorescence correlation spectroscopy in membrane structure elucidation. *Biochimica et Biophysica Acta (BBA) - Biomembranes*, 1788(1):225–233.
- Colagiorgi, A., Di Ciccio, P., Zanardi, E., Ghidini, S., and Ianieri, A. 2016. A Look inside the *Listeria monocytogenes* Biofilms Extracellular Matrix. *Microorganisms*, 4(3):22.
- Cole, N. B. 2013. Site-Specific Protein Labeling with SNAP-Tags. In *Current Protocols in Protein Science*, volume 73, pages 30.1.1–30.1.16. John Wiley & Sons, Inc., Hoboken, NJ, USA.
- Cranfill, P. J., Sell, B. R., Baird, M. A., Allen, J. R., Lavagnino, Z., de Gruiter, H. M., Kremers, G.-J., Davidson, M. W., Ustione, A., and Piston, D. W. 2016. Quantitative assessment of fluorescent proteins. *Nature Methods*, 13(7):557–562.
- Dalal, R. B., Digman, M. A., Horwitz, A. F., Vetri, V., and Gratton, E. 2008. Determination of particle number and brightness using a laser scanning confocal microscope operating in the analog mode. *Microscopy research and technique*, 71(1):69–81.
- Deptuła, T., Buitenhuis, J., Jarzebski, M., Patkowski, A., and Gapinski, J. 2015. Size of Submicrometer Particles Measured by FCS: Correction of the Confocal Volume. *Langmuir*, 31(24):6681–6687.
- Dertinger, T., Pacheco, V., von der Hocht, I., Hartmann, R., Gregor, I., and Enderlein, J. 2007. Two-Focus Fluorescence Correlation Spectroscopy: A New Tool for Accurate and Absolute Diffusion Measurements. *ChemPhysChem*, 8(3):433–443.
- Di Rienzo, C., Piazza, V., Gratton, E., Beltram, F., and Cardarelli, F. 2014. Probing short-range protein Brownian motion in the cytoplasm of living cells. *Nature Communications*, 5:5891.
- Digman, M. A., Brown, C. M., Sengupta, P., Wiseman, P. W., Horwitz, A. R., and Gratton, E. 2005. Measuring fast dynamics in solutions and cells with a laser scanning microscope. *Biophysical journal*, 89(2):1317–27.

- Digman, M. A., Dalal, R., Horwitz, A. F., and Gratton, E. 2008. Mapping the number of molecules and brightness in the laser scanning microscope. *Biophysical journal*, 94(6):2320–2332.
- Digman, M. A. and Gratton, E. 2009. Imaging Barriers to Diffusion by Pair Correlation Functions. *Biophysical Journal*, 97(2):665–673.
- Dittrich, P. S. and Schwille, P. 2002. Spatial Two-Photon Fluorescence Cross-Correlation Spectroscopy for Controlling Molecular Transport in Microfluidic Structures. *Analytical Chemistry*, 74(17):4472–4479.
- Dörlich, R. M., Chen, Q., Niklas Hedde, P., Schuster, V., Hippler, M., Wesslowski, J., Davidson, G., and Nienhaus, G. U. 2015. Dual-color dual-focus line-scanning FCS for quantitative analysis of receptor-ligand interactions in living specimens. *Scientific Reports*, 5(1):10149.
- Eggeling, C., Ringemann, C., Medda, R., Schwarzmann, G., Sandhoff, K., Polyakova, S., Belov, V. N., Hein, B., von Middendorff, C., Schönle, A., and Hell, S. W. 2009. Direct observation of the nanoscale dynamics of membrane lipids in a living cell. *Nature*, 457(7233):1159–1162.
- Einstein, A. 1905. Über die von der molekularkinetischen Theorie der Wärme geforderte Bewegung von in ruhenden Flüssigkeiten suspendierten Teilchen. *Annalen der Physik*, 322(8):549–560.
- Elson, E. L., Schlessinger, J., Koppel, D. E., Axelrod, D., and Webb, W. W. 1976. Measurement of lateral transport on cell surfaces. *Progress in clinical and biological research*, 9:137–47.
- Enderlein, J. and Erdmann, R. 1997. Fast fitting of multi-exponential decay curves. *Optics Communications*, 134(1-6):371–378.
- Etoc, F., Balloul, E., Vicario, C., Normanno, D., Liße, D., Sittner, A., Piehler, J., Dahan, M., and Coppey, M. 2018. Non-specific interactions govern cytosolic diffusion of nanosized objects in mammalian cells. *Nature Materials*, 17(8):740–746.
- Fahey, P. F., Koppel, D. E., Barak, L. S., Wolf, D. E., Elson, E. L., and Webb, W. W. 1977. Lateral diffusion in planar lipid bilayers. *Science (New York, N.Y.)*, 195(4275):305–6.
- Finan, K., Raulf, A., and Heilemann, M. 2015. A Set of Homo-Oligomeric Standards Allows Accurate Protein Counting. *Angewandte Chemie International Edition*, 54(41):12049–12052.
- Flemming, H.-C. and Wingender, J. 2010. The biofilm matrix. *Nature Reviews Microbiology*, 8(9):623–633.
- Foo, Y. H., Naredi-Rainer, N., Lamb, D. C., Ahmed, S., and Wohland, T. 2012. Factors affecting the quantification of biomolecular interactions by fluorescence cross-correlation spectroscopy. *Biophysical journal*, 102(5):1174–83.

- Fricke, F., Beaudouin, J., Eils, R., and Heilemann, M. 2015. One, two or three? Probing the stoichiometry of membrane proteins by single-molecule localization microscopy. *Scientific Reports*, 5(1):14072.
- Ganesan, M., Knier, S., Younger, J. G., and Solomon, M. J. 2016. Associative and Entanglement Contributions to the Solution Rheology of a Bacterial Polysaccharide. *Macromolecules*, 49(21):8313–8321.
- Ghosh, A., Karedla, N., Thiele, J. C., Gregor, I., and Enderlein, J. 2018. Fluorescence lifetime correlation spectroscopy: Basics and applications.
- Godin, A. G., Costantino, S., Lorenzo, L.-E., Swift, J. L., Sergeev, M., Ribeiro-da Silva, A., De Koninck, Y., and Wiseman, P. W. 2011. Revealing protein oligomerization and densities in situ using spatial intensity distribution analysis. *Proceedings of the National Academy of Sciences of the United States of America*, 108(17):7010–5.
- Grußmayer, K. S., Yserentant, K., and Herten, D.-P. 2019. Photons in - numbers out: perspectives in quantitative fluorescence microscopy for in situ protein counting. *Methods and Applications in Fluorescence*, 7(1):012003.
- Harris, T. J. C. and Tepass, U. 2010. Adherens junctions: from molecules to morphogenesis. *Nature Reviews Molecular Cell Biology*, 11(7):502–514.
- Harrison, O. J., Jin, X., Hong, S., Bahna, F., Ahlsen, G., Brasch, J., Wu, Y., Vendome, J., Felsovalyi, K., Hampton, C. M., Troyanovsky, R. B., Ben-Shaul, A., Frank, J., Troyanovsky, S. M., Shapiro, L., and Honig, B. 2011. The extracellular architecture of adherens junctions revealed by crystal structures of type I cadherins. *Structure (London, England : 1993)*, 19(2):244–56.
- Haupts, U., Maiti, S., Schwille, P., and Webb, W. W. 1998. Dynamics of fluorescence fluctuations in green fluorescent protein observed by fluorescence correlation spectroscopy. *Proceedings of the National Academy of Sciences of the United States of America*, 95(23):13573–8.
- Heinze, K. G., Jahnz, M., and Schwille, P. 2004. Triple-Color Coincidence Analysis: One Step Further in Following Higher Order Molecular Complex Formation. *Biophysical Journal*, 86(1):506–516.
- Hellriegel, C., Caiolfa, V. R., Corti, V., Sidenius, N., and Zamai, M. 2011. Number and brightness image analysis reveals ATF-induced dimerization kinetics of uPAR in the cell membrane. *The FASEB journal : official publication of the Federation of American Societies for Experimental Biology*, 25(9):2883–2897.
- Hendrix, J., Flors, C., Dedecker, P., Hofkens, J., and Engelborghs, Y. 2008. Dark states in monomeric red fluorescent proteins studied by fluorescence correlation and single molecule spectroscopy. *Biophysical journal*, 94(10):4103–13.

- Hendrix, J., Schrimpf, W., Höller, M., and Lamb, D. 2013. Pulsed Interleaved Excitation Fluctuation Imaging. *Biophysical Journal*, 105(4):848–861.
- Hennen, J., Hur, K.-H., Karuka, S. R., Luxton, G. G., and Mueller, J. D. 2019a. Protein oligomerization and mobility within the nuclear envelope evaluated by the time-shifted mean-segmented Q factor. *Methods*, 157:28–41.
- Hennen, J., Hur, K.-H., and Mueller, J. D. 2019b. Quantitative modeling of self-oligomerization of proteins in the nuclear envelope by fluorescence fluctuation analysis. *Analytical Biochemistry*, 582:113359.
- Höfling, F. and Franosch, T. 2013. Anomalous transport in the crowded world of biological cells. *Reports on Progress in Physics*, 76(4):046602.
- Hufnagel, D. A., Depas, W. H., and Chapman, M. R. 2015. The Biology of the Escherichia coli Extracellular Matrix. *Microbiology Spectrum*, 3(3).
- Huppa, J. B. and Davis, M. M. 2003. T-cell-antigen recognition and the immunological synapse. *Nature Reviews Immunology*, 3(12):973–983.
- Hur, K.-H., Macdonald, P. J., Berk, S., Angert, C. I., Chen, Y., and Mueller, J. D. 2014. Quantitative measurement of brightness from living cells in the presence of photodepletion. *PloS one*, 9(5):e97440.
- Hwang, L. C., Gösch, M., Lasser, T., and Wohland, T. 2006. Simultaneous Multicolor Fluorescence Cross-Correlation Spectroscopy to Detect Higher Order Molecular Interactions Using Single Wavelength Laser Excitation. *Biophysical Journal*, 91(2):715–727.
- Indra, I., Choi, J., Chen, C.-S., Troyanovsky, R. B., Shapiro, L., Honig, B., and Troyanovsky, S. M. 2018. Spatial and temporal organization of cadherin in punctate adherens junctions. *Proceedings of the National Academy of Sciences of the United States of America*, 115(19):E4406–E4415.
- Jacques, M., Aragon, V., and Tremblay, Y. D. 2010. Biofilm formation in bacterial pathogens of veterinary importance.
- Jazani, S., Sgouralis, I., Shafraz, O. M., Levitus, M., Sivasankar, S., and Pressé, S. 2019. An alternative framework for fluorescence correlation spectroscopy. *Nature Communications*, 10(1):3662.
- Jenkins, E., Santos, A. M., O’Brien-Ball, C., Felce, J. H., Wilcock, M. J., Hatherley, D., Dustin, M. L., Davis, S. J., Eggeling, C., and Sezgin, E. 2018. Reconstitution of immune cell interactions in free-standing membranes. *Journal of cell science*, 132(4):jcs219709.
- Kaden, D., Voigt, P., Munter, L.-M., Bobowski, K. D., Schaefer, M., and Multhaup, G. 2009. Subcellular localization and dimerization of APLP1 are strikingly different from APP and APLP2. *Journal of cell science*, 122(Pt 3):368–377.

- Kannan, B., Guo, L., Sudhaharan, T., Ahmed, S., Maruyama, I., and Wohland, T. 2007. Spatially Resolved Total Internal Reflection Fluorescence Correlation Microscopy Using an Electron Multiplying Charge-Coupled Device Camera. *Anal. Chem.*, 79(12):4463–4470.
- Kapanidis, A. N., Lee, N. K., Laurence, T. A., Doose, S., Margeat, E., and Weiss, S. 2004. Fluorescence-aided molecule sorting: analysis of structure and interactions by alternating-laser excitation of single molecules. *Proceedings of the National Academy of Sciences of the United States of America*, 101(24):8936–41.
- Kapusta, P., Machan, R., Benda, A., and Hof, M. 2012. Fluorescence Lifetime Correlation Spectroscopy (FLCS): Concepts, Applications and Outlook. *International Journal of Molecular Sciences*, 13(12):12890–12910.
- Kaur, G., Costa, M. W., Nefzger, C. M., Silva, J., Fierro-González, J. C., Polo, J. M., Bell, T. D., and Plachta, N. 2013. Probing transcription factor diffusion dynamics in the living mammalian embryo with photoactivatable fluorescence correlation spectroscopy. *Nature Communications*, 4(1):1637.
- Kim, S. A., Heinze, K. G., Bacia, K., Waxham, M. N., and Schwille, P. 2005. Two-Photon Cross-Correlation Analysis of Intracellular Reactions with Variable Stoichiometry. *Biophysical Journal*, 88(6):4319–4336.
- Kim, S. A., Tai, C.-Y., Mok, L.-P., Mosser, E. A., and Schuman, E. M. 2011. Calcium-dependent dynamics of cadherin interactions at cell-cell junctions. *Proceedings of the National Academy of Sciences of the United States of America*, 108(24):9857–62.
- Körstgens, V., Flemming, H.-C., Wingender, J., and Borchard, W. 2001. Influence of calcium ions on the mechanical properties of a model biofilm of mucoid *Pseudomonas aeruginosa*. *Water Science and Technology*, 43(6):49–57.
- Krieger, J. W., Singh, A. P., Bag, N., Garbe, C. S., Saunders, T. E., Langowski, J., and Wohland, T. 2015. Imaging fluorescence (cross-) correlation spectroscopy in live cells and organisms. *Nature Protocols*, 10(12):1948–1974.
- Lawrence, J., Swerhone, G., Kuhlicke, U., and Neu, T. 2007. In situ evidence for microdomains in the polymer matrix of bacterial microcolonies. *Canadian Journal of Microbiology*, 53(3):450–458.
- Liu, B., Mavrova, S. N., Van Den Berg, J., Kristensen, S. K., Mantovanelli, L., Veenhoff, L. M., Poolman, B., and Boersma, A. J. 2018. Influence of Fluorescent Protein Maturation on FRET Measurements in Living Cells. *ACS Sensors*, 3(9):1735–1742.
- Magde, D., Elson, E., and Webb, W. W. 1972. Thermodynamic Fluctuations in a Reacting System - Measurement by Fluorescence Correlation Spectroscopy. *Physical Review Letters*, 29(11):705–708.

- Manley, S., Gillette, J. M., Patterson, G. H., Shroff, H., Hess, H. F., Betzig, E., and Lippincott-Schwartz, J. 2008. High-density mapping of single-molecule trajectories with photoactivated localization microscopy. *Nature Methods*, 5(2):155–157.
- Mayer, M. C., Kaden, D., Schauenburg, L., Hancock, M. A., Voigt, P., Roeser, D., Barucker, C., Than, M. E., Schaefer, M., and Multhaup, G. 2014. Novel zinc-binding site in the E2 domain regulates amyloid precursor-like protein 1 (APLP1) oligomerization. *The Journal of biological chemistry*, 289(27):19019–30.
- Mayer, M. C., Schauenburg, L., Thompson-Steckel, G., Dunsing, V., Kaden, D., Voigt, P., Schaefer, M., Chiantia, S., Kennedy, T. E., and Multhaup, G. 2016. Amyloid precursor-like protein 1 (APLP1) exhibits stronger zinc-dependent neuronal adhesion than amyloid precursor protein and APLP2. *Journal of Neurochemistry*, 137(2):266–276.
- McCulloch, T. W., MacLean, D. M., and Kammermeier, P. J. 2019. Comparing the Performance of mScarlet-I, mRuby3, and mCherry as FRET Acceptors for mNeonGreen. *bioRxiv*.
- Metzler, R., Jeon, J.-H., and Cherstvy, A. 2016. Non-Brownian diffusion in lipid membranes: Experiments and simulations. *Biochimica et Biophysica Acta (BBA) - Biomembranes*, 1858(10):2451–2467.
- Metzler, R., Jeon, J.-H., Cherstvy, A. G., and Barkai, E. 2014. Anomalous diffusion models and their properties: non-stationarity, non-ergodicity, and ageing at the centenary of single particle tracking. *Phys. Chem. Chem. Phys.*, 16(44):24128–24164.
- Monzel, C., Schmidt, D., Kleusch, C., Kirchenb uchler, D., Seifert, U., Smith, A. S., Sengupta, K., and Merkel, R. 2015. Measuring fast stochastic displacements of bio-membranes with dynamic optical displacement spectroscopy. *Nature Communications*, 6.
- M uller, B. K., Zaychikov, E., Br auchle, C., and Lamb, D. C. 2005. Pulsed Interleaved Excitation. *Biophysical Journal*, 89(5):3508–3522.
- M uller, J. D. 2004. Cumulant Analysis in Fluorescence Fluctuation Spectroscopy. *Biophysical Journal*, 86(6):3981–3992.
- M uller, J. D., Chen, Y., and Gratton, E. 2000. Resolving Heterogeneity on the Single Molecular Level with the Photon-Counting Histogram. *Biophysical Journal*, 78(1):474–486.
- M uller, U. C., Deller, T., and Korte, M. 2017. Not just amyloid: Physiological functions of the amyloid precursor protein family.
- Padilla-Parra, S., Audug e, N., Coppey-Moisan, M., and Tramier, M. 2011. Dual-color fluorescence lifetime correlation spectroscopy to quantify protein-protein interactions in live cell. *Microscopy Research and Technique*, 74(8):788–793.

- Perrin, J. 1916. *Atoms*. London : Constable, London.
- Perrin, J. 1926. Jean Baptiste Perrin - Nobel Lecture: Discontinuous Structure of Matter.
- Petersen, N. O. 1986. Scanning fluorescence correlation spectroscopy. I. Theory and simulation of aggregation measurements. *Biophysical journal*, 49(4):809–15.
- Petrásek, Z. and Schwille, P. 2008. Precise measurement of diffusion coefficients using scanning fluorescence correlation spectroscopy. *Biophysical journal*, 94(4):1437–48.
- Puchner, E. M., Walter, J. M., Kasper, R., Huang, B., and Lim, W. A. 2013. Counting molecules in single organelles with superresolution microscopy allows tracking of the endosome maturation trajectory. *Proceedings of the National Academy of Sciences of the United States of America*, 110(40):16015–20.
- Reverey, J. F., Jeon, J.-H., Bao, H., Leippe, M., Metzler, R., and Selhuber-Unkel, C. 2015. Superdiffusion dominates intracellular particle motion in the supercrowded cytoplasm of pathogenic *Acanthamoeba castellanii*. *Scientific reports*, 5:11690.
- Ridgeway, W. K., Millar, D. P., and Williamson, J. R. 2012a. Quantitation of ten 30S ribosomal assembly intermediates using fluorescence triple correlation spectroscopy. *Proceedings of the National Academy of Sciences of the United States of America*, 109(34):13614–13619.
- Ridgeway, W. K., Millar, D. P., and Williamson, J. R. 2012b. The Spectroscopic Basis of Fluorescence Triple Correlation Spectroscopy. *The Journal of Physical Chemistry B*, 116(6):1908–1919.
- Rienzo, C. D., Gratton, E., Beltram, F., and Cardarelli, F. 2013. Fast spatiotemporal correlation spectroscopy to determine protein lateral diffusion laws in live cell membranes. *Proceedings of the National Academy of Sciences*, 110(30):12307–12312.
- Ries, J., Bayer, M., Csúcs, G., Dirkx, R., Solimena, M., Ewers, H., and Schwille, P. 2010a. Automated suppression of sample-related artifacts in Fluorescence Correlation Spectroscopy. *Optics Express*, 18(11):11073.
- Ries, J., Chiantia, S., and Schwille, P. 2009a. Accurate determination of membrane dynamics with line-scan FCS. *Biophysical journal*, 96(5):1999–2008.
- Ries, J., Chiantia, S., and Schwille, P. 2009b. Accurate Determination of Membrane Dynamics with Line-Scan FCS. *Biophysical Journal*, 96(5):1999–2008.
- Ries, J., Petrášek, Z., García-Sáez, A. J., and Schwille, P. 2010b. A comprehensive framework for fluorescence cross-correlation spectroscopy. *New Journal of Physics*, 12(11):113009.
- Ries, J., Petrášek, Z., García-Sáez, A. J., and Schwille, P. 2010c. A comprehensive framework for fluorescence cross-correlation spectroscopy. *New Journal of Physics*, 12(11):113009.

- Ries, J. and Schwille, P. 2006. Studying Slow Membrane Dynamics with Continuous Wave Scanning Fluorescence Correlation Spectroscopy. *Biophysical Journal*, 91(5):1915–1924.
- Ries, J., Yu, S. R., Burkhardt, M., Brand, M., and Schwille, P. 2009c. Modular scanning FCS quantifies receptor-ligand interactions in living multicellular organisms. *Nature Methods*, 6.
- Sankaran, J., Bag, N., Kraut, R. S., and Wohland, T. 2013. Accuracy and Precision in Camera-Based Fluorescence Correlation Spectroscopy Measurements. *Analytical Chemistry*, 85(8):3948–3954.
- Sankaran, J., Tan, N. J. H. J., But, K. P., Cohen, Y., Rice, S. A., and Wohland, T. 2019. Single microcolony diffusion analysis in *Pseudomonas aeruginosa* biofilms. *npj Biofilms and Microbiomes*, 5(1):35.
- Santuy, A., Rodríguez, J.-R., DeFelipe, J., and Merchán-Pérez, A. 2018. Study of the Size and Shape of Synapses in the Juvenile Rat Somatosensory Cortex with 3D Electron Microscopy. *eNeuro*, 5(1).
- Savtchenko, L. P. and Rusakov, D. A. 2007. The optimal height of the synaptic cleft. *Proceedings of the National Academy of Sciences*, 104(6):1823–1828.
- Schermelleh, L., Ferrand, A., Huser, T., Eggeling, C., Sauer, M., Biehlmaier, O., and Drummen, G. P. C. 2019. Super-resolution microscopy demystified. *Nature Cell Biology*, 21(1):72–84.
- Schilling, S., Mehr, A., Ludewig, S., Stephan, J., Zimmermann, M., August, A., Strecker, P., Korte, M., Koo, E. H., Müller, U., Kins, S., and Eggert, S. 2017. APLP1 is a synaptic cell adhesion molecule, supporting maintenance of dendritic spines and basal synaptic transmission. *The Journal of Neuroscience*, pages 1875–16.
- Schneider, F., Waithe, D., Clausen, M. P., Galiani, S., Koller, T., Ozhan, G., Eggeling, C., and Sezgin, E. 2017. Diffusion of lipids and GPI-anchored proteins in actin-free plasma membrane vesicles measured by STED-FCS. *Molecular Biology of the Cell*, 28(11):1507–1518.
- Schrimpf, W., Lemmens, V., Smisdom, N., Ameloot, M., Lamb, D. C., and Hendrix, J. 2018. Crosstalk-free multicolor RICS using spectral weighting. *Methods*, 140-141:97–111.
- Schwille, P., Kummer, S., Heikal, A. A., Moerner, W. E., and Webb, W. W. 2000. Fluorescence correlation spectroscopy reveals fast optical excitation-driven intramolecular dynamics of yellow fluorescent proteins. *Proceedings of the National Academy of Sciences of the United States of America*, 97(1):151–6.
- Schwille, P., Meyer-Almes, F., and Rigler, R. 1997. Dual-color fluorescence cross-correlation spectroscopy for multicomponent diffusional analysis in solution. *Bio-*

- physical Journal*, 72(4):1878–1886.
- Serra, D. O., Richter, A. M., Klauck, G., Mika, F., and Hengge, R. 2013. Microanatomy at cellular resolution and spatial order of physiological differentiation in a bacterial biofilm. *mBio*, 4(2).
- Simmons, M., Drescher, K., Nadell, C. D., and Bucci, V. 2018. Phage mobility is a core determinant of phage-bacteria coexistence in biofilms. *The ISME Journal*, 12(2):531–543.
- Singh, R., Sahore, S., Kaur, P., Rani, A., and Ray, P. 2016. Penetration barrier contributes to bacterial biofilm-associated resistance against only select antibiotics, and exhibits genus-, strain- and antibiotic-specific differences. *Pathogens and Disease*, 74(6):ftw056.
- Sisan, D. R., Arevalo, R., Graves, C., McAllister, R., and Urbach, J. S. 2006. Spatially resolved fluorescence correlation spectroscopy using a spinning disk confocal microscope. *Biophysical journal*, 91(11):4241–52.
- Skinner, J. P., Chen, Y., and Müller, J. D. 2008. Fluorescence Fluctuation Spectroscopy in the Presence of Immobile Fluorophores. *Biophysical Journal*, 94(6):2349–2360.
- Soba, P., Eggert, S., Wagner, K., Zentgraf, H., Siehl, K., Kreger, S., Löwer, A., Langer, A., Merdes, G., Paro, R., Masters, C. L., Müller, U., Kins, S., and Beyreuther, K. 2005. Homo- and heterodimerization of APP family members promotes intercellular adhesion. *The EMBO Journal*, 24(20):3624–3634.
- Stewart, P. S. and Franklin, M. J. 2008. Physiological heterogeneity in biofilms. *Nature Reviews Microbiology*, 6(3):199–210.
- Südhof, T. C. 2018. Towards an Understanding of Synapse Formation. *Neuron*, 100(2):276–293.
- Tepass, U., Truong, K., Godt, D., Ikura, M., and Peifer, M. 2000. Cadherins in embryonic and neural morphogenesis. *Nature Reviews Molecular Cell Biology*, 1(2):91–100.
- Thevathasan, J. V., Kahnwald, M., Cieśliński, K., Hoess, P., Peneti, S. K., Reitberger, M., Heid, D., Kasuba, K. C., Hoerner, S. J., Li, Y., Wu, Y.-L., Mund, M., Matti, U., Pereira, P. M., Henriques, R., Nijmeijer, B., Kueblbeck, M., Sabinina, V. J., Ellenberg, J., and Ries, J. 2019. Nuclear pores as versatile reference standards for quantitative superresolution microscopy. *Nature Methods*, 16(10):1045–1053.
- Trullo, A., Corti, V., Arza, E., Caiolfa, V. R., and Zamai, M. 2013. Application limits and data correction in number of molecules and brightness analysis. *Microscopy Research and Technique*, 76(11):1135–1146.
- Vámosi, G., Mücke, N., Müller, G., Krieger, J. W., Curth, U., Langowski, J., and Tóth, K. 2016. EGFP oligomers as natural fluorescence and hydrodynamic standards.

- Scientific reports*, 6:33022.
- Vidakovic, L., Singh, P. K., Hartmann, R., Nadell, C. D., and Drescher, K. 2018. Dynamic biofilm architecture confers individual and collective mechanisms of viral protection. *Nature Microbiology*, 3(1):26–31.
- Wagner, C. E., Turner, B. S., Rubinstein, M., McKinley, G. H., and Ribbeck, K. 2017. A Rheological Study of the Association and Dynamics of MUC5AC Gels. *Biomacromolecules*, 18(11):3654–3664.
- Wawrezynieck, L., Rigneault, H., Marguet, D., and Lenne, P.-F. 2005. Fluorescence Correlation Spectroscopy Diffusion Laws to Probe the Submicron Cell Membrane Organization. *Biophysical Journal*, 89(6):4029–4042.
- Weidemann, T., Mücksch, J., and Schwille, P. 2014. Fluorescence fluctuation microscopy: a diversified arsenal of methods to investigate molecular dynamics inside cells. *Current Opinion in Structural Biology*, 28:69–76.
- Weiss, M. 2014. Crowding, Diffusion, and Biochemical Reactions. *International Review of Cell and Molecular Biology*, 307:383–417.
- Weiss, M., Elsner, M., Kartberg, F., and Nilsson, T. 2004. Anomalous subdiffusion is a measure for cytoplasmic crowding in living cells. *Biophysical journal*, 87(5):3518–3524.
- Wohland, T., Shi, X., Sankaran, J., and Stelzer, E. H. 2010. Single Plane Illumination Fluorescence Correlation Spectroscopy (SPIM-FCS) probes inhomogeneous three-dimensional environments. *Optics Express*, 18(10):10627.
- Wu, B., Chen, Y., and Müller, J. D. 2008. Fluorescence correlation spectroscopy of finite-sized particles. *Biophysical Journal*, 94(7):2800–2808.
- Wu, B., Chen, Y., and Müller, J. D. 2009. Fluorescence Fluctuation Spectroscopy of mCherry in Living Cells. *Biophysical Journal*, 96(6):2391–2404.
- Wu, B. and Müller, J. D. 2005. Time-Integrated Fluorescence Cumulant Analysis in Fluorescence Fluctuation Spectroscopy. *Biophysical Journal*, 89(4):2721–2735.
- Wu, B., Singer, R. H., and Mueller, J. D. 2013. Time-Integrated Fluorescence Cumulant Analysis and Its Application in Living Cells. *Methods in Enzymology*, 518:99–119.
- Wu, Y., Kanchanawong, P., and Zaidel-Bar, R. 2015. Actin-delimited adhesion-independent clustering of E-cadherin forms the nanoscale building blocks of adherens junctions. *Developmental cell*, 32(2):139–54.
- Zhao, Z. W., White, M. D., Alvarez, Y. D., Zenker, J., Bissiere, S., and Plachta, N. 2017. Quantifying transcription factor-DNA binding in single cells in vivo with photoactivatable fluorescence correlation spectroscopy. *Nature Protocols*, 12(7):1458–1471.

Eigenständigkeitserklärung (Declaration)

Hiermit versichere ich, dass ich die vorliegende Arbeit mit dem Titel

*Fluorescence fluctuation spectroscopy techniques to quantify molecular interactions
and dynamics in complex biological systems*

ohne unzulässige Hilfe Dritter und ohne Benutzung anderer als der angegebenen Hilfsmittel angefertigt habe; die aus fremden Quellen direkt oder indirekt übernommenen Gedanken sind als solche kenntlich gemacht. Die Arbeit wurde bisher weder im Inland noch im Ausland in gleicher oder ähnlicher Form einer anderen Prüfungsbehörde vorgelegt.

Diese Arbeit wurde von Januar 2016 bis Dezember 2019 unter der Betreuung von Prof. Dr. Salvatore Chiantia an der Universität Potsdam angefertigt.

Ort, Datum

Valentin Dunsing

I herewith declare that I have produced this thesis

*Fluorescence fluctuation spectroscopy techniques to quantify molecular interactions
and dynamics in complex biological systems*

without the prohibited assistance of third parties and without making use of aids other than those specified; notions taken over directly or indirectly from other sources have been identified as such. This thesis has not been previously presented in identical or similar form to any other german or foreign examination board.

The thesis work was conducted between January 2016 and December 2019 under the supervision of Prof. Dr. Salvatore Chiantia at the University of Potsdam.

City, Date

Valentin Dunsing